

Experimental investigation of magnetism in natural silk polymers

Varun Ranade

*A dissertation submitted for the partial fulfilment of degree of Doctor of
Philosophy in Physical Science*



Indian Institute of Science Education and Research, Mohali

May 2023

Certificate of Examination

This is to certify that the dissertation titled **Experimental investigation of magnetism in natural silk polymers** submitted by **Varun Ranade** (Reg. No. MP15016) for the partial fulfillment of Integrated MS-Ph.D. Dual Degree programme of the institute, has been examined by the thesis committee duly appointed by the institute. The committee finds the work done by the candidate satisfactory and recommends that the report be accepted.

[Thesis Committee Member 1]

[Member 2]

[Member 3]

Dr. Kamal P. Singh
(Supervisor)

Dated: [16.05.2023]

Declaration

The work presented in this dissertation has been carried out by me under the guidance of Dr. Kamal P. Singh at the Indian Institute of Science Education and Research, Mohali.

This work has not been submitted in part or in full for a degree, a diploma, or a fellowship to any other university or institute. Whenever contributions of others are involved, every effort is made to indicate this clearly, with due acknowledgment of collaborative research and discussions. This thesis is a bonafide record of original work done by me and all sources listed within have been detailed in the bibliography.

Varun Ranade
(Candidate)

Dated: [05.01.2023]

In my capacity as the supervisor of the candidates project work, I certify that the above statements by the candidate are true to the best of my knowledge.

Dr. Kamal P. Singh
(Supervisor)

Dated: [16.05.2023]

Acknowledgements

I express my sincere gratitude to Dr. Kamal P. Singh for providing lab facilities and helping to prepare manuscripts. I thank my doctoral committee, Dr. Sudeshna Sinha and Dr. Anant Venkatesan, for their timely input regarding my work. I also thank Dr. Sameer Biswas and Dr. Sanjeev Kumar for their valuable time acting as substitute committee members during my comprehensive and SRF presentations. I thank Dr. Ram J. Choudhary for his valuable time, effort, and lab facilities. I thank Dr. Dhanveer S. Rana and Dr. Dinesh K. Shukla for providing valuable input and Sumit Sarkar, Sofia, and Priyanka for their help in performing experiments. I thank Biswajit Panda for his effort to provide computational DFT calculations explaining my experimental results. I thank my labmates and friends, Dr. Sunil Dahiya, Dr. Komal Choudhary, Shivali Sokhi, Akansha Tyagi, Nagendra Singh, Akanksha Gautam, Vishwas Kamal, Sarthak Sahoo, and Sanath K. Ghosh for their company during my time at the institute. I also thank other former and current lab members, Dr. Bhavesh, Jayant Dewara, and Sandeep Jhakhar, for making a healthy scientific environment in the lab and providing help whenever required.

I would thank all my teachers during my M.S. years for their valuable time and effort. I also thank Dr. Devendra S. Mehta for fruitful scientific discussions and encouragement during my research. I would thank my parents, Prof. Ravi Kumar and Ms. Hema Sharma, my sister, Ms. Akanksha Ranade, and my wife, Ms. Sajal Shradha, for their immense emotional support.

I want to thank IISER Mohali for their financial support and accommodation during my degree. I would especially like to thank the IISER Mohali library for providing a comfortable and serene environment to study. I thank UGC-DAE CSR Indore center and RRCAT for funding and provision of experimental facilities like SQUID magnetometer, XPS, FTIR, and XAS. I thank NIT Hamirpur, SAIF-IIT Bombay, SAIF-PU Chandigarh, and CIF- IISER Bhopal for providing EDX, EPR, ICPMS, and SQUID magnetometer facilities.

Abstract

Over 400 million years of evolution, Nature has perfected the structure of silks secreted by arthropods to support various aspects of their life. Extensive research has discovered that the molecular structure of silks has been engineered to encapsulate many remarkable mechanical, optical, and biological properties surpassing even artificial materials. Surprisingly, these insects produce multi-functional silk biopolymers using elementary processing of simple amino acids in water. Materials like steel and Kevlar require much more complex manufacturing processes but still fail to match (spider and silkworm) silk's toughness, albeit their mechanical strength is equivalent to silk's. In short, natural silks are a model material for the future and a fine example of how much Nature has to offer humanity if we look closely enough. A large part of recent research is focused on mimicking silks to produce advanced materials for biomedical and technological applications as they offer eco-friendly, biocompatible, and sustainable alternatives to existing solutions.

In the present work, we discuss the intrinsic magnetic properties of natural silk polymers, namely spider dragline silks and mulberry silkworm silks. We present a thorough magnetic study of silks, like their magnetic behavior, the possible origin of magnetism, and magnetic ordering. We discovered silk biopolymers act as amorphous magnets with a stable, sustainable ferromagnetic character from very low (5 K) to high temperatures (400 K). Notably, the magnetization of spider dragline silks is more significant than most organic magnets. Investigation into the source of magnetism revealed that the magnetism possibly originates due to the presence of persistent organic radicals in natural silks. Therefore, silks offer a new novel route to fabricate stable organic magnets with exceptional strength and toughness unmatched by the presently known ones. We established our claims by experimenting on more than 20 silk samples obtained from multiple spiders (*Araneus* and *Neoscona* families) and silkworms (*Bombyx mori*) using SQUID magnetometry, EPR spectroscopy, and various elemental analysis techniques like EDX, XPS, XAS, and ICPMS. These are the first reports of magnetic experiments to show that atomic defects in the building blocks of pure silk fibers induce significant permanent magnetization, thereby opening their direct magnetic applications.

Atomistic defects in silks result in the formation of radicals in them. These radicals are sterically protected in silk's structure up to very high temperatures. Radicals in close

vicinity tend to interact with each other directly. These interactions can be ferromagnetic or anti-ferromagnetic, depending on the configuration and distance of neighboring radicals. The interacting radicals form small clusters trapped in the glassy state in the silk protein matrix and are distributed throughout the silk's structure, leading to an overall magnetic response. We showed that one could externally control the magnetization of silks by manifesting additional defects (or deformations) in their structure using simple techniques like stretching and cutting. Moreover, during the thermomagnetic analysis, we discovered a unique magnetic transition in all silk samples around 120 K, irrespective of their host insect, i.e., spiders or silkworms.

Using a sensitive torsion pendulum that mimicked a spider suspending from its dragline silk, we discovered that even a micrometer-thin silk thread of spider dragline silk could sense magnetic fields up to $30 \mu\text{T}$ in ambient conditions. We demonstrate that silks can act as bio-magnetosensors. Moreover, we also developed unique silk-based tiny swimmers/propellers that act as organic magnetic robots (Bio-Magbots). These silk-based bio-magbots can be controlled externally under small magnetic fields to manipulate microscopic organic and inorganic matter. We explicitly illustrated that silk-based magnetic robots could perform the non-contact on-demand translation and rotatory motions. Silk-based magnetic robots could also magnetically trap organic and inorganic material at a specific location using small localized magnetic fields ($\approx 20 \text{ mT}$). In a remote-controlled fashion, we demonstrated the transport of various cargo, such as plant tissues, animal tissues, polymer bundles, and non-magnetic immiscible chemicals, on the surface of the water using silk swimmers.

Silk-based bio-magbots can perform targeted drug delivery, magnetic trapping, and bioremediation in a cell-like liquid environment. Furthermore, magnetically actuated artificial muscles and scaffolds for tissue engineering could be developed using silk and silk-based materials. Our work also opens the intriguing potential of silk in developing ultralightweight and thin bio-magnetosensors and nanoelectromechanical systems (NEMS) made from sustainable materials.

The present research establishes natural silk polymers as amorphous magnets and opens a new route to developing organic magnets by biomimicking silk proteins. Unlike most organic magnets, silks can sustain their ferromagnetism for a very long time (years) without any decrease in their magnetization. They can be easily stored at room temperature and

50% relative humidity. Natural silks can be an archetypal polymer for developing organic magnets that sustain ferromagnetism up to high temperatures and simultaneously have silk's excellent physical properties (mechanical, optical, etc.). Such protein-based magnets will have a unique advantage in biomedical sectors. The work has implications in material science, materiomics, quantum biology, biomedical engineering, and mechanical engineering.

List of Figures

1.1	Types of Spider silks. Schematic overview of different silk types produced by female orb-weaving spiders (<i>Araneae</i>). Each silk type (highlighted in red) is tailored for a specific purpose. (Taken from [1])	3
1.2	Silk structure at a glance. figure (a) and (c) describes the hierarchical shell-core structure of silkworm silk and spider silk, respectively. (b), (d) shows that the core is made of many fibrils (tertiary structure), and those fibrils are comprised of crystallites made of β -sheets and the amorphous chains made of helices and turns. (Adapted from [2, 3])	5
1.3	Conformation of different motifs in silk. The above table shows the different conformations that amino acid sequence motifs take under ambient conditions in silk. We can see that the amorphous part consists of 3_{10} - helices, β - turns formed by GGX and GPGXX motifs in spider silk, and the crystalline part consists of β - sheets formed by $(GA)_n, (A)_n$ motifs in spider and silkworm silks. Besides these structures, random coils are formed by many non-conserved motifs in both silks. These random coils are also part of the amorphous portion of silk. (Adapted from [1].)	7
1.4	Standard magnetic orderings in crystals.	12
1.5	Magnetic characteristics of major magnetic orderings in crystals.	14
1.6	Major magnetic orderings in amorphous materials. The magnetic orderings in the last row are apparent in amorphous materials and disordered solid crystals. In the case of amorphous materials exchange interaction energy, J is replaced by \bar{J} (see eq. 1.2), as J is no longer fixed and has a distribution. (Adapted from [4, 5])	15
1.7	MH of major amorphous magnetic orderings. A schematic presentation of different sorts of magnetic ordering based on the distribution function of the exchange interactions $P(J)$ and the corresponding $M(H)$ magnetization curve: (a) disordered ferromagnetism, (b) asperomagnetism, (c) speromagnetism and (d) spin glass.(Taken from [6])	17

1.8	Ideal spin glass and clustered spin glass systems. The atomic concentration of magnetic impurity in ideal glass is $\leq 1\%$ while in clustered glass is 30%-50%.	19
1.9	Cluster glass phase diagram. Phase diagram for a metallic spin-glass system as a function of concentration and temperature.	19
1.10	Radical pair mechanism. Reaction scheme of radical pairs generated from singlet and triplet precursors. Singlet and triplet radical pairs are represented by $1[\dots]$ and $3[\dots]$, respectively. $K_{SO,PE}$ are the rates of reactions. (Taken from [7])	22
1.11	Structure and magnetic character of MagR-Cry complex. (a) A nanoscale Cry/MagR magnetosensor complex with intrinsic magnetic polarity acts as a light-dependent biocompass. Linear polymerization of Fe-S cluster-containing magnetoreceptors (MagR) leads to the formation of a rod-like biocompass at the center (core, yellow), surrounded by photoreceptive cryptochromes (Cry; the outer layer, cyan). Cross-section on the right side, indicating that electron transportation from the FAD group in Cry to the Fe-S cluster in MagR upon light stimulation may be possible. (b) Magnetic properties of the clCry4/clMagR magnetosensor complex. Room temperature magnetization as a function of the field for the clCry4/clMagR magnetosensor complex was obtained by subtracting the contribution of a buffer from the solution. A hysteresis loop indicates the ferrimagnetic behavior of the clCry4/clMagR complex. (Taken from [8])	23
1.12	Sterically protected radicals. Examples of persistent organic radicals formed due to steric hindrance by bulky functional groups. "*" represents the free radical. [9, 10]	26
1.13	Stable α-nitronyl nitroxide radical. The above radical is stable due to aids from large steric hindrance, charge densities on the NO group, and delocalization.	27
1.14	Free persistent organic radicals.	27
1.15	Nitronyl aminoxyl derivatives. Molecular magnetic solids are formed using the above molecules at extremely low temperatures. The star "*" represents the stable radical. The Curie temperatures of individual molecular solids are given below the molecule.	28
1.16	Superexchange in organic molecular magnets. The far free radicals hybridize with the diamagnetic bridges to interact among themselves.	29

1.17	McConnell I mechanism. Different magnetic couplings (a), (b), and (c) for three distinct orientations of two parallel, close-packed benzyl radicals. Here (a) and (c) show ferromagnetism and (b) shows antiferromagnetism. (Taken from [11])	29
1.18	Non-Kekule structures and their respective ground states. (Taken from [12])	30
1.19	Metal-organic molecular magnets. Here are a few examples of metal-organic complex molecular magnets. These show ferro/ferri- magnetic behaviors at very low temperatures $\approx 2\text{K}$. (Taken from [13])	32
1.20	Polymer Magnets. Examples of a few polymer magnets with their respective Curie temperatures. We can see that there have been few successful attempts at producing room-temperature polymer magnets. However, these magnets (room-temperature) are very brittle.	33
1.21	Graphene Nanoribbons. A carbon nanoribbon with six zigzag chains. The system is periodic along the x-direction. The edges along the y-direction have the armchair termination, while the edges along the x-direction have zigzag termination.	35
2.1	SQUID magnetometer schematic. Basic schematic of SQUID magnetometer with 2 nd order gradiometer. The cross symbols on SQUID denote two Josephson junctions on a dc SQUID. The inset shows the SQUID response V_{SQUID} versus sample position (x-pos.). Electronic circuitry used to measure the V_{SQUID} has been omitted for simplicity. (Adapted from [14] for MPMS 3 Quantum Design.)	41
2.2	DC SQUID device. Two identical superconducting half rings are joined together with two insulating barriers. These superconductor-insulator-superconductor barriers are known as Josephson junctions. The current enters from the left side and is split into two branches with no magnetic flux passing through the ring. We observe an oscillating voltage as soon as a magnetic flux passes through the SQUID device. The oscillations are proportional to magnetic flux quanta passing through the device so one can calculate the magnetic moment. Quantum Design MPMS 3 uses such a SQUID device. However, other commercial SQUID magnetometers might use the rf-SQUID device. (Taken from [15])	42

2.3	Principle of EDXRF. The inner K shell electron is ionized, causing electrons from the upper shell (with higher energy) to occupy its place. These electrons release their excess energy by releasing a photon in X-ray frequency shown here as K_α , K_β , and L_α . K lines are the primary signature of the element, and subsequent x-rays can be used to verify the presence of the element.	47
2.4	Principle of XPS. High energy beam of x-ray photons leads to the ejection of photoelectrons from the inner shells of the atom. Since the electronic energy structure of each atom is unique, so is its binding energy. Hence detection of electrons at specific binding energies provides information about the element to which they belong.	51
2.5	Basic XPS setup. The x-ray obtained from beamline or laboratory sources with energies of about 1.5 keV are bombarded on samples kept under a high vacuum. The photoelectrons generated are accelerated to the hemispherical sector analyzer (HSA), where only electrons with a selected energy band (pass energy, E_p) can pass to reach the electron detector. The data is recorded and stored on the computer.	52
2.6	Typical XAS spectrum. The figure shows the XAS spectrum of FeO powder at the absorption edge of Fe. We can distinguish the XANES and EXAFS regimes from the spectrum. The x-axis is the energy of the x-ray absorbed, while the y-axis denotes the coefficient of absorption of the material. (Taken from [16].)	57
2.7	XAS beamline set up. Setup of Indus 2 synchrotron, RRCAT, Indore, Madhya Pradesh. (Taken from RRCAT Indore website.)	58
2.8	ICPMS stepwise procedure. Once the sample is prepared, we go through the above procedure to reach the final results.	60
2.9	ICPMS setup. Cross section schematic of an ICP-MS. (Taken from [17].)	60
2.10	Ion source and interface in ICP MS. The plasma is at atmospheric pressure, and the range of pressures for the two interface vacuum stages is given in Torr. (Taken from [18].)	61
2.11	Quadrupole mass analyzer. The schematic of the quadrupole mass analyzer and the ion path through it. The diagonal rods are charged oppositely, maintaining a high ac voltage with dc offset.	62
2.12	Basic Principle of EPR. (a) Schematic of basic EPR setup. (b) Zeeman splitting for an electronic system with $S = \frac{1}{2}$	65
2.13	Basic Setup of EPR.	67

- 3.1 **Preparation of pristine silk sample for five magnetic essays.** (a)-(b) Pictures of typical garden spiders. Coin diameter: 23 mm. (c)-(f) Step-by-step procedure for forceful extraction of dragline silk from the spiders. A fully awake spider was taken out of the box and made to rest on the hand (wearing clean latex gloves), and its silk was carefully extracted. The silk was continuously pulled and wrapped around pipet-heads attached to a motor rotating at a speed of 3-5 cm/s. A single sample was kept in a sealed and sterilized microtube (MCTs), as shown in (f). (g)-(k) Schematic illustration of the five magnetic assays described in the text. Note that no metallic equipment/tool was used during this process. Before silk collection, the pipet heads were thoroughly cleaned with ethanol and acetone, and MCTs were sterilized. 72
- 3.2 **M-H using SQUID at 300 K.** (a): At high magnetic fields, the diamagnetic contribution of spider silk dominates heavily over ferromagnetic contributions typically above 2000 Oe. M^* stands for data before diamagnetic subtraction. (b): M-H relation after subtracting diamagnetic contribution at 300 K. Lower inset: zoom of hysteresis loop showing coercivity and remnant magnetization. Upper inset: distribution of H_c , M_r and M_s for four samples. Mean values of these parameters are $M_s = 0.0278 \pm 0.0041$ emu/g, $H_c = 42.9 \pm 9.0$ Oe and $M_r = 0.0011 \pm 0.0003$ emu/g. . . . 74
- 3.3 **Comparison between MH data for empty tube background and with silk.** The background SQUID data was obtained with an empty tube (Black). The yellow color band in silk data denotes variability of the MH data across four silk samples. We note that the background is negligibly diamagnetic compared to spider silk (SS). Hence, throughout the experiments, we performed diamagnetic background subtraction by using high field data (of SS) at 300 K. Bottom graph shows zoom near zero field. The background does not show any hysteresis. It must be noted that an empty holder means a quartz half tube with teflon tape but without silk samples. 75

3.4	M-H data of spider silks at 10 K. (a): The magnetization of silk has increased significantly, which is evident at both low as well as high magnetic fields when compared with data collected at 300 K. (b): M-H relation after subtracting diamagnetic contribution at 10 K. We can see that the magnetization doesn't saturate even at even magnetic fields of 7 T and keeps increasing linearly. This suggests the coexistence of ferromagnetically interacting ($J > 0$) and non-interacting spins in silk samples. Average remnant magnetization increases to $M_r = 0.00325 \pm 0.00082 \text{ emu/g}$ and coercive field, $H_c = 113.9 \pm 21.4 \text{ Oe}$. The average paramagnetic susceptibility, $\chi_p = 1.470.41 \times 10^{-6} \text{ emu/(g} \cdot \text{Oe)}$	77
3.5	Comparing M-H curves of silk at different temperatures. The data depicts the soft ferromagnetic character of silks at 10 K, 300 K, and 400 K. Left inset: Comparison of H_c and M_r at these temperatures. As the temperature increases, we can see a steady drop in M_r and H_c . Right Inset: Zoom of data near zero field.	78
3.6	XPS survey scan for three pristine silk samples. The consistent peaks corresponding to carbon (C), oxygen (O), and nitrogen (N) are clearly visible in both survey as well as core scans. We also got weak signals for other known elements like calcium (350 eV). However, clearly, there was no signal of any transition d-block and f-block elements in the survey scan. These measurements were performed on uncoated silk samples. Target plate area was $1 \text{ cm} \times 1 \text{ cm}$. The scan area of XPS is typically in μm^2 , and scanning depth is up to 10 nm. Measurements were performed in a high vacuum of 10^{-9} mbar	80
3.7	Core XPS scans confirming the absence of ferromagnetic elements. We further took dedicated core scans to detect the key elements (Fe, Co, Ni) that can be ferromagnetic at room temperature. The above results were obtained after five complete scans near their specified energy spectra; still, no signal was found above the background noise level. Fe's expected primary 2p signal lies from 706 eV to 710 eV. Ni's expected primary 2p signal lies from 852 eV to 855 eV. Expected primary 2p signal of Co lies from 778 eV to 779 eV [NIST XPS Database].	81
3.8	XAS spectrum of silk samples. The absorption edges of C, N, and O are visible. No absorption could be detected for heavy ferromagnetic atomic numbers (lower graph) like Fe, Ni, Co, or Mn.	82

- 3.9 **Magnetometry with pristine and tensile ruptured silk.** Procedure of a series of experiments performed by stretching the silk is depicted along with the photographs of the actual silk sample. (a) shows the silk in its pristine form before stretching. This silk was stretched to its breaking point (at a strain of 50%), shown in (b). Later the same silk was ruptured into multiple small pieces by further stretching shown in (c). (d) Magnetometry data of the above three cases ((a) through (c)) at 300 K and 10 K (e). The inset on the left (d) shows a zoom of the data near zero magnetic field to highlight the comparison of M_r and H_c of breaking point, ruptured and pristine silk samples. The inset on the right (d) shows a bar graph to compare the M_s of breaking point, ruptured and pristine silk samples. The error bar highlights that the observed change in M_s is well above the experimental error. 85
- 3.10 **Magnetometry with pristine and cut silk.** Procedure of a series of experiments performed by cutting silk is depicted along with photographs of the actual silk sample. (a) shows the silk in its pristine form before cutting. This silk was cut to over 100 pieces/cm using ceramic scissors, as shown in (b). (c) Magnetometry data of the above two cases ((a) and (b)) at 300 K and at 10 K (d). The inset on the left (c) shows a zoom of the data near zero magnetic field to highlight the comparison of M_r and H_c of cut and pristine silk samples. The inset on the right (c) shows a bar graph to compare the M_s of cut and pristine silk samples. The error bar highlights that the observed change in M_s is well above the experimental error. 87
- 3.11 **EPR signals at room temperatures.** ESR spectra of silk show the presence of free radicals (marked with 3) and ferromagnetically coupled clusters of radicals (marked with 1 and 2). The results of all silk samples are consistent, implying that magnetism originates from the repeating core of spider silks and is an intrinsic property of these materials, not because of some external factor. EPR spectrum of empty quartz tube is also shown as a reference to show no background signal from impurities exists. 88

- 3.12 **FC-ZFC DC magnetization of four samples SS1-SS4.** (a-d): The FC data was taken at 1 kOe field. Oxygen background has been subtracted from all samples (Appendix C). We can see that the magnetic transition near 120 K is consistent for all silk samples (highlighted by a box in each graph). The inset of graph (a) shows the magnetic transition near 120 K in FC and ZFC data. Inset of graph (b) compares the normalized ZFC data of all silk samples (differentiated by color) to show that the magnetic phase transition consistently occur around 120 K in all samples. A slight crossover between FC-ZFC curves of sample SS 3 (near 200K) is probably due to an offset in the positioning of the sample. 90
- 3.13 **Comparison of MT data between empty tube background and silk.** The MT data of background in the absence of spider silk (black) show negligible magnetization for ZFC and FC with an applied magnetic field of 1000 Oe. Even at low temperatures, < 40 K, empty tube magnetization data is negligible compared to spider silk, thus confirming the presence of non-interacting spins in silks. The yellow color band in silk data shows the variability across all four pristine silk samples. The silk data shown here is corrected by subtracting the oxygen background from them using the procedure explained in appendix C. There was no oxygen signature in an empty tube. 92
- 3.14 **Magnetic representation of spider dragline silks.** Based on our experimental results, we expect a magnetic model of silks as described in this figure. Free (isolated) and interacting radical spins (shown in pink bubble) formed due to atomistic defects in silk coexist. β -turns and 3_{10} helices structures are represented by helices (purple) for simplicity. β -sheets are depicted as two-dimensional planes (green) for brevity. A thorough theoretical modeling of silk structure is required to understand the molecular origin of magnetism in spider dragline silks. 94
- 3.15 **Silk Bio-Magnetosensor.** (a) Snapshots showing synchronous rotation of a silk-wick (top-view) when the torsion silk compass is subjected to rotating B field (instantaneous direction of the magnetic field is indicated using compass needle (red and blue)). (b) Angle of silk (θ_p) vs angle of magnetic field (θ_m) for $B = 30$ mT. Error bars are within the size of squares. Inset: schematic of the setup. (c) Permanent attachment of the silk wick to an approaching magnet. 95

- 3.16 **Geomagnetic sensitivity of Silk Bio-Magnetosensor.** (a): The Earth-scale magnetic field is produced by an electromagnet powered by an on-off modulated current. The field is measured at the position of the silk wick. The change in the angular position of silk wick is captured by a camera and analyzed with an imaging software frame-by-frame. The all-silk pendulum is enclosed in a glass chamber to prevent air-flow noise. The anchor of the all-silk pendulum is electrically grounded to avoid any stray electrostatic effects. (b): θ_p vs. time for 50 μ T on-off field, (c): Sub-geomagnetic responsivity of silk compass. Error bars denote angular fluctuation in the steady state. 96
- 3.17 **Magnetic driving of silk swimmers.** (a) Schematic of the setup used to show magnetically assisted driving of miniaturized silk swimmers in de-ionized water. The swimmers can be driven on the surface of the water in any suitable manner by controlling the magnetic field produced by the magnet kept below the petri dish. (b) The snapshots of supplementary video 2 (Video-2_Magnetic_Driving) demonstrate this phenomenon. We can see that bunched-up silk swimmers are being driven from the left side of the petri dish to its right side under the influence of a magnetic field of 35 mT. (c) Distance vs. time graph of silk swimmers extracted from Video-2_Magnetic_Driving. 99
- 3.18 **Force exerted on silk swimmers.** (a) Schematic of the setup used to estimate the force experienced by miniaturized silk swimmers in de-ionized water under the magnetic field gradient generated by a stationary magnet. The swimmers get pulled from a place with a low magnetic field to a place with the highest magnetic field, as illustrated. (b) Shows the field gradient generated by a stationary magnet in our experimental setup with respect to x and y dimensions depicted in (a). (c) Shows the applied force experienced by silk swimmers due to strong magnet $\left(\frac{d(\mu \cdot \vec{B})}{dx}\right)$ with respect to their distance from magnet. We can see that magnet exerts a maximum force of 90 nN in a field of 45 mT and a maximum force of 30 nN in a field of 30 mT. As shown in the next section, such forces are strong enough for contactless manipulation and transportation of organic material in liquid media. 101

3.19	Magnetic rotation of silk swimmers. (a) Shows the schematic of the setup used to show the magnetically assisted rotation of miniaturized silk swimmers in de-ionized water. The swimmers can be maneuvered in any suitable manner by controlling the magnetic field produced by the magnet kept below the petri dish. (b) The snapshots of supplementary video 3 (Video-3_Magnetic_Rotation) demonstrate this phenomenon. We can see that bunched-up silk swimmers are rotated clockwise and anti-clockwise under a magnetic field of 35 mT. (c) Rotation angle vs. time graph of silk swimmers while being rotated in a clockwise manner in the Video-3_Magnetic_Rotation.	102
3.20	Magnetic trapping of a fleet of silk swimmers. (a) Shows the schematic of the experiment demonstrating magnetic trapping of silk swimmers at any desired location in de-ionized water with the field of ≈ 35 mT. (b) shows the snapshots of the supplementary video 4 (Video-4_Magnetic_Trapping) showing magnetic trapping of miniaturized silk swimmers. Video also demonstrates that even if we disturb the system by applying external forces (shaking) to scatter the silk swimmers, they return to their trapped location very quickly. This imply that silks can be used as magnetic tweezers for biological materials.	103
3.21	Magnetic transport of cargo leaf using silk swimmers. (a) Schematic of the experiment showing magnetic transport of cargo leaf using silk swimmers. Tiny silk magbots (magnetic robots) surround a leaf and help in its transportation from one end of petri dish to another end under the influence of magnetic field (b) Snapshots of the supplementary video 5 (Video-5_Leaf_Transport) demonstrating this magnetic transport phenomenon. (c) Distance vs. time graph showing silk-assisted transport of leaf obtained from the Video-5_Leaf_Transport. No displacement of the leaf was possible in the magnetic field without the silk.	105
3.22	Magnetic transport of onion peel using silk swimmers. (a) Schematic of the experiment showing magnetic transport of onion peel using silk swimmers. Tiny silk magbots (magnetic robots) surround an onion peel and help in its transportation from one end of petri dish to another end under the influence of magnetic field (b) The snapshots of the supplementary video 6 (Video-6_Onion_peel_Transport) demonstrate this phenomenon. (c) Distance vs. time graph showing silk-assisted transport of onion peel obtained from Video-6_Onion_peel_Transport. Without silk swimmers, the onion peel could not be magnetically transported.	106

3.23 **Magnetic transport of human skin using silk swimmers.** (a) Schematic of the experiment showing silk swimmers transporting a piece of dead human skin (from lips) in de-ionized water. Tiny silk magbots (magnetic robots) surround a human skin tissue and help in its transportation from one end of petri dish to another end under the influence of magnetic field (b) Snapshots of the supplementary video 7 (Video-7_Human_Skin_Transport) demonstrate this phenomenon. (c) Distance vs. time graph showing silk-assisted transport of human skin obtained from Video-7_Human_Skin_Transport. Without the silk, no transport was possible in a magnetic field. 107

3.24 **Silk-assisted magnetic transport of human hair fiber.** (a) Schematic of an experiment showing silk swimmers transporting a bundle of human hair. Tiny silk magbots (magnetic robots) surround a human hair strand and help in its transportation from one end of petri dish to another end under the influence of magnetic field (b) Snapshots of the supplementary video 8 (Video-8_Human_Hair_Transport) demonstrate this phenomenon. (c) Distance vs. time graph showing silk-assisted transport of human hair obtained from Video-8_Human_Hair_Transport. The hair could not be magnetically transported without the silk. 108

3.25 **Magnetic transport of non-magnetic oil drop using silk swimmers.** (a) Schematic of an experiment showing silk swimmers transporting an immiscible liquid. Tiny silk magbots (magnetic robots) surround an immiscible liquid and help in its transportation from one end of petri dish to another end under the influence of magnetic field (b) Snapshots of the supplementary video 9 (Video-9_Immiscible_Liquid_Transport) demonstrate this phenomenon. (c) Distance vs. time graph showing silk-assisted transport of liquid drop obtained from Video-9_Immiscible_Liquid_Transport. The drop does not respond to the magnetic field without the silk. 109

3.26 **Controlled merging of two fluid drops by magnetic silk swimmers.** (a) Schematic of an experiment showing miniaturized silk swimmers combining one immiscible liquid drop with another stationary drop. Tiny silk magbots (magnetic robots) surround one drop of immiscible liquid and help in its transportation from one end of petri dish to combine with another stationary drop under the influence of magnetic field. (b) Snapshots of the supplementary video 10 (Video-10_Combining_Liquid_Drops) demonstrate this phenomenon. (c) Distance vs. time graph showing silk-assisted merging of droplets obtained from the Video-10_Combining_Liquid_Drops. Capillary force is observed when the two droplets are too close, and the magnetic field is removed. These experiments show possible applications in controlling droplets in biological settings [19, 20]. 110

4.1 **Schematic of the all silk pendulum experiment.** (a): Shows the detailed procedure of preparation of spider silk rod with the image of one of the actual rod prepared for the experiment. (b): Shows the pendulum made using the silk rod. (c): Complete experimental setup where the pendulum is placed in a glass enclosure to eliminate effects of surrounding air flow. The silk rod experiences a uniform magnetic field produced by the Helmholtz coils. A gauss meter was also placed in order to note the magnitude of magnetic field produced by the coils. An overhead camera was used to record the entire experiment. 116

4.2 **Results of all silk pendulum.** The graphs show the experimental results of our all silk pendulum kept in a uniform magnetic field. In this experiment, we experimentally confirmed that $\theta \propto B^2$ with a small error of ± 0.04 radians in pendulum 1 and ± 0.05 radians in pendulum 2. The data is in strong agreement with the theory. 118

- 4.3 **All silk torsion pendulum mimicking spider.** (a) Explains the technique of extracting a single spider dragline silk thread from the spider. A spider is made to fall from the top of a cardboard frame. While freely falling, the spider releases its dragline silk to ensure it safely reaches the ground. As it reaches the bottom end of the frame, we take the silk released by the spider and use it to make our pendulum. (b) shows the picture of the actual frame and spider used to make the pendulum. We found that the spider releases its silk at a natural rate of approximately 1 cm/s. (c) shows the final pendulum made using a thin plastic film that can partially reflect light. We ensured that the weight of the plastic film (non-magnetic) is equivalent to that of the spider, so silk receives equivalent stress as it does from an abseiling spider. 119
- 4.4 **Experimental setup to detect the magnetic response of spider silk.** A probe beam deflection technique (PBDT) was employed by attaching a thin plastic film to the spider silk under study, this plastic beam reflects a small amount of light falling on it, and the reflected spot acts as an indicator of the angular position of the pendulum. The dynamics of the reflected beam were recorded using a camera, and the video was later analyzed using motion tracking software. The magnetic coil is used to excite the silk pendulum locally. A rectangular square wave signal was used to drive the coil for repeated on/off cycles, and the current was measured using an ammeter. A laser diode was also connected as an indicator for on/off cycles. The pendulum was enclosed in an air-tight glass chamber. The entire experiment was kept on a non-magnetic honeycomb vibration-free table. 120
- 4.5 **Geomagnetic sensing by dragline silks.** (a-c) shows the one-to-one rotational response of 3 different spider dragline silks to the magnetic field of different magnitudes differentiated by the color code given in the index. The similar frequency of changing magnetic field and rotation of spider silk pendulum implies a strong correlation between them. The 0 and 1 in magnetic field graphs represent the period for which the magnetic field signal was switched off and on, respectively. Moreover, we can also see that the magneto-mechanical response of dragline silk at a subgeomagnetic field changes well below ($66 \mu\text{T}$). These results depict that spiders might get magnetoreception cues from their dragline silk when it experiences changes in magnetic fields. (d) shows the rotation of pendulums with respect to the applied magnetic field for all three pendulums. The colored lines are for visual aid. We can see that even a "single silk thread" can detect geomagnetic fields in all three cases. 123

5.1 **Preparation of pristine silk samples:** The figure shows a detailed step-by-step procedure for preparing pristine silkworm silk samples for magnetization experiments. (a) shows the picture of *B. mori* silk cocoon membranes (SCM) collected from a silk farm. (b) shows the pieces of SCM after cutting them with ceramic scissors. Ceramic scissors were used instead of metallic ones to avoid contamination of SCM with metallic impurities. (c-e) Degumming the silks removes unwanted impurities and sericin from SCM's surface. The cut silk pieces were cleaned in 0.02 M solution of Na_2CO_3 for 7 hours and later were cleaned with deionized water for 2 hours. These silks were then air-dried for about 18 hours to remove moisture. (f) Shows the sample kept in cleaned and sterilized MCT for experimentation. Utmost care was taken to avoid any metallic contamination of silk and samples were handled only using clean latex gloves. 126

5.2 **MH of silkworm silk at 300 K.** (a): At high magnetic fields, the diamagnetic contribution of silk dominates heavily over its ferromagnetic contributions typically above 3000 *Oe*. M^* stands for data before diamagnetic subtraction. (b): M-H relation after subtracting diamagnetic contribution at 300 K. Upper inset: zoom of hysteresis loop showing coercivity and remnant magnetization. Lower inset: distribution of H_c , M_r and M_s for two samples. Mean values of these parameters are $M_s = 2.8 \pm 0.33 \times 10^{-3} \text{ emu/g}$, $H_c = 65 \pm 20.0 \text{ Oe}$ and $M_r = 2.22 \pm 0.55 \times 10^{-4} \text{ emu/g}$ 128

5.3 **Comparison between MH data for empty tube background and with silk.** The background SQUID data was obtained with an empty tube (Black). We note that the background is negligibly diamagnetic compared to silkworm silk (SS). Hence, throughout the experiments, we performed diamagnetic background subtraction by using high field data (of CS) at 300 K. Bottom graph shows zoom near zero fields. The background does not show any hysteresis. It must be noted that an empty holder means a quartz half tube with Teflon tape but without silk samples. 130

5.4	MH data of silkworm silks at 10 K. (a): The magnetization of silk has increased significantly when compared with data collected at 300 K. (b): MH relation after subtracting diamagnetic contribution at 10 K. We can see that the magnetization doesn't saturates even at magnetic fields of 7 T and keeps increasing linearly. This suggests the coexistence of ferromagnetically interacting ($J > 0$) and non-interacting spins in silk samples. Average remnant magnetization increases to $M_r = 7.91 \pm 0.8 \times 10^{-4} \text{ emu/g}$ and coercive field, $H_c = 223 \pm 27 \text{ Oe}$. The average paramagnetic susceptibility, $\chi_p = 3.1 \pm 0.11 \times 10^{-7} \text{ emu}/(g \cdot \text{Oe})$	131
5.5	Comparing M-H curves of silk at different temperatures. The data depicts the soft ferromagnetic character of silks at 10 K, 300 K, and 400 K. Left inset: Comparison of H_c and M_r at these temperatures. As the temperature increases, we can see a steady drop in M_r and H_c . Right Inset: Zoom of data near zero field.	132
5.6	XPS survey scan for three pristine silkworm silk samples. The consistent peaks corresponding to carbon (C), oxygen (O), and nitrogen (N) are visible in both survey as well as core scans. We also got weak signals for other known elements like calcium (350 eV). However, there was no signal of any transition d-block and f-block elements in the survey scan. These measurements were performed on uncoated silk samples. Target plate area was $1 \text{ cm} \times 1 \text{ cm}$. The scan area of XPS is typically in μm^2 , and scanning depth is up to 10 nm. Measurements were performed in a high vacuum of 10^{-9} mbar	134
5.7	Core XPS scans confirming the absence of ferromagnetic elements. We further took dedicated core scans to detect the key elements (Fe, Co, Ni) that can be ferromagnetic at room temperature. The above results were obtained after five complete scans near their specified energy spectra; still, no signal was found above the background noise level. Fe's expected primary 2p signal lies from 706 eV to 710 eV. Ni's expected primary 2p signal lies from 852 eV to 855 eV. Expected primary 2p signal of Co lies from 778 eV to 779 eV [NIST XPS Database].	135
5.8	XAS spectrum of silkworm silk samples. The absorption edges of C, N, and O are visible. No absorption could be detected for heavy ferromagnetic atomic numbers (lower graph) like Fe, Ni, Co, or Mn.	136

- 5.9 **Magnetometry with pristine and tensile ruptured silk.** Procedure of a series of experiments performed by stretching the silk is depicted along with the photographs of the actual silk sample. (a) shows the silk in its pristine form before stretching. This silk was ruptured into multiple small pieces by the stretching mechanism shown in (b). (c) Magnetometry data of the above two cases ((a) and (b)) at 300 K and 10 K (d). The inset on the left (c) shows a zoom of the data near zero magnetic field to highlight the comparison of M_r and H_c of ruptured and pristine silk samples. The inset on the right (c) shows a bar graph to compare the M_s of ruptured and pristine silk samples. The error bar highlights that the observed change in M_s is well above the experimental error. 139
- 5.10 **Magnetometry with pristine and cut silk.** Procedure of a series of experiments performed by cutting silk is depicted along with photographs of the actual silk sample. (a) shows the silk in its pristine form before cutting. This silk was cut to over 100 pieces/cm using ceramic scissors, as shown in (b). (c) Magnetometry data of the above two cases ((a) and (b)) at 300 K and 10 K (d). The inset on the left (c) shows the zoom of the data near zero magnetic field to highlight the comparison of M_r and H_c of cut and pristine silk samples. The inset on the right (c) shows a bar graph to compare the M_s of cut and pristine silk samples. The error bar highlights that the observed change in M_s is well above the experimental error. 141
- 5.11 **FC-ZFC DC magnetization of silk samples.** (a-b): The FC data was taken at 1 kOe field. The background of oxygen has been subtracted from the samples. We can see that the magnetic transition near 120 K is consistent for all independent silk samples (highlighted by a box in each graph). The inset of the graph (a) shows the transition in FC and ZFC near 120 K. Inset of graph (b) shows the zoom ZFC curves of both CS 1 and CS 2 to highlight consistency in magnetic phase transition in silkworm silks. 142
- 5.12 **Comparison of MT data between empty tube background and silk.** The MT data of the background in the absence of silkworm silk (black) show negligible magnetization for ZFC and FC with an applied magnetic field of 1000 Oe. Even at low temperatures < 40 K, magnetization data of empty tube is negligible as compared to spider silk, thus confirming the presence of non-interacting spins in silks. The silk data shown here is corrected by subtracting the oxygen background from them using the procedure explained in Appendix C. No oxygen correction was done in the empty tube. . 143

5.13	Magnetic representation of silkworm silk. The figure indicates that atomic defects in crystalline β sheets (green structures) of silk fibroin lead to the existence of free (isolated) and interacting radicals (shown in pink bubble).	144
B.1	Comparison of magnetic transition in silk and oxygen at T = 60 K. Comparison of magnetic moments of solid oxygen and spider dragline silks data. Note that the silk's magnetic signatures are consistent in all four samples and transition at 60 K correlates with two magnetic transitions of solid oxygen. The oxygen data is taken from [21] Below 30 K, the paramagnetism of silk samples overwhelms the α magnetic transition of oxygen solid, and hence it does not appear in our data. The magnetization data of silk are normalized for ease of comparison.	152
C.1	FC-ZFC DC magnetization of four pristine samples SS1-SS4. (a-d): The FC data was taken at 1 kOe field without subtracting the oxygen data. We can see large Para-AFM transition bumps in the temperature range of 40 K - 60 K, highlighted with rectangular boxes. These belong to oxygen. These samples were prepared in ambient atmospheric conditions.	153
C.2	Preparation of oxygen-free silk sample for SQUID magnetometry. The degassing/purging process of the silk is quantified in terms of the pressure in the chamber vs. time. After the pressure was reduced to 7.0×10^{-7} mbar, argon was pumped into the chamber till the pressure reached back to over 1 bar. The oxygen-free sample was carefully sealed in the argon-purged capsule in the argon environment.	154
C.3	MT graph on silk in argon environment. Note that the magnetic hump (near 60 K) disappeared once the air (oxygen) was replaced with argon. We also observe that the magnetic phase transition (see inset) persists at 120 K, which is consistent with all the silk samples as shown in Fig. 3.12.	155
C.4	Purification of silk's magnetism from low-temperature oxygen background. The hump-like feature around 60 K was subtracted from the original data (top curve) using a polynomial fitting.	157

List of Tables

1.1	Comparison of mechanical properties of natural silks with other synthetic fibers. (Taken from [22])	8
1.2	Summary of potential applications of silk materials. [23, 24, 25, 26, 27]	10
3.1	EDX Analysis. Atomic concentration of selected elements in three independent samples of the spider silk.	79
3.2	Concentration of ferromagnetic elements in silks.	83
5.1	EDX Analysis. Atomic concentration of selected elements in three independent samples of the silkworm silk.	133
5.2	Concentration of ferromagnetic elements in silks.	137
A.1	Conversion table for magnetic units. Multiply the value of "Quantity" expressed in cgs or Gaussian units by the "Conversion factor" to get the equivalent value in "SI units." (Adapted from IEEE magnetics.)	150

Contents

Abstract	VI
List of Figures	IX
List of Tables	XXVI
1 Introduction to Natural Silk Polymers and Organic Magnets	1
1.1 Introduction	1
1.2 Natural silks	2
1.2.1 Structure and Composition	4
1.2.2 Physical properties and applications of Silkworm and Spider silks	8
1.3 Amorphous Magnets	11
1.3.1 Introduction	11
1.3.2 Magnetic Orderings of Amorphous Materials	14
1.4 Proteins in Magnetic Field	20
1.4.1 Diamagnetic anisotropy of proteins	20
1.4.2 Magnetoreception proteins	21
1.5 Organic Magnets	24
1.5.1 Persistent organic radicals	25
1.5.2 Magnetic exchange interaction	27
1.5.3 Future Perspectives	32
1.6 Magnetism in Carbon allotropes	34
1.7 Research Work	36
2 Experimental Techniques	39
2.1 Introduction	39
2.2 Magnetic Characterizations	39
2.2.1 SQUID Magnetometer	40
2.3 Elemental analysis techniques	46
2.3.1 Energy Dispersive X-Ray Florescence (EDXRF)	47

2.3.2	X-ray photoelectron spectroscopy (XPS)	50
2.3.3	X-Ray Absorption Spectroscopy (XAS)	56
2.3.4	Inductively Coupled Plasma Mass Spectroscopy (ICPMS)	59
2.4	Electron Paramagnetic Resonance Spectroscopy	64
2.4.1	Instrumentation and Procedure	66
2.5	Conclusion	68
3	Intrinsic Magnetism of Spider Dragline Silk	69
3.1	Introduction	69
3.2	Preparation of pristine spider silk samples	70
3.3	Magnetometry of Spider Dragline Silks	73
3.4	Origin of Magnetism in Spider Dragline Silks	78
3.4.1	Elemental Analysis	78
3.4.2	Enhancement in magnetism of silk by tensile rupturing and cutting .	83
3.4.3	Electron Paramagnetic Resonance (EPR)	88
3.5	Magnetic Ordering in Spider Dragline Silks	90
3.6	Representation of Magnetic spins in Spider Dragline Silks	93
3.7	New Potential Applications of Spider Dragline Silks	95
3.7.1	Spider Dragline Silk as a Bio-Magnetosensor	95
3.7.2	Silk based Bio-Magbots	97
3.8	Conclusion	111
4	Spider Dragline Silk as a Geomagnetic Compass	113
4.1	Introduction	113
4.2	Basic Idea of Experiment	114
4.3	All Silk Torsion Pendulum experiment again !	114
4.3.1	Experimental set up	115
4.3.2	Experimental Results	117
4.4	Dragline Silk as Geomagnetic Compass	117
4.4.1	Experimental setup	119
4.4.2	Experimental Results	122
4.5	Conclusions	124
5	Intrinsic Magnetism of Silkworm Silks	125
5.1	Introduction	125
5.2	Preparation of pristine silkworm silks	126
5.3	Magnetometry of Silkworm Silks	127
5.4	Origin of Magnetism in Silkworm Silks	133

5.4.1	Elemental Analysis	133
5.4.2	Enhancement in magnetism of silk by tensile rupturing and cutting .	138
5.5	Magnetic Ordering of silkworm silks	142
5.6	Representation of magnetic spins in silkworm silks	144
5.7	Comparison of magnetic properties of silk fibroin and spidroin	145
6	Concluding Remarks and Future Perspectives	148
6.1	Summary	148
6.2	Future Perspectives	149
A	Magnetic units conversion from CGS to SI	150
B	Magnetic Transitions of Oxygen	151
C	Sample preparation and thermomagnetic analysis of oxygen-free spider silk	153
C.1	Isolation of silk's magnetic signals from molecular oxygen near 60 K . . .	156
D	Calculation of magnetic moment per molecule for both silks	158

Chapter 1

Introduction to Natural Silk Polymers and Organic Magnets

1.1 Introduction

With the advent of climate change, the present century has seen an emergence of the search for new eco-friendly, efficient, and functional materials as a replacement for plastics and metals as well as sources of energy. A few notable examples of high-functioning sustainable materials are carbon nanotubes, graphene, cellulose-based fibers, carbon fibers, natural silk-based materials, biofuels, etc. History reveals that inspiration from nature and natural evolution has always played a significant role in the development of engineering marvels that were previously considered impossible. As an example, the aerodynamic structures of birds and the design of their beaks have inspired designs of high-speed airplanes, maglev trains, and surgical tools. Likewise, the design of helicopters and submarines was motivated by dragonflies and deep-sea whales, respectively. Hence, taking a closer look at nature will again help us in our search for high-performance, biodegradable and non-toxic materials. One brilliant example of such a material is the natural silk produced by arthropods (insects).

Silks are proteinous structures produced by insects and play many vital roles, like protection and metamorphosis in these organisms, including providing nutrition to them in harsh environmental conditions. Ancient historical evidence reveals that silks were used for sewing wounds by Romans, while the Chinese have used them as a fabric since 3630 BC. Moreover, it was also one of the first items in the world to be traded globally and is widely used in the textile industry to date. However, beyond being a textile raw material, it has excellent mechanical properties like high tensile strength and toughness. Surprisingly, the strength of silk protein is not because of strong ionic or covalent bonds as in other materials but is due to hydrogen bonds, which are considered one of the weakest bonds in nature. Silks present a strong example of a case where weak molecular forces like hydrogen

bonds, when working collectively in unison, can exhibit incredible strength and toughness unmatched by any other natural or manufactured fiber. Due to their excellent mechanical and medical properties, silks have been an important topic of interest for many research groups worldwide. In this chapter, we will learn a good deal about structure, composition, physical properties, and applications of spider dragline silks and cocoon membrane silks of *Bombyx mori*.

1.2 Natural silks

Arthropods secrete silks to provide structural support for various life functions such as catching prey, metamorphosis, etc. In that sense, silks are a unique class of proteins that function outside these organisms' bodies, unlike other proteins that either function inside or at the interface of the body and outside environment (e.g., keratin)[28]. Cocoon silk of *Bombyx mori* and dragline silk of spiders, in particular, has gained much interest in research due to their remarkable mechanical properties such as strength and toughness, which surpass even artificial strong materials like Kevlar and steel. Silks can have strength in GPa ranges similar to steel, whereas their toughness is two times more than that of steel or Kevlar while having a much lower density than these materials. A more attractive feature of silks is that these fibers are produced by simply processing proteins in water under ambient conditions [29, 1, 30, 31, 28].

Orb weaving spider produces seven different types of silks to support itself. Each silk serves a different purpose and thus has different structures that suit its function. Figure 1.1 briefly describes all the different types of silks that spiders produce and their respective functions. A brief description of all its silks is given below:

1. **Major Ampullate (Dragline silk):** This is the strongest silk produced by a spider and is also known as dragline silk. It provides a firm structure to the web and is also known as the lifeline of a spider. The following section will discuss more details about its structure, functions, and properties.
2. **Flagelliform silk (Capture silk):** This silk is commonly known as the capture silk as it is specifically designed to capture and trap the prey of a spider. It has high energy dissipation property to absorb the kinetic energy of the flying prey. It also has a unique capability to capture water from air [32]. It covers the most area on the web, as can be found in fig. 1.1. Its structure is entirely made of helices with no to few beta sheets.
3. **Aggregate silk:** This is cementing silk that not only helps the different silks present in the web attach but also acts as a sticky coating on the capture silk helping the prey

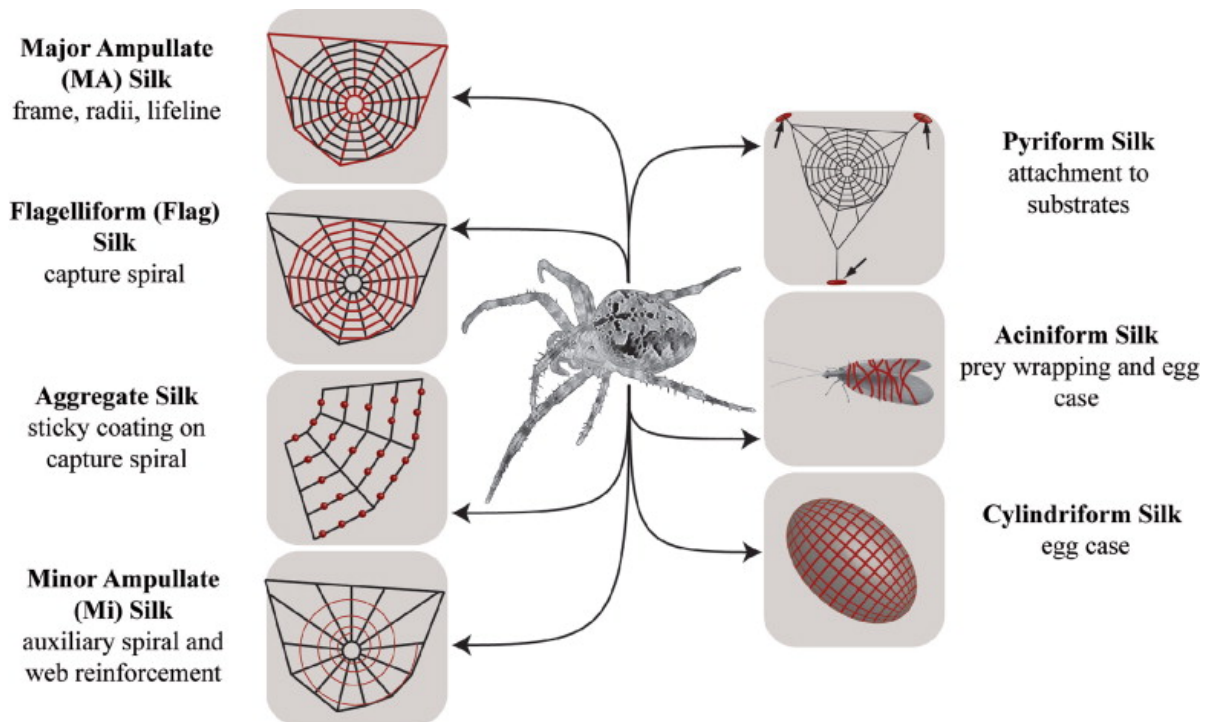


Figure 1.1: **Types of Spider silks.** Schematic overview of different silk types produced by female orb-weaving spiders (*Araneae*). Each silk type (highlighted in red) is tailored for a specific purpose. (Taken from [1])

get stuck on it.

4. **Minor Ampullate:** Another type of spider silk used to reinforce the spider web. It forms a spiral structure towards the center of the spider web. It has high tensile strength as the major ampullate but is not as elastic as it.
5. **Pyriform silk:** This silk is another type of cementing silk that helps the web to get attached to the surrounding structures. Fig. 1.1 depicts it quite aptly.
6. **Aciniform silk:** A spider uses this silk to wrap its prey once captured. The same silk is also found on the outer case of the eggs laid by the spider. Hence it acts as a shield for the preservation and protection of its interiors.
7. **Cylindriform silk:** This silk is found on the inner side of the egg case of a spider.

The main focus of my research is mainly on the dragline silk or major ampullate.

Bombyx mori or mulberry silkworm produces a silk cocoon membrane for itself during molting from dormant pupae to an adult moth. These cocoons act as robust growth incubators for the silkworm during their metamorphosis while maintaining appropriate temperatures, humidity, light, and gaseous balance as well as protecting from UV rays and predators [33].

Apart from their remarkable mechanical properties, in recent years, silks have found use in more diverse areas such as optics, photonics, clothing apparel for casual as well as military grade, flexible electronics, biomedical devices, and other research purposes. Astonishingly, a violin was also made using strings of spider silk [23, 34, 25, 24]. Biomimicry of silk proteins to produce a lightweight, minimalist, biodegradable, and yet functional material can be of great importance for a sustainable future.

This section will discuss the basic structure, composition, properties, and applications of *B. mori* cocoon silk and spider dragline silk before briefly describing my research problem. From here on, the term cocoon silk will be used for *B. mori* cocoon silk and spider silk will be used for spider dragline silk.

1.2.1 Structure and Composition

Superior mechanical properties of silk fibers relative to other proteins can be owed to their amino acid sequence and spinning technique. These factors ensure the appropriate ratio of microstructures to fulfill silk's mechanical functions. The silkworm silk protein is known as fibroin, whereas the spider silk protein is known as spidroin. Various research tools like X-ray diffraction, solid-state NMR, circular dichroism, SAXS, IR, Raman, and mass spectroscopies have revealed their structure, and composition [35, 36, 37, 38, 39, 40, 41, 42, 43, 44, 45]. It has been observed that both spider silk and silkworm silk structurally have a skin-core model (figure 1.2) [2]. Silkworm silk has thicker skin and two silk cores compared to spider silk, which only has a single core and thinner skin. The shell cover of silkworm silk is typically made of sericin, while the shell cover of spider silk is made of lipids and glycoprotein (fig.1.2 (a,c)). The cores are the fibroin/spidroin proteins which in turn consist of many protein microfibrils (fig. 1.2(b,d)). Spidroin comprises two heavy protein chains known as MaSp1 and MaSp2, which are linked with disulfide bonds [46] whereas fibroin is made of heavy fibroin (H-fibroin) and light fibroin (L-fibroin). The net molecular weight of the entire spider dragline silk is reportedly *ca.* 600 *kDa*. Whereas that of silkworm silk is, *ca.* 350 *kDa* [47]. The primary structure of both types of silks and constituent proteins of spider silk collected from different spider species are given below (The accession numbers for the sequences are P05790, P19837, P46804, AAC47009, and AAC47010 respectively [48]).

***Bombyx mori* fibroin:**

GAGAGSGAGAGSGAGAGSGAGAGSGAGAGSGAGAGYGAGVGVGYGAGYGAGAGA
 GYGAGAASGAGAGSGAGAGSGAGAGSGAGAGSGAGAGSGAGAGSGAGAGSGAGAG
 SGAGAGSGAGAGSGAGAGSVYGAGYGAGVGVGYGAGAGAGSGAGAGSGAGAGSGA
 GAGSGAGAGSGAGAG

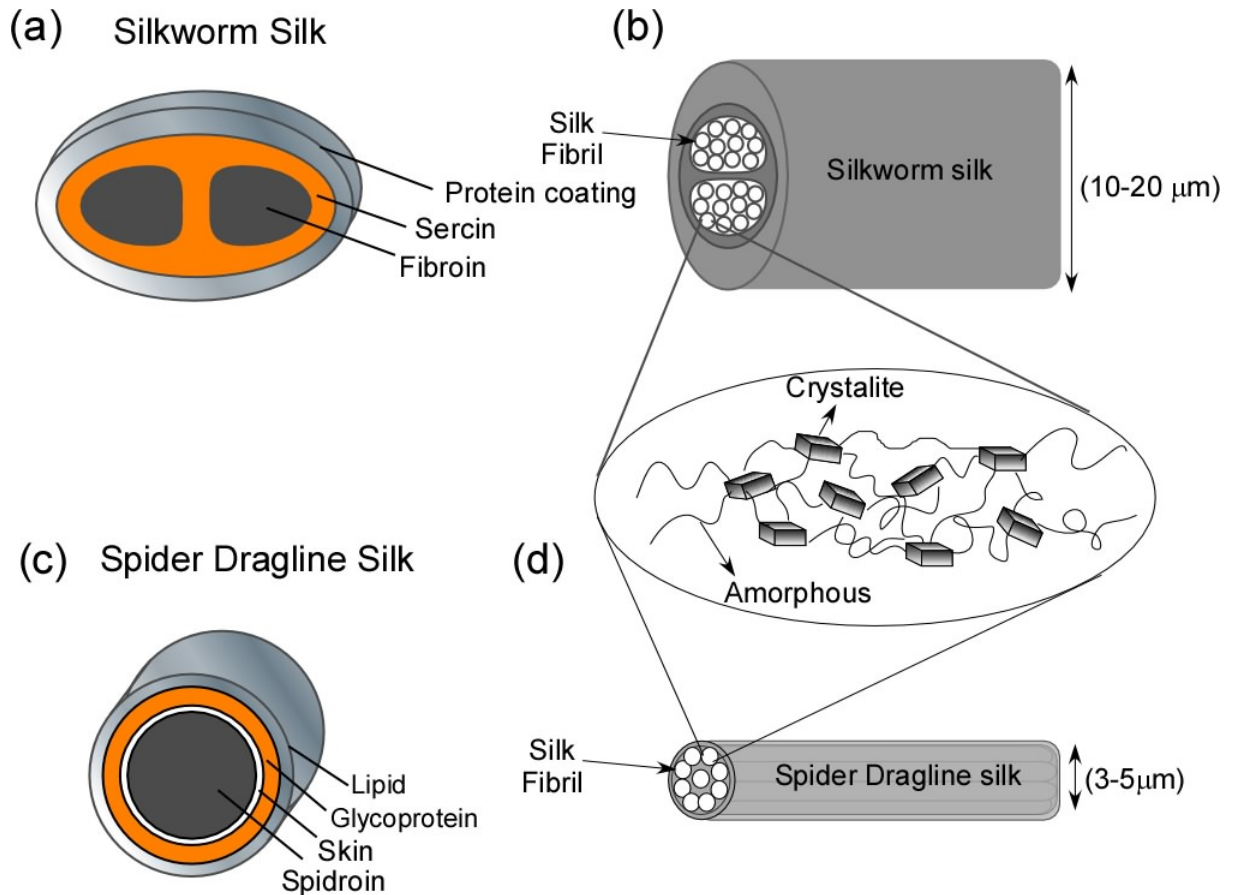


Figure 1.2: **Silk structure at a glance.** figure (a) and (c) describes the hierarchical shell-core structure of silkworm silk and spider silk, respectively. (b), (d) shows that the core is made of many fibrils (tertiary structure), and those fibrils are comprised of crystallites made of β -sheets and the amorphous chains made of helices and turns. (Adapted from [2, 3])

Nephila clavipes MaSp1:

AAAAAAGGAGQGGYGGGLGSQGAGRGLGGQGAGAAAAAGGAGQGGYGGGLGGQ
GAGQGGYGGGLGSQGAGRGLGGQGAGAAAAAA

Nephila clavipes MaSp2:

AAAAAAAASGPGQQGPGGYGPGQQGPGGYGPGQQGPSGPGSAAAAAAAASGPGQQ
GPGGYGPGQQGPGGYGPGQQGLSGPGSAAAAAAA

Araneus diadematus MaSp1:

AAAAAAAAVGAGGGGQGGGLSGGAGQGYGAGLGGQGGASAAAAAGGQGGQGG
QGGYGGGLGSQGAGGAGQLGYGAGQESAAAAAAA

Araneus diadematus MaSp2:

AAAAAAGGYGPGSGQQGPGQQGPGQQGPGGQGYGPGASAAAAAGGYGP

GSGQQGPGGQGPYGPSSAAAAAA

The primary repetitive amino acid sequence (or core) domains of fibroin are hexapeptides, including GAGAGS, GAGAGY, GAGAGA, and GAGYGA. Here G, A, Y, and S stands for glycine, alanine, tryosine, and serine. Spider silk's (spidroin) repetitive core domains for MaSp1 are GGX (X stands for a random amino acid) and poly alanine, $(A)_n$ and the core domain of MaSp2 are GPGGXX and poly alanine, $(A)_n$. P stands for proline. Since spidroin and fibroin are fibrous proteins, these domain units are repeated several hundred times in a silk structure and thus govern the macroscopic properties of silk. The non-repetitive domains of silk are also essential for fiber formation. The conformational geometry of the central core domains of the protein is shown in figure 1.3. Polyalanine $(A)_n$ and poly-glycine-alanine $(GA)_n$ domains form β -sheet structures (highlighted by red color in the above-mentioned amino acid sequence). These domains are also hydrophobic. β -sheets formed by these core domains are tightly packed and impenetrable by water. These β -sheets are behind the rigidity and stiffness of silks, despite being held together by hydrogen bonds, which are the amongst the weakest bonds found in nature. The collective behavior of these hydrogen bonds provides an extraordinary stiffness to β - sheets of silk proteins [49]. β -sheets in spider silks are formed by the intramolecular folding of protein chains in addition to intermolecular hydrogen bonding among the protein chains. The repetitive domain formed by GGX results in 3_{10} -helices, while that formed by GPGGXX conforms to elastic β - turns. These helices and β - turns provide elasticity to spider silks and hence are responsible for the superior toughness of spider silks. These hydrophilic domains act as linkers connecting hydrophobic β - sheets. Thus, the tertiary structure formed by the composition of these secondary structures has hydrophobic components at the core of the fibril and hydrophilic components towards the outer surface. The ratio of hydrophobic to hydrophilic domains of amino acids governs the secondary structure and polymer connectivity that, in turn, results in different material properties of silk.

Research has revealed that β -sheets (also known as crystalline domain) constitute 50%-70% of the structure of silkworm silk, and the rest 30%-50% is made of amorphous or non-crystalline domains [50]. The crystalline domain of silks is sometimes referred to as the ordered part of the silk, and the amorphous or non-crystalline domain is the disordered part of silk. We have previously discussed that the β - sheet of silkworm silks is made of hexapeptide domains mostly with $(GA)_n$ motifs. A typical β - sheet is known to have a monoclinic space group with a rectangular unit cell of $a = 0.938 \text{ nm}$, $b = 0.949 \text{ nm}$, $c = 0.698 \text{ nm}$ [35, 36]. The amorphous regions help to cross-link these crystalline sheets. All the crystallites are aligned along the fiber axis of silk.

Spider silk is known to have about 30% to 40% of crystalline or ordered portion made of β -sheets formed dominantly by $(A)_n$ domains and also have β -sheets made of $(GA)_n$


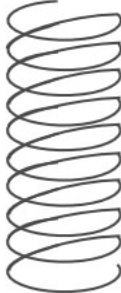

Sequence Motif	GGX	GPGXX	$(GA)_n, (A)_n$
Structural role	Amorphous	Elastic	Crystalline
Structure			
	3_{10} - Helix	β - Turn	β - Sheets

Figure 1.3: **Conformation of different motifs in silk.** The above table shows the different conformations that amino acid sequence motifs take under ambient conditions in silk. We can see that the amorphous part consists of 3_{10} - helices, β - turns formed by GGX and GPGXX motifs in spider silk, and the crystalline part consists of β - sheets formed by $(GA)_n, (A)_n$ motifs in spider and silkworm silks. Besides these structures, random coils are formed by many non-conserved motifs in both silks. These random coils are also part of the amorphous portion of silk. (Adapted from [1].)

domains [51]. 60% - 70% of spider silk is comprised of 3_{10} -helices and beta-turn formed by GGX and GPGGXX domains, as mentioned earlier, along with some random coils. The primary structure of silk (fig.1.2) gives us a good idea that its overall structure can be shown as tiny crystals embedded in an amorphous matrix. The size and dimensions of these small crystals in a single thread were found to be $2 \times 5 \times 7 \text{ nm}$ using x-ray diffraction patterns [37, 38, 43]. Also, the inter-crystallite distance along the fiber obtained using SAXS was 13-18nm. Studies of solid-state NMR on dragline silk have divulged that most helical and coil structures, as well as β -sheet structures, are well aligned along the axis of spider silk. [51, 52].

The ratio of crystalline to amorphous domains of silk is very much dependent on the temperature, pressure, humidity levels, and the spinning speed at which the silk is being extracted [29, 1]. Moreover, just knowing the composition of the silk alone does not imply that one can artificially produce silk materials with similar mechanical properties as that of natural silks. Artificially produced silk (also known as recombinant silk) is known to have much inferior mechanical properties compared to that produced by silkworms and spiders,

Fibers	Stiffness (GPa)	Strength (GPa)	Extensibility (%)	Toughness (MJm^{-3})
<i>B. mori</i> Cocoon silk	7	0.6	18	70
<i>A. diadematus</i> dragline silk	10	1.1	27	180
<i>A. diadematus</i> capture silk	0.003	0.5	270	150
Wool	0.5	0.2	5	60
Elastin	0.001	0.002	15	2
Nylon fiber	5	0.95	18	80
Kevlar 49 fiber	130	4	1.3	25
Carbon fiber	300	4	1.3	25
High-tensile steel	200	1.5	0.8	6

Table 1.1: **Comparison of mechanical properties of natural silks with other synthetic fibers.** (Taken from [22])

albeit their compositions are very much alike. Therefore the knowledge of the spinning technique used by spiders and silkworms is of utmost importance [53, 54, 1].

We will now briefly discuss the various physical properties of natural silks.

1.2.2 Physical properties and applications of Silkworm and Spider silks

Several remarkable properties of silks were discovered over six decades of extensive research.

Silks are mainly known for their spectacular **mechanical properties**. Spider silk is the toughest naturally occurring fiber known to humanity, surpassing even artificial materials like steel, Kevlar, and carbon fiber in toughness. In terms of strength, silks are stronger than any naturally occurring fiber. Table 1.1 compares mechanical properties like strength and toughness of natural silks with other mass-produced artificial materials [55, 22]. The exceptional elasticity and extensibility of spider silk are attributed to its 3_{10} -helices and β -turns, which upon excessive shear stress, unwind. On the other hand, the strength is attributed to its crystalline β -sheets. The crystallites' size and distribution among the fiber play an important role in deciding the fiber's strength.

Silk's mechanical strength and toughness make it a potential construction material for utilities like ropes, nets, parachutes, seat belts, etc. Its remarkable energy dissipation property makes it a perfect fit for bulletproof wearables as an eco-friendly and more efficient replacement for Kevlar.

Besides their highly regarded mechanical properties, silks also possess brilliant **piezo-**

electric behavior. Silk's intrinsic piezoelectricity arises due to the non-centrosymmetric monoclinic space group acquired by β - sheets of silk [56]. The dipole interaction leading to hydrogen bonds is highly ordered in nature, giving an overall dipole moment to helices and β -sheets. A high degree of orientation in the silk secondary structure enhances this property. Shear stress on silkworm silks shows a piezoelectric response of $\approx 1 \text{ pC}/N$ (in the perpendicular direction to stress) as compared to $\approx 2 \text{ pC}/N$ of quartz crystal.

Silks exhibit brilliant **optical properties** and have been quoted as "mother nature's super lens" because it was observed that spider silk could resolve a 100 nm distance using white light. Spider silk can aid in super-resolution imaging by acting as cylindrical super-lens and thus overcome the field of view shortcomings of microsphere lenses [57]. Moreover, being transparent in the visible light region with a refractive index of 1.54 - 1.55, silks can be used as waveguides to transmit multimode signals, and this was indeed demonstrated experimentally [58, 59]. Silks can become an ideal material for interface in the biological and optical world for biomedical applications. By processing silk, they can be transformed into multiple shapes and sizes, forming lenses, waveguides, diffraction gratings, microlens arrays, etc. [60].

An astonishing property of spider silk is its high **thermal conductivity**, nearly equal to the thermal conductivity of copper, the second-best thermal conductor after diamond [61]. It was also observed that applying a minor strain to spider and silkworm silks increases their thermal conductivity and diffusivity.

The most promising applications of silks can be seen in the medical industry, where they can be used for several purposes like surgical threads, bandages, etc. Several research articles have proposed that silks can be used to make artificial bones, tendons, ligaments, and muscles without any side effects [31, 23, 25, 62]. Silks have also been used to create surgical implants and replacements that are more efficient than conventional ones in providing support to the body and other blood vessels and are non-toxic in nature [27].

We have covered many potential applications of silks across several industries. We now summarize these applications in table 1.2.

Millions of years of evolution have led nature to engineer such a great fiber possessing many extraordinary properties in a single protein polymer. However, silks obtained by spiders are low in quantity, and several attempts to replicate this fiber synthetically have been carried out. Artificially produced spider silk fibers, known as recombinant spider silk, are very close to the natural ones but not a perfect replica. We have discussed almost all spider silk's physical properties known to date. A crucial lesson to remember is that the assembly pattern of nanostructure domains is the most influential factor determining the macroscopic properties of biomaterials, especially in silks. Lessons learned from nature keep inspiring us to push ourselves to produce high-performance biodegradable materials.

Industry	Applications
Defense	Bulletproof apparels
Utilities	Ropes, seat belts, parachutes, nets, plastic bottles, etc.
Optics and Photonics	Lenses, microscope, fiber optic cables, fiber optic biosensors (FOBs), diffraction gratings, photonic lattices, etc.
Electronics	Nanogenerators, watches, pressure sensors, air flow sensors, voice recorders, thermal cooling of microchips and lasers, wireless charging of microdevices, OTFTs, etc.
Medical	Bio-sensors, pacemakers, voice recognition devices, nanogenerators for batteries used in prosthetic body parts, drug delivery, hearing aids, surgical implants, artificial bones, muscles, tendons, implantable electronics, etc.
Scientific	Polymer Research, biomimetics, etc.

Table 1.2: **Summary of potential applications of silk materials.** [23, 24, 25, 26, 27]

As we conclude this section, we must point out that despite several years of research on silks, their inherent magnetic properties have remained unknown.

The present research deals with the magnetic properties of pristine natural silks. The following sections will introduce the readers to the wonderful field of organic and carbon-based magnetism. We'll start by briefly revising the fundamental magnetic characteristics (diamagnetism, paramagnetism, ferromagnetism, antiferromagnetism, and ferrimagnetism) found in crystalline materials and extend our discussion toward the behavior of magnetic ions in amorphous materials. This is essential for understanding and analyzing the results of the present research work.

In the later sections, we'll learn about organic and carbon-based magnets and discuss the existing research in the field of organic magnetism, its challenges, and its advantages. This knowledge is essential to realize the importance of the present research work. The chapter will end by paving the path for my research problem.

1.3 Amorphous Magnets

1.3.1 Introduction

We can remind ourselves about the five major magnetic orderings in solid crystalline materials that we learned in high school:

- Diamagnetism
- Paramagnetism
- Ferromagnetism
- Anti-Ferromagnetism
- Ferrimagnetism

Diamagnets repel the magnetic fields and does not let them pass through themselves. Thus the magnetic susceptibility of diamagnets is always negative. The origin of diamagnets can be traced to completely filled orbitals of atoms. In molecules with completely filled orbitals, diamagnetism is the dominant magnetic character. Organic aromatic compounds have a prominent diamagnetic character due to the delocalized p-electrons, which can move around in large rings. Aromatic compounds also exhibit a significant diamagnetic anisotropic effect, i.e., diamagnetism is maximum when the plane of the rings is perpendicular to the applied magnetic field compared to when the plane of the ring is parallel to the fields. Examples of diamagnets are water, copper, glass, etc. Most organic materials are diamagnetic in nature.

Paramagnets, on the other hand, are attracted to magnetic fields and let them pass through themselves. The magnetic susceptibility of paramagnets is positive. The origin of paramagnetism can be traced to the presence of partially filled orbitals of atoms and molecules. Electrons in these partially filled orbitals oscillate around the nucleus (or nuclei), forming atomic current loops with a magnetic moment. However, their net magnetic moment averages to zero without an external magnetic field. On applying an external magnetic field, the internal magnetic moment (due to partially filled orbitals) of atoms try to align themselves with the direction of external magnetic field. Thus the overall material feels an attractive force. Examples of paramagnets are aluminum, titanium, iron oxide (FeO), oxygen etc.

However, in the case of systems, with partially filled localized orbitals, the unpaired electrons in these orbitals start interacting. This interaction provides electrons an additional degree of freedom and is known as the exchange interaction. Paul Dirac described their

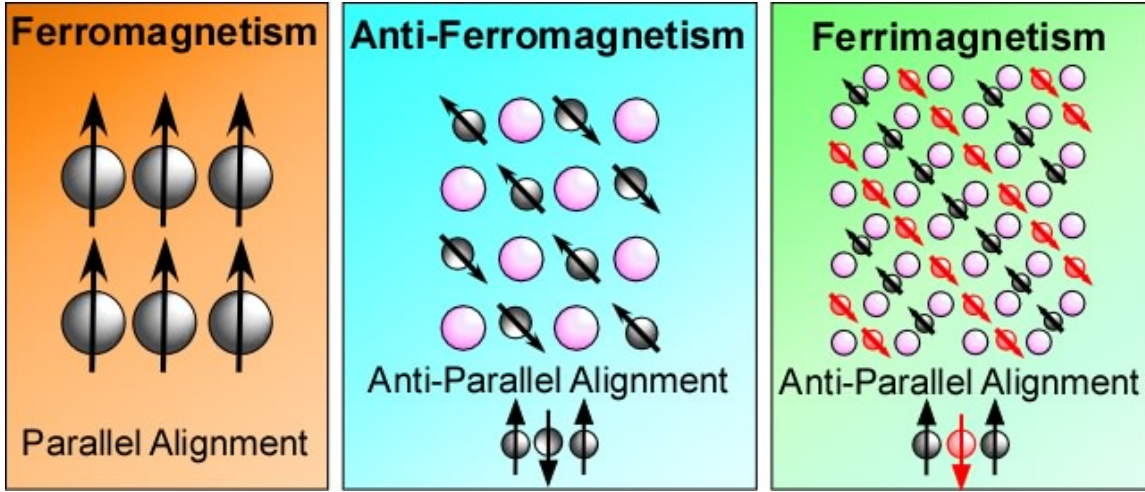


Figure 1.4: **Standard magnetic orderings in crystals.**

interaction energy in a simple expression known as Heisenberg interaction Hamiltonian [5]:

$$H = -2 \sum_{a>b} J_{ab} \hat{S}_a \cdot \hat{S}_b \quad (1.1)$$

J is mostly expressed in terms of temperature by dividing it by k_B , which is known as Boltzmann's constant. \hat{S}_i is the Dirac spin- $\frac{1}{2}$ operator of i^{th} electrons. J_{ab} expresses the exchange interaction energy between a^{th} and b^{th} electron. Note that we have used the spin angular momentum in eq.(1.1) and not total angular momentum because, for 3d transition metals, \hat{S} is a better quantity to determine the magnetic moment (as has been verified experimentally), whereas, in 5f transition metals, the spin-orbit coupling becomes significant. Therefore total angular momentum \hat{J} replaces \hat{S} in the equation. Hence H is the sum of all exchange energies of all the pairs of atoms in a lattice. However, when the interaction only includes the nearest neighboring atoms (as observed in crystal lattices), J is reduced to a single number. If $J > 0$, the interaction is said to be ferromagnetic, and if $J < 0$, the interaction is said to be antiferromagnetic. Ferromagnetic interaction means the spin of the electrons aligns parallel to each other, whereas, in antiferromagnetic interaction, their spins tend to align antiparallely. Moreover, if $J = 0$, the system is paramagnetic. The interatomic exchange coupling can only be ferromagnetic or antiferromagnetic.

The interaction amongst spins of partially filled orbitals leads to other magnetic orderings like ferromagnetism, antiferromagnetism, and ferrimagnetism (figure 1.4).

Ferromagnets are materials that are strongly attracted to magnetic fields and have a high internal magnetic moment because of the strong interaction ($J > 0$) among the unpaired electrons (fig. 1.4(a)). They make strong magnets, and their magnetic moment retains even in the absence of a magnetic field (known as remnant magnetic moment). The

strong coupling of spins in this material can be broken by heating the material to an exact temperature, known as Curie's temperature (expressed as T_c). Above T_c , ferromagnets behave as paramagnets. The net magnetization (total magnetic moment of the material per unit volume or mass) of a ferromagnet can also be reduced to zero by applying an external magnetic field (known as a coercive field) in the opposite direction to the internal magnetic field produced by the material (ferromagnet) itself. Examples of ferromagnetic materials are iron, nickel, cobalt, etc.

Anti-ferromagnets materials are not attracted in the presence of magnetic fields, but the spins show strong interaction among themselves. An antiferromagnetic solid is thought of as a solid having two sublattices, A and B. Each sublattice has equal magnetization in magnitude, but the direction is opposite, and hence the net magnetization of the entire crystal lattice is zero (fig. 1.4(b)). The temperature at which the net interaction energy of spins in both sublattices reduces to zero is known as Neel temperature (expressed as T_N). Above T_N , we observe an antiferromagnetic to paramagnetic transition. Examples of antiferromagnets are $\alpha - Fe_2O_3$, chromium, FeMn, NiO, etc.

Sometimes, due to structural constraints, the antiparallel spins in the material do not align perfectly, and there is some angle ($< 180^\circ$) between the spins. In such cases, one can observe a small remnant magnetization and a coercive field. Such orderings are known as **canted antiferromagnets**. As a famous example, $\alpha - Fe_2O_3$ undergoes antiferro to canted antiferro magnetic ordering when cooled below 10° C, known as Morin's transition.

Just as in an antiferromagnet, **ferrimagnet** solid can be considered to have two different sublattices with different magnetizations M_A and M_B , both having opposite signs. However, in this case $\vec{M}_A \neq \vec{M}_B$. Therefore, the net magnetization $\vec{M} = \vec{M}_A + \vec{M}_B \neq 0$. There is spontaneous magnetization, and a ferrimagnet's behavior in the presence of a magnetic field is similar to that of a ferromagnet. At the critical temperature T_c , the interaction energy amongst the spins starts decreasing very fast just, and this temperature is called the ferrimagnetic Neel temperature. Above T_c , both lattices lose their magnetism and start showing paramagnetism. Examples of ferrimagnets are $\gamma - Fe_2O_3$, Fe_3O_4 , $MnFe_2O_4$ etc.

In fig. 1.5, we briefly discuss all major magnetic orderings' magnetometry (MH) and thermomagnetic (MT) characteristics.

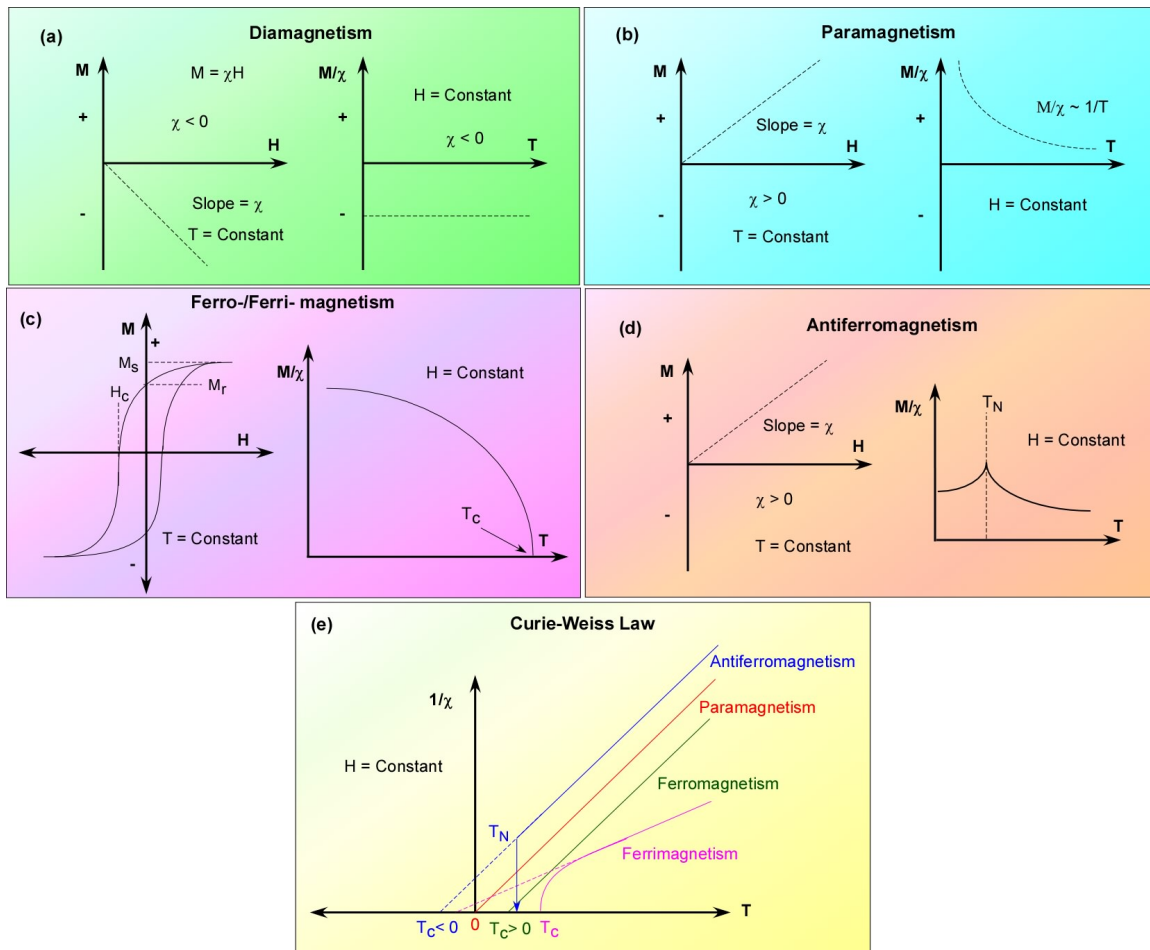


Figure 1.5: **Magnetic characteristics of major magnetic orderings in crystals.**

Here we have only briefly discussed the standard theory of magnetism and skimmed over the majority of details as a thorough discussion about these orderings and their properties are beyond the scope of this thesis.

In the next section, we will discuss the magnetic orderings of amorphous magnets.

1.3.2 Magnetic Orderings of Amorphous Materials

In solid crystals, the interaction J is between the nearest neighboring atomic sites and next to the nearest neighboring sites. Since the structure is crystalline, the interatomic distances are well defined and remain constant except for a few defects. Thus the value of J is fixed. However, the interatomic distances are not fixed in amorphous structures where there is no long-range atomic ordering. Therefore, instead of a fixed value of spin interaction constant, J , we have a distribution of its value. This leads to many new orderings of magnetism which are, in general, derivatives of the above main magnetic orderings listed above. The following flowchart in fig. 1.6 will help us glimpse the family tree of magnetic orderings in amorphous materials.

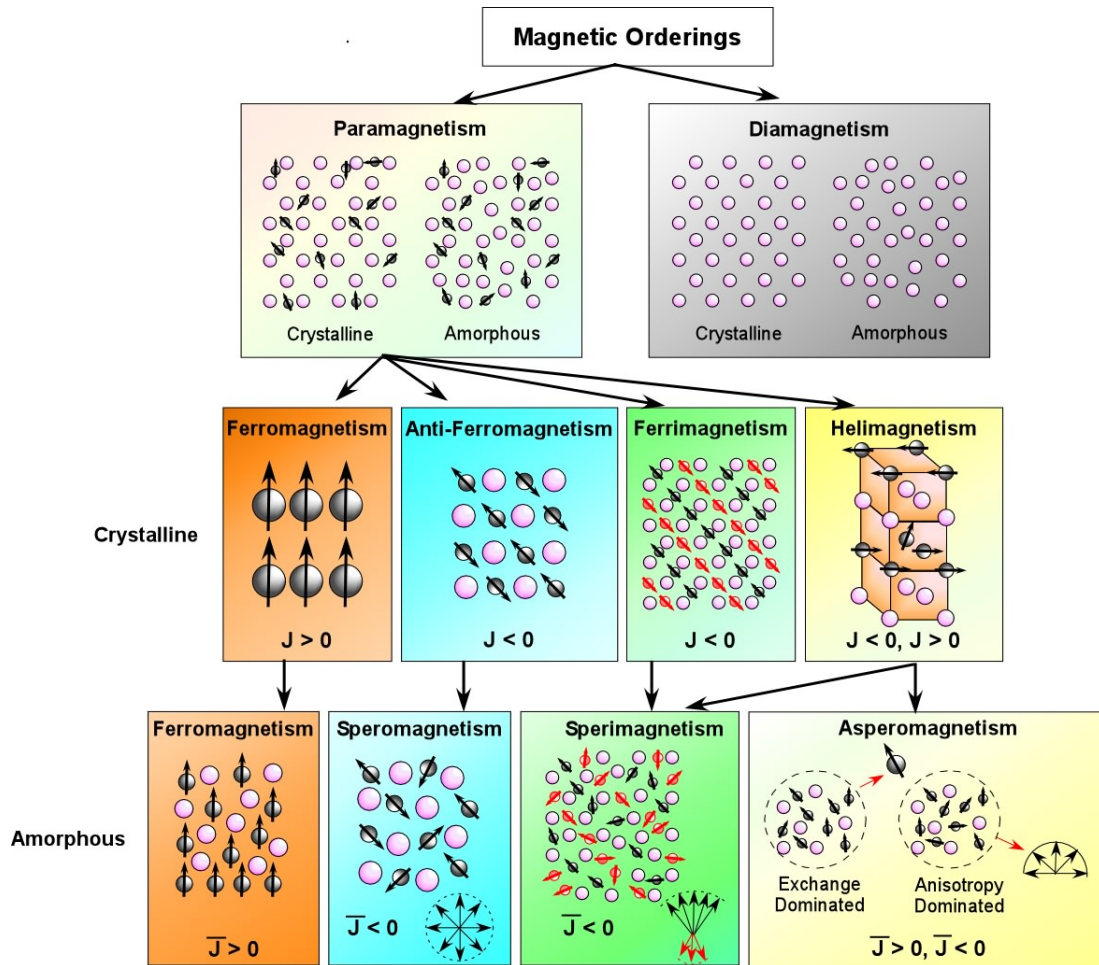


Figure 1.6: **Major magnetic orderings in amorphous materials.** The magnetic orderings in the last row are apparent in amorphous materials and disordered solid crystals. In the case of amorphous materials exchange interaction energy, J is replaced by \bar{J} (see eq. 1.2), as J is no longer fixed and has a distribution. (Adapted from [4, 5])

The magnetic orderings in the last row of figure 1.6 are not only limited to amorphous solids. They are also observed in disordered solids where different atoms irregularly occupy sites of a regular crystalline solid.

We can make amorphous magnets by doping dielectric amorphous materials with magnetic elements or compounds, e.g., common glass doped with iron oxide. However, in such cases, the concept of percolation threshold becomes quite important [63, 64]. Normally, doping amorphous material with ferromagnetic elements will not lead to ferromagnetism because the concentration of ions will be so low that they will be too distant for any exchange interactions. The percolation threshold, n_p , gives the minimum concentration of ferromagnetic impurities needed to turn a diamagnetic amorphous material into a soft ferromagnet. Generally $n_p = 2/Z_c$, where Z_c is the cation-cation coordination number.

As mentioned before, here, instead of a single value of exchange constant, we get a

distribution of it as:

$$\bar{J} = J + \Delta J \quad (1.2)$$

Now depending on the width of ΔJ , \bar{J} can either be positive as in amorphous ferromagnets or can be negative as in speromagnets or can have a distribution that spans from positive to negative as in asperomagnets (fig. 1.7). Both anisotropy and exchange constant play a significant role in deciding the Heisenberg interaction Hamiltonian of the system. Anisotropy means that magnetization in one direction will be more than in others. Here, we introduce the concept of single-point anisotropy. In an amorphous material, the crystal field changes from point to point. Therefore, the magnetic ions at every site try to align their moment along the easy local axis governed by the corresponding crystal field at their location. If D_i is the local axial crystal field strength at site 'i' and $S(z)_i$ is the total spin of the magnetic ion along easy axis direction 'z,' then the Heisenberg interaction in amorphous material is modified as :

$$H = - \sum_i D_i (S_z)_i^2 - 2 \sum_{ij} \bar{J} S_i \cdot S_j \quad (1.3)$$

Here we have assumed an axial symmetry of the crystal field for simplicity.

In the case of **amorphous ferromagnets**, magnetic properties like anisotropy and magnetostriction can be tuned by varying the composition to one's preference. Such ability is not permitted in rigid crystalline ferromagnets. Although one can understand there cannot be any magnetocrystalline anisotropy since there are no crystal lattices in amorphous magnets. Moreover, it has been observed that the Curie temperature of amorphous materials is not very different from that of crystalline counterparts, although magnetization falls quicker in the case of amorphous magnets. A few examples of amorphous ferromagnets are $Fe_{80}B_{20}$, $Fe_{100-x}Co_x$ etc.

Speromagnetism, on the other hand, is the case where the interaction constant J is completely negative. In the case of amorphous materials, this means that spins are all in a random direction creating a frustrated spin state (fig. 1.6). The interaction is generally through superexchange (of some kind). The randomized spins lead to a magnetic response similar to paramagnets at a temperature above a critical temperature called T_{so} . T_{so} is the temperature where the spins freeze; below this temperature, spins attain a random configuration just as in a frustrated spin system. This critical temperature is smaller than the paramagnetic Curie temperature, T_p . There can be multiple frozen spin states, and all are degenerate in nature. The M-H characteristics of Speromagnetism is shown in fig. 1.7(c). Examples include YFe_2 , FeF_3 , $\alpha - Re$, etc..

Sperimagnetism is the amorphous analog of ferrimagnetism, as has been presented in

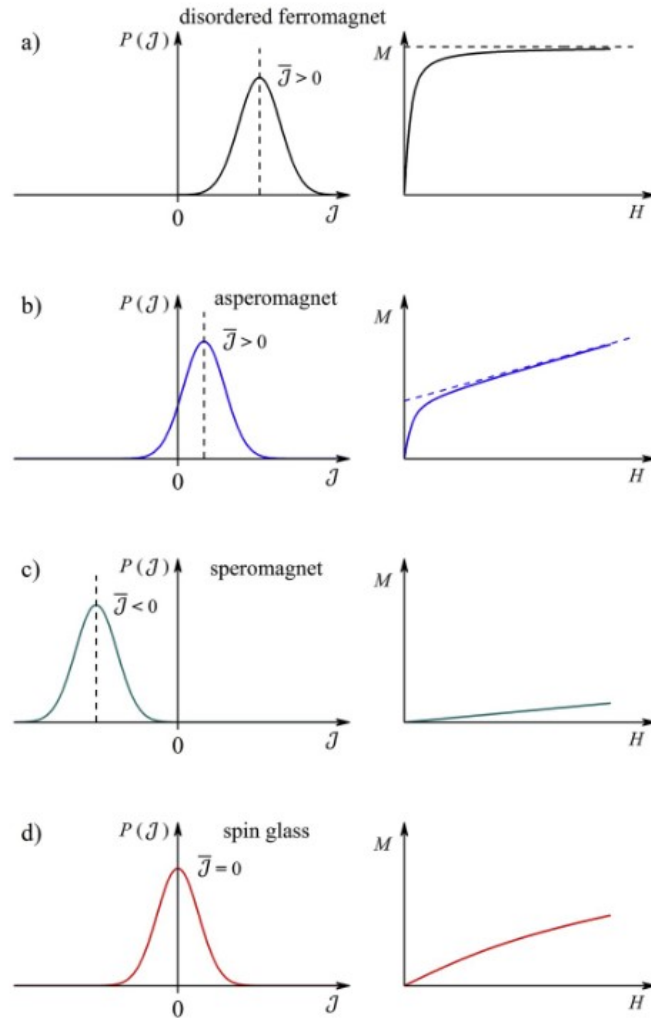


Figure 1.7: **MH of major amorphous magnetic orderings.** A schematic presentation of different sorts of magnetic ordering based on the distribution function of the exchange interactions $P(J)$ and the corresponding $M(H)$ magnetization curve: (a) disordered ferromagnetism, (b) asperomagnetism, (c) speromagnetism and (d) spin glass. (Taken from [6])

figure 1.6. Here there are two or more magnetic species, mainly made of both 3d-4f transition atoms, unlike speromagnets and asperomagnets. Atoms interact ferromagnetically with members of their series and antiferromagnetically with atoms of other series. The system have a non-zero remnant magnetization.

Asperomagnets, as represented in fig.1.7(b), have a range of J in both positive and negative values. This type of interaction again is frustrated in nature, and the spins are randomly oriented. However, the spin alignment is more likely parallel than antiparallel in local environment, causing microdomain formation within the structure. Therefore, a remnant magnetization is present. The interaction between such spins is not as strong as in ferromagnets. Since the aligned spins can have a favorable direction, anisotropy plays a big

role. The competition between exchange interaction and anisotropy is crucial and has consequences on net magnetization with respect to the applied field. If $|J| > |D|$, each domain acts independently as a single spin and is unaffected by the large fields, and magnetization does not saturate. However, if $|D| > |J|$, the domains are affected by the external field, and the magnetization saturates depending on the direction of local easy axis with respect to the field. Examples are YFe_3 , $TbAg$, $GdAl_2$ etc.

Spin glass are a special category of magnetic systems which have very dilute magnetic impurities ($< 1\%$) in a glass-like amorphous matrix. These systems can be both metallic and non-metallic. The impurity concentration is far less than the percolation threshold needed for impurities to interact directly and form any clusters. Thus, in the case of metallic materials, their primary source of interaction is through the indirect or RKKY method. The distribution of the interaction constant, \bar{J} , is centered at zero, and the width is symmetrically extended in both positive and negative directions (fig. 1.7(d)). One of the key signatures of a spin-glass is a difference in MT (Magnetization v. Temperature) measurements of material depending on whether it is cooled under the presence or absence of a magnetic field (field-cooled (FC) and zero-field cooled (ZFC)). This cusp arises below a critical spin freezing temperature, T_{SG} . Below this temperature, the spins of the magnetic impurities freeze into one of the many possible degenerate configurations. Under the influence of a magnetic field (FC), the configuration with maximum moment gets selected, and we observe a net magnetization. In contrast, in the absence of a field (ZFC), the spins freeze in random directions, and the magnetization below T_{SG} approaches zero. Thus, a divergence between ZFC and FC. Such divergences are not visible in ferromagnets under small magnetic fields (unless there is a strong anisotropy). Examples of ideal spin glasses are $CuMn$ and $AuFe$.

Interestingly, the spin glass system is not limited to amorphous materials but can occur in crystalline materials too. Spin glasses are a general system with disorderedness and frustrated magnetic interactions, and therefore, magnetic orderings like speromagnetism and asperomagnetism can be considered variants of spin glasses. As we keep on increasing the concentration of magnetic atoms, they start forming magnetic clusters in the host material that interact directly; this leads to a **cluster glass** magnetic ordering (fig. 1.8). Again, on continuous addition of magnetic impurities, it transition from cluster glass to an amorphous ferromagnet. Interestingly, when the concentration of magnetic atoms per unit volume n is close to percolation threshold n_p , we can observe a unique transition in the magnetic ordering of the overall material as we vary temperature (fig. 1.9). Below Curie temperature, ferromagnetic interaction aligns the atomic magnetic spins. However, as we keep lowering the temperature, a critical temperature, T_{xy} , comes below which we observe a magnetic transition from ferromagnetic to asperomagnetism ordering. The local field anisotropy, $|D|$, causes the transverse components of magnetic spins to be frozen in random directions and

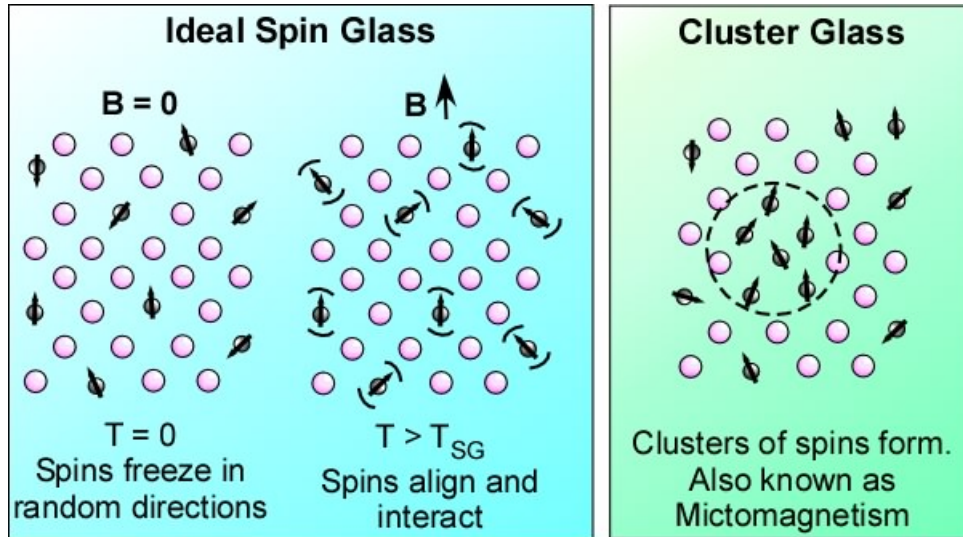


Figure 1.8: **Ideal spin glass and clustered spin glass systems.** The atomic concentration of magnetic impurity in ideal glass is $\leq 1\%$ while in clustered glass is 30%-50%.

we observe a decrease in net magnetization of the material.

At the end of this section, we have laid down the basic foundation of magnetism and its concept, at least for the scope of this thesis. We will now discuss various new concepts that have emerged and challenged our fundamental understanding of conventional magnetism, especially the emergence of magnetism in organic materials.

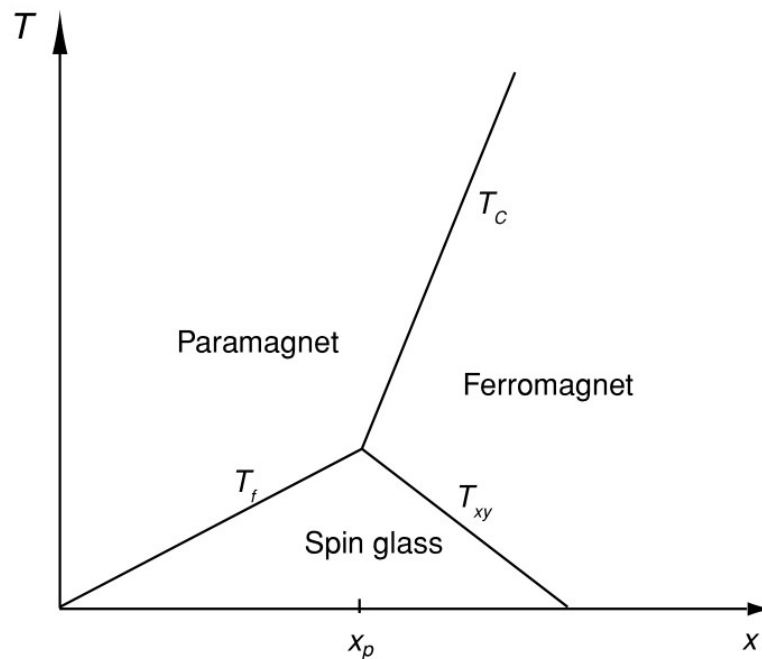


Figure 1.9: **Cluster glass phase diagram.** Phase diagram for a metallic spin-glass system as a function of concentration and temperature.

1.4 Proteins in Magnetic Field

Before exploring organic magnets, we will take a break and return to proteins. In section 1.2, we described that silks are protein fibers. We will now study what happens when a protein is kept under a magnetic field.

1.4.1 Diamagnetic anisotropy of proteins

Amino acids are made of carbon, hydrogen, nitrogen, and oxygen. Hence amino acids and proteins are diamagnetic in nature [65]. However, things get interesting when we keep proteins under very high magnetic fields (> 2 T) because we observe the diamagnetic anisotropy of proteins in action. Such high magnetic fields can only be produced in laboratories. When kept in a high magnetic field, protein structures like α -helix or β -sheet, collagen, etc. align themselves in a magnetic field such that the diamagnetic repulsion is maximum. The magnetic stabilization energy is given as:

$$\Delta E = \frac{\mu_0}{2} |\Delta\chi| H^2 \quad (1.4)$$

Here, $\Delta\chi$ is the diamagnetic anisotropy in susceptibility of protein and is given by $\Delta\chi = \chi_{\parallel} - \chi_{\perp}$. H is the magnetic field strength. χ_{\parallel} and χ_{\perp} are the susceptibilities of protein when the peptide bond plane is parallel and perpendicular to the direction of the applied magnetic field. The protein structure is oriented magnetically when $\Delta E > k_B T$. This behavior is not limited to proteins but is also observed in other biopolymers like DNA and polysaccharides and is utilized in polymer processing. Moreover, strong magnetic fields help form protein crystals faster, and the crystals formed under the influence of high magnetic fields have increased crystallinity [66, 67].

Now, the question remains, what is the origin of this diamagnetic anisotropy? The answer to this lies in the structure of peptide bonds. The conjugated nature of peptide bonds, i.e., the partial double bond between the -CNO bond, leads to diamagnetic anisotropy [68]. Delocalized electrons in the partial double bonds result in the diamagnetism of molecules, as discussed in section 1.4.1. α -helical structures show the most significant anisotropy. The peptide bonds in α -helices are parallel to its axis, making it the direction of smallest diamagnetic susceptibility. Thus α -helices align parallel to the magnetic field directions. In β -sheets, on the other hand, the peptide bonds are oriented parallel to the sheet. β -sheets also align themselves parallel with magnetic fields, i.e., the normal vector from the plane of the sheet is perpendicular to the direction of the field. Similarly, in the case of collagens, the peptide bonds are oriented 45° to the axis; hence the orientation of collagens is perpendicular to the magnetic field lines. Compared to aromatic ring structures, the anisotropy of

peptide bonds is about one order of magnitude lesser.

1.4.2 Magnetoreception proteins

Magnetoreception is the ability of living beings to sense earth's magnetic field. This helps many organism to navigate their home and migrate from one place to another during climate changes across the year. These abilities have been discovered in simplest organism like bacteria to complex organism like reptiles, birds and most mammals (except humans). Magnetoreception capabilities of living beings have long been speculated to be connected with light sensing cryptochrome (Cry) proteins found in the retina of the eye of living beings. A possible mechanism through which protein can sense or be affected by small magnetic fields (μT s) is by the formation of radical pairs (RP) [69]. Recently, another possible explanation for magnetoreception was given by discovering a new magnetic protein called MagR, a complex made by cryptochrome and iron-sulfur-based protein system [8]. We will discuss both these proteins one by one.

Radical pair mechanism and Cry protein

Radical pair formation is an intermediate step when a protein reaction occurs via photochemical, thermal, or radiative processes. Radicals are formed due to electron transfer, hydrogen transfer, or decomposition of spin-singlet or triplet excited states and are short-lived in nature. The state that produces singlet radical pairs are called S-precursors, and those producing triplet pairs are called T-precursors. These radicals can be influenced by external magnetic fields and thus can change the pathways and kinetics of the protein reaction. A brief description of the radical pair mechanism is given in figure 1.10.

The reaction starts with forming radical singlet or triplet pairs from their respective S and T precursors [70]. These radicals are surrounded by a chemical solvent depicted with +R. Now, as these radicals are generated, they are nearby; thus, the pair of radicals are called close (Close RP). We know that the spin singlet state (antisymmetric) can easily recombine and form a stable ground state complex known as cage product. At the same time, the triplet state (symmetric) will have to overcome a Coulombic barrier to recombine. However, singlet pairs can sometimes convert into triplet pairs in radicals with heavy central atoms. If the cage product is not formed, the close pair radicals diffuse away from each other into the solvent and eventually form separate pairs (Separated RP). These separate pairs recombine with radicals formed by other pairs, producing a stable product. The external magnetic field can manipulate the conversion of the S-T pair and, thus, the overall chemical reactions. A detailed quantum mechanical approach to the process can be found in literature and is beyond the scope of this thesis.

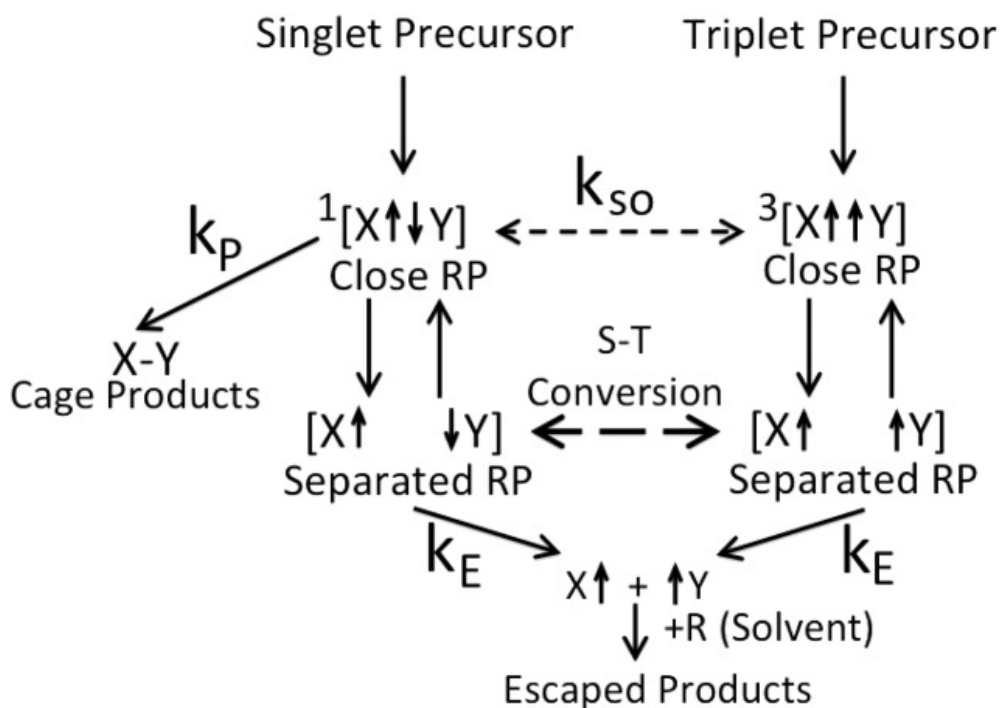


Figure 1.10: **Radical pair mechanism.** Reaction scheme of radical pairs generated from singlet and triplet precursors. Singlet and triplet radical pairs are represented by $1[...]$ and $3[...]$, respectively. $K_{SO,P,E}$ are the rates of reactions. (Taken from [7])

The idea of the RP mechanism as a source of magnetoreception in migratory birds was first interpreted in 1978 [71] and has been an active topic for research ever since. After long scrutiny, various conditions were put on the kind of protein responsible for magnetoreception to narrow down the possible candidates. Finally, it was proposed that a protein named cryptochrome (Cry protein) has the potential to induce magnetoreception abilities in a living organism. It is found in the retina and is a photoreceptor protein. It has also been found in parts of the forebrain responsible for vision processing and absorbs blue-green light. The complete mechanism of Cry has been presented in multiple papers [72, 73, 74]. Cryptochrome consists of flavin adenine dinucleotide (FAD) and a chain of tryptophans (Trp). On absorbing blue light, it produces $[FAD^* - TrpH^{*+}]$ and $[FAD^* TrpH^*]$. On application of static magnetic field, only the former RP can go back to its ground state of $[FAD + TrpH]$ while the other RP is spin forbidden to revert to its ground state. These changes are easily detectable and indicate the presence of a magnetic field, and hence changes in the yield of chemical products lead to magnetoreception.

MagR-Cry protein complex

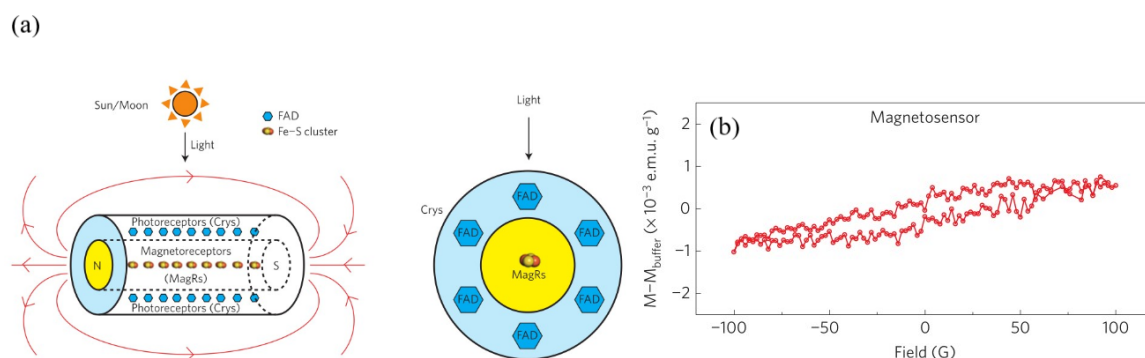


Figure 1.11: Structure and magnetic character of MagR-Cry complex. (a) A nanoscale Cry/MagR magnetosensor complex with intrinsic magnetic polarity acts as a light-dependent biocompass. Linear polymerization of Fe–S cluster-containing magnetoreceptors (MagR) leads to the formation of a rod-like biocompass at the center (core, yellow), surrounded by photoreceptive cryptochromes (Cry; the outer layer, cyan). Cross-section on the right side, indicating that electron transportation from the FAD group in Cry to the Fe–S cluster in MagR upon light stimulation may be possible. (b) Magnetic properties of the cIcry4/cIMagR magnetosensor complex. Room temperature magnetization as a function of the field for the cIcry4/cIMagR magnetosensor complex was obtained by subtracting the contribution of a buffer from the solution. A hysteresis loop indicates the ferrimagnetic behavior of the cIcry4/cIMagR complex. (Taken from [8])

Recently researchers have found a new protein biocompass to explain magnetoreception in animals. The said protein biocompass was extracted from the retina of *Drosophila melanogaster* and is proposed to be present in all insects, birds, rodents, etc., including humans. It is a complex made up of a magneto-sensitive iron-sulfur cluster protein named MagR and the Cry. The proposed structure is shown in fig. 1.11(a). This protein assists in light-magnetism coupled magnetoreception [8]. Moreover, the crystalized protein obtained from the complex was analyzed using a SQUID magnetometer for M-H characteristics (fig. 1.11(b)). A hysteresis loop was observed with a coercivity of 20 G (2 mT), and scientists proposed that the complex formed is ferrimagnetic in nature. These results are, however, very controversial since the iron atoms couple antiferromagnetically in all Fe-S clusters and sometimes exhibit paramagnetism in the case of mixed valence states of the involved iron

atoms.

Iron binding proteins

At this point, we must discuss metalloproteins, particularly iron-binding proteins, and describe how they interact in magnetic fields. Many iron-binding proteins are known to us, and they are vital to our existence. Hemoglobin is an essential protein responsible for oxygen transport in our body through blood. Ferritin is the iron-storing protein that releases iron in case our body has iron deficiency. Ferredoxin is present in plants, humans, and bacteria. It helps in the process of photosynthesis in plants and anaerobic electron transport in bacteria. In humans, it is essential for the functioning of mitochondria. Rubredoxin is another iron-containing essential protein responsible for electron transfer in biological systems. Likewise, there are many more proteins with an abundance of iron content. However, the iron in all these proteins has either no unpaired electrons or whenever unpaired electrons are present, they often interact antiferromagnetically. It also infers that the mere presence of iron does not guarantee ferro-/ferri-magnetism in biological systems. Complete knowledge of the structure and binding state of iron is essential. No protein has been found that exhibits ferromagnetism (except the MagR-Cry complex), even though there are proteins like deoxyhemoglobin and ferritin that are paramagnetic at room temperature.

Magnetogenetics is a new field that utilizes genetic encoding to develop protein assemblies that are sensitive to magnetic fields and can be used to control cell behavior. Recently, a research group engineered a ferritin-containing protein crystal by loading it with iron *in vitro*. The proteins showed apparent ferromagnetic behavior and moved towards a magnet. Such a response was replicated when the engineered protein was inserted into the cell *in vitro*; the entire cell started moving towards the magnet [75]. This is a significant step toward functional magnetogenetics and the development of organic protein-based magnets.

1.5 Organic Magnets

The knowledge of magnetism acquired so far has elucidated that magnetism is a quantum phenomenon. The angular momentum of an electron is the root source of an atom's magnetic moment, and the interaction of these magnetic moments leads to magnetic orderings in a solid. Hence the requirements to become a magnet (ferromagnet) can be stated as (1) the presence of a stable magnetic moment, (2) interaction among these magnetic moments with an appropriate exchange interaction with $J > 0$ (ferromagnets) or an overall majority of parallelly aligned magnetic moments (ferrimagnets, asperomagnets, and sperimagnets) and (3) arrangement of these interacting moments over the large region across the material.

However, one must have observed that throughout our discussion of magnetism, we

have only come across examples that are inorganic or metallic, except for section 1.5, where we dealt with proteins. The discovery of the first organic molecular magnet was made in 1991 in p-nitrophenyl nitronyl nitroxide radical (p-NPNN) [76] even though its Curie temperature was just 0.6 K. Since then, organic magnets have been a hot topic for research. Organic magnets hold key advantages over inorganic ones: biocompatibility, biodegradability, plasticity, flexibility, solubility in common organic solvents, and electrical insulation. All these properties can be helpful in multiple biomedical and spintronic applications. Moreover, organic magnets already have the upper hand in magneto-optical switching applications and in applications requiring the manipulation of light polarization due to their superior optical properties compared to the inorganic magnets [77]. Their biodegradability and low cost of production make them even more advantageous over traditional inorganic magnets. In addition, one can tune their physical properties very easily by modifying their synthesis process.

Even though organic magnets seem very attractive, developing such magnets is not easy. As mentioned earlier, an organic compound or polymer must fulfill all three requirements to become a magnet. Fulfilling each of these requirements has challenges. We know that a compound with completely filled orbitals is diamagnetic. All organic compounds are predominantly diamagnetic in nature, and in order to have a stable magnetic moment, they must have an unpaired electron or a radical. The problem is that organic compounds with free radicals are generally highly reactive (because of lack of localized d or f orbitals) and, therefore, unstable. The second challenge is that even if we manage to have unpaired electrons by adding 3d transition metals or forming stable radicals in p-orbital, it is found that whenever these unpaired electrons are nearby, they tend to interact antiferromagnetically and have zero net magnetic moments. Nevertheless, scientists have devised new strategies and techniques to overcome these two obstacles. We will discuss them in this section.

The critical development of organic magnets is seen in two types of materials: (1) Magnetic polymers and (2) Molecular magnetic solids. We will discuss both these types under this section in the following subsections.

1.5.1 Persistent organic radicals

The preparation of a persistent radical in an organic molecule is a big challenge due to its highly reactive nature. The word persistent is more appropriate and often used than stable because these radical configurations are not stable, just more persistent in time [11]. There are three ways in which these highly reactive radicals can be made persistent. However, the formation of persistent radicals is still a sporadic case, and only a handful of examples exist. Most of the molecular magnets synthesized are usually derivatives of this handful of functional groups. The primary three techniques or strategies for making a free radical

persistent in time are:

- **Steric hindrance:** The presence of a bulky and large number of stable molecules or functional groups around the free radicals prevents these radicals from reacting with their environment. This has been a very effective strategy for producing some of the most persistent radicals (e.g., fig. 1.12). Nevertheless, this steric hindrance can also become a bane if proper care is not taken as it can isolate the radicals completely and hence obstruct the possible pathways of their interaction among themselves, which are crucial for a ferromagnetic response.

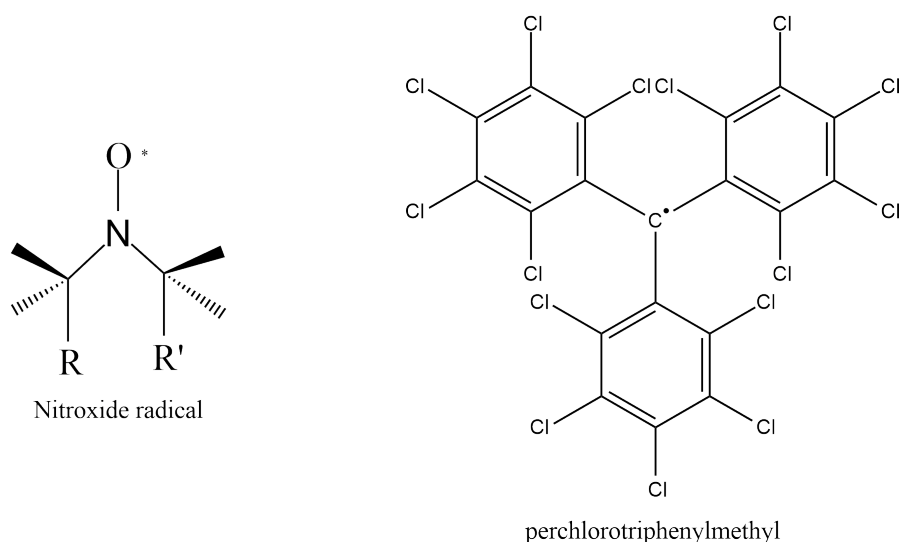


Figure 1.12: **Sterically protected radicals.** Examples of persistent organic radicals formed due to steric hindrance by bulky functional groups. "*" represents the free radical. [9, 10]

- **Heteroatoms:** Introduction of a negative charge by an electronegative heteroatom, along with an already existing free radical, helps increase the latter's persistence. The Coulomb repulsion between the radical and negative ion prevents their dimerization and hence the persistence of free radicals.
- **Delocalization:** Increasing the delocalization of an unpaired electron can help increase the persistence of free radicals.

In order to obtain very persistent radicals, one must simultaneously use these strategies in a stable solid structure (fig. 1.13). A few examples of highly stable free radical molecules are given in figure 1.14.

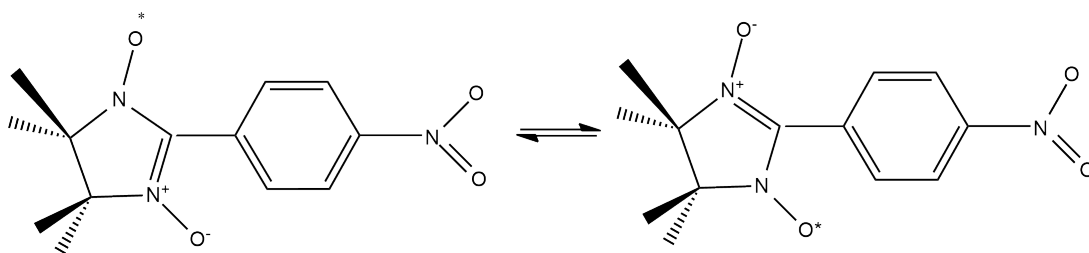


Figure 1.13: **Stable α -nitronyl nitroxide radical.** The above radical is stable due to aids from large steric hindrance, charge densities on the NO group, and delocalization.

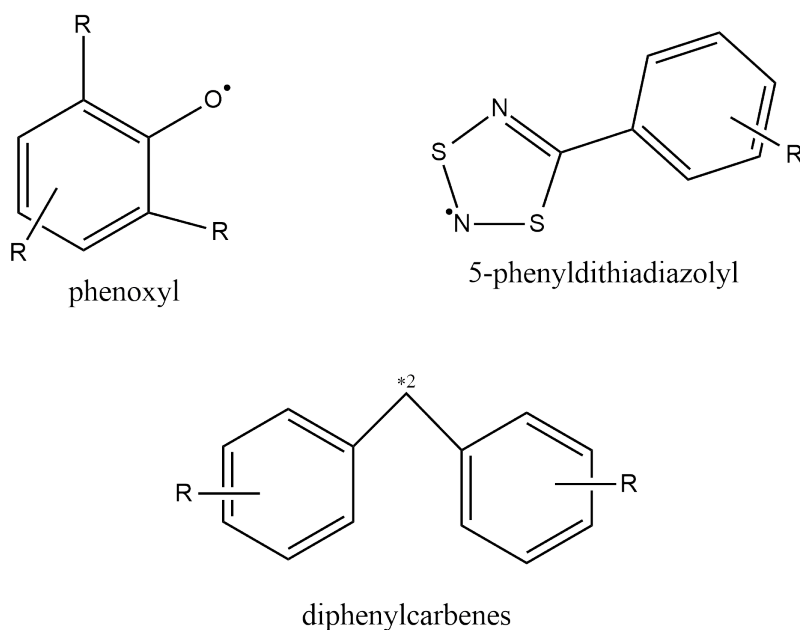


Figure 1.14: **Free persistent organic radicals.**

1.5.2 Magnetic exchange interaction

Two unpaired electrons are ferromagnetically coupled if they reside in two localized orthogonal magnetic orbitals that share as much as possible the same spatial region [12]. This rule is the baseline for all interaction mechanisms responsible for observed ferromagnetism in organic compounds. As we discussed, there are two types of organic magnets based on the assemblies of the persistent spin-containing units: molecular magnetic solids and magnetic polymers. Organic magnets have several intramolecular spin coupling exchange mechanisms, as explained below. The first three mechanisms operate in molecules with strongly localized spins and produce magnets that are only stable at very low temperatures. The last spin coupling mechanism operates in highly delocalized molecules and produces magnets with high overall spins and are found to be stable up to high temperatures in particular examples.

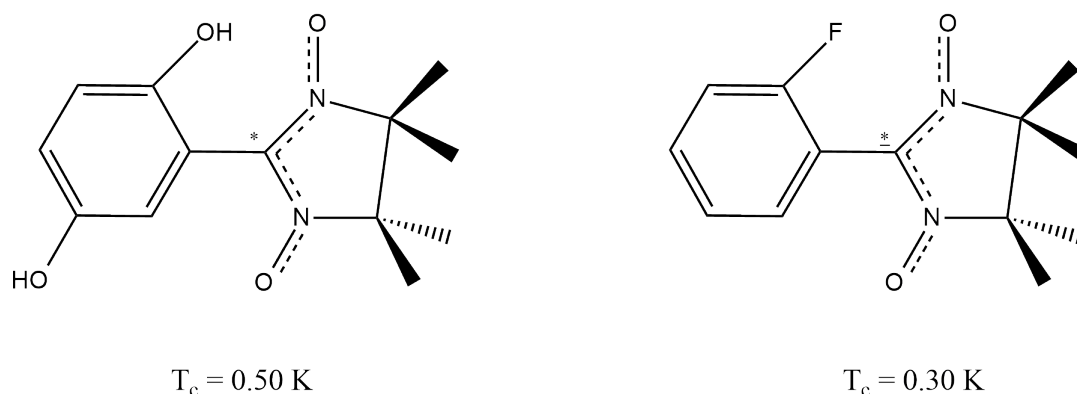
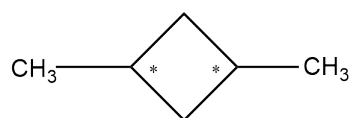


Figure 1.15: **Nitronyl aminoxy derivatives.** Molecular magnetic solids are formed using the above molecules at extremely low temperatures. The star "*" represents the stable radical. The Curie temperatures of individual molecular solids are given below the molecule.

- Orthogonal orbital mechanism:** This mechanism is exactly what its name suggests. One tries to form a molecular structure where the unpaired electrons exist in close proximity and same spatial region; however, they are in orthogonal orbitals, and hence interaction is ferromagnetic or weakly ferromagnetic. The triplet state, in such cases, is lower in energy than the single state. The better the condition is followed, the stronger the chances of ferromagnetic coupling. Small molecular structures like carbenes ($:CH_2$), nitronyl aminoxy, nitriles ($-CN$), and nitrenes ($-NR$) are successful examples of molecular magnets formed by this mechanism. Thus, many molecular magnetic solids have been attempted based on derivatives of these structures. A few successful structures are given in fig. 1.15, along with their Curie temperatures. However, the environment of the solvent or rotational and vibrational degrees of freedom of the molecule can sometimes interfere and cause the singlet state to be lower in energy leading to an antiferromagnetic coupling. Thus an orthogonal-orbital mechanism is fragile.
- Superexchange:** This mechanism is not different from the ordinary superexchange interaction. When the singly occupied magnetic orbitals (SUMOs) of spin-containing units (free radicals) are far apart to couple directly, their hybridization with the completely filled magnetic orbitals of diamagnetic bridges can lead to ferromagnetic interaction. Nevertheless, the conditions for ferromagnetic coupling in such situations are again very strict. This mechanism is mainly seen in diradicals formed on a cyclic organic structure, as shown in fig. 1.16. This mechanism can produce very robust high spin molecules.



1,3-disubstituted cyclobutanediyl

Figure 1.16: **Superexchange in organic molecular magnets.** The far free radicals hybridize with the diamagnetic bridges to interact among themselves.

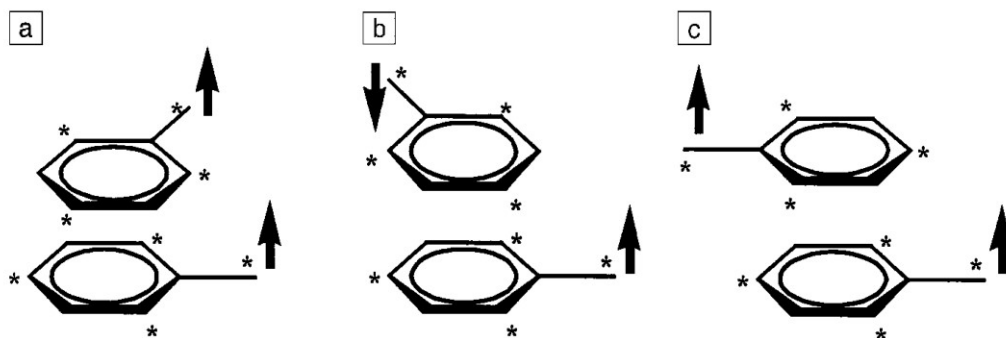


Figure 1.17: **McConnell I mechanism.** Different magnetic couplings (a), (b), and (c) for three distinct orientations of two parallel, close-packed benzyl radicals. Here (a) and (c) show ferromagnetism and (b) shows antiferromagnetism. (Taken from [11])

- McConnell I Mechanism:** This is an intermolecular exchange mechanism rather than an intramolecular mechanism like the previous two mechanisms. This mechanism explores the possibility of ferromagnetic exchange among closely packed molecular structures containing free radicals based on their spatial arrangements. Spin-containing units have a set of positive spin-density atoms and negative spin-density atoms. The spatial arrangements of atoms in these units can influence the configuration interaction between nearby spin-containing units' singly occupied molecular orbitals (SOMOs). An example of this behavior is shown in fig. 1.17. A star represents the positive spin density of atoms. If the atoms with opposite spin densities are placed on top of one another, the net interaction is ferromagnetic. In contrast, if the atoms with similar spin densities are placed on top of each other, an antiferromagnetic interaction is observed [78].
- Topological symmetry degeneration:** Persistent spin-containing units can be prepared in delocalized molecular systems. While the above three exchange mechanisms involve strongly localized spins, this exchange mechanism involves highly delocalized ones. Non-Kekule structures are conjugated systems with two or more

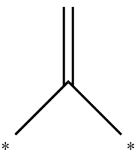
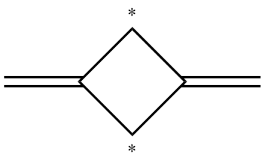
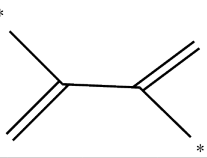
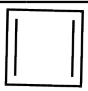
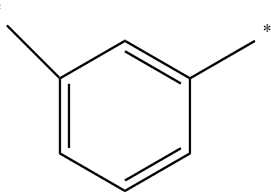
S. No.	Compound	Ground state
1		Triplet
2		Triplet
3		Triplet
4		Singlet
5		Singlet

Figure 1.18: **Non-Kekule structures** and their respective ground states. (Taken from [12])

free radicals and thus cannot form a resonance structure. These free radicals occupy non-bonding molecular orbitals (NBMOs), equivalent or nearly equivalent in energy. However, the spin state depends on whether the molecule is disjoint or nondisjoint. The simplest non-Kekule structures are trimethylmethane (TMM) (structure 1 in fig. 1.18) and trimethylethane (TME) (structure 3 in fig. 1.18). If the two free radicals containing atoms share a common atom, the molecule is called nondisjoint, and the triplet states, in such cases, will also be lower in energy. TMM is a nondisjoint molecule. In cases like TME, the free radical-containing atoms do not share any common carbon atom; therefore, they are disjoint molecules. Singlet and triplet states are nearly degenerate in disjoint cases, and ground state of spin depends from system to system. A table in fig. 1.18 below gives examples of hydrocarbons where a triplet state is preferred, and ferromagnetic exchange dominates via this exchange mechanism.

Designing nondisjoint molecules for making high spin robust organic magnets is usu-

ally common practice. Most organic magnets are designed by making derivatives of the above nondisjoint hydrocarbons. However, defects in such hydrocarbon systems reduce their spin state severely.

Molecular Magnetic Solids

The practical use of the above-discussed organic molecule magnets is only possible by assembling them in macromolecular structures with high spins. One approach is to create magnetic solids. Magnetic solids are formed by the extension of magnetic molecules in three dimensions. Since there are no ways to control the 3D packing in an organic molecule, the resulting magnetic solids are only possible at very low temperatures. The molecules come together at low temperatures and eventually have a 3D magnetic ordering. $V[TCNE]_x$ and its derivatives are a few exceptions that form thin film and powder form and can show magnetic ordering at room temperature. The magnetic dimension of a molecular magnetic solid depends upon the number of exchange pathways molecules have along different dimensions. Thus a molecular magnetic solid can have a magnetic dimension different from its spatial dimensions. Generally, all magnetic molecular solids have been discovered accidentally.

Several examples of purely organic magnetic molecular solids and their mode of interactions have been discussed. Besides purely organic magnets, initial research in organic magnets utilized metal complexes with organic ligands carrying radicals. These molecules (fig. 1.19) have coupled 3d spins of transition metals and 2p spins of organic ligands to give Ferro/ferri-magnetic orderings in 0D, 1D, 2D, and 3D. The choice of exchange mechanism among the spins of such complexes is either direct exchange (in case of metal-metal interaction or metal-ligand interaction) or superexchange (in case of metal-ligand-metal interaction). Complexes like $V^{II}[TCNE]_2$, $Mn(hfac)_2$ and $Cu(hfac)_2$ have achieved T_c up to 400 K and 220K respectively. Various nitrile containing TCNE based and cyanide containing metal-organic complexes like $[Fe(C_5Me_5)_2] + [TCNE] \cdot -$, $Li[TCNE]$, $M^{II}(TCNE)[C_4(CN)_8]_{1/2}$ (M = Mn, Fe) and $[M(CN)_6]^{n-}$ (M is metal ion) [79, 80] etc., have shown immensely strong ferromagnetic signatures, but these complexes again, becomes strong magnets only at very low temperature (typically < 10 K) and are highly reactive and unstable in ambient conditions. Recently, chromium-pyrazine-based metal-organic ferrimagnets were prepared with critical temperatures up to 242°C, and a 7500-oersted room-temperature coercivity [81].

Magnetic Polymers

Another approach to achieving high magnetic spin and robust structure is extending molecular magnets to form polymer magnets. Polymeric magnets interact via the topological symmetry degeneration approach. Magnetic polymers have potential applications such as

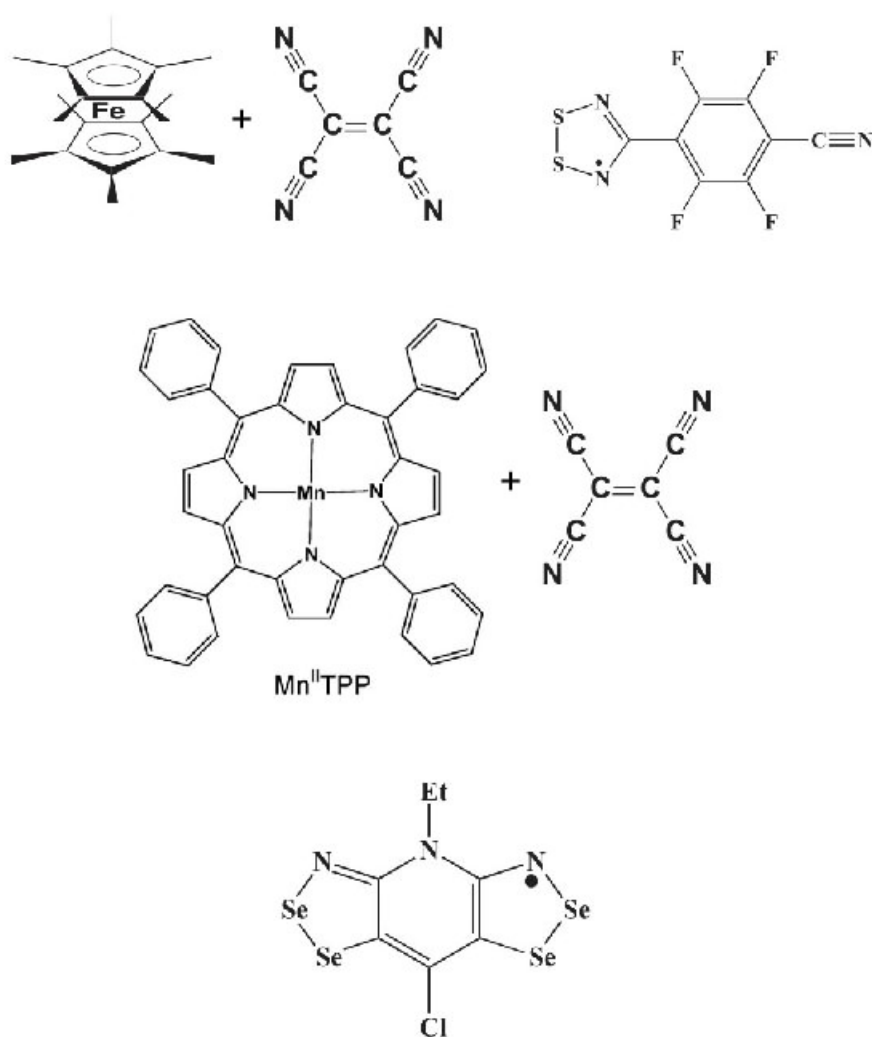


Figure 1.19: **Metal-organic molecular magnets.** Here are a few examples of metal-organic complex molecular magnets. These show ferro/ferri- magnetic behaviors at very low temperatures $\approx 2\text{K}$. (Taken from [13])

magnetic recording materials, magnetic shield coatings, magnetic bio-imaging agents, etc. Small defects or minor distortion in the planarity of polymer structures can disrupt their ferromagnetic coupling pathways and reduce the net magnetic moment, making their development challenging. In the last two decades, a few polymer magnets showing room temperature ferromagnetism have emerged [82, 83, 84]. Examples of a few polymeric magnets are given in figure 1.20.

1.5.3 Future Perspectives

Some of the key advantages of organic magnets have been discussed earlier in this section. A few key areas where organic magnets holds unique advantage is their multi-property behavior and the ease of tuning their magnetic moment. Organic magnets can couple magnetic

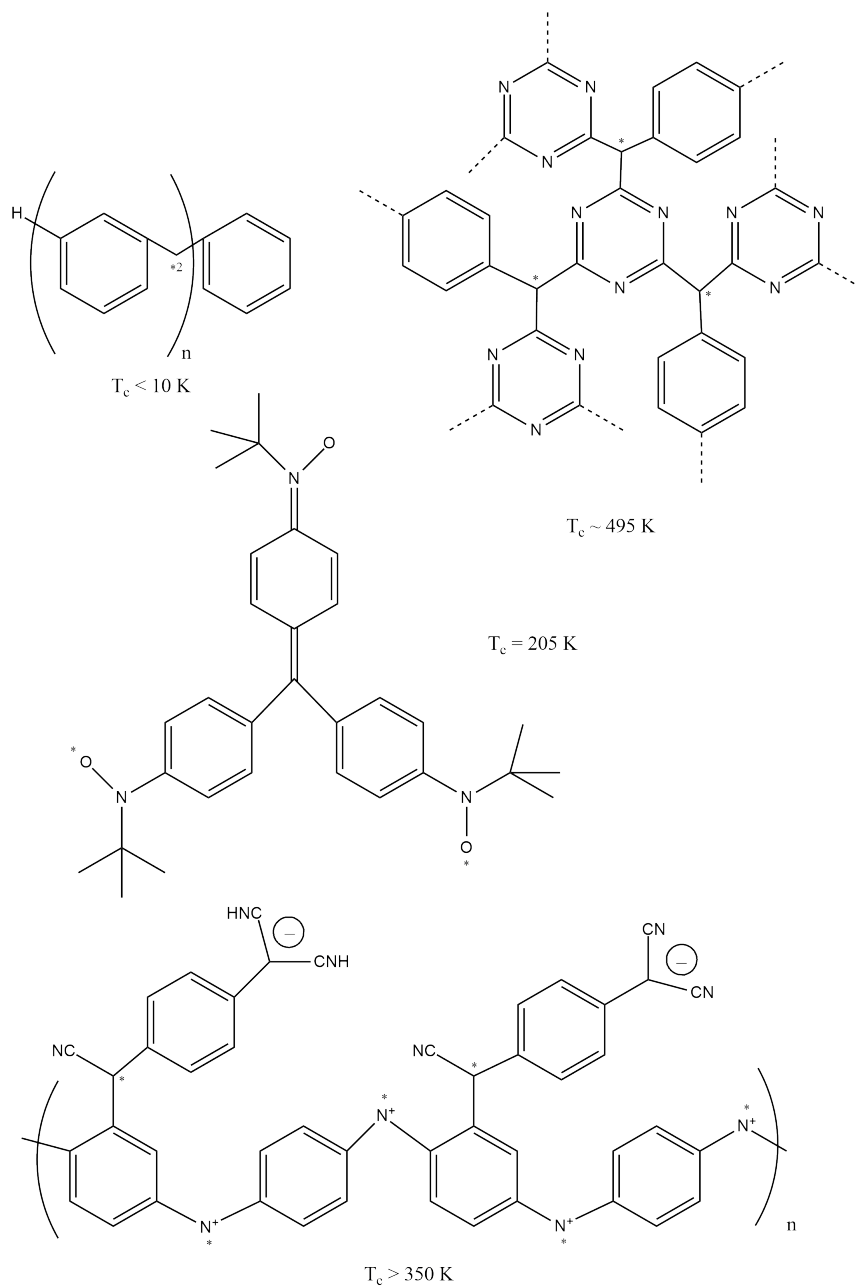


Figure 1.20: **Polymer Magnets.** Examples of a few polymer magnets with their respective Curie temperatures. We can see that there have been few successful attempts at producing room-temperature polymer magnets. However, these magnets (room-temperature) are very brittle.

behavior with electrical, optical, mechanical, and chemical properties. Their magnetic behavior can also be easily mediated by the stimulus of stress, temperature, pressure, photons, electrons, etc. This has potential applications in micro-/nano- scale switching mechanisms and data storage devices. From our present knowledge of organic magnetism we can also predict that organic high spin bulk magnetic materials can only exhibit magnetic orderings illustrated by amorphous magnets discussed in section 1.4.2.

1.6 Magnetism in Carbon allotropes

Carbon is one of the most versatile and essential elements, without which life on earth is impossible. Almost all of the organic matter on earth is made from carbon. Moreover, research on understanding the properties of carbon has been going on for centuries, and still, it keeps astonishing us. One such astonishing discovery was the origin of magnetism in allotropes of carbon. We will now move on to discuss the origin of magnetism in pure carbon!

Besides organic compounds, several allotropes of carbon like graphite, graphene nanoribbons, carbon nanotubes (CNTs), carbon nanoparticles, carbon nanofoam as well as carbon thin films [85, 86, 87, 88, 89, 90, 91, 92] have shown magnetic character which is quite surprising since carbon is diamagnetic in nature. After their discovery, room temperature magnetism for pyrolytic graphite and carbon thin films formed using high-power laser got much attention.

Defects induced in the structure of highly oriented pyrolytic graphite (HOPG) and proton irradiated carbon thin films are responsible for these systems' observed robust ferromagnetic phase. This was confirmed using magnetic force microscopy (MFM), x-ray magnetic circular dichroism (XMCD), as well as computational methods [93]. There are mainly two types of defects that can be held responsible for ferromagnetic ordering in these two systems: point defects and hydrogen atom's adsorption on their surface [94, 95]. Increasing the fluence of proton beams irradiating the graphite and carbon thin films would increase the number of defects induced in them and thus their magnetization, which has been confirmed experimentally. The vacancy defect in graphite causes a Jahn-Teller distortion bringing the nearest neighbors of the vacancy closer and forming a pentagon shape. However, in addition to this, one atom is raised normally to the surface of the graphite sheet by about 0.18 Å. The net magnetic moment due to vacancy is $1 \mu_B$. It was found that the adsorption of hydrogen atoms increases the magnetic moment significantly. H atom is adsorbed at the vacancy and gives rise to bulk ferromagnetism by enhancing the stability and magnitude of the magnetic moment of dangling carbon bonds and therefore has a crucial role in overall ferromagnetic ordering in graphite and carbon films. It was also observed that irradiation of

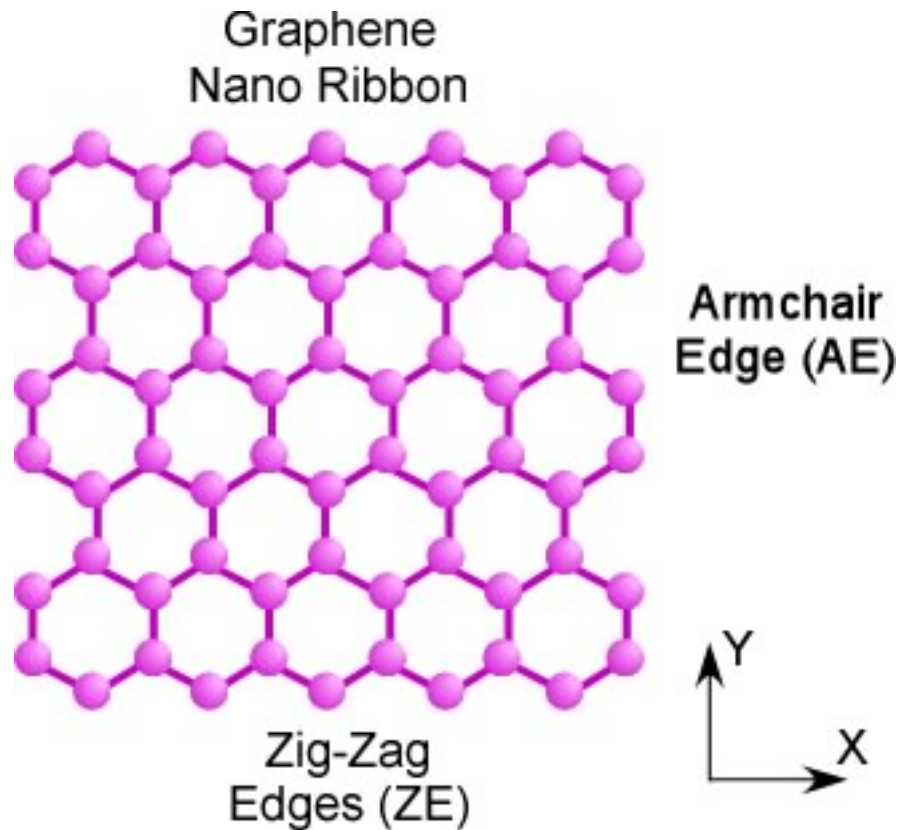


Figure 1.21: **Graphene Nanoribbons.** A carbon nanoribbon with six zigzag chains. The system is periodic along the x-direction. The edges along the y-direction have the armchair termination, while the edges along the x-direction have zigzag termination.

these materials with protons (H^+) gives higher magnetization than irradiation with Helium (He) ions. It is also suggested that the magnetism of HOPG is due to previously bound H atoms on the graphite layer before irradiation. The percolation limit of cavities required for bulk ferromagnetism in these systems is 4%. Additionally, N-doping in carbon-based systems has yielded better magnetizations than induced cavities [96, 97]. Planar defects at grain boundaries also support ferromagnetic ordering in HOPG, as has been confirmed using MFM [98]. In addition, line defects also confirmed the ferromagnetic phase at defect sites at room temperature.

Graphene is an extraordinary allotrope of carbon, just a single sheet of graphite. It has been an active hot topic for research worldwide since its discovery. Recently, functionalized graphene was created by doping with Fluorine (F) and a hydroxyl group (OH). The doping ratio (F/OH) helps tune the sp^2 - sp^3 hybridization ratio of C atoms. Hence, one can tune the ferromagnetic behavior of graphene [85]. Moreover, ferromagnetism is also observed in nanoribbons formed from infinitely extended 2D graphene layers. Just as in graphite, the boundaries of these ribbons have been found to have dangling carbon bonds, which provides a net magnetic moment of $0.2 \mu_B$ per edge atom. Two types of edges are formed in

a nanoribbon: armchair edge (AE) and zigzag edge (ZE), as described in fig.1.21. The topic of which type of edge is more stable is debatable. However, it is agreed that AE dangling bonds are non-magnetic, while ZEs contribute to the observed magnetism. Adding free charge carriers by p- or n-type doping can severely decrease or destroy the spin polarization in graphene nanoribbons [99].

C_{60} fullerenes on doping with nitrogen shows ferromagnetism but the T_C is very small (< 15 K)[100]. Carbon nanoparticles produced by pulsed arc in ethanol show ferromagnetism with T_C above 300 K [101]. CNTs are other complex systems where room temperature ferromagnetic ordering is found as soon as they come in contact with metallic ferromagnet [89]. New research has shown that stretching and cutting of Teflon and parafilm create dangling bonds in their structure that interact ferromagnetically. Hence, on stretching, they exhibit weak room temperature ferromagnetism [102]. However, it was observed that dangling bonds created by stretching and cutting other basic polymers like polythene, natural rubber, polyvinylidene fluoride (PVDF), and polypropylene (PP) do not interact, and only paramagnetism is exhibited in these systems [103].

1.7 Research Work

We have discussed a vast range of superb properties manifested by naturally occurring silkworm cocoon silks and spider dragline silks. Therefore, they appear as an interesting subject for research. Their biodegradable, organic, and non-toxic/ bio-compatible nature only amplifies the importance of research on these advanced functional materials, especially while looking forward to a sustainable future. Silks (and silk-based materials) are an excellent bridge between the natural and technological worlds. In the previous sections, we have encountered numerous properties of natural silks; however, one finds that the intrinsic magnetic properties of natural silks have remained undiscovered. The reason for that can be understood from the fact that proteins are usually diamagnetic in nature. In fact, as discussed in section 1.4, only one natural protein, MagR, has been discovered to show soft ferromagnetism at room temperature to date. Usually, proteins have a property called diamagnetic anisotropy, which leads them to align in the magnetic field of huge magnitudes (≥ 1 T), which can only be produced in laboratory conditions. Recent discoveries of the emergence of ferromagnetism in several carbon-based organic and inorganic compounds like graphite, graphene, carbon nanotubes, PTFE (Teflon), carbon thin films, and other organic molecules have revitalized the field of magnetism. The room temperature ferromagnetism in these materials is not due to the presence of d- or f- transition metals but free carbon radicals and dangling carbon bonds, which interact ferromagnetically with each other. A detailed mechanism of such ferromagnetism is presented in this chapter.

Previous studies have shown the presence of stable carbon radicals in silks at room temperature. Atomic and structural defects in naturally occurring spider and silkworm silks have also been confirmed by SEM, EPR and NMR experiments previously. This motivated us to inspect the magnetic character of natural silks. Hence, experimental exploration of the magnetic properties of natural silks and their magnetic characterization and potential applications have been the primary focus of my present research.

The main objectives of my research have been focused on the following topics:

- To study the magnetic properties of spider dragline silks and silkworm cocoon membrane silks and characterize them.
- To understand the origins of magnetism in silk materials.
- To develop potential applications of their magnetic properties.

The observations are pretty intriguing and can be very useful for developing new technologies and applications.

We discovered that both spider dragline silk and silkworm cocoon membrane silk demonstrate ferromagnetism in their pristine state and act as organic metal-free magnets at low, ambient, and high temperatures (up to 400 K). We also demonstrate simple mechanisms of enhancing silk's magnetism by stretching and cutting them, deforming their structure and possibly creating defects in them. A comparison of magnetism found in spider silks and silkworm silk has also been discussed. Furthermore, we successfully demonstrate potential biomedical applications of silks as a new type of magnetically driven advanced biological micro/nano-meter sized robots (termed as bio-magbotsTM). Silk-based bio-magbots perform various functions, such as remotely controlled and magnetically assisted trapping and transporting organic/inorganic materials (like cells, drugs, and tissues) in a liquid environment. In the technological sector, we show that silks can be used as bio-magnetosensors that can sense a change in the magnetic field of a few microteslas. Moreover, we also demonstrate how spiders can manifest the soft magnetism of their silk for magnetoreception simply by freely suspending themselves from dragline silk. This was demonstrated using a simple and efficient technique of torsion pendulum.

Chapter 2 will discuss the experimental techniques used for the research. The knowledge attained in the first three chapters will then be applied in chapter 3, which provides complete detail of experiments exploring the magnetic properties of spider silk and their potential applications. Chapter 4 discusses spider dragline silk's potential role in spiders' magnetoreception. We performed experiments using simple but very sensitive spider silk torsion pendulums mimicking a spider suspended from its dragline silk. This type of magnetoreception technique is unique from that usually found in nature. Chapter 5 discusses

the differences and similarities in magnetic properties of silkworm silks and spider silks. I summarize and conclude my research in chapter 6.

Chapter 2

Experimental Techniques

2.1 Introduction

Previous chapter dealt with the basics of proteins, the structure and properties of natural silks, and the fundamentals of magnetism in organic materials. This section will discuss the experimental techniques used to understand the magnetic properties of natural silks. The chapter is going to be divided into three sections. The first section will deal with the experimental techniques used to quantify the magnetic properties of the materials; the second part will deal with spectroscopic techniques used to understand the elemental compositions of the material; the third part will discuss electron spin resonance. Though several techniques are available for these purposes, we will only discuss the ones I have used for my research.

We will discuss the silk sample preparation techniques for different experiments in chapters 3 - 5. Here we only discuss the experimental techniques used to analyze the samples that were common in all experiments.

2.2 Magnetic Characterizations

Measurement of the magnetic moment of the sample under the influence of a uniformly changing magnetic field is known as magnetometry. Two ways one can accomplish magnetometry are (i) flux and (ii) force magnetometry. In the first method, the flux of the magnetic field generated by the sample is measured via a pickup coil (with the help of induced electromotive force). The second method measures the force exerted by or on the sample by applying an external magnetic field. There are several techniques utilizing each of the above methods.

- Flux Magnetometer

- Vibrating sample magnetometer (VSM)
- Superconducting Quantum Inference Device (SQUID) magnetometer
- Force magnetometer
 - Faraday magnetometer
 - Cantilever magnetometer
 - Piezoresistive magnetometer
 - Alternate gradient magnetometer
 - Torsion magnetometer

In my experiment, I used a SQUID magnetometer (MPMS 3, Quantum Design Inc.). In this section, we will learn the basics of a SQUID magnetometer and the proper procedure for carrying out magnetometry of a sample using this magnetometer.

2.2.1 SQUID Magnetometer

SQUID magnetometer is one of the most sensitive flux magnetometers. It is the best magnetometer for investigating the magnetic moments of biological samples. Unlike other flux magnetometers using simple pickup coils to measure induced emf and then compute the material's magnetization, these have a unique SQUID component. A basic schematic of the SQUID magnetometer is given in fig. 2.1. The brief description of the main components is given below:

- **Superconducting magnet:** This is the source of the applied magnetic field, (B_{ext} as shown in fig. 2.1) in the system. The magnet is constructed using a coil as an electromagnet made of superconducting material (Titanium-niobium alloy). The superconductivity of the coil is maintained with the help of liquid helium. Typically, such a magnet in commercial machines can produce a maximum field from 7 T to 9 T. The coil must produce a very uniform magnetic field.
- **Superconducting pick up coils:** The pickup coil in SQUID magnetometers is made of superconductors for obvious reasons. The coil is also kept at a low temperature with the help of liquid helium. These magnetometers usually have two pairs of pickup coils (2nd order gradiometer). The number of turns in pickup coils is much less than VSM to match the SQUID's low inductance. The sample is made to oscillate through these coils slower than the frequency of VSM. A peak-to-peak generation of the emf is necessary for the working of the magnetometer. The sample oscillates with an amplitude higher than the length of the coil for this purpose (figure 2.1).

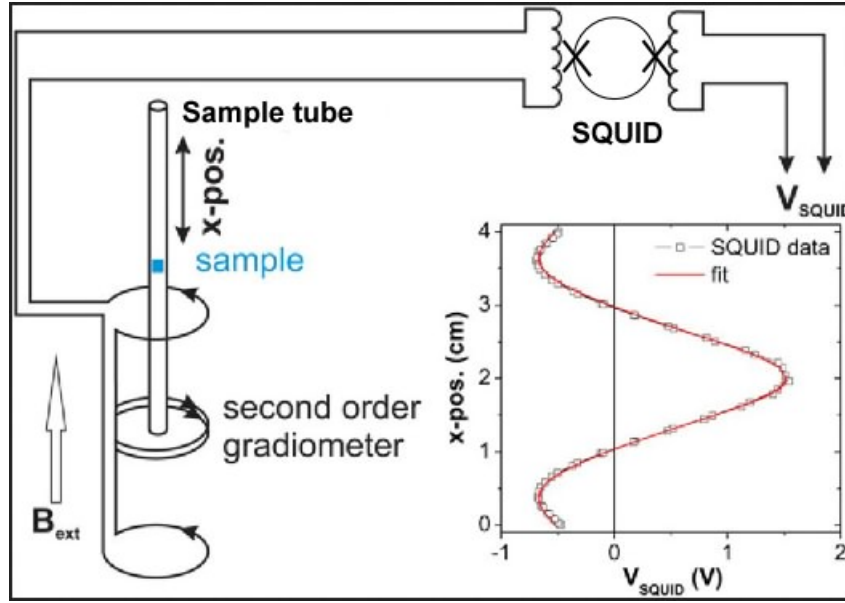


Figure 2.1: **SQUID magnetometer schematic.** Basic schematic of SQUID magnetometer with 2nd order gradiometer. The cross symbols on SQUID denote two Josephson junctions on a dc SQUID. The inset shows the SQUID response V_{SQUID} versus sample position (x-pos.). Electronic circuitry used to measure the V_{SQUID} has been omitted for simplicity. (Adapted from [14] for MPMS 3 Quantum Design.)

- **SQUID:** In addition, this magnetometer uses SQUID to measure the change in the magnetic flux of order of $0.001 \phi_0$. Here ϕ_0 is called the quantum of magnetic flux given by $\frac{h}{2e} = 2.067 \times 10^{(-15)} Tm^2$. Typical sensitivity of a SQUID magnetometer is of order $10^{(-14)} Am^2$. It is an extremely sensitive instrument that is made using superconducting loops and two Josephson junctions and has capabilities to detect extremely subtle magnetic fluxes with lower output noises than $\frac{3 fT}{\sqrt{Hz}}$ (see fig. 2.2). It is also operational over various frequencies, typically from dc to gigahertz. The instrument is directly connected to the pickup coils and must be kept in a low-field region with a superconducting shield. Superconductors being perfect diamagnets, shield SQUID from any residual or stray magnetic fields in the environment and the superconducting solenoid magnet within the machine.

The data collection process in SQUID magnetometers is relatively slow. In order to change the magnetic field produced by the electromagnet, we first make the pickup coil non-superconducting to reduce the current that will flow through it on changing the magnetic field. Then we ramp the magnetic field up or down from the present value to its new value. When the field is persistent and uniform, we make the pickup coils superconduct again and oscillate the sample to collect the new readings of the magnetic moment. This process is repeated for every data point. In commercial machines, this process is automated.

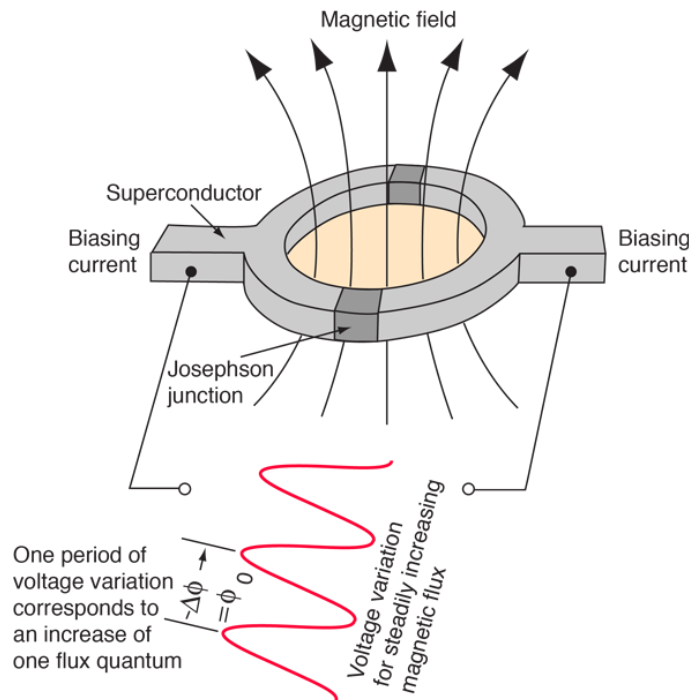


Figure 2.2: **DC SQUID device.** Two identical superconducting half rings are joined together with two insulating barriers. These superconductor-insulator-superconductor barriers are known as Josephson junctions. The current enters from the left side and is split into two branches with no magnetic flux passing through the ring. We observe an oscillating voltage as soon as a magnetic flux passes through the SQUID device. The oscillations are proportional to magnetic flux quanta passing through the device so one can calculate the magnetic moment. Quantum Design MPMS 3 uses such a SQUID device. However, other commercial SQUID magnetometers might use the rf-SQUID device. (Taken from [15])

Magnetometry

The following procedure must be followed for mounting the sample into the machine before starting the measurements.

- **Calibration:** Just as in any measurement, the first step is to calibrate your instrument. For this purpose, we must use a standard sample with a known magnetic moment at set temperatures. Usually, commercial machines come with a standard sample for system calibration. A spherical sample of pure Ni with a mass of 10 mg is a reliable source for calibration. Above 1 T magnetic field, the saturation magnetization of the sample is 55.1 emu/g at 300 K, and 58.6 emu/g at 4.2 K. Ni does not get oxidized and hence is suitable for such calibration purposes.
- **Sample size and mass:** SQUID magnetometer measures the magnetic moment of the sample under applied magnetic field at a fixed temperature. However, this data is

only helpful if we normalize the magnetic moment to magnetization. Mass is a much more stable quantity than volume; therefore, mass magnetization (emu/g or Am^2/kg . Check appendix A for unit conversion) is mainly used. Hence one must measure the mass of the sample accurately before mounting it on the magnetometer.

The sample size is also critical as, ideally, the sample must be point sized. A point-sized sample can be thought of as an ideal magnetic dipole. Larger sizes lead to more errors as the measured magnetic moment becomes dependent on the position of the sample. Errors for various sample sizes have been observed and reported in research papers [104]. Typically, the sample size must not exceed 3 mm for high accuracy of the measurement results. Biological samples usually have a very low density and tiny magnetic moments. Hence, to get an accurate measurement, we must compress the sample as much as possible so that a large sample can be used for measurements in a limited volume. This is done for tissues and related materials by dry freezing and compressing the sample.

- **Sample positioning:** Knowledge of the position of the sample inside the pickup coil is essential for the entire measurement duration. Before starting the main measurements on the material, we ensure that the sample is mounted at the center of the superconducting coil to ensure maximum accuracy of the measured moment. This process is known as the 'centering' of the sample inside the pickup coil. Radial displacement of the sample inside the coil can bring about an error of 30% in the magnetic moment measurement. While the sample oscillates, small displacements are possible; hence, knowing the sample's position becomes essential so that appropriate adjustments can be made and related errors are appropriately reported. In order to ensure the minimum displacement of the sample, one must mount it tightly on the sample tube.
- **Sample temperature:** As we have studied in the previous chapter, the magnetization of the material is very crucially dependent on the temperature of the material. Ideally, the sensitivity of the temperature sensor should be independent of the magnetic field. However, this is not true for real cases. Hence, the temperature sensor of the system must be calibrated properly, keeping in mind the effect of changing the magnetic field on the sensor's sensitivity. In addition, the sensor must be placed as close to the sample as possible to monitor its temperature accurately. At low temperatures, the sample and sensor's heat capacity, increases rapidly with a small temperature increase. Therefore, a quasi-static approach must be adopted to achieve a stable sample temperature. SQUID magnetometers can operate in a wide range of temperatures using appropriate setups. Helium gas cooling is required for the temperature range

of $5\text{ K} \leq T \leq 300\text{ K}$. While liquid He^4 is required to reach temperature ranges of $1.5\text{ K} \leq T \leq 5\text{ K}$. For temperature ranges of $0.3\text{ K} \leq T \leq 1.5\text{ K}$, liquid He^3 is required. Going beyond 0.3 K requires a dilution refrigerator. For temperatures higher than 300 K, an oven is integrated into the system that can take the temperatures up to 1000 K if needed. Therefore, we need different arrangements and appropriate sensors for different objectives to measure temperatures in different ranges accurately with the least possible error.

- **Magnetization measurement:** SQUID magnetometer MPMS 3 from Quantum Design Inc. is an entirely automated system. After calibration and providing a basic set of commands required for the M-H, such as range of field, fixed temperature, sample position, step size, etc. measurement, the rest of the data is collected by the system, and the observed data is displayed on the computer screen in real-time. One can monitor all parameters from the computer, and the system keeps running unless the given task is completed. As mentioned above, SQUID magnetometry is a slow process, and the system might take a day to complete measurements on one sample.

Besides the points listed above, usually, there are several other considerations, like correcting for the demagnetization field, which depends on the sample shape. Another correction factor is the crystallographic orientation of the sample with respect to the direction of the magnetic field in the case of anisotropic materials. Thus, knowledge about the sample can help reduce errors and measurement time. SQUID magnetometers and VSMs have coils to produce magnetic fields in all three directions to find magnetic anisotropy in such samples. In strongly ferromagnetic powder and thin film samples, a magnetic field might produce torque and rotate the samples, thus altering their orientation and giving faulty readings. Hence samples with these morphologies must be mounted to immobilize them. However, these corrections have never been reported in biological samples and are not of concern in our case.

- **Data analysis:** After the completion of the measurement of M-H characteristics of the sample, data is ready to be analyzed. Biological samples are usually diamagnetic, and it is common to observe a diamagnetic signal at a large magnetic field value. Suppose the system has a ferromagnetic or paramagnetic source embedded in them. In that case, they will show their characteristic behavior near the origin (low magnetic fields), where the diamagnetic component will be weaker ($M \propto H$). The diamagnetic behavior is insignificant and must be subtracted from the raw data. For this purpose, we measure the diamagnetic susceptibility of the material from part of the data collected at high magnetic fields. Using this value, we subtract the diamagnetic component of magnetization from the rest of the data. We are now left with valuable

data that needs to be analyzed.

Sometimes, when the magnetic moment of the sample is sufficiently small, one can take the magnetization measurement of the empty sample holder to ensure that the diamagnetic signal is from the sample itself.

The data is analyzed by applying our knowledge gained from the previous chapter, and appropriate conclusions can be reached after a detailed analysis.

This section describes the experimental method of magnetometry using a SQUID magnetometer. We used the above procedure to understand the magnetic behavior of natural silks in the experiments explained in the next chapter. Now we'll discuss how to do a thermomagnetic analysis of a sample.

Thermomagnetic Analysis

While magnetometry helps us understand the magnetic behavior of a sample at a given temperature, we need to do a thermomagnetic analysis of the material to understand the material's magnetic ordering deeply. The word '*thermo*' means related to heat ('*therm*' means heat in Greek), and thermomagnetic means temperature-related magnetic characteristic or M-T characteristics. For this purpose, we maintain the sample under the influence of a fixed magnetic field and measure the magnetic moment of the sample by varying the temperature. Unlike magnetometry, thermomagnetic analysis can only be done using flux magnetometers. For measuring the magnetic moment of the sample, one can use SQUID or VSM magnetometer. The same MPMS 3 SQUID machine was used in our experiments for both magnetometric and thermomagnetic analysis. Therefore, the system's mounting and calibration procedure are the same as that above.

Commercially available SQUID magnetometers can sweep temperatures from 1.7 K to 400 K in standard mode. The highest reachable temperature with appropriate system arrangements is 1000 K – 1100 K. As mentioned before, most SQUID systems are entirely automated, and the data collection can take much time, sometimes days, depending on your chosen procedure. For amorphous magnetic materials (like ours), both zero field cooled (ZFC) and field cooled (FC) thermomagnetic characteristics must be obtained. For MT data collection, we first enter the temperature range for which the experiment needs to be done, along with the constant magnetic field required to experiment. After providing the required inputs, the sample is made to cool down stepwise to the minimum set temperature under zero applied magnetic field (ZFC). Once the minimum is reached, we apply the fixed magnetic field and start heating the sample at a fixed rate while measuring its magnetic moment at every step. The sample is heated up to its maximum set value in this manner. After the ZFC M-T data is collected, we cool the sample back to the minimum set temperature

value, but this time, under the influence of a set magnetic field (FC). Once the minimum temperature is reached, we measure the magnetic moment while simultaneously heating the sample with a set temperature increase rate. After collecting FC and ZFC data, the actual analysis is commenced.

Many samples undergo structural phase transitions under changes in temperature, and these structural phases significantly impact the material's magnetic phases. These thermomagnetic behaviors can be analyzed using SQUID magnetometers. Crystalline material might go from a lattice structure that supports a magnetic character to another lattice structure that might be non-magnetic upon changing temperature. In the case of amorphous magnetic materials or materials with no long-range ordering, structural phase transitions become pretty interesting, with multiple structural reorderings leading to multiple magnetic phase transitions. Thus, thermomagnetic analysis can also act as a probe for structural phase transitions of the sample under varying temperatures.

In the previous chapter, we have discussed χ^{-1} vs. T graphs of multiple magnetic orderings (fig. 1.5). Knowledge of these M-T characteristics is beneficial in analyzing the thermomagnetic behavior of our sample. In addition, this knowledge also helps us understand the magnetic phase transitions occurring in the sample as we vary the temperature. Furthermore, it provides insight into the sample material's structural phase transformations.

The combined MH and MT data of the sample provide us with its entire magnetic picture. There are further experiments that can be done for objectives like understanding the structure of magnetic domains of a sample or understanding magnetotransport properties of the sample etc., to get even more information about the sample. However, these experiments are irrelevant to our research. With this, we conclude this section. In the next section, we'll discuss several elemental analysis methods used by us in order to investigate the source of magnetism in our silk samples.

2.3 Elemental analysis techniques

After observing the magnetic behavior of silks, the curiosity about the source of this magnetism lead us to a thorough investigation of elemental analysis of spider draglines and silkworm silks. This section will discuss the various techniques used for this purpose. We'll start with electron energy dissipative spectrum (EDXRF) and move towards x-ray photoelectron spectroscopy (XPS), x-ray absorption spectroscopy (XAS) and inductively coupled plasma mass spectroscopy (ICPMS). Generally, room temperature magnetism is only exhibited by four elements: iron (Fe), nickel (Ni), cobalt (Co), and gadolinium (Gd). Therefore, observation of room temperature magnetism in silks naturally leads to an investigation of the presence of these elements in the silk samples. Their presence has never been

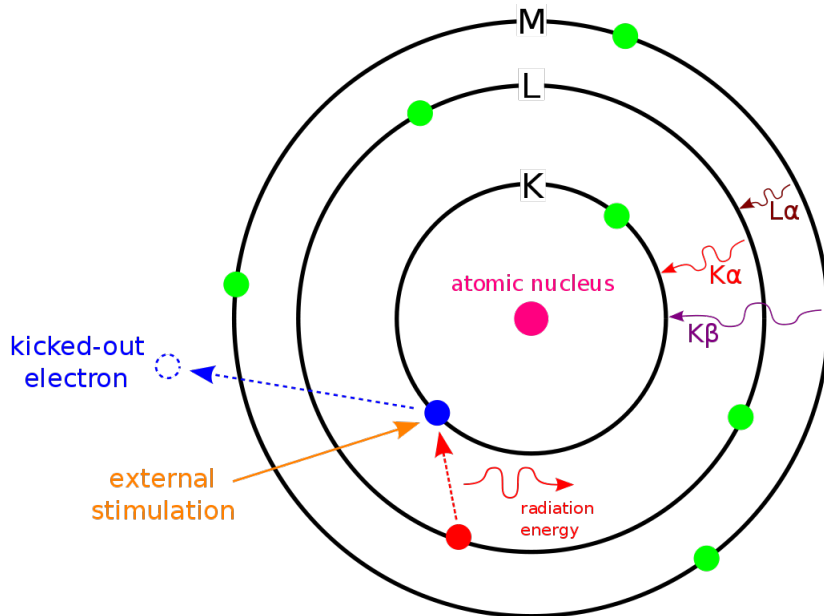


Figure 2.3: **Principle of EDXRF.** The inner K shell electron is ionized, causing electrons from the upper shell (with higher energy) to occupy its place. These electrons release their excess energy by releasing a photon in X-ray frequency shown here as K_{α} , K_{β} , and L_{α} . K lines are the primary signature of the element, and subsequent x-rays can be used to verify the presence of the element.

reported before; therefore, a thorough investigation was required to compare the results using different techniques with varying sensitivities. The results of the following experiments will be discussed in the following chapters. This chapter aims to introduce these techniques, their working principles, procedure of experimentation, and precautions to be taken during the analysis of the results.

2.3.1 Energy Dispersive X-Ray Florescence (EDXRF)

Each atom has electrons filled in discrete energy levels. We can excite these atoms by providing energy using photons, electrons, or ions. If the excitation energy is significant, it might cause ionization of the material. The basic principle for this technique is to excite the inner shell electrons of atoms of the samples. When the inner shell electrons get excited, the electrons from higher energy levels decay to acquire their place and, in doing so, lose their energy (fig. 2.3). This energy is emitted by the atom in the form of x-ray emissions. Since each atom has a unique atomic structure (due to the uniqueness of its nucleus), x-rays emitted by each atom are unique (known as K_{α} , K_{β} , and L_{α} , etc.). Thus, accurately detecting these emitted x-rays from excited atoms can yield information about the atoms. This technique determines the unknown elements present in a given sample.

When it comes to the detection of x-rays, there are three main challenges that an ideal

EDS (Energy Dispersive Spectrometer) must overcome to be a suitable elemental detector.

- The detector must be able to detect the energy radiations in the range of 100 eV to 100 KeV with high resolution (Typically 0.1 eV or better).
- Ability to detect multiple radiation signals parallelly for efficient measurement.
- If only sequential detections can be made, each detection must have a short duration.
- The detector must not add any noise to the original radiation energy signal.

Commercial EDS machines usually use silicon or germanium detectors cooled to liquid nitrogen temperatures to reduce thermal noise. Si can provide a high-efficiency detection range of 100 eV to 20 KeV, while 20-30 KeV radiations can be detected with slightly reduced efficiency. Ge detectors can, however, detect from 100 eV to 100 KeV. Most of the commercial instruments used for EDS use an automated computerized system to detect and interpret the signal from Si/Ge detectors and provide outputs.

The ideal sample for best analysis using electron beam EDXRF spectroscopy should have a well-polished and flat surface with a thickness of about 50 nm. EDXRF spectroscopy is a very surface-sensitive technique and can obtain only information about elemental composition within 2-3 nm from the surface. Hence the thin samples are ideal. To reduce the x-ray self-absorption, one needs a flat and polished surface. The problem of self-absorption is of great concern for lighter elements ($Z \leq 15$).

In the case of an insulating sample, one must first coat a conductive layer onto the sample. This layer can be either carbon or gold. Our experiment used a gold coating on natural silk samples. The coating is connected to the electrical ground. This is done to alleviate the chances of charge accumulation on the insulating surface of the sample by the direct electron beam. In the case of biological samples, volatile components and water might get lost under the radiation of the electron beam. Sometimes these energies are high enough to break weak organic bonds, hence the removal of volatile components of the sample. To compensate for such results, a method was developed by Hall (1968) to replace the peaks with bands of high energy bremsstrahlung radiation scaled with the mass of electron-excited volume [105]. More details about this technique can be found. Lower beam energies are generally used for EDS of biological or organic samples.

Nowadays, EDS spectrometers are integrated with SEM systems. The high-energy electron beams can be controlled to hit the target sample precisely with the known energy of the electron beam. In our experiment, we used an EDS system from Bruker corporation. Another challenge is analyzing the data once the experiment is commenced with proper care. Since each element has a set of K, L, and M peak families, these families can interfere among themselves, making the analysis a tough challenge. Usually, it is found that

detection of lighter elements like C, O, K, etc. with x-ray signature energy < 1 keV is more challenging than that of heavy elements like Fe, Pb, Ti, Au, etc. It is standard practice to compare your observed results with the expected values given in the literature to confirm the presence of an element in the sample. In order to analyze the data effectively, one must follow the following set of rules:

- First of all, one must analyze the x-ray peaks above 5 keV, as the detector works best in this region and the resolution is high. Thus, one can easily search and distinguish elements in this range. Start from the peaks with the highest energy and then come down to the lower ones.
- After one has identified a peak and assigned it to an element (after matching with literature), search for all the K, L, and M families of this element. The energy position and intensity ratio must match the element's standard values to confirm the element.
- Always remember, energetically, $K > L > M$ lines. If above 5 keV, K lines of an element have been found, it means L and M lines of these elements will also be present at lower energy values.
- Elements with $Z \leq 9$ (F) and below only have a single line. The K lines for lighter atoms ($Z < 15$) are < 1 keV, and their intensities are reduced due to x-ray absorption by the semiconductor detector.
- After confirming the heavy elements and identifying their lower energy L and M lines, the detection of lighter elements must proceed with the classification of lines with maximum energy first and descending to lower energy lines.
- One must always investigate what other trace elements might be present in the sample whose signals got hidden due high intensity of other heavy element signals.

This sums up how to qualitatively analyze the obtained data from EDS. Quantitative analysis is, however, much more complex. A good quality quantitative analysis requires high-resolution data of EDS. This can be done by increasing the integration time of the detector to get a proper shape of the peak. Once we have obtained sufficiently good spectra, it undergoes various processes to be fit for final analysis. These processes include background correction, deconvolution of overlapping peaks, and matrix correction. Each of these processes is based on complicated statistical and computational algorithms. More about these can be read in detailed literature. Modern EDS systems use a standardless analysis technique for which one does not need to repeatedly check the system's accuracy by measuring the spectra of standard elements. The standardless analysis technique makes the analysis of

spectra very simple. The software adjusts for all aspects of x-ray generations, propagation of x-ray through solid target and background, etc. The user only needs to put the excitation beam energy and x-ray take-off angle. One can also add the elements that need to be quantified manually, or the software automatically provides the list of detected elements. However, such an analysis can have significant errors. One must never take the obtained concentration output at its face value. In order to state the presence of an element in the sample, one must use the following rule:

- If the concentration of elements is > 10 wt.%, it is a major component of the sample.
- If the concentration of elements is $1 \text{ wt.}\% < C < 10 \text{ wt.}\%$, it is a minor component of the sample.
- If the concentration of elements is $< 1 \text{ wt.}\%$, it might be present in a trace amount in the sample or utterly absent in the sample.

One must also provide the error report while providing the concentration of elements determined by standardless analysis.

2.3.2 X-ray photoelectron spectroscopy (XPS)

XPS uses an approach of bombarding the sample material with high-energy x-rays to ionize its atoms by knocking out its core electrons. In XPS, we measure the kinetic energy of the outgoing inner-shell electron and determine the atom's binding energy (B.E.). The electronic structure of each element's atom is unique, and hence the B.E. of electrons reveal their information. The technique can be used for all solids in various forms, like polymers, powders, fibers, foils, and thin films. This is a non-destructive analysis technique, but the results are surface sensitive. We can only extract information about a few nanometers beyond the surface exposed to the x-rays. Compared to a similar technique called Auger Electron Spectroscopy (AES), XPS is less surface sensitive. AES uses electron beams instead of x-rays to ionize the core electrons. X-rays have more penetration depth (up to 3 – 5 nm beyond the surface) than electron beams (< 1 nm), making XPS much more efficient than EDXRF and AES. The sensitivity of this technique ranges from 1000 ppm to as low as 50 ppm for heavy elements in a matrix of light elements [106]. However, it varies from element to element, and thus, the machine must be calibrated for all elements.

Besides giving us information about elemental composition, the data can be used to find the charge state of that element and understand the chemical nature of the compounds, like their oxidation states and hybridization. The obtained spectrum is so sensitive that samples exposed to the air show a large concentration of oxygen (due to oxidation of the sample)

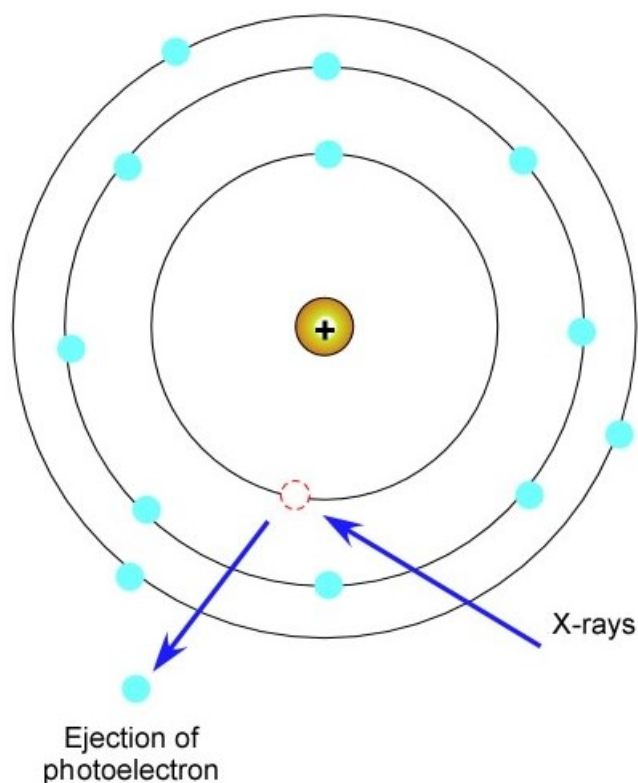


Figure 2.4: **Principle of XPS.** High energy beam of x-ray photons leads to the ejection of photoelectrons from the inner shells of the atom. Since the electronic energy structure of each atom is unique, so is its binding energy. Hence detection of electrons at specific binding energies provides information about the element to which they belong.

and carbon. However, XPS requires a very high vacuum of the order of 10^{-9} mbar to prevent high-energy electrons from ionizing the air molecules. Ionization of air molecules can cause a large, noisy interference and loss of electrons from reaching the detector. The requirement of ultrahigh vacuum is one of the significant disadvantages of this technique as all samples cannot be maintained in such a high vacuum and start outgassing.

Instrumentation

The XPS setup consists of three main parts (i) source of x-ray beam, (ii) analyzer, and (iii) electron detector (fig. 2.5). The entire setup has to be housed in an ultrahigh vacuum chamber ($10^{-8} - 10^{-9}$ mbar). The instrument is shielded with μ -metal to prevent the earth's magnetic field from modifying the electron path. Now we will discuss each of these parts in detail.

1. **Source:** There are two methods of producing x-rays (i) standard laboratory source and (ii) synchrotron x-ray source. The standard laboratory source is used in commercial machines. In commercial systems, a tungsten wire is heated by passing a current

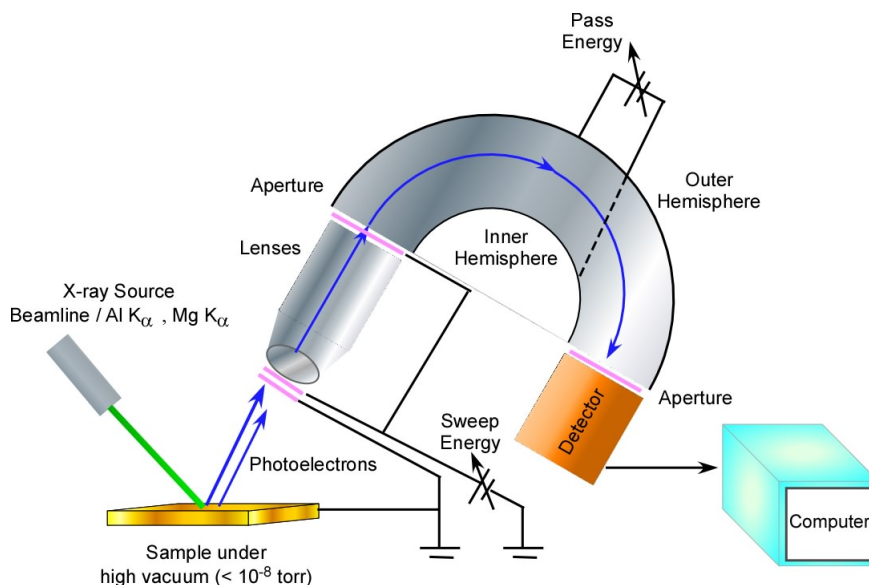


Figure 2.5: **Basic XPS setup.** The x-ray obtained from beamline or laboratory sources with energies of about 1.5 keV are bombarded on samples kept under a high vacuum. The photoelectrons generated are accelerated to the hemispherical sector analyzer (HSA), where only electrons with a selected energy band (pass energy, E_p) can pass to reach the electron detector. The data is recorded and stored on the computer.

through it, emitting electrons. These electrons are accelerated towards a metal surface using a high voltage of about 10-20 kV. The collision between an electron beam and a metal surface produces two types of x-rays – Bremsstrahlung (deacceleration of electrons) and emission lines (x-rays from metal excitation). The former has a very low intensity and broad energy spectrum and therefore is irrelevant. The most used x-ray source metals are Aluminum (K_α ; 1486.6 eV) and Magnesium (K_α ; 1253.6 eV). However, other metals can be used for the production of lower energy rays. Many commercial XPS systems come with both sources. The source x-rays themselves have line broadening of 0.85 eV for Al K_α and 0.7 eV for Mg K_α , which also influences the line broadening of the XPS spectrum. Moreover, the emission spectrum of both x-ray sources has satellite x-rays (secondary emission lines). These lead to additional satellite peaks in the spectrum of the sample, however, these peaks are at 7 eV lower B.E. than the main peak. To overcome these shortcomings, many commercial systems are equipped with x-ray monochromators made of crystal to diffract the x-ray beam onto the sample. The use of monochromators reduces the line width of the x-ray source, lowers the intensity of bremsstrahlung radiation background, and reduces the chance of sample damage due to lower x-ray flux and prevention from electron bombardment because of damaged x-ray windows.

The synchrotron x-ray source has many advantages over laboratory sources like tun-

ability of x-ray energies, production of high flux, no satellite x-rays, narrow line widths, and lower background intensities. However, synchrotron beam sources can only be present at a few places and have to be scheduled beforehand, and beam times are available only for a fixed time interval.

2. **Analyzer:** XPS systems have a hemispherical sector analyzer (HSA) that acts as an electron energy selector unit. The detailed schematic of the HAS system can be seen in figure 2.5. The electrons emitted from the sample travel in a field-free zone until they reach the lens's entrance. The entering point of this lens is at the same potential as that of the sample, but the two terminals of the lens have a potential gradient providing a retarding potential. This retarding potential allows only electrons with specific threshold energies to pass through the lens and enter the HSA. The analyzer has two hemispherical sectors, which are kept at different potentials. This HSA acts as an energy selector; the potential difference between the two hemispheres only allows electrons with specific energy known as pass energy E_p to reach the detector. Electrons with K.E. $> E_p$ are lost to the outer hemisphere, while electrons with K.E. $< E_p$ are lost to the inner hemisphere. The pass energy is given by:

$$E_p = K_s \Delta V \quad (2.1)$$

$$K_s = \left(\frac{R_o}{R_i} - \frac{R_i}{R_o} \right)^{-1} \quad (2.2)$$

Here, ΔV is the potential gradient between the two hemispheres, K_s is the spectrometer constant, R_o is the outer hemisphere's radius, and R_i is the inner hemisphere's radius.

It has been observed that only electrons with K.E. $= E_p \pm \Delta E_a$ can pass through the analyzer and reach the detector. ΔE_a is known as the resolution of the spectrometer. This also adds to a line broadening of the spectrum. The resolution depends on the angle α , at which the electrons enter the HSA with respect to the normal. If the slit width is W and the optimal path across the HSA to the detector has radius R_p , then the resolution energy of XPS is given by:

$$\frac{\Delta E_a}{E_p} = \sqrt{\frac{W}{R_p}} \quad (2.3)$$

For commercial systems $\frac{\Delta E_a}{E_p} \cong 0.1$ is the standard. The larger the radius of the analyzer hemispheres, the better the resolution. For high-resolution spectra, one must

keep the E_p constant and only vary the retarding potential of the lens. Thus, only electrons with $\text{K.E.} = E_p$ will be allowed to pass. It also helps keep the spectrum's resolution constant across the K.E.s. The survey scans are taken at high E_p to get a high signal-to-noise ratio in a small time interval, while the high-resolution core scans are done at lower E_p and thus require multiple scans to produce a high-quality spectrum.

3. **Detector:** There are three types of electron detectors, one of which can be found in an XPS system. These are electron multipliers, channeltrons, and channel plate arrays. These are standard electron detectors used in many different systems. All of these run at very high voltages of at least 5 kV and have gain factors of 103 to 106, i.e., one detected electron produces a signal generated by 103 to 106 electrons inside the detectors. The second stage again amplifies the signals produced by these detectors to boost the signal. Commercial machines might have multiple detectors to detect the maximum number of electrons reaching the detectors, thereby increasing the signal-to-noise ratio.

Procedure

For XPS, the sample needs to be clean. The oxidation and other contaminants on the surface must be removed thoroughly. Ideally, the sample must be prepared in a vacuum. The sample must be a few mm thick (1-5 mm) and has a size of 1-3 cm. It is preferred to have a homogenous composition. Most importantly, the sample must have very low outgassing. Typically, thin films, powders, polymers, fibers, pellets, and foils can be detected. A high flux of x-ray can damage or degrade the sample.

The XPS spectroscopy for a sample with unknown elemental composition is done in two steps:

1. **Survey Scan Spectrum:** This is an exhaustive full range energy scan, i.e., this scan covers the entire energy spectrum and searches for all the possible elements in a sample. The instrument scans the number of electrons emitted by the sample with different K.E.s for the scan duration. This is done in a sequential method, i.e., detecting each K.E. slowly across the entire energy spectrum. The survey scans generally take about 5 to 10 mins. Each atom and its orbitals have a unique B.E. value. Thus, by comparing the data obtained from an unknown sample with the standard spectra of different elements, one can figure out the sample's elemental composition. As we know, binding energies of electrons residing in p, d, and f orbital of n^{th} shell are different depending on the J quantum number determined by L-S coupling, and one can observe that electron with $J = L + S$ coupling has a different energy from electrons

with $J = L - S$ coupling in XPS spectra. The peaks of electrons emitted from p, d, and f orbitals of an atom show a split because of the difference in their binding energies based on their L-S coupling. The width of the split depends upon the strength of L-S coupling, which depends upon $\langle \frac{1}{r^3} \rangle$, where r is the radius of the orbital—the larger the principal quantum number 'n,' the narrower the split width. The strength of the split increases with an increase in atomic number. The peak width is attributed to natural broadening (Heisenberg's uncertainty principle) and inelastic scattering. The inelastic interaction of an escaped electron can be with other electrons or phonons. These inelastic scatterings can reduce the K.E of the electrons. Sometimes the loss of energy can prevent the electron from escaping. However, those who manage to escape have lower energy than expected. This happens quite often in the actual XPS experiment; therefore, we observe that the intensity of electrons with low K.E. (high B.E.) is exceptionally high. Consequently, determining the XPS peak of an element with B.E. within ≈ 100 eV of the x-ray energy ($h\nu$) is complicated due to enhanced background noise.

- 2. High-Resolution Core Spectrum:** After getting the elemental composition results of an unknown sample from the survey spectrum, we take a high-resolution XPS spectrum of each element by repeating the experiment for only their particular defined energy range. This spectrum is for a short range of energy and can be taken multiple times (called sweeps). This accumulates and integrates the data collected over a long duration of time. The typical time for one sweep can be about 3- 5 mins. The longer the integration time, the better the results; however, sometimes, certain materials might degrade under long-time exposure to high-energy x-ray flux. Core spectra help us get good quality information about the chemical state and nature of the element of interest in our sample. One can observe that the spectrum might have shifted from the theoretical position of binding energy or the presence of satellites on both sides of the prominent peaks. This is attributed to multiple reasons like phonon scattering, auger electron emission, relaxation process due to rehybridization, shake-up and shake-off processes, and multiplet splitting. A detailed study on the reason for the occurrence of these processes and their effect on the spectrum's shape can be found in specialized literature [105, 106]. The shape and breadth of the peak are also affected by the chemical state shifts, inhomogeneous matrix, and charging shifts. These shape changes reveal details about the chemical state of the element and the charge state, as well as the elements or functional group the element is bound. Chemical shift changes are more prominently observed in lighter than heavier atoms.

For our experiment, we used an XPS system from Scienta Omicron GmbH and an Al

K_{α} x-ray source with a typical resolution of 0.47 eV and probing depth of 2-10 nm beyond the surface. After the data acquisition is made, one can proceed with the analysis. The three basic parameters essential for analysis are area under the curve, peak width (full width at half maxima (FWHM)), and peak position. The best way to know the sample's composition is to match the peaks with traditional values. However, to confirm the presence of an element, one must also find other peaks that might appear from the same element and its AES peaks if the selected energy range covers them. One can fit high-resolution peaks using open source software like XPS peak, CASA XPS, etc., and then match their results with the NIST database to get the conclusion of those peaks. A detailed XPS analysis can be found in dedicated literature.

The most prominent problem in the XPS spectrum can be the charging shifts, as was stated while explaining the high-resolution core scan spectrum. Insulating, polymeric, and ceramic materials suffer this type of problem. The surface of the sample gets positively charged, and hence the K.E. of the electron is reduced. This effect is uniform for all electrons from the same and different atoms (of elements). There are three methods to deal with this, (i) coating the sample with conducting materials, (ii) addition of electrons to the sample using a separate filament to maintain the balance of charges, or making contact with conducting material like carbon tape, and (iii) post spectra data resetting. The first method will add additional signals to the spectra. In the second method, the bombardment of electrons can damage the sample, and also it is not easy to get the dose of electrons right to balance the charge. For the third method, we need a standard signal with whom we can compare and reset the spectra. This standard is C 1s peak at 284.6 eV. A better practice to report XPS data is to have one standard peak and compare the distance of others with respect to them to normalize the charging effect. More information of XPS can be find in [105].

2.3.3 X-Ray Absorption Spectroscopy (XAS)

Each element has unique x-ray absorption energy owed to its unique atomic structure. This property of an element can be exploited to identify the elements present in an unknown material. Besides elemental detection, XAS can reveal necessary information about the structure and state of a given element in the sample; thus, it is also referred to as the x-ray absorption fine structure (XAFS) technique. The absorption peak is called the absorption edge of the element, and the region within 20-50 eV of the absorption edge, reveals the information on the type of neighboring atoms, type of bonding with them, the interatomic distances and coordination number of the absorbing atoms. The analysis of this region is called x-ray absorption near edge structure (XANES). It is susceptible to the element atom's chemical nature and site symmetry. The oscillating spectrum beyond 50 eV from

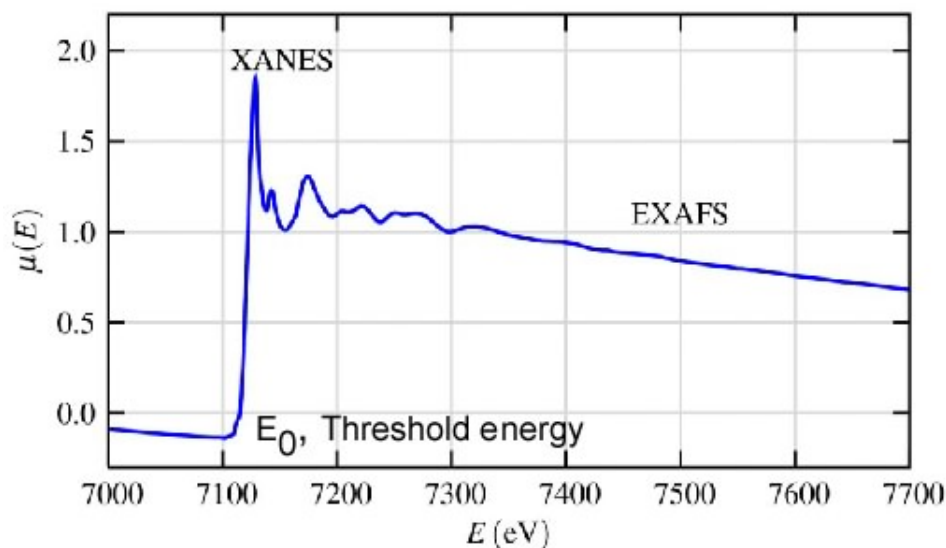


Figure 2.6: **Typical XAS spectrum.** The figure shows the XAS spectrum of FeO powder at the absorption edge of Fe. We can distinguish the XANES and EXAFS regimes from the spectrum. The x-axis is the energy of the x-ray absorbed, while the y-axis denotes the coefficient of absorption of the material. (Taken from [16].)

the absorption edge is called the extended x-ray absorption fine structure (EXAFS) and helps understand the atoms' interatomic distances and coordination numbers. EXAFS can extend up to 1000 eV from the absorption edge. XAS requires no constraints on sample preparation and can be performed on any solid (crystalline or amorphous), liquid, or even gas. This is one of the significant strengths of XAS. Commonly analyzed absorption edges of an element are K edge ($1s$ initial state) and L_3 edge ($2p_{3/2}$ initial state). However, unlike XPS, which can be done with either laboratory x-ray or synchrotron x-ray sources, XAS can only be done at synchrotron sources as it requires variable x-ray energies and more excellent tunability. We used the XAS facility available at synchrotron Indus 2, RRCAT, Indore, Madhya Pradesh.

An example of a typical XAS spectrum can be seen in fig. 2.6. As shown in the fig, in XAS, we are interested in knowing the relation of absorption coefficient, μ , as a function of the energy of x-ray. The oscillations represent a quantum interference pattern of an electron wave as it is emitted by an atom and is scattered by its neighboring atoms. The repeated scattering produces an interference pattern. It was observed that atoms have a unique and characteristic backscattering amplitude and phase shift variation. This helps researchers reveal information about neighboring atoms of an element. Nevertheless, in our experiment, we only used this technique for the qualitative detection of elements present in the silk samples. More specifically, we used this technique to check the presence of d-transition metals.

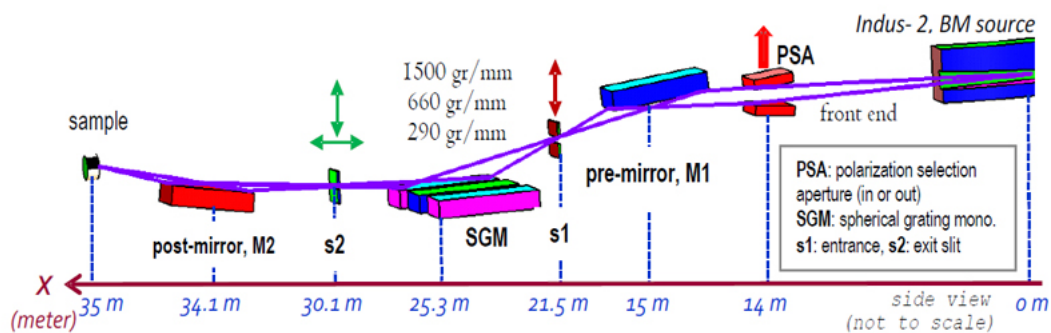


Figure 2.7: **XAS beamline set up.** Setup of Indus 2 synchrotron, RRCAT, Indore, Madhya Pradesh. (Taken from RRCAT Indore website.)

Conventional XAS is done in either transmission or fluorescence mode. In our experiment, we used the total electron yield (TEY) mode of XAS. This mode is surface sensitive and detects the emitted photoelectrons upon exposure of the sample to x-rays of increasing energy. This electron detection is done by conducting contact with the sample. As the photoelectrons are generated from the sample, they travel through the conducting contact wire, and the current thus generated is detected. The current is of order of pico-ampere ($1\text{pA} = 10^{-12}\text{ A}$). The dominant contributor to the current thus generated are Auger electrons. The Auger electrons go through many scattering events before reaching the surface where the conducting contact is. Therefore, the photocurrent generated in TEY mode is similar to that observed in transmission or fluorescence mode.

Generally, for transmission mode, the sample is preferred to be thin as a foil as it reduces the chances of self-absorption and the attenuation of x-ray intensity. Low intensities are challenging to detect. Self-absorption is also a pitfall of the fluorescence mode. TEY mode does not have any issue with self-absorption and can be done for thick samples. The probing depth of the x-rays in XAS in TEY mode is greater than the probing depth of XPS but in the nanometer range and is dependent on the energy E (keV) of the beam as well as density $\rho = (g/cm^3)$ of the sample.

Instrumentation

The critical components of the experimental setup are a source of x-ray, a monochromator, and the current detector. The beamline setup is shown in figure 2.7

1. **X-Ray source:** The source of the x-ray is a synchrotron. A beamline is used to extract x-rays of energy 0.1-10 keV from a synchrotron emitting radiations of several frequencies. A monochromator is used to direct the radiations of specific energy towards the sample. Energy calibration is essential and must be checked before commencing the experiment.

2. **Monochromator:** The monochromator uses Bragg's law to diffract x-rays of selected energy. The crystals used for this purpose are chosen based on their energy resolution. All beams have divergence, and so do the diffracted beams. Crystals that produce high resolution (low divergence) are needed. Silicon crystal is the most commonly used monochromator for x-ray energies > 2 keV. The crystals used for this purpose are almost perfect crystals and the resolution of Si is $\frac{\Delta E}{E} = 1.3 \times 10^{-4}$. Even higher resolution can be obtained using Si crystal by fabricating the crystals with different lattice planes. A set of gratings is also used to increase the resolution of x-ray beams.

Detector: The detector for XAS in TEY mode has a Copper mesh-like structure that is kept in close contact with the sample. The mesh is connected to the high voltage power supply, an amplifier, and an ammeter to detect the current value as photoelectrons from the sample pass through the circuit.

In TEY mode,

$$\mu(E) \propto \frac{I_d}{I_b} \quad (2.4)$$

Here I_d is the detector current, and I_b is the x-ray beam current.

Maintaining an ultrahigh vacuum is essential to prevent air molecules from absorbing the x-rays and reducing their intensity severely before reaching the sample.

Like other instruments, XAS is also an automated facility. This is essential as XAS beamlines are inside the synchrotron facilities, and it is not advisable to stay near the setup once the experiment has started because the radiation levels inside the chamber designated for the beamline increase significantly.

Data analysis is done by matching the observed data with the XAS database. Softwares like Athena are used to normalize the absorption coefficient and further processing of signal in terms of wave vector $\vec{k} = \sqrt{\frac{2m(E - E_0)}{\hbar^2}}$. Here m is the mass of the electron.

2.3.4 Inductively Coupled Plasma Mass Spectroscopy (ICPMS)

ICPMS, as the name suggests, is a technique of mass spectroscopy. The key concept is to break down the sample to its atoms (called atomizing) and later check the atoms for their mass-to-charge (m/Z) ratio to recognize them. Each element has a unique mass-to-charge ratio. Hence, unlike the other techniques used previously, this elemental analysis method is destructive to the sample. ICPMS can detect both metallic and non-metallic components of a sample with an accuracy of parts per billion (ppb). One can also distinguish the isotopes and isobars of an element using ICPMS. The technique uses plasma to atomize the samples and hence its name.

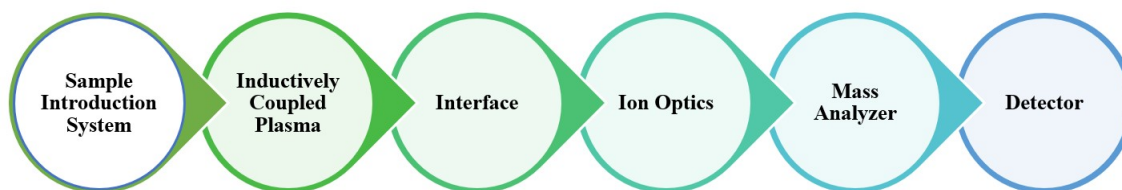


Figure 2.8: **ICPMS stepwise procedure.** Once the sample is prepared, we go through the above procedure to reach the final results.

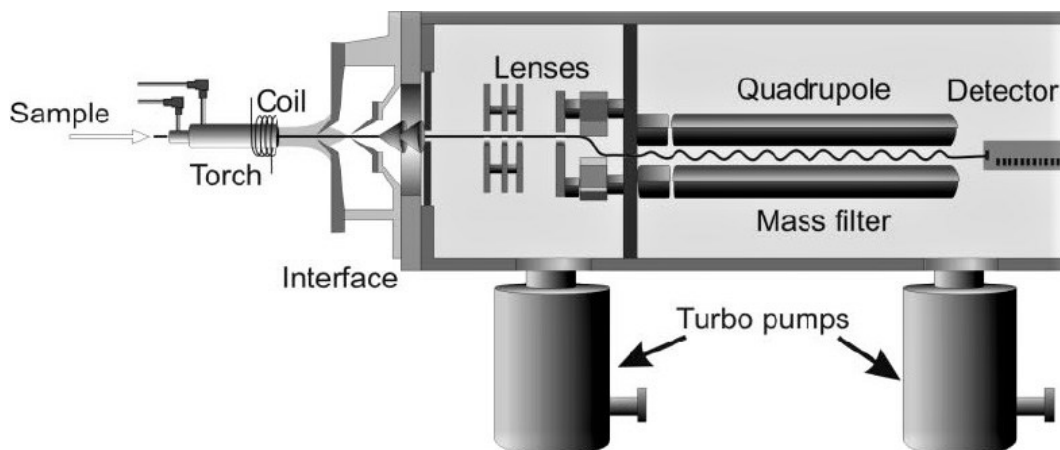


Figure 2.9: **ICPMS setup.** Cross section schematic of an ICP-MS. (Taken from [17].)

Instrumentation

We will explain each part of the ICPMS process explained in figure 2.8. The typical design of the machine is shown in figure 2.9

1. **Sample Introduction:** The sample introduction system consists of two components:
 - a Nebulizer: This component takes the liquid sample and nebulizes the solution converting it to aerosol.
 - b Spray Chamber: The aerosolized solution from the nebulizer then reaches the spray chamber. The spray chamber filters the large droplets ($> 10 \mu\text{m}$ diameter) from the tiny droplets, and only droplets with a diameter $< 10 \mu\text{m}$ enter the plasma chamber. This is important as plasma can only atomize small-size droplets efficiently. Due to this aerosol filtration, only the smallest droplets, i.e., 1-2% of the aerosol sample, reach the plasma, and the rest is drained as waste.

2. **Inductively coupled plasma (ICP):** The primary purpose of this step is to atomize the aerosolized solution using plasma. This technique is known as hard atomization in contrast to other atomizing techniques like electrospraying. ICP atomizes most

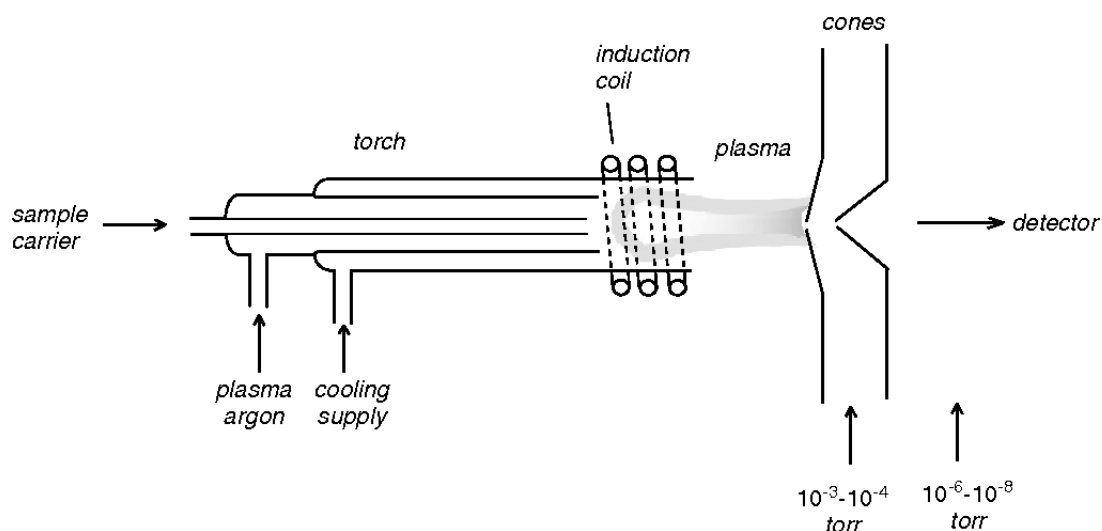


Figure 2.10: **Ion source and interface in ICP MS.** The plasma is at atmospheric pressure, and the range of pressures for the two interface vacuum stages is given in Torr. (Taken from [18].)

of the molecules in a solution completely. Most of the systems use argon gas to produce plasma. The sample aerosol is mixed with the argon gas, and the mixture passes through three concentric quartz tubes. The setup of these three tubes is called the torch (see fig. 2.10). At the end of the torch lies a copper coil driven by a radiofrequency generator to produce an alternating magnetic field inside the torch. As the mixture passes through the torch, a high-voltage discharge spark is generated to ionize the argon gas. The ions thus produced by the argon gas get influenced by the a.c. field generated by the coil and collide with each other ionizing even more of the mixture. This process repeats multiple times and soon produces an avalanche of ions in the mixture of argon and aerosol, forming a scorching plasma (≈ 10000 K). The plasma's temperature and the element's ionization potential are essential in determining the extent to which an element has been ionized. Since most elements have lower ionization potentials than argon (15.76 eV), ICP generated in the torch can ionize almost the entire periodic table. Therefore, ICPMS can detect nearly all elements present in nature.

3. **Interface:** The third step after plasma generation is the interface, where the ions generated by the plasma particles now enter a vacuum chamber enclosed by two coaxial cones (fig. 2.10) known as sample and skimmer cones. These cones are generally made up of nickel or platinum. The opening in the first cone (sample cone) is only about 1 mm. Thus, only a few ions enter the region between the cones. This region is maintained at low pressure of about 1.5 to 2 torr produced by a roughing pump. Due to low pressure, the stream of ions entering the region expands, and only

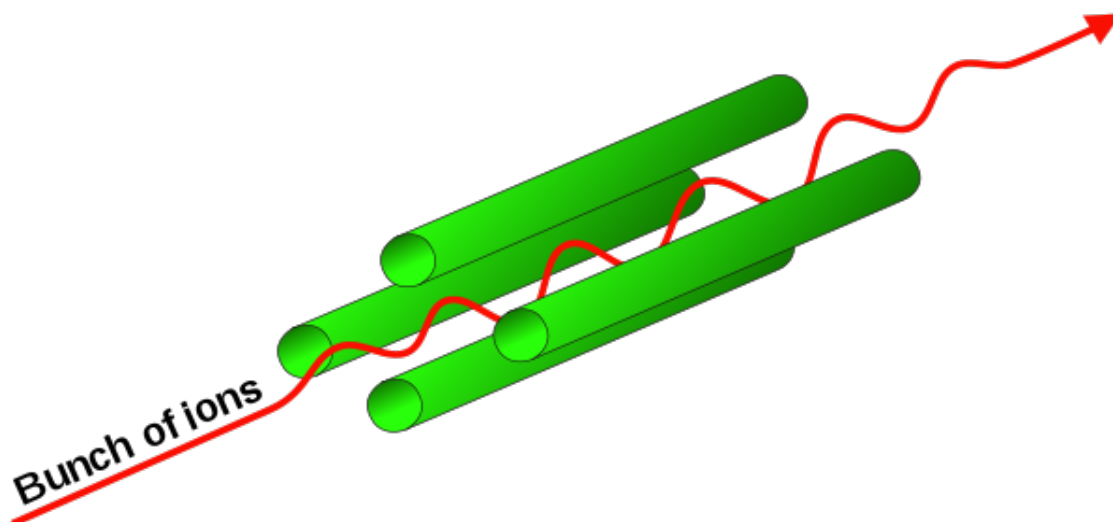


Figure 2.11: **Quadrupole mass analyzer.** The schematic of the quadrupole mass analyzer and the ion path through it. The diagonal rods are charged oppositely, maintaining a high ac voltage with dc offset.

a few of these ions exit the region from the opening in the second cone (skimmer cone). The second cone's opening is smaller than the first cone's, i.e., 0.45 mm. The ions exiting the second cone enter a high vacuum region of the pressure of about 10^{-6} to 10^{-8} torr. :

4. **Ion Optics:** This setup is made to guide the ions extracted from the plasma via skimmer cones to the mass analyzer. The secondary function of this setup is to prevent other species, like photons or neutral atoms, that might have escaped from plasma and the skimmer cones, from reaching the mass analyzer.
5. **Mass Analyzer:** This is the part where ions are filtered or separated based on their mass-to-charge ratio. Nowadays, there are multiple types of mass analyzers used in ICPMS; however, the most common mass analyzer used by most manufacturers in these machines is a quadrupole mass analyzer. A quadrupole mass analyzer is made using 4 parallel metallic rods. Ideally, these rods must be hyperbolic. However, commercially available analyzers are cylindrical and are approximately 15-20 cm long. The configuration is shown in fig. 2.11. These rods are connected to an a.c. power source with a d.c. potential offset. Diagonally opposite rods have opposite polarities, and the charged ions are made to pass through the configuration shown in the figure 2.11. Only ions with a selected m/Z ratio can pass through the analyzer for a given combination of a.c. and d.c. voltages. Therefore, we can filter out or detect ions with particular mass-to-charge ratios by setting the right combination of a.c. and d.c. potential combinations. The time taken by the analyzer to detect the m/Z ratio of

an ion is called the dwell time. The time the analyzer takes to analyze the entire m/Z range can be a few milliseconds to seconds. Commercial machines come with single as well as triple quadrupole analyzers.

6. **Detector:** The final part of the process is the detector counting the number of ions with particular m/Z ratios present in the sample. The most commonly used detectors are electron multipliers. The output current is representative of the concentration of a particular element.

Procedure

The first part of the experiment starts with sample preparation. The sample preparation is crucial in this technique. The sample material must be dissolved into a solvent that can dissolve all the elements of interest (the elements one wants to test for) or the entire sample. Thus, solvents must be chosen very carefully. These can be either dilute acids (like hydrochloric acid (HCl) or nitric acid (HNO₃), dilute bases (like ammonium hydroxide (NH₄OH), or deionized water. Moreover, these solvents must match an ICP-grade or trace element purity, i.e., purity of more than or equal to 99.999%. The chemical manufacturers provide the trace amount of impurities in ICP-grade acids or bases, typically less than 10 ppb for all metallic and non-metallic elements. Solid samples like tissues, protein fibers, and silks must be digested chemically and dissolved completely to prepare a sample solution. The digestion can also be done at room temperature or by heating if required. The sample solution's total dissolved solids (TDS) must be < 0.2%. The sample solution should appear to be very clear. For silks, conc. HNO₃ is used to digest the sample. The complete procedure of the process for our sample is provided in chapters 3 and 5.

Just as with any other technique, calibration of the machine is very important for proper output. Before testing for the unknown sample, the machine is first calibrated using solutions of standard samples with known concentrations. The intensity (counts per second (CPS)) of the output signal obtained at different concentrations is noted. This intensity must be directly proportional to the concentrations of the element in standard samples. A calibration curve is thus generated. This type of calibration is known as external calibration.

The apparatus used for sample preparation must be free of contamination. For this purpose, we must clean the beakers and equipment like LDPE tubes (used for storing the sample solution) with HNO₃ for at least 72 hours before sample preparation starts. This process is called "leaching," ensuring that any impurities from the apparatus do not contaminate our solution. It is preferred to use PTFE beakers for sample preparation.

Another extremely essential process is to perform a "blank test" before testing the ICPMS of the unknown sample. In a blank test, a blank solution is prepared using the

same chemicals (acid and water) in the exact quantities used to prepare the sample solution but without adding the unknown sample. This blank solution is tested for elements of interest using ICPMS to check the contamination in acid, water, and apparatus. This step is necessary to estimate the exact concentration of elements in an unknown sample.

In the next section, we will discuss electron paramagnetic resonance spectroscopy. We used this method to understand the nature of spins leading to the magnetic behavior of silks.

2.4 Electron Paramagnetic Resonance Spectroscopy

Electron paramagnetic resonance (EPR) spectroscopy is a method used to detect the presence of unpaired electrons and paramagnetic centers in a sample. It is also known as electron spin resonance (ESR) spectroscopy. The primary objective is to probe the electron spin of the material by keeping it in a uniform magnetic field which causes a Zeeman splitting of the degenerate energy levels of electrons (fig. 2.12). The electrons in the presence of the magnetic field will split into two energy levels based on their spin quantum number. We can cause the transition of electrons in between these levels by applying an alternating magnetic field to the sample in the perpendicular direction of the appropriate frequency. The absorption of this second alternating magnetic field by the sample provides information on the nature of spins in the material and their local environment. This technique is equivalent to nuclear magnetic resonance (NMR) spectroscopy, where instead of electrons, we try to probe the spin of the nucleus.

In case of unpaired electrons, the spin quantum number $\hat{S} = \frac{1}{2}$ and therefore the corresponding magnetic spins are $M_s = \pm \frac{1}{2}$. From basic quantum mechanics, we know the magnetic moment of an unpaired electron can be given as $\vec{m} = g\mu_B\vec{S}$. Here, g is the *Lande g-factor* of the electron and μ_B is the *Bohr magneton*. Hence in the presence of a uniform magnetic field, \vec{B} , the energy applied to the electrons is:

$$\begin{aligned} E &= -\vec{m} \cdot \vec{B} \\ &= -g\mu_B S_z B \end{aligned} \tag{2.5}$$

S_z is the z component of the spin quantum number, which is parallel with the applied magnetic field. Since a unity separates the energy levels, the energy difference will be $\Delta E = g\mu_B B = \hbar\omega_0$, where ω_0 is the frequency of the applied magnetic field in the perpendicular direction. Therefore:

$$\omega_0 = \gamma B \tag{2.6}$$

Hence the frequency that the electrons will absorb depends only upon the applied mag-

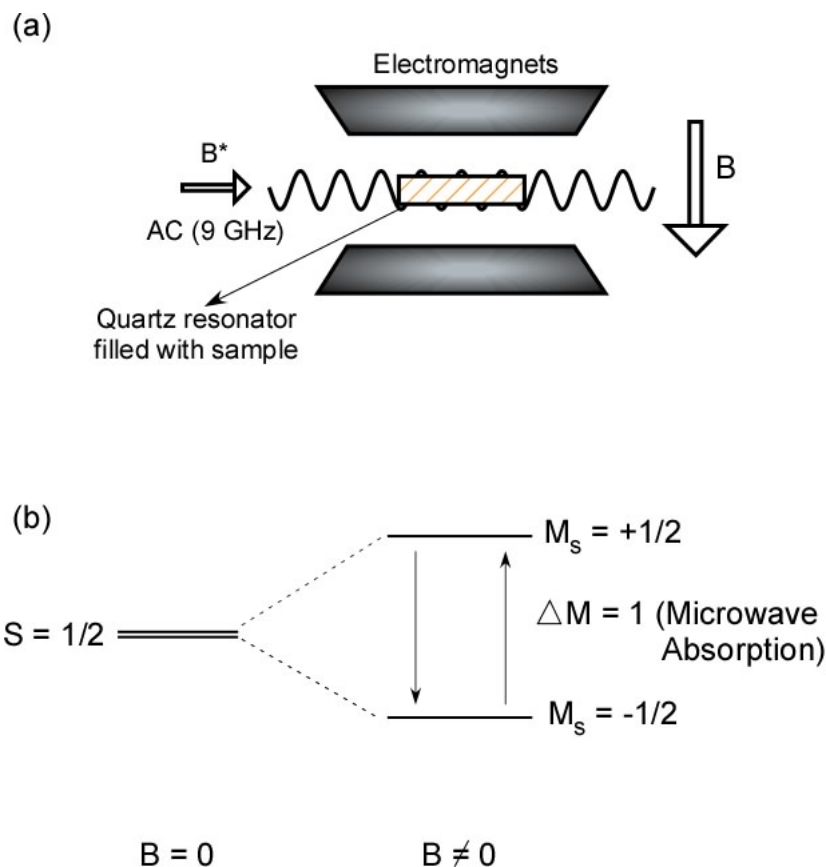


Figure 2.12: **Basic Principle of EPR.** (a) Schematic of basic EPR setup. (b) Zeeman splitting for an electronic system with $S = \frac{1}{2}$.

netic field and gyromagnetic ratio, γ of electrons. In case of free electron, we know $\gamma = 176.1 \times 10^9 s^{-1} T^{-1}$ and therefore the frequency of perpendicular magnetic field absorbed by the electrons will be $28.02 GHz T^{-1}$. In the case of H^1 NMR, since the mass of a proton is 658 times greater than that of an electron (thus $\gamma_p \ll \gamma_e$), the typical frequency of magnetic field absorbed by the hydrogen nucleus is of MHz range.

From the EPR spectrum of the material, one can calculate the integrated intensity, g-value, hyperfine splitting, and line shape of the signal. The characteristics of the signal depending on temperature, pressure, and the chemical environment of the material. However, ESR is technically much more challenging to analyze than NMR. There are many types of ESR spectroscopy experiments like continuous wave (CW) ESR at X band or Q band, pulsed/Fourier transform EPR, Electron-Nucleus Double Resonance (ENDOR) spectroscopy, etc. However, in our case, CW ESR spectroscopy at X band was used; hence, only this experiment will be discussed.

2.4.1 Instrumentation and Procedure

At room temperatures, the magnetic energy is relatively small in comparison to the thermal energy ($k_B T$); hence the equilibrium energy population between the two energy levels is tiny (ratio of population is in order of 10^{-4}). Therefore, to detect any transition between these levels, the system must be extremely sensitive. For enhanced sensitivity, it is better to vary the applied magnetic field on the sample while keeping the oscillating field at a constant frequency. Magnetic fields can be controlled precisely in laboratory conditions while maintaining the sample under constant (standing wave) frequency a.c. field. This method increases the signal-to-noise ratio of the ESR signal.

Standard laboratory ESR machines usually operate at X-band (9 GHz) microwave frequencies (using a klystron source) which get absorbed around 300-320 mT applied field and can be easily produced by laboratory electromagnets. Some ESR setups operate at higher Q-band frequencies (33 - 50 GHz). Basic setup of ESR spectrometer is shown in fig. 2.13. ESR spectroscopy is performed on solid and liquid samples in routine use. A good quality ESR spectrum requires the sample to be prepared so that the spin-containing species are extremely dilute in the sample and do not interact. Interaction among the spins causes the dephasing of spins and broadens their resonance line width. The sample is placed in a rectangular (commonly used but not limited to rectangular shape) cavity known as the resonator. This resonator must maintain a standing wave of ac magnetic field to increase the sample's signal-to-noise (S/N) absorption of this field. When the sample is placed in the resonator and the a.c. field is applied, the spectrometer detects the reflected wave energy from the cavity. The applied magnetic field (B in eq.2.5) is generally swept from minima (0 T) to the maximum value (≥ 1 T) by modulation at 100 kHz (commonly used) to increase the S/N ratio of detection of absorbed EPR signal. This is done by a spectrometer using a phase-sensitive lock-in amplifier at the same modulation frequency. The modulation amplitude of the applied field can be set from 1-10 G. The spectrum obtained from ESR spectroscopy is the first derivative of the absorption spectrum of the sample.

We have discussed that the difference in population between two different spin energy states is minor at room temperature. Another factor that plays a vital role in determining the ESR signal is spin-lattice interaction. Here the environment surrounding the radicals transfers the thermal energy to the radicals and thereby affects the ESR signal by determining the spins' relaxation time, ΔT . Relaxation time can be defined as the time the excited spins take to regain thermal equilibrium between the two energy states. The shorter is ΔT , the greater the signal's line width ΔB (Heisenberg's uncertainty principle).

If the rate of exciting the radicals increases than the rate at which these radicals relax, the spectra get very broad. This is called saturation. Hence, it should be noted that to detect

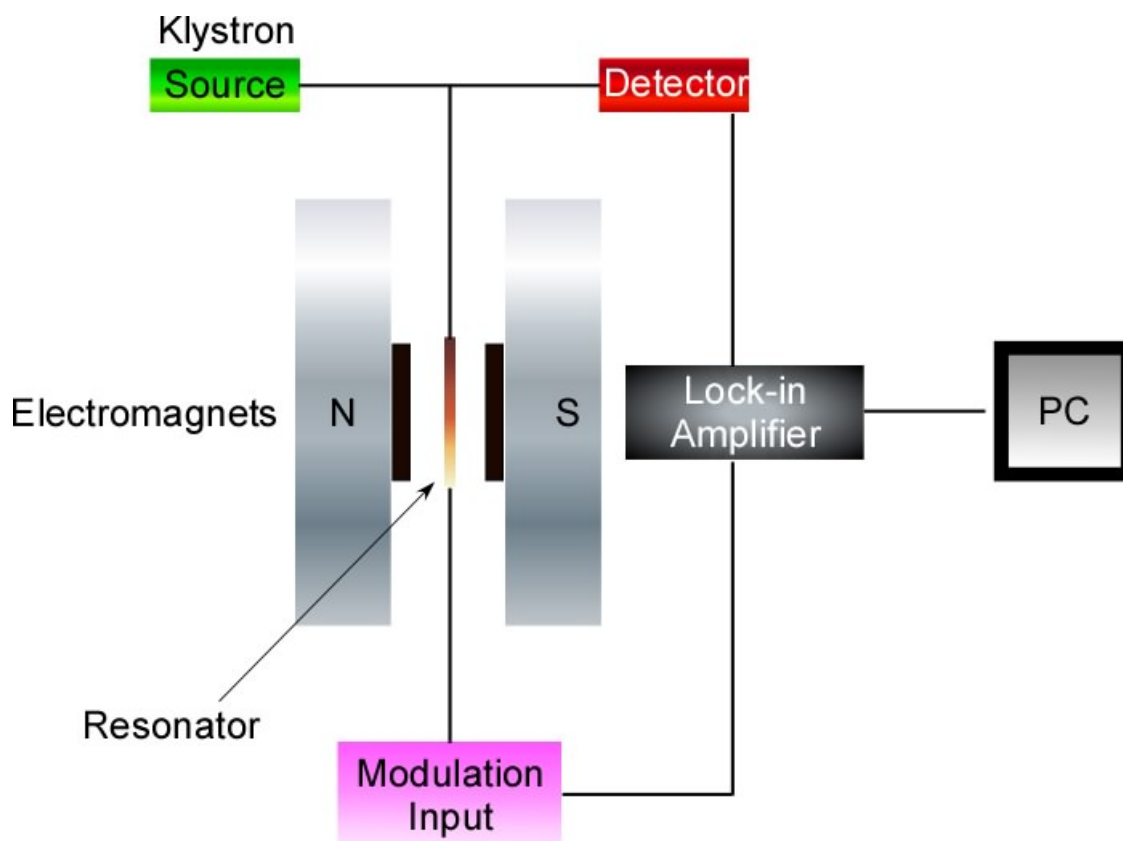


Figure 2.13: **Basic Setup of EPR.**

good absorption spectra from organic radicals, one must keep the microwave power low to avoid saturation. Similarly, we must set the modulating amplitude of the applied field accordingly to meet our requirements from experimental results.

The critical parameters obtained from the ESR spectrum are intensity, line width, and peak magnetic field absorbed. The peak magnetic field absorbed by the material is generally expressed in g - value because every machine setup can have a slight deviation in its resonant frequency that can affect the peak absorption field of the sample. However, the g -value is independent of the experimental setup and is an intrinsic value of the material and therefore remains constant irrespective of the machine used. The sample holder unit of ESR can be combined with a variable temperature unit, and sample temperature can be controlled, resulting in a variable temperature ESR spectroscopy.

The absorption spectrum can get influenced by the nuclear spin of elements in the close vicinity of the radical, causing a hyperfine splitting of the signal. The hyperfine splitting is generally of order 0.1-1 mT. It provides information about the environment of the radicals and the spread of electron clouds over their nuclei. A detailed study of ESR can be found in literature [107].

2.5 Conclusion

This chapter discussed the fundamental magnetic, thermomagnetic, elemental analysis, and magnetic resonance spectroscopy techniques that I have used in my experiments and the methodology of performing and analyzing these experiments. Section 2.2 discussed how to perform magnetometry experiments on a sample using a SQUID magnetometer and the experimental precautions one needs to take before starting the experiment and while analyzing the obtained data. The following subsection discusses performing and analyzing the characteristic thermomagnetic experiment on a sample using a SQUID magnetometer. In section 2.3, we discussed various experimental techniques to analyze and determine the elemental composition of a sample. These techniques include EDX, XPS, XAS, and ICPMS. The last section discussed the basic principle, experimental setup, and methodology of electron paramagnetic resonance (EPR/ESR) spectroscopy. We discussed in detail the construction and working principle of all experimental techniques used and the precautions one must take to analyze the results correctly.

In the following chapters, we'll discuss my experiments of exploring and analyzing the magnetic properties of spider dragline silks and silkworm silks. We will use the knowledge acquired in the first three chapters to analyze the results.

Chapter 3

Intrinsic Magnetism of Spider Dragline Silk

3.1 Introduction

As we have discussed briefly in chapter 1, much research in recent history has been diverted to find alternatives to the traditional inorganic magnets made of d and f transition metals like iron, nickel, and cobalt and their alloys and intermetallics. Traditional magnets not only require exhaustive energetic means of mining but are also brittle, non-biodegradable, toxic, and cause severe environmental pollution. On the other hand, room temperature polymeric and organic magnets are cheaper and require less energy to produce, are biodegradable and non-toxic as well as eco-friendly [13, 108]. Despite their advantages, several nitrile (-CN) containing tetracyanoethylene (TCNE) based complexes [109], including photo-induced organic magnets [110] as well as engineered π -conjugated organic polymer [111] magnets have shown ferromagnetic ordering only at low temperatures [88]. New experiments have shown carbon-based polymers exhibiting ferromagnetic ordering at room temperature [83, 84, 82]. Room temperature magnetism can be induced by introducing vacancy defects in common polymers like polythene and Teflon by merely stretching and cutting [102]. Similar results have been achieved by introducing defects in graphene [112] and graphite [113, 86, 114]. Another mechanism of introducing room temperature magnetism is tuning the sp^2 - sp^3 hybridization ratio of hydrocarbon compounds as reported in functionalized graphene [85]. Investigation of more efficient organic magnets thus is an exciting area as it can find numerous applications.

Magnetically activated polymers can significantly impact medical science as they can be manipulated externally, providing a non-contact and non-abrasive surgical approach [115, 116, 19]. Silk polymers have become a non-toxic and excellent substitute for artificial bones, blood vessels, muscles, skin, and tissues [62] etc. Moreover, magnetically activating

the spider silk by doping with magnetic nanomaterials can help surgeries [117, 118, 119]. However, the magnetic character of spider silk in its pristine state has never been explored. Our experiments explored the behavior of undoped natural spider dragline silk. We report that spider silk shows ferromagnetism at room temperature in its native state without any magnetic doping. The magnetic origins of spider silk are attributed to stable free radicals (dangling bonds) generated because of microscopic defects in protein structure. These spins are trapped in a glassy state in a protein matrix and interact both ferromagnetically and antiferromagnetically, leading to multiple coexisting magnetic phases in spider silk, as will be discussed in this chapter. Interestingly, we also show that the silk can sustain its ferromagnetic properties even at sufficiently high temperatures of 400 K. A thorough investigation of the magnetic properties of spider silk was done, including magnetometry, thermomagnetic analysis, magnetic resonance spectroscopy, and elemental analysis. In addition, we also showed that silk's magnetism could be manipulated by increasing the number of defects in its structure, hence offering significant proof of the magnetism arising due to atomic defects in silk's structure.

We also show a controlled experimental demonstration of the interaction of spider dragline silk with a strong magnet and how spider silks can be used as a bio-magnetosensor to detect magnetic fields lower than the earth's magnetic field itself ($\leq 33 \mu T$). Moreover, we later show how spider silks can be used as biological magnetic bio-robots to remotely manipulate organic materials like cells, tissues, drugs, etc., in a liquid environment.

In the following sections, we will discuss the experiment's step-by-step process, starting with the sample preparation technique following the magnetic characterization, thermomagnetic characterization, elemental characterization, and electron spin resonance. Later we will discuss the potential applications of spider silks' magnetic properties.

3.2 Preparation of pristine spider silk samples

To investigate the intrinsic magnetism of pure spider silk, we prepared spider dragline samples taking extreme measures to avoid any contamination during silk collection, storage, and measurements. The silk was obtained from randomly picked multiple female spiders (*Araneus* and *Neoscona* families) from gardens of the Indian Institute of Science Education and Research (IISER) Mohali, India. These were kept in cleaned plastic jars for the period of sample collection. The silk was forcibly obtained from fully awake female spiders following a step-by-step silk collection procedure as depicted in Fig.3.1.

Briefly, a spider was taken out and held with a hand (wearing clean latex gloves), and the silk was taken out carefully by stimulating the spinnerets on its abdomen with a soft stick. After the emergence of dragline silk threads from the spigots, the threads were wrapped

around pipet-heads (cleaned with acetone) fixed onto a controllable motor. The silk was pulled out at a speed of $3 - 5\text{ cm/s}$ using a motorized setup. Silk was taken out at 300 K and $\approx 50\%$ relative humidity. The process was repeated for several days in various shifts to collect a sufficient amount. For example, the required mass of silk for each SQUID sample was about $\geq 5\text{ mg}$ (amounting to about 1.5 km silk length).

Extreme care was taken to avoid magnetic contamination of our pristine silk samples. Notably, no metallic tools were used anytime, exposure to ambient dust was avoided by silking in a closed clean-air chamber, and the samples were not brought in contact with any uncleaned surface. The SQUID samples were stored in closed sterilized microtubes (MCTs) in ambient conditions ($T=300\text{ K}$, $RH \sim 50\%$).

Since it is known that there is a natural variation in the structure and property of silk, it was important to establish the robustness of magnetic signals over many silk samples. For this purpose, we randomly prepared 24 independent silk samples and grouped them into five batches. The following five magnetic assays were performed:

- Assay-1: Four samples were used for SQUID measurements, and the same samples were later used for elemental analysis (Section 3.4.1) and EPR measurements (section 3.4.3) to establish the absence of ferromagnetic d-block elements like Fe, Ni, Co, etc.
- Assay-2: Two samples were prepared to control silk's magnetism by simple stretching and cutting mechanisms (section 3.4.2),
- Assay-3: One sample was prepared and stored in Argon gas for SQUID measurements to isolate silk's magnetism from molecular oxygen. For more detail, see appendix B.
- Assay-4: Three silk samples were used to build all-silk torsion biocompass (section 3.6.1),
- Assay-5: Three fleets of miniature silk swimmers for magnetically controlled transport of solid and liquid cargo in a fluid environment (section 3.6.2).

The positive results from all the assays mentioned above are described in detail in the following section.

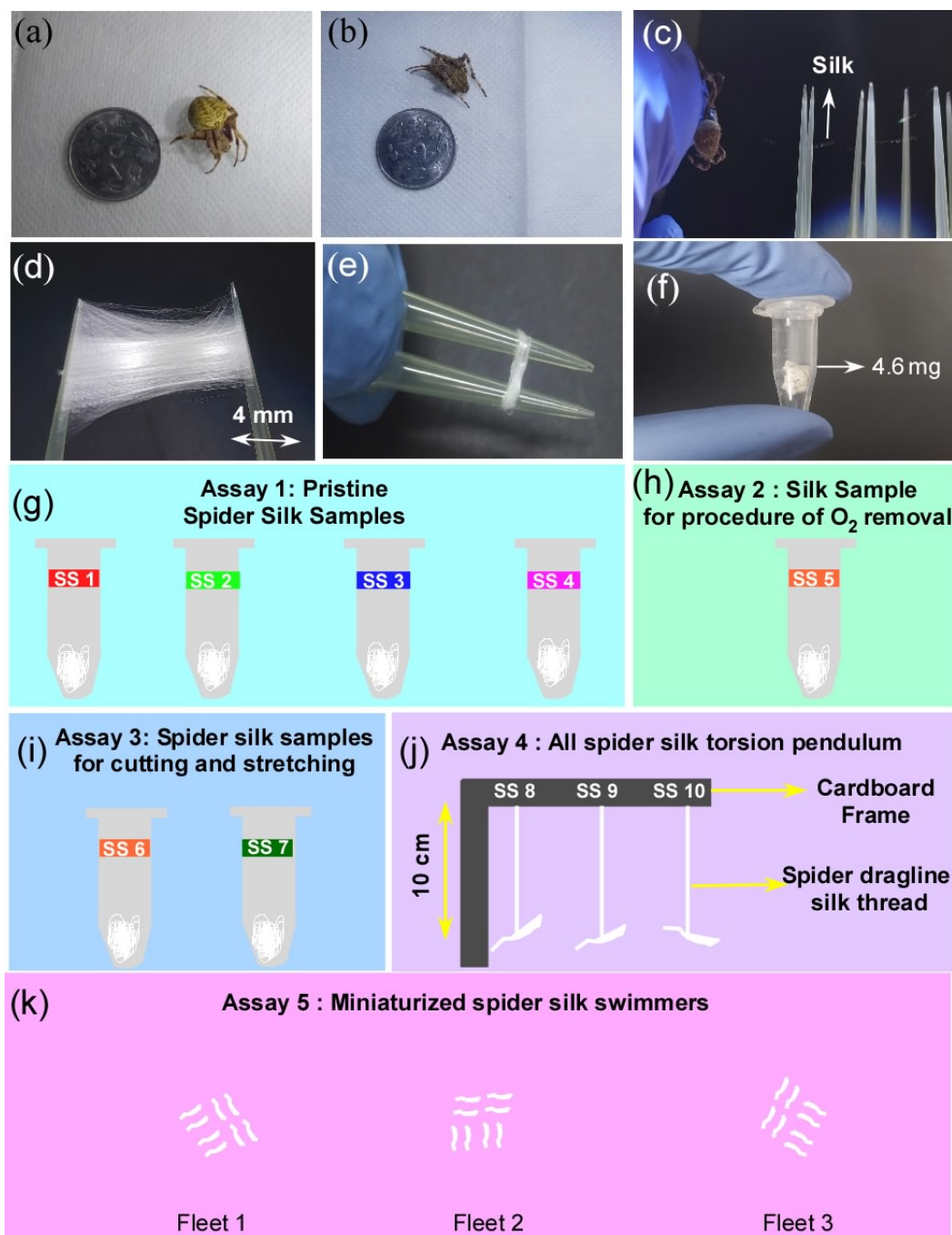


Figure 3.1: Preparation of pristine silk sample for five magnetic assays. (a)-(b) Pictures of typical garden spiders. Coin diameter: 23 mm. (c)-(f) Step-by-step procedure for forceful extraction of dragline silk from the spiders. A fully awake spider was taken out of the box and made to rest on the hand (wearing clean latex gloves), and its silk was carefully extracted. The silk was continuously pulled and wrapped around pipet-heads attached to a motor rotating at a speed of 3-5 cm/s. A single sample was kept in a sealed and sterilized microtube (MCTs), as shown in (f). (g)-(k) Schematic illustration of the five magnetic assays described in the text. Note that no metallic equipment/tool was used during this process. Before silk collection, the pipet heads were thoroughly cleaned with ethanol and acetone, and MCTs were sterilized.

3.3 Magnetometry of Spider Dragline Silks

After completing the dragline silk sample collection, we first carried out the magnetization experiments using a SQUID magnetometer. Quantum design MPMS3 SQUID magnetometer was used for all magnetic and thermomagnetic characterizations. All samples were accurately weighed before commencing the experiment. Silk was compressed using physical pressure (with hands, wearing latex gloves) to the size of $\leq 3 \text{ mm}$, wrapped around the quartz half tube using teflon tape, and inserted into the sample-holding straw in order to perform the experiment. Magnetometric measurements were taken at 300 K (room temperature), 10 K, and 400 K. The results of isothermal magnetometric measurements are shown in figures 3.2-3.5.

It is common knowledge that almost all proteins and organic compounds, as well as tissues, are diamagnetic in nature; hence one expects a strong diamagnetic background from these types of samples. The diamagnetic signature can overpower the small magnetic character of biological samples (if any) at high magnetic fields. However, since diamagnetism is proportional to the applied magnetic field, the sample's magnetic signatures are visible at low applied fields (near zero), and one must subtract the diamagnetic signature to reveal the hidden magnetic character of the sample. The data for SQUID magnetization of all silk samples at 300 K are given in figure 3.2. Figure 3.2 (a) shows the raw magnetization data without diamagnetic subtraction. For large magnetic field $> 8000 \text{ Oe}$, the silk is overwhelmingly diamagnetic, with a diamagnetic susceptibility of $\chi_D = -1.37 \pm 0.29 \times 10^{-8} \text{ emu}/(g \cdot \text{Oe})$ (average of 4). Figure 3.2(b) shows the data after diamagnetic subtraction from raw data depicting clear saturation magnetization, $M_s = 0.0278 \pm 0.0041 \text{ emu}/g$ (average of 4 samples) and coercive field, $H_c = 42.9 \pm 9.0 \text{ Oe}$ (average of 4 samples) in all silk samples. A remnant magnetization $M_r = 0.0011 \pm 0.0003 \text{ emu}/g$ (average of 4 samples) is also observed in all silk samples. Section 3.4.2 shows that one can increase magnetic parameters like M_s , H_c , M_r by deforming spider silk's structure. The inset of figure 3.2(b) provides a close-up look at the data after subtraction. Using the known molecular weight of dragline silk of ca. 600 kDa [120], we get a magnetic moment of $\sim 3 \mu_B$ per protein molecule at room temperature (see Appendix D for details of calculations). Such magnetic behavior of spider silks has never been known hitherto. The magnetometric analysis implies that spider dragline silk exhibits a soft ferromagnetic character at temperatures up to 400 K. We did not take readings for higher temperatures to prevent the silk from undergoing an irreversible glass transition and destroying its inherent structure.

To ensure that the magnetic signals from silk are clean and much above the background, we compared the magnetization data MH and MT obtained from the spider silk samples with the background data from the empty sample holder (the quartz half tube and teflon

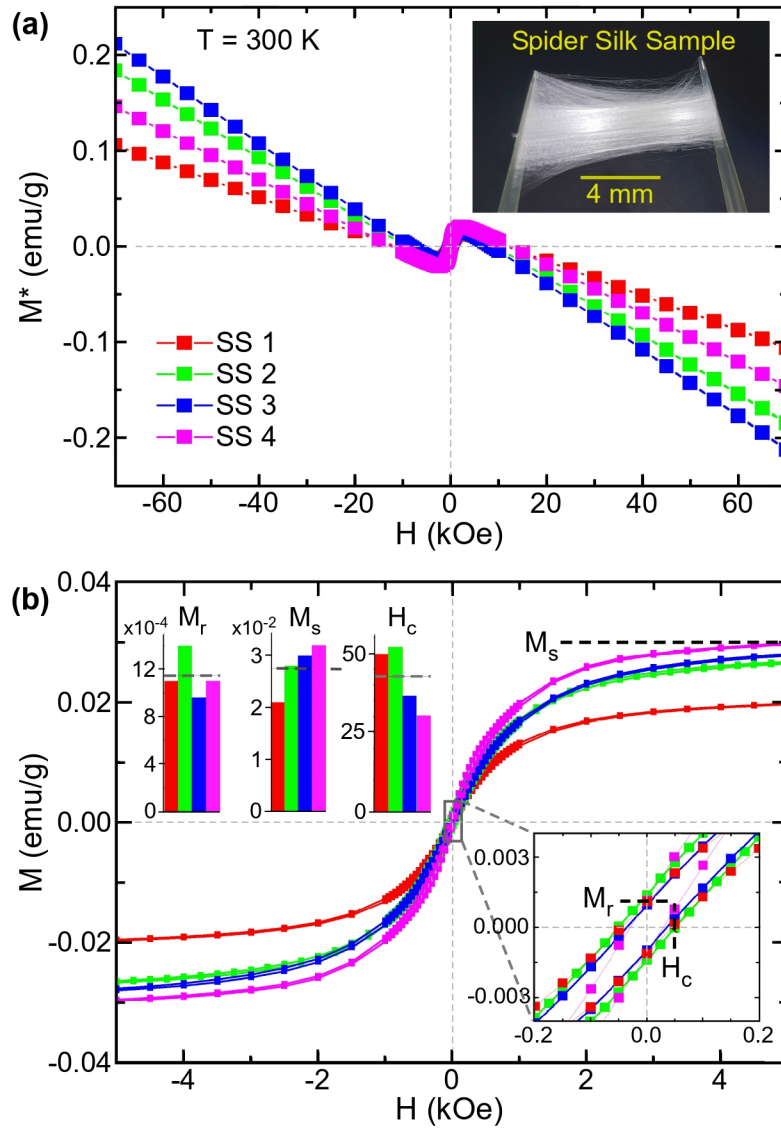


Figure 3.2: **M-H using SQUID at 300 K.** (a): At high magnetic fields, the diamagnetic contribution of spider silk dominates heavily over ferromagnetic contributions typically above 2000 Oe. M^* stands for data before diamagnetic subtraction. (b): M-H relation after subtracting diamagnetic contribution at 300 K. Lower inset: zoom of hysteresis loop showing coercivity and remnant magnetization. Upper inset: distribution of H_c , M_r and M_s for four samples. Mean values of these parameters are $M_s = 0.0278 \pm 0.0041$ emu/g, $H_c = 42.9 \pm 9.0$ Oe and $M_r = 0.0011 \pm 0.0003$ emu/g.

without the silk samples) under otherwise identical conditions. Fig 3.3 shows that the background of the empty sample holder is negligibly small. Notably, the empty sample holder is only weakly diamagnetic and, as expected, did not see any hysteresis (see zoom below 2 kOe). Also, for the fields (e.g., 60 kOe), the diamagnetic response of silk is much larger than the background.

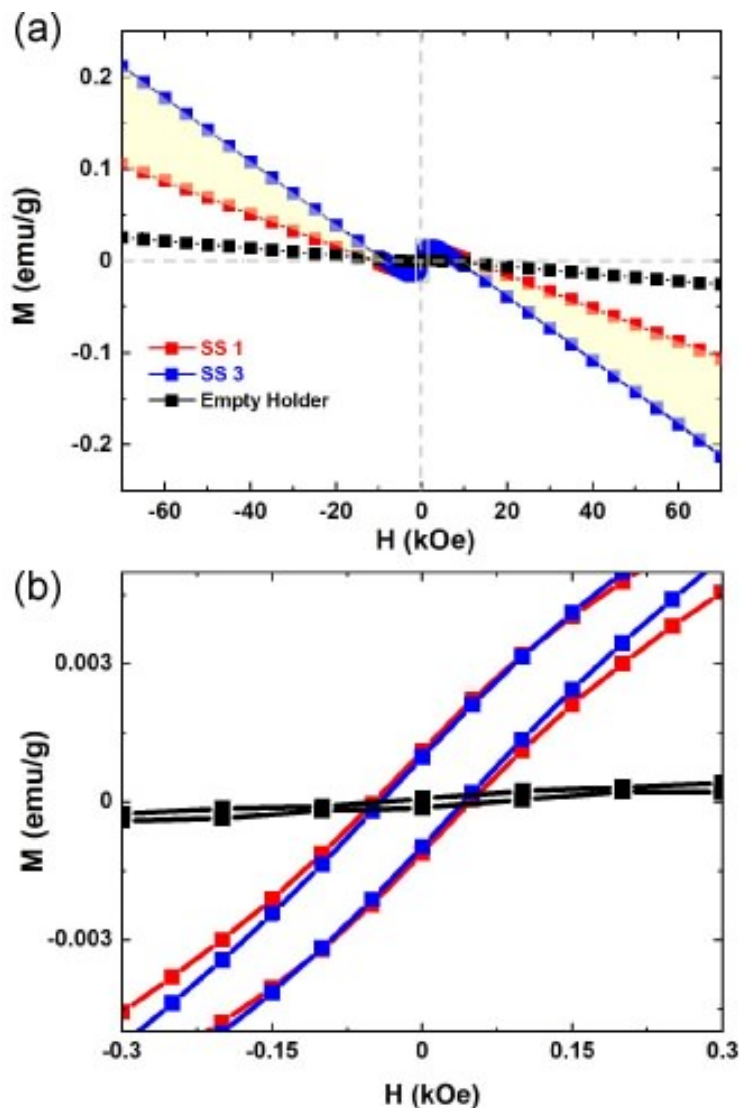


Figure 3.3: **Comparison between MH data for empty tube background and with silk.** The background SQUID data was obtained with an empty tube (Black). The yellow color band in silk data denotes variability of the MH data across four silk samples. We note that the background is negligibly diamagnetic compared to spider silk (SS). Hence, throughout the experiments, we performed diamagnetic background subtraction by using high field data (of SS) at 300 K. Bottom graph shows zoom near zero field. The background does not show any hysteresis. It must be noted that an empty holder means a quartz half tube with teflon tape but without silk samples.

Magnetization data at 10 K of all spider dragline silk samples is shown in figure 3.4. Figure 3.4 (a) shows the raw MH data without diamagnetic subtraction, and figure 3.4(b) shows the data after diamagnetic subtraction from raw data depicting clear enhancement of magnetic character with a significant increase in remnant magnetization, $M_r = 0.00325 \pm 0.00082 \text{ emu/g}$ and coercive field, $H_c = 113.9 \pm 21.4 \text{ Oe}$ as well as lack of saturation in magnetization even at a very high magnetic field of 7 T in all silk samples. The inset of figure 3.4(b) provides a close-up look at the data after subtraction to show the presence of hysteresis. The analysis of this MH data implies that spider dragline silk exhibits the coexistence of ferromagnetically interacting and non-interacting magnetic spins. The paramagnetic susceptibility of all silk samples at 10 K was found to be $\chi_p = 1.47 \pm 0.41 \times 10^{-6} \text{ emu/(g} \cdot \text{Oe)}$ (average of 4). A prominent source of paramagnetism in spider silk can be the free radicals formed due to microscopic defects within its structure during the spinning process [121]. However, a thorough investigation of dragline silks must be done to check the presence of ferromagnetic impurities like iron, nickel, cobalt, etc. More discussion over the magnetic order of spider silks will be discussed in section 3.4.

The magnetization results were reproducible for all our samples and the magnetic moment was stable over quite a long time as the samples were stored at room temperature and 50% relative humidity. This implies that such organic magnets can be stored for a very long time. More surprisingly, we find silk's magnetic character well preserved at temperatures significantly higher than ambient, i.e., at 400 K (127°C). However, high temperatures usually cause proteins to denature and lose their physical and chemical properties. Spider silk is known to survive up to 473 K before getting denatured irreversibly [28, 122]. Moreover, silk is known to get carbonized at high temperatures to graphene-like structures [122]. Therefore, we did not go at higher temperatures as it would have permanently damaged our samples for further experimentation.

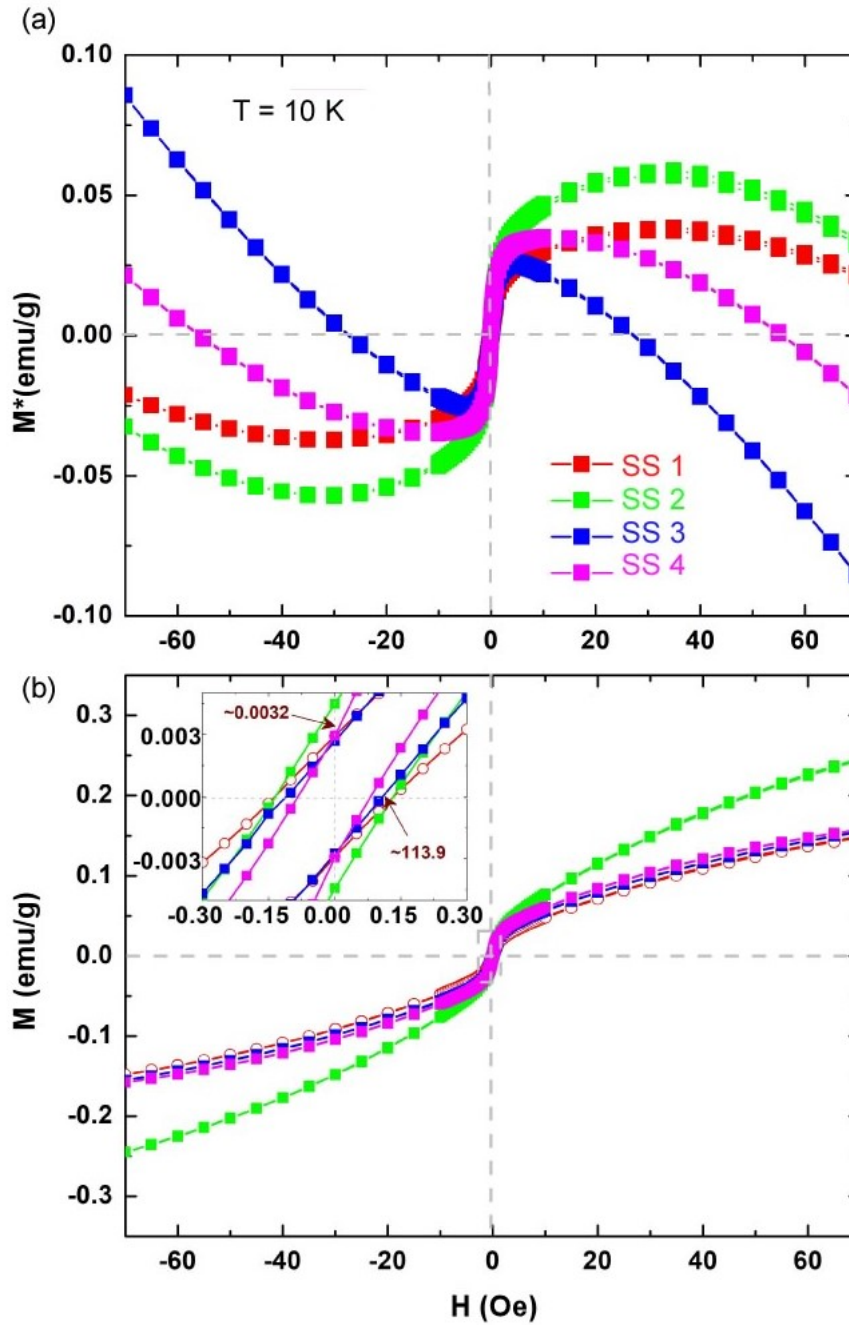


Figure 3.4: **M-H data of spider silks at 10 K.** (a): The magnetization of silk has increased significantly, which is evident at both low as well as high magnetic fields when compared with data collected at 300 K. (b): M-H relation after subtracting diamagnetic contribution at 10 K. We can see that the magnetization doesn't saturate even at even magnetic fields of 7 T and keeps increasing linearly. This suggests the coexistence of ferromagnetically interacting ($J > 0$) and non-interacting spins in silk samples. Average remnant magnetization increases to $M_r = 0.00325 \pm 0.00082$ emu/g and coercive field, $H_c = 113.9 \pm 21.4$ Oe. The average paramagnetic susceptibility, $\chi_p = 1.470.41 \times 10^{-6}$ emu/(g · Oe).

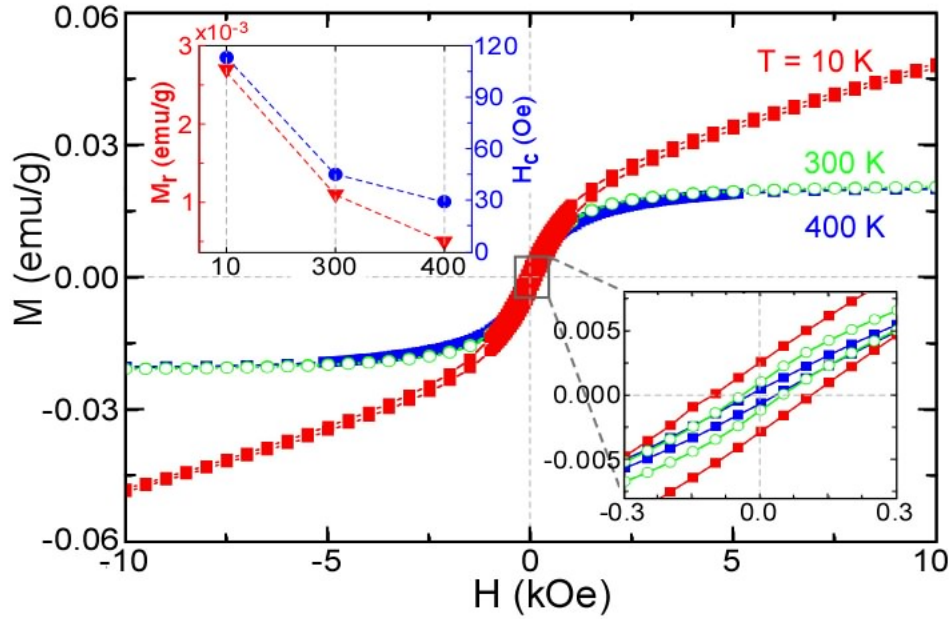


Figure 3.5: **Comparing M-H curves of silk at different temperatures.** The data depicts the soft ferromagnetic character of silks at 10 K, 300 K, and 400 K. Left inset: Comparison of H_c and M_r at these temperatures. As the temperature increases, we can see a steady drop in M_r and H_c . Right Inset: Zoom of data near zero field in M_r and H_c .

3.4 Origin of Magnetism in Spider Dragline Silks

We have discovered the ferromagnetic character of silk, but what is the probable cause for such a magnetic character? In the past several organic materials have shown ferromagnetism because of contamination of iron impurities. Even though we took extreme measures to ensure that silk does not get contaminated with any metallic impurities during sample preparation (section 3.2), we must confirm the absence (or presence) of ferromagnetic impurities (especially d-block elements) in spider dragline silks. Elemental characterization is essential to discover the origin of magnetism in these materials.

3.4.1 Elemental Analysis

In this section, we use four independent techniques to confirm the absence of any ferromagnetic impurity in our samples by elemental analysis of our spider dragline silk samples. This provides additional experimental proof that the observed magnetic properties of spider silk are not due to any metallic impurities.

We performed a detailed elemental analysis to detect d-block elements (Fe/Ni/Co) in the same samples recovered after the (non-invasive) SQUID measurements. We employed three different techniques adequate to analyze a small quantity of sample mass (around

5 mg) with maximum possible precision: (1) Energy dispersive X-ray spectrum (EDX), (2) X-ray photoelectron spectrum (XPS), and (3) X-ray absorption spectroscopy (XAS) in total energy yield (TEY) mode in all the silk samples. Our results are also consistent with previous structural studies on silk and atomistic modeling, where the ferromagnetic impurities were either absent or incompatible with its structure. In addition, we also did inductively coupled plasma mass spectroscopy of our samples, a chemically destructive technique requiring a significantly large amount of silk (≥ 150 mg). New silk samples were prepared for this experiment with identical techniques and conditions described in section 3.2.

We could not find any trace of iron, nickel, manganese, or cobalt in our samples with all the non-destructive techniques. The ICPMS results showed a negligible amount of iron content in our silk samples (≈ 1 ppm) which cannot be responsible for the significant ferromagnetic magnetic character of silk samples that we observed (see ICPMS results for details). At 1 ppm concentration (mass/mass), the saturation magnetization of iron in silk samples will be a hundred times smaller than our observation. Our elemental characterization results agree with previous structural studies in undoped pristine spider silk [123]. Our elemental data and concluding analysis are detailed below:

Elements	Atomic No.	Series	Unn. Conc. (Wt.%)	Norm. Conc. (Wt.%)	Atomic Conc. (at. %)	Error (Wt. %)
C	6	K-Series	66.81	66.81	72.02	12.2
O	8	K-Series	23.39	23.39	18.93	7.9
N	7	K-Series	9.80	9.80	9.06	6.4
Fe	26	K-Series	0	0	0	0
Ni	28	K-Series	0	0	0	0
Mn	25	K-Series	0	0	0	0
Co	27	K-Series	0	0	0	0
Cr	24	K-Series	0	0	0	0
		Total	100.00	100.00	100.00	

Table 3.1: **EDX Analysis.** Atomic concentration of selected elements in three independent samples of the spider silk.

- (1) **Energy dispersive X-ray spectrum (EDX):** The silk samples were coated with gold of 1-2 nm thickness, and their EDX spectrum was taken using an electron beam of energies from 10 to 20 KeV. The typical spot size of the beam was a few μm^2 . The instrument was benchmarked and calibrated prior to measurements. We scanned

about 4 to 5 locations on each sample.

The results obtained are shown in Table 3.1. The dominant contribution in the sample was C, N, O. But we detected zero concentration of Fe, Mn, Ni, and Co for all the silk samples. The minimum detection limit of the EDX spectroscopy was 3000 ppm.

- (2) **X-ray photoelectron spectrum (XPS):** Prior to the experiment, we calibrated the XPS system using pure silver thin film. It was found that spectra were shifted ≈ 4 eV in survey scans. Three silk samples were used for the XPS scan. The X-ray source was Aluminium (Al) K_{α} . Silk samples were uniformly spread with the help of carbon tape and used to stick the silk on the copper target plate. The survey scan is shown in Fig. 3.6 for all samples. The major atomic components like carbon (C), oxygen (O), and nitrogen (N) were visible. However, there was no detectable signal for any ferromagnetic transition element in the d-block or f-block (Fe, Ni, Co, Gd).

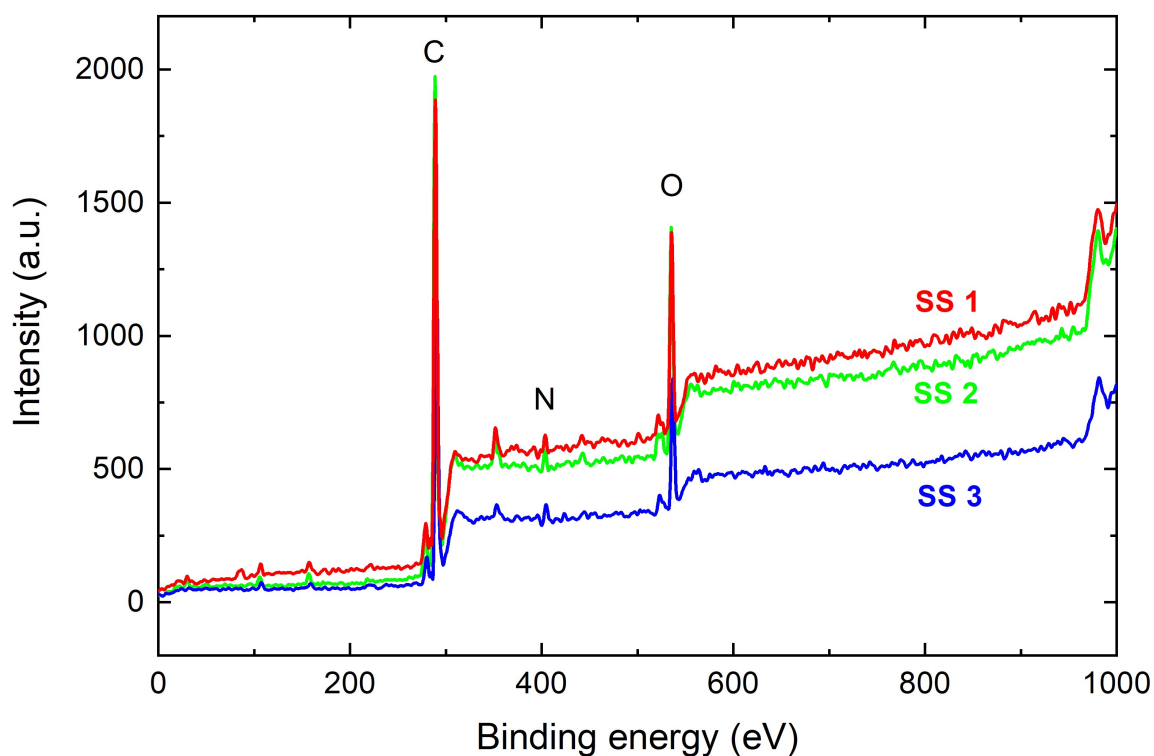


Figure 3.6: **XPS survey scan for three pristine silk samples.** The consistent peaks corresponding to carbon (C), oxygen (O), and nitrogen (N) are clearly visible in both survey as well as core scans. We also got weak signals for other known elements like calcium (350 eV). However, clearly, there was no signal of any transition d-block and f-block elements in the survey scan. These measurements were performed on uncoated silk samples. Target plate area was $1\text{ cm} \times 1\text{ cm}$. The scan area of XPS is typically in μm^2 , and scanning depth is up to 10 nm. Measurements were performed in a high vacuum of 10^{-9} mbar

To reconfirm their absence in silk, we repeated dedicated core scans for Fe, Ni, and Co, as shown in Fig.3.7. The core scans were obtained by 5 complete scans of the specified energy range, where their signals are expected, and yet no signal was detected. The detection period per scan was set at 300 s. The XPS can accurately detect the presence of an element on the surface of samples up to an atomic concentration of a hundred parts per million (ppm).

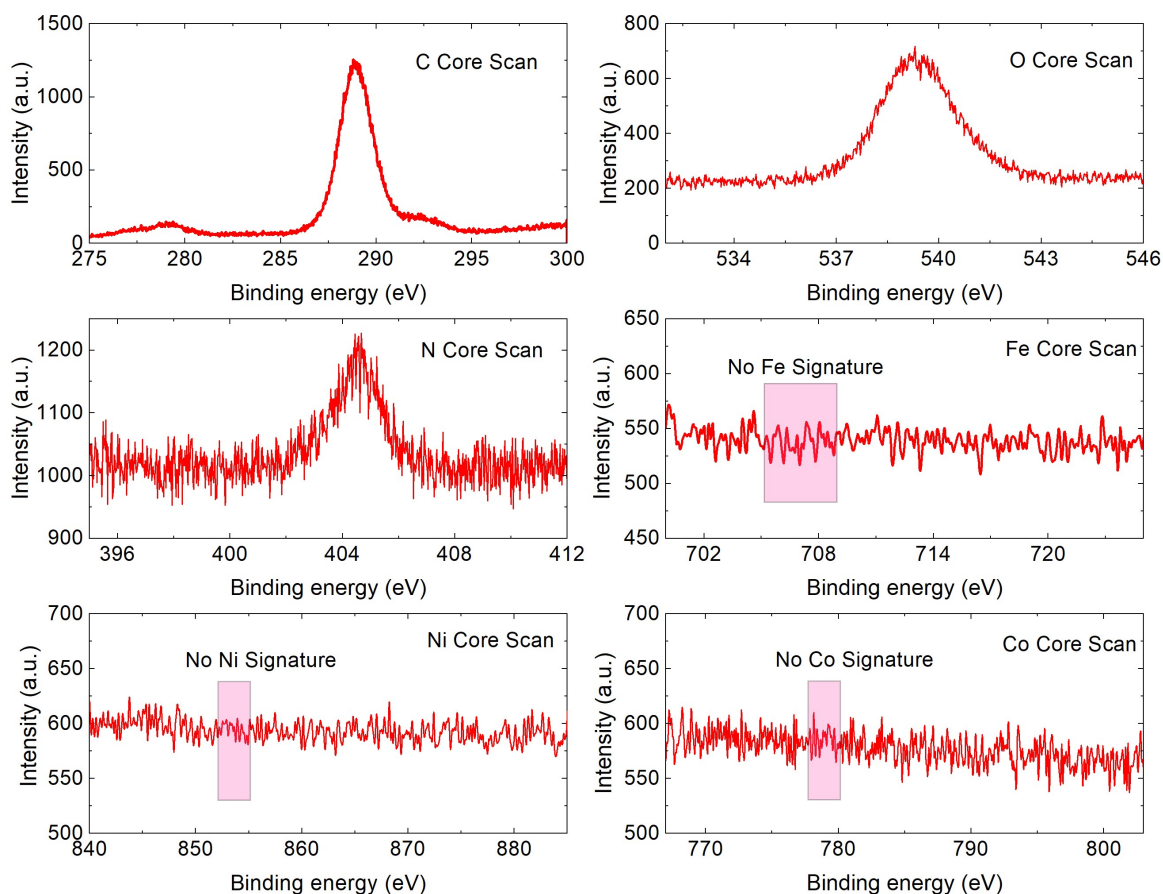


Figure 3.7: Core XPS scans confirming the absence of ferromagnetic elements. We further took dedicated core scans to detect the key elements (Fe, Co, Ni) that can be ferromagnetic at room temperature. The above results were obtained after five complete scans near their specified energy spectra; still, no signal was found above the background noise level. Fe's expected primary 2p signal lies from 706 eV to 710 eV. Ni's expected primary 2p signal lies from 852 eV to 855 eV. Expected primary 2p signal of Co lies from 778 eV to 779 eV [NIST XPS Database].

- (3) **X-ray absorption spectroscopy (XAS):** Silk bundle samples were analyzed using XAS in total electron yield (TEY) mode. The X-ray source was Indus 2, a synchrotron at Raja Raman Center for Advanced Technology (RRCAT), Indore, India. The obtained spectrum is shown in Fig. 3.8. We could easily detect the primary

atomic constituents of spider silk like C, N and O. However, the scan for heavy transition metals (Fe, Ni, Co, and Mn) showed no detectable signal.

XAS in TEY mode can detect the presence of an element in a sample for more considerable depths (beneath the surface) than the XPS scan, with accuracies of about 10 ppm. The absence of any signal in this range also means that the d-block ferromagnetic elements were absent.

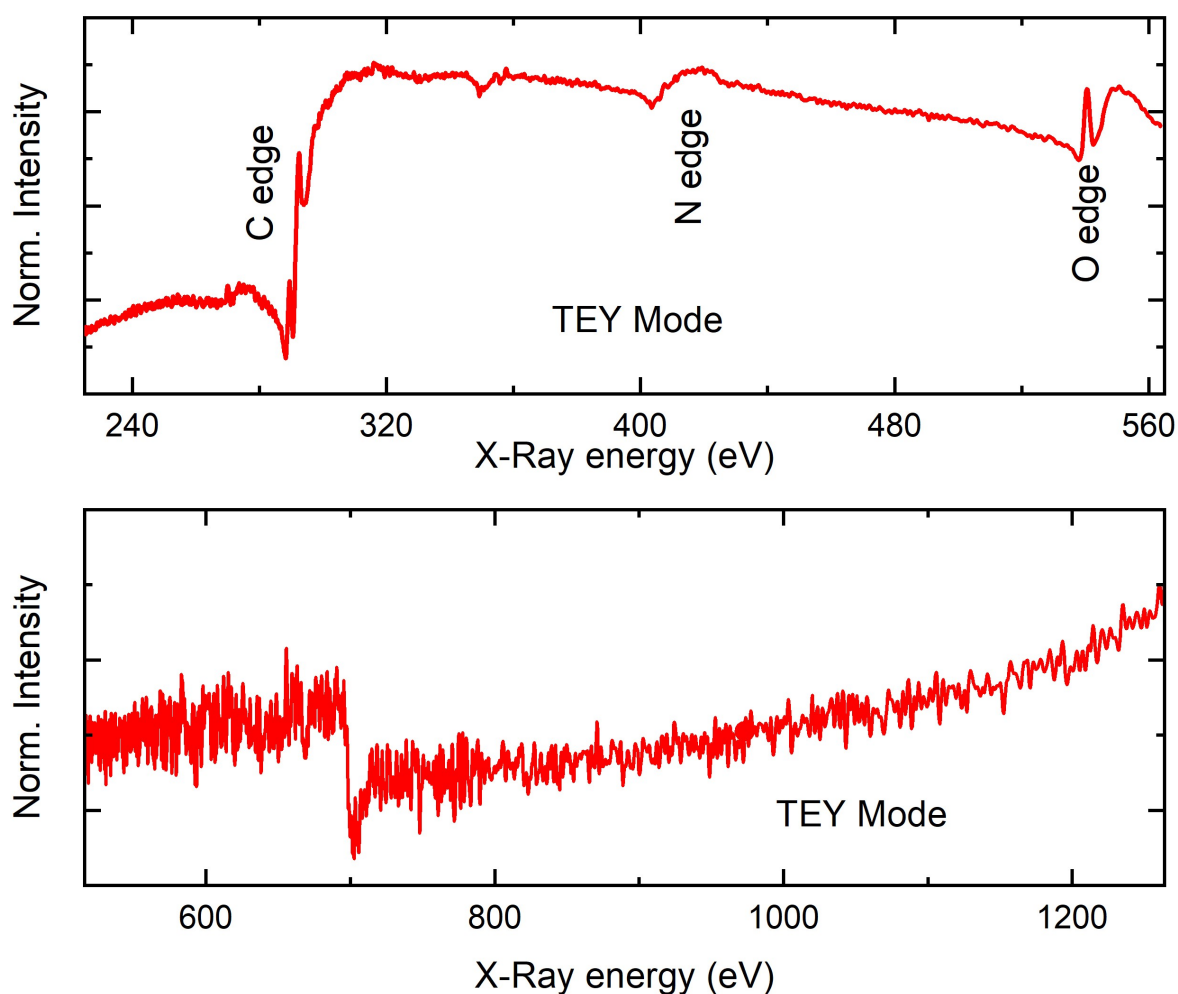


Figure 3.8: **XAS spectrum of silk samples.** The absorption edges of C, N, and O are visible. No absorption could be detected for heavy ferromagnetic atomic numbers (lower graph) like Fe, Ni, Co, or Mn.

- (4) **ICP-MS:** New samples were prepared for this technique as it requires quite a large quantity of silk in comparison to other techniques. ICPMS grade HNO_3 and HCl were used for digestion, and high-performance liquid chromatography (HPLC) grade water was used for dilution purposes. 200 mg of spider dragline silks was used for this experiment. The silk was microwave digested in a mixture of 5 ml of HNO_3 and 3 ml of HCl acids for 1 hour at a temperature of 190°C . After the silk was com-

pletely dissolved, 1 ml of the solution was diluted using 99 ml of water. Later the solution was filtered using a 0.45 μm PTFE syringe filter. The filtered solution was then ready for experimentation. The calibration standards for ICPMS were then prepared from 1 ppb conc. to 1 ppm conc. Thermofisher ICP-MS (iCAP-RQ) instrument was used for the experiment. For assurance of the reliability of our results, we first experimented on a blank solution (sample without silks) to check the conc. of ferromagnetic impurities in the background solution. We used the same equipment and chemicals (acid, water, and syringe filter) to prepare the blank and silk solutions. We find that the concentration of ferromagnetic impurities in silk is $\ll 0.1\%$ (see table 3.2). Such a small conc. of ferromagnetic impurities cannot result in high saturation magnetization observed for silk. As one can calculate, the saturation magnetization of silks due to iron with 1.23 mg/kg conc. will be a hundred times smaller than the one expressed by our silk samples. Hence iron impurity cannot be envisaged as the source of ferromagnetism in our system.

Element	Iron	Nickel	Cobalt	Manganese
Concentration in blank solution	$< 0 \text{ ng/kg}$	$0.21 \mu\text{g/kg}$	$< 0 \text{ ng/kg}$	$0.48 \mu\text{g/kg}$
Concentration in spider silk	1.23 mg/kg	$0.32 \mu\text{g/kg}$	$1.47 \mu\text{g/kg}$	$55.55 \mu\text{g/kg}$

Table 3.2: **Concentration of ferromagnetic elements in silks.**

Our elemental characterization results indicate that ferromagnetic transition metals are almost absent in the silk samples, with experimental evidence of accuracy up to 0.1 ng/kg. Coupled with the fact that ferromagnetic ions/ atoms with atomic concentration $< 1\%$ can not lead to long-range ferromagnetism in a protein-based material (Chapter 1), we conclude that the observed ferromagnetic response is a result of the ferromagnetic coupling of free radicals (or dangling bonds) that are present in spider silk.

However, to verify this conjecture, we must see if increasing the defects (or deforming) in spider dragline silks can increase their magnetic characteristics.

3.4.2 Enhancement in magnetism of silk by tensile rupturing and cutting

To confirm the magnetostructural relationship of spider dragline silks, we designed a series of experiments to enhance atomic defects in spider dragline silk by simple mechanisms such as excessive tensile loading or mechanical cutting. Our results showed an enhancement in deformed silk's saturation magnetization, implying an increased number of ferromagnetically coupled spins in silk's hierarchical structure.

Below we elaborate on the two mechanisms used to deform the silk: (a) rupturing by tensile loading and (b) cutting into multiple small pieces.

Enhanced magnetization by tensile rupturing

Spider dragline silk consists of nanocrystals of β -sheets made of poly-(Ala) and poly-(Gly-Ala), which are embedded in an amorphous helical matrix of (GGX) and (GPGGX) repeat motifs (see chapter 1 for details). Stretching spider dragline silk affects its structure. Under extreme stress, the nanocrystals break in a slip-stick motion while the helices uncoil and rupture [3]. In effect, stretching could enhance the atomic defects in silk due to rupture and shear deformation of its secondary structures (β -sheets and helices). After extreme tensile loading, we observed that the silk sample's saturation magnetization increases than its value in a pristine state (Fig. 3.9). The schematic illustration of the procedure to stretch the silk is shown in Fig. 3.9(a-c). We performed the following magnetization measurements sequentially:

- (1) First, the M-H curve of the pristine spider dragline silk was measured at T=300K and T=10K (Sample label: SS 6 Pristine).
- (2) The same sample was then stretched near its breaking point (SS 6 Breaking point), and the magnetization was measured again.
- (3) Further rupturing the same silk to small pieces by excessive stretching (SS 6 Ruptured) and the magnetization was measured a third time.

Stretching silk at a constant strain rate of 5 mm/sec till its breaking point increased the saturation magnetization of silk by three folds (200% increase), implying that the number of ferromagnetically coupled dangling bonds increases with the increase in the number of defects in silk. The enhancement is observed at T=300K and low temperature at T=10K. However, further rupturing the silk into small pieces by stretching causes the breakdown of its secondary structure and makes interaction among radicals difficult. Hence we observe a decrease in saturation magnetization of silk, albeit, in comparison to the pristine silk sample, the ruptured silk still shows a 50 % increase in saturation magnetization. Moreover, comparing the paramagnetic behavior of the silk in three cases observed at 10 K, we can see that ruptured silk has the highest paramagnetic susceptibility χ_p ; indicating that continued stretching increased the number of dangling bonds in silk, but they could not interact due to reason stated above. We also observed an increase in the remnant magnetization of stretched and ruptured silks compared to pristine silk. Tuning of magnetic properties of spider silk by mechanical stretching confirmed silk's magneto-structural relationship while ruling out any other possible origin of its magnetism.

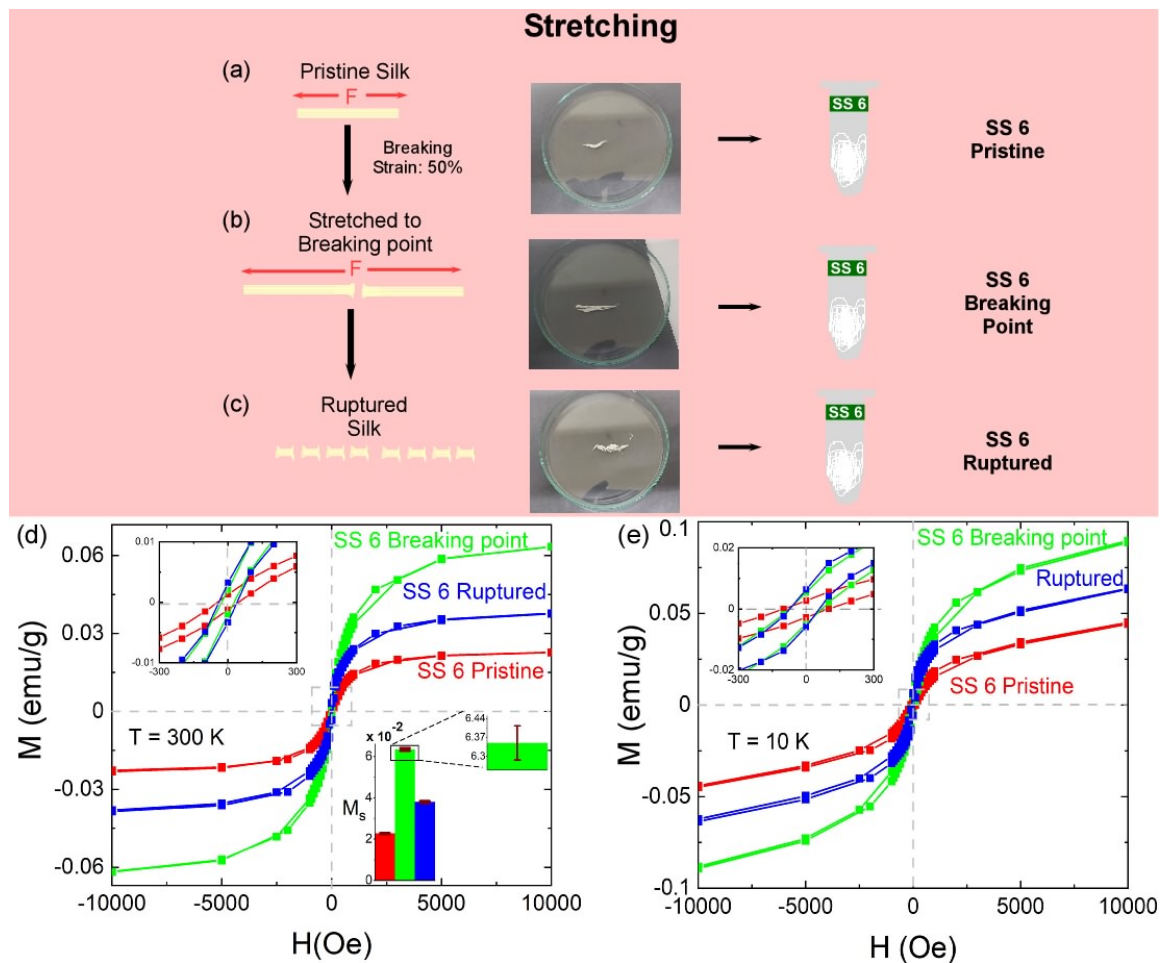


Figure 3.9: **Magnetometry with pristine and tensile ruptured silk.** Procedure of a series of experiments performed by stretching the silk is depicted along with the photographs of the actual silk sample. (a) shows the silk in its pristine form before stretching. This silk was stretched to its breaking point (at a strain of 50%), shown in (b). Later the same silk was ruptured into multiple small pieces by further stretching shown in (c). (d) Magnetometry data of the above three cases ((a) through (c)) at 300 K and 10 K (e). The inset on the left (d) shows a zoom of the data near zero magnetic field to highlight the comparison of M_r and H_c of breaking point, ruptured and pristine silk samples. The inset on the right (d) shows a bar graph to compare the M_s of breaking point, ruptured and pristine silk samples. The error bar highlights that the observed change in M_s is well above the experimental error.

Enhanced magnetization by mechanical cutting

Another method of deforming silk is mechanical cutting, as illustrated in Fig. 3.10. We used clean ceramic scissors to cut the pristine spider dragline silks into small pieces. A ceramic scissors was used to avoid any potential metallic contamination. We cut the silk with an approximate cut density of 110 cuts/cm. The magnetic measurements of this type were performed sequentially in the following manner :

- (i) First, the pristine spider dragline silk was measured at $T=300\text{K}$ and $T=10\text{K}$ (SS7 Pristine).
- (ii) The same sample was cut into multiple pieces, and the cut silk (SS 7 Cut) was measured again.

Upon cutting the silk, its saturation magnetization increases by 10% compared to that of pristine silk, which is above the experimental error. The enhancement is modest in magnitude compared to the previous stretching mechanism because stretching deforms the entire silk and produces defects throughout the silk sample compared to cutting, where defects are formed only where a cut has been made. Moreover, cutting causes minimal shear deformation in β -sheet nanocrystals. The magnetization at 10 K (figure 3.10(d)) shows that the paramagnetic susceptibility of cut spider silk is significantly higher than that of pristine silk, meaning cutting increased the number of dangling bonds in silk. Nevertheless, the results again provide conclusive evidence that the magnetic properties of silk are directly related to silk's structure and atomic defects within.

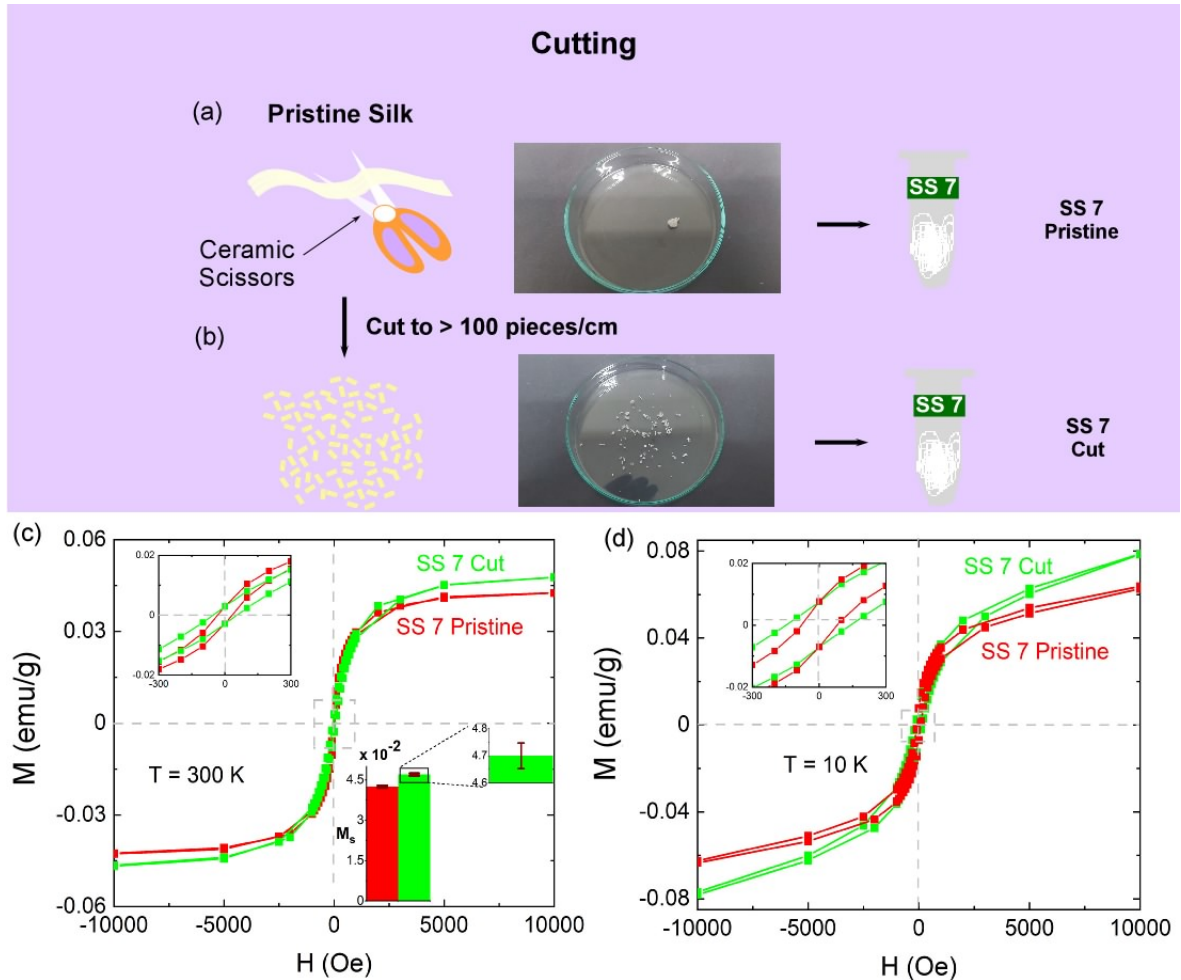


Figure 3.10: **Magnetometry with pristine and cut silk.** Procedure of a series of experiments performed by cutting silk is depicted along with photographs of the actual silk sample. (a) shows the silk in its pristine form before cutting. This silk was cut to over 100 pieces/cm using ceramic scissors, as shown in (b). (c) Magnetometry data of the above two cases ((a) and (b)) at 300 K and at 10 K (d). The inset on the left (c) shows a zoom of the data near zero magnetic field to highlight the comparison of M_r and H_c of cut and pristine silk samples. The inset on the right (c) shows a bar graph to compare the M_s of cut and pristine silk samples. The error bar highlights that the observed change in M_s is well above the experimental error.

3.4.3 Electron Paramagnetic Resonance (EPR)

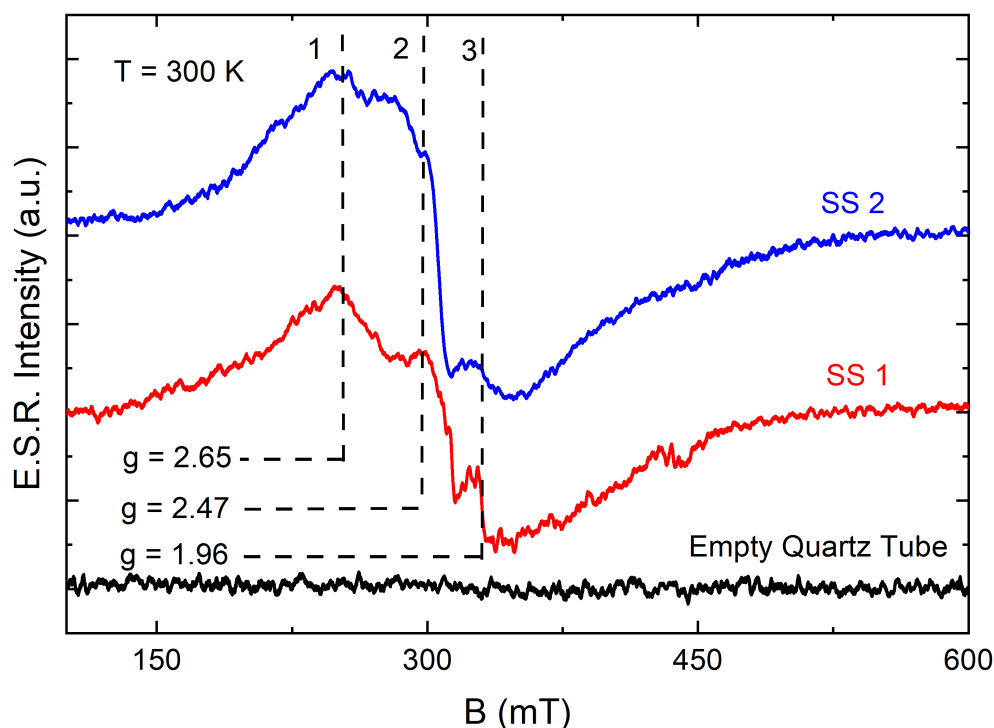


Figure 3.11: **EPR signals at room temperatures.** ESR spectra of silk show the presence of free radicals (marked with 3) and ferromagnetically coupled clusters of radicals (marked with 1 and 2). The results of all silk samples are consistent, implying that magnetism originates from the repeating core of spider silks and is an intrinsic property of these materials, not because of some external factor. EPR spectrum of empty quartz tube is also shown as a reference to show no background signal from impurities exists.

In order to understand the nature of unpaired electrons leading to ferromagnetism in spider silks, electron spin resonance (ESR) spectroscopy was carried out. ESR spectroscopy was performed using JEOL FA 2000 ESR machine. The microwave frequency used for room temperature ESR spectroscopy was 9.44 GHz (X-band), and the power was kept at 0.3 mW. The modulation amplitude was 10 G, and the modulation frequency was 100 kHz. The same silk samples were used for ESR spectroscopy and magnetometry. We detected the presence of stable radicals in pristine silk, which were previously unknown for spider dragline silks. The samples showed very complex spectra with absorption occurring around $g = 2$ shown in figure 3.11 at room temperature. Besides the expected $g \approx 2$ for free radicals (3 in fig. 3.11), we can see other broad and asymmetric resonance lines with $g \geq 2$ (1 and 2 in fig. 3.11). These broad resonance lines are a result of exchange interaction among radicals. Ferromagnetic interactions cause a shift in silk's g -values. Figure 3.11 shows that results are reproducible in multiple samples of spider dragline silks. These

spectra reconfirm the presence of free and ferromagnetically interacting radicals in silk's structure. Coexistence of a variety of persistent radical species having $g = 1.96$, $g = 2.47$, and $g = 2.65$ was observed. The resonance line with $g = 1.96$ corresponds to free radicals, while the broader lines with $g = 2.47$ and 2.65 indicate a cluster of interacting spins. The slight shift in the g value of free radicals ($g = 1.96$) from tradition 2.0023 results from the strong anisotropic structure of spider silk [40]. In summary, ESR disclosed that several independent and interacting radical species exist in spider silks. These results agree with our observation of MH characteristics at room and low temperatures (section 3.2). The high stability of these carbon radicals is a consequence of the significant steric hindrance of hierarchical silk structure [124]. We observed persistent radicals of silk even at high temperatures of 100°C . When residing in localized orthogonal orbitals that share the same spatial region, radicals couple ferromagnetically (see chapter 1). In amorphous structures like spider silk, one can expect the coexistence of ferromagnetic, anti-ferromagnetic, paramagnetic, and spin glass orders [83, 84]. Thermomagnetic analysis to unravel the magnetic ordering of spider dragline silks will be discussed in following section. Furthermore, we can again confirm that no signals corresponding to $g = 3.3$ were observed in our samples even at low temperatures of (-150°C), which is a characteristic signature of Fe^{3+} ions [125, 126]. Hence, we can again confirm iron impurities' absence (or negligible presence) in our samples. This observation allowed us to build magnetic models of silk where various radicals can interact ferromagnetically or antiferromagnetically based on their position (host atom), and configuration (distance from other radicals) [127].

3.5 Magnetic Ordering in Spider Dragline Silks

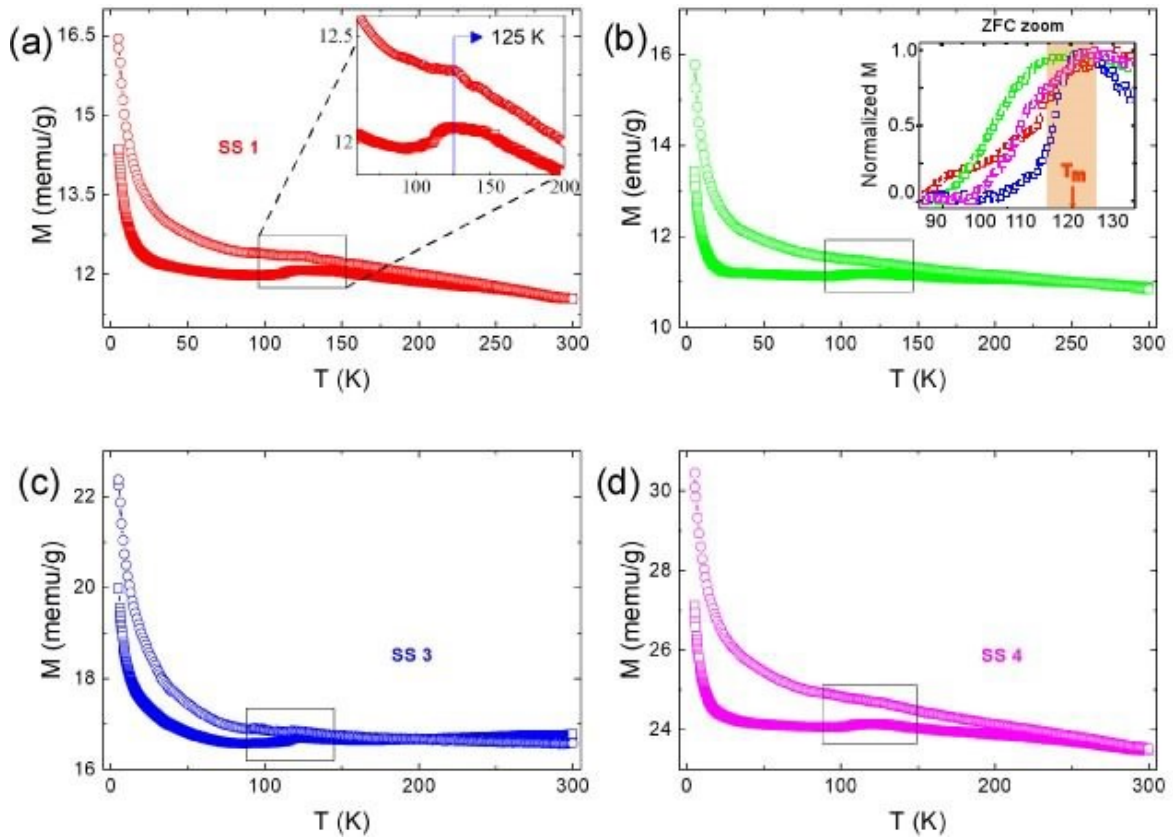


Figure 3.12: **FC-ZFC DC magnetization of four samples SS1-SS4.** (a-d): The FC data was taken at 1 kOe field. Oxygen background has been subtracted from all samples (Appendix C). We can see that the magnetic transition near 120 K is consistent for all silk samples (highlighted by a box in each graph). The inset of graph (a) shows the magnetic transition near 120 K in FC and ZFC data. Inset of graph (b) compares the normalized ZFC data of all silk samples (differentiated by color) to show that the magnetic phase transition consistently occur around 120 K in all samples. A slight crossover between FC-ZFC curves of sample SS 3 (near 200K) is probably due to an offset in the positioning of the sample.

Through a thorough investigation, we established that the magnetism of spider silks originates from atomic defects in their structure. However, from our MH and EPR results, it is clear that non-interacting radical spins coexist with ferromagnetically interacting radicals in silk samples. Therefore, it is essential to understand the exact nature of magnetic ordering of spider dragline silk samples.

To unravel the magnetic ordering of spider dragline silk, we did a thermomagnetic analysis on spider silk samples, where silk's magnetization was measured at a constant magnetic field with respect to temperature (MT characteristics). The same SQUID magnetometer

(section 3.3) was used to analyze spider dragline silk samples' MT behavior. Furthermore, as mentioned previously, we used the same samples for this experiment. The experiments were performed at a constant magnetic field of 1000 Oe. The temperature range set for the experiment was from 5 K - 300 K. As mentioned in section 3.3, performing experiments at higher temperatures can lead to the denaturation of silk samples. Thus the maximum temperature for experimentation was limited to 300 K. Both zero field cooled (ZFC) and field cooled (FC) responses were taken. The results of our thermomagnetic characterization are provided in figure 3.12.

Before we start the analysis, one must understand that due to the fibrous nature of the samples, when we compress the silk sample into a ball of diameter ≤ 3 mm, some air is trapped in these samples. When the temperature of silk during the MT experiment reaches below 90 K, oxygen gas (from air) trapped in these samples starts undergoing several phase transitions. These weak magnetic transitions (see Appendix B) are of a similar order of magnitude as our silk and therefore interfere with our magnetization data, especially the para-AFM transition of solid oxygen occurring at 60 K. Therefore, one must isolate silk's magnetic behavior from that of oxygen. We systematically prepared oxygen-free silk samples (by siphoning the ambient air from silk bundles and storing them in argon environment) for the SQUID magnetometry to obtain the magnetic signals from the pristine silk only, particularly at low temperatures. The details of this sample preparation are given in Appendix C. The procedure of removing oxygen's magnetization data from spider silk's data at low temperature is also given in Appendix C.

Having established this, one can see that the MT characteristics of all silk samples are similar in nature. Going from 300 K to 5 K (right to the left), we see that ZFC and FC curves diverge near room temperature (290 K to 300 K). Such a divergence in magnetization is a clear signature of a spin-glass ordering unless there is a strong magnetic anisotropy [84]. On further cooling, we can see another re-entrant transition occurring at around temperature $T = 120 \pm 5$ K, highlighted in the graphs in fig. 3.12 (a-d) using a rectangular box. Such re-entrant transition is reminiscent of spin cluster-glass order (chapter 1). It shows a crossover from ferromagnetic to asperomagnetic ordering (see fig. 1.9 for reference) as, on further freezing the sample, the transverse components of the spin are frozen in random directions, and only the longitudinal component shows ferromagnetic interaction. Thus there is a slight decrease in net magnetization. Remarkably, all independent silk samples show similar MT characteristics despite belonging to different spiders and being prepared at different times. This indicates that observed magnetic ordering is a universal character of spider dragline silks.

Below 40 K, we can see that paramagnetism due to non-interacting, isolated radicals in silk starts dominating the magnetization data. This can be understood since the magnetic

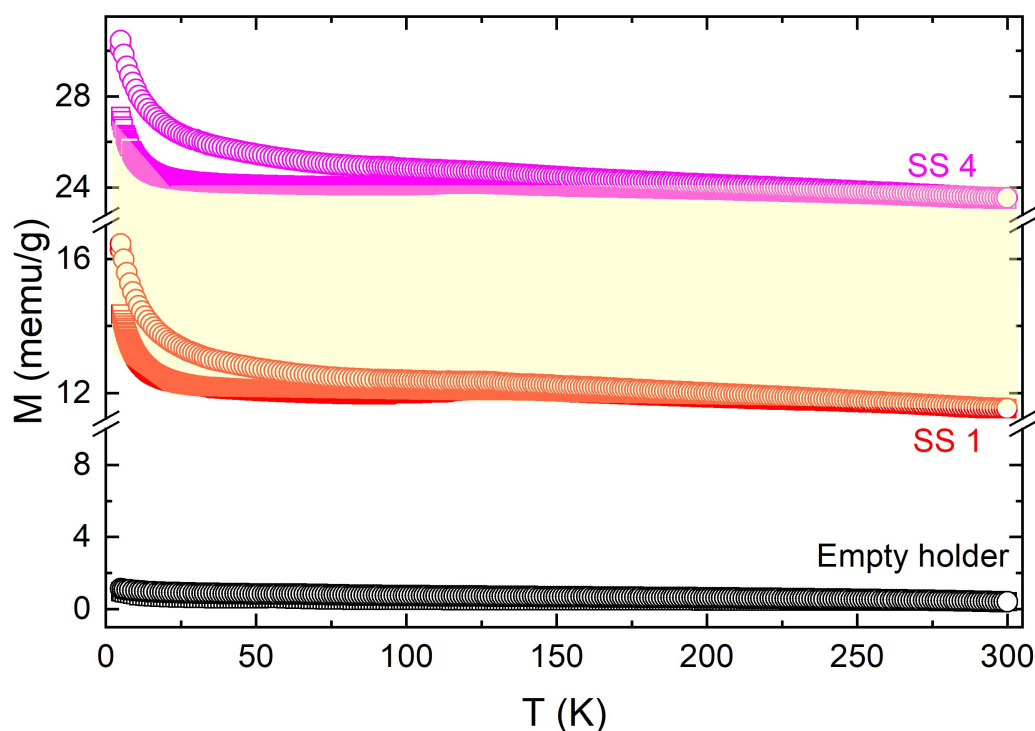


Figure 3.13: **Comparison of MT data between empty tube background and silk.** The MT data of background in the absence of spider silk (black) show negligible magnetization for ZFC and FC with an applied magnetic field of 1000 Oe. Even at low temperatures, < 40 K, empty tube magnetization data is negligible compared to spider silk, thus confirming the presence of non-interacting spins in silks. The yellow color band in silk data shows the variability across all four pristine silk samples. The silk data shown here is corrected by subtracting the oxygen background from them using the procedure explained in appendix C. There was no oxygen signature in an empty tube.

moment of paramagnets is inversely proportional to temperature ($M \propto \frac{1}{T}$). This is another confirmation of the presence of stable free radicals in silk in addition to EPR and MH (at 10 K) data (sections 3.4.3 and 3.3). However, to ensure that these are the paramagnetic signature of spider silk and not because of impurities from the background, we compared the MT results obtained from silk data to MT data of quartz holder and Teflon without the silk samples present in them (fig. 3.13).

Spider silk comprises amorphous helical protein structures with small amounts of nanocrystalline beta pleated sheets embedded in them (Fig. 1.13). The same is reflected in the combined results of M-H and M-T analysis, which suggests that spider silk behaves as an amorphous magnet with spins trapped in the glassy state in a protein matrix. Our thermomagnetic analysis establishes that spider silk exhibits spin-glass (or spin cluster glass) magnetic order. Random trapping of radicals in an amorphous protein matrix brings out the coexistence of a variety of magnetic orders in silk structure, such as ferromagnetism ($J > 0$),

antiferromagnetism ($J < 0$), and paramagnetism ($J = 0$). All results were reproducible in all silk samples with minimal variations.

3.6 Representation of Magnetic spins in Spider Dragline Silks

From our detailed experiments to understand the origin of magnetism in pristine spider dragline silks, it is clear that the source of magnetism cannot be linked to usual ferromagnetic d-block elements like iron, cobalt, nickel, etc. In fact, one can tune their magnetism by deforming the silk (by stretching and cutting) and increasing the number of defects in spider dragline silks. We concluded that the source of magnetism is indeed the persistent radicals generated in silk's structure due to atomic defects in its structure. These defects arise during the silk spinning process undertaken by a spider. Spider pulls its silk rapidly while it undergoes liquid to solid phase transition, leading to several microscopic defects. The presence of such microvoids and defects has been discussed in literature [121, 128]. From our magnetic studies, we found that spider silk consists of interacting as well as non-interacting magnetic spins. The interacting spins form a cluster glass-like magnetic ordering in spider dragline silks. As suggested by our experimental results, a brief magnetic picture of spider dragline silks is depicted in fig. 3.14.

The high stability (or persistence) of radicals formed in spider silks is astonishing. Radicals are volatile species and tend to form bonds very quickly to stabilize their atomic energies and are, therefore, highly reactive species. The stability of radicals is attributed to the remarkable secondary structure of anti-parallel β -sheets formed by a highly conserved sequence of polyalanine (A_n) and poly-glycine-alanine (GA_n) motifs (see section 1.2.1) in silk proteins. These beta-sheets form highly rigid, dense, and compact crystallite structures of nanometer dimensions. The dimensions of these crystallites are optimized to provide maximum shear strength to sustain high tensile loads, and thus the superior mechanical properties of spider silk [49]. The radicals formed on these β -sheet crystallites are compactly packed and protected sterically; thus, they can remain stable in the room and at high temperatures. Moreover, the constraint structure of β -turns made of GPGGX motifs can also result in stable radicals in spider dragline silks.

Computationally, it was found by the theoreticians in our group that small number of radicals created in beta sheets do not affect their mechanical stiffness. The formation energy of defected β -sheets when radicals are formed on the side chains of $((GA)_n)$ motifs [127] is slightly more than perfect ones. We, therefore, predict that radicals formed on β -sheets of spider dragline silks are the prominent source of its magnetism. On stretch-

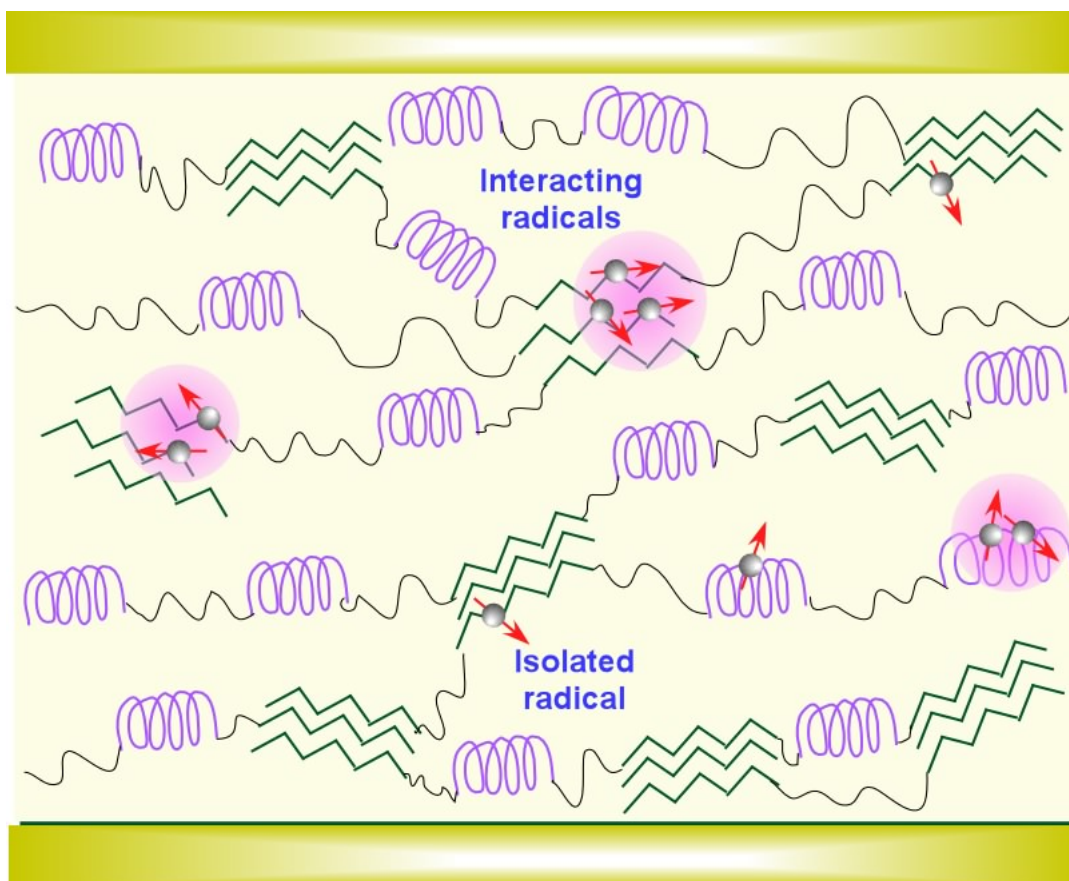


Figure 3.14: **Magnetic representation of spider dragline silks.** Based on our experimental results, we expect a magnetic model of silks as described in this figure. Free (isolated) and interacting radical spins (shown in pink bubble) formed due to atomistic defects in silk coexist. β -turns and 3_{10} helices structures are represented by helices (purple) for simplicity. β -sheets are depicted as two-dimensional planes (green) for brevity. A thorough theoretical modeling of silk structure is required to understand the molecular origin of magnetism in spider dragline silks.

ing silks, β -sheets undergo a slip-stick motion causing shear stress in their structure. This shear stress leads to displacement and rotation of amino acid chains forming the β -sheet, i.e. $((GA)_n$ and A_n motifs), thereby reorienting these sheets by breaking and reforming hydrogen bonds while maintaining the structural integrity of β sheets. Reorientation of radicals changes in their relative distances and conformation angles, affecting their ground state magnetic interactions (exchange constant, J). Hence, one can tune silk's magnetic properties by controlling the strain and stress applied to it. However, a further theoretical investigation is required to give a robust model of silk explaining its magnetic character.

3.7 New Potential Applications of Spider Dragline Silks

We have discussed a wide variety of applications of silk in section 1.2.2, owing to their extraordinary properties. Now that we have discovered the magnetic properties of spider silks, we can add a few more potential applications of spider dragline silks to the list.

3.7.1 Spider Dragline Silk as a Bio-Magnetosensor

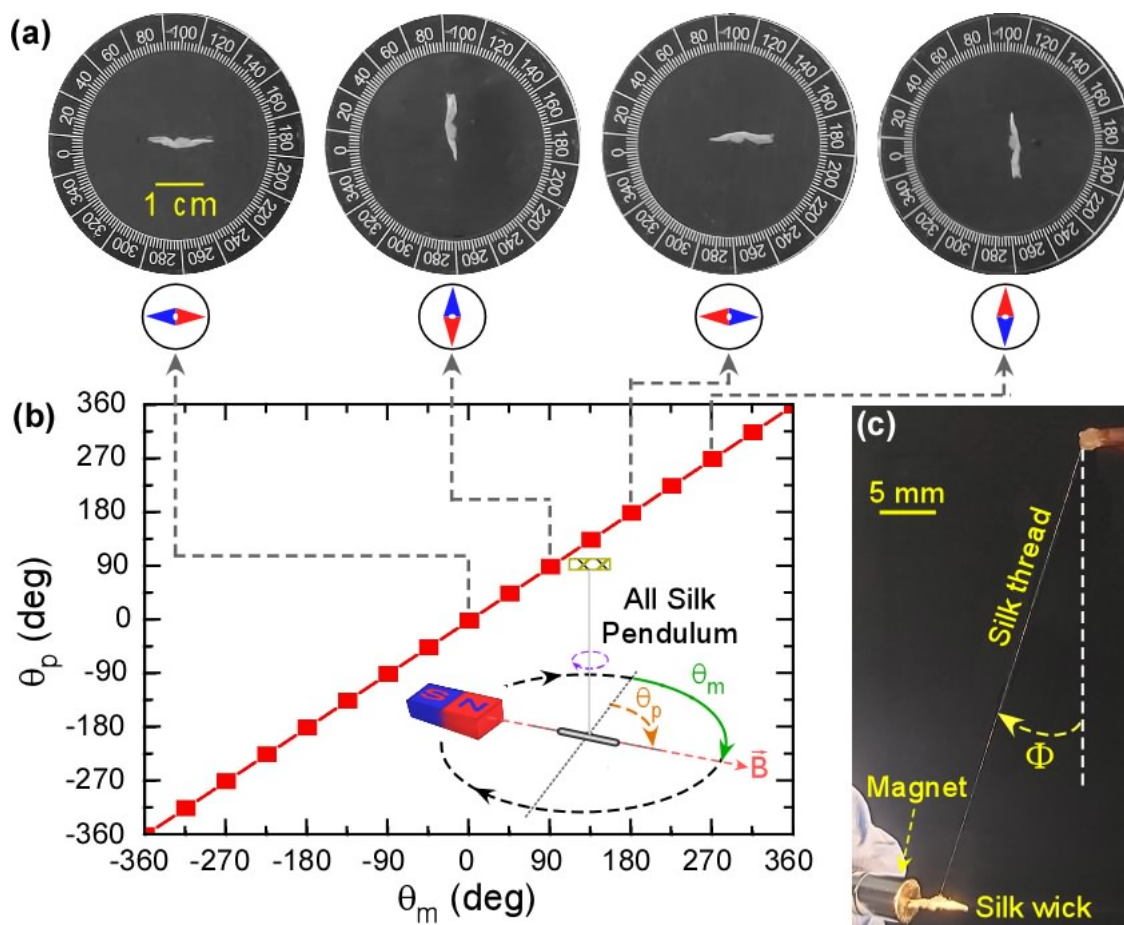


Figure 3.15: **Silk Bio-Magnetosensor.** (a) Snapshots showing synchronous rotation of a silk-wick (top-view) when the torsion silk compass is subjected to rotating B field (instantaneous direction of the magnetic field is indicated using compass needle (red and blue)). (b) Angle of silk (θ_p) vs angle of magnetic field (θ_m) for $B = 30$ mT. Error bars are within the size of squares. Inset: schematic of the setup. (c) Permanent attachment of the silk wick to an approaching magnet.

Besides understanding the magnetic properties of the silk, we wondered if this magnetic property of silk can be exploited for functional purposes. To this end, we designed experiments with an all-silk pendulum. We built an all-silk torsion pendulum where a single

spider dragline silk ($L = 10 \text{ cm}$) holds a freely suspended silk wick (mass $\approx 100 \mu\text{g}$). The torsion pendulum was enclosed in a glass container to protect it from environmental noise and the surrounding air. This torsion pendulum is a very sensitive sensor due to the thin dragline silk thread ($d \approx 1 \mu\text{m}$) to which the silk wick is tied. As soon as one brings a permanent magnet near the silk thread, the silk wick gets stuck to it. This is shown in figure 3.15(c), where a magnet could pull the wick sideways when it was brought too close, confirming its ferromagnetic character.

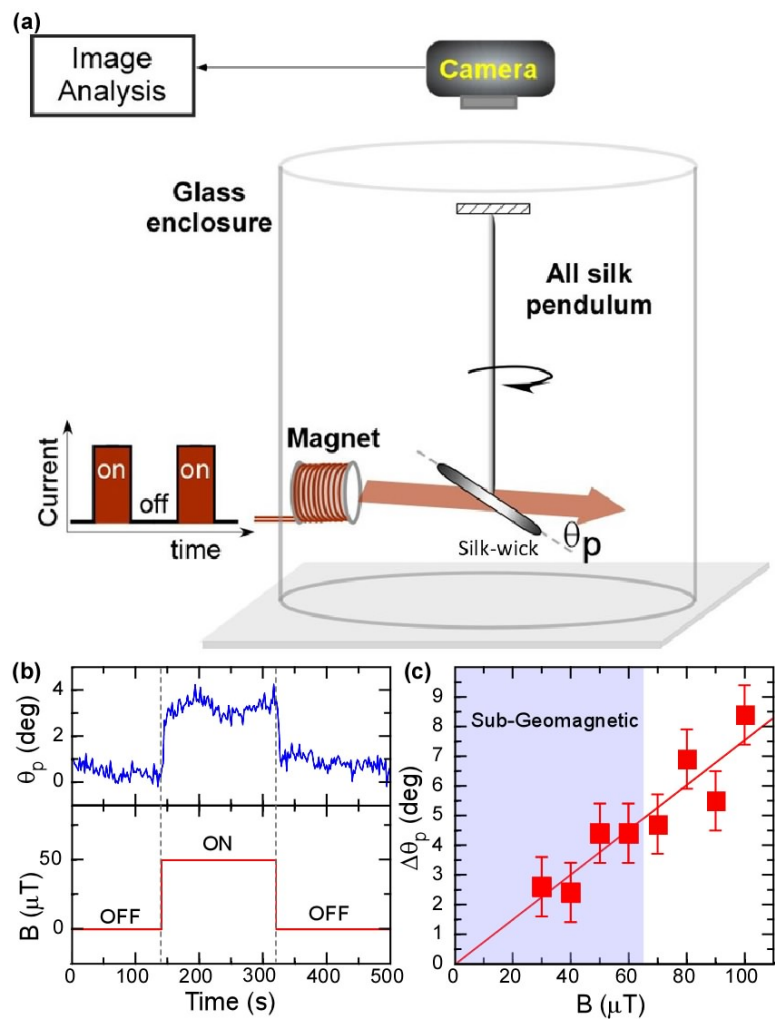


Figure 3.16: **Geomagnetic sensitivity of Silk Bio-Magnetosensor.** (a): The Earth-scale magnetic field is produced by an electromagnet powered by an on-off modulated current. The field is measured at the position of the silk wick. The change in the angular position of silk wick is captured by a camera and analyzed with an imaging software frame-by-frame. The all-silk pendulum is enclosed in a glass chamber to prevent air-flow noise. The anchor of the all-silk pendulum is electrically grounded to avoid any stray electrostatic effects. (b): θ_p vs. time for $50 \mu\text{T}$ on-off field, (c): Sub-geomagnetic responsivity of silk compass. Error bars denote angular fluctuation in the steady state.

We fixed a neodymium magnet on a rotation stage, which can be controlled electronically to move in either a clockwise or anti-clockwise direction. This magnet (fixed on the stage) was brought near the silk pendulum. When the silk-wick was subjected to a slowly rotating magnetic field (30 mT), its angular position synchronously followed the rotation of the field in clockwise and counter-clockwise directions maintaining permanent alignment, as shown in Fig. 3.15(a)-(b). We also recorded a video of this experiment available for demonstration (Video-1_Silk_pendulum_bio-magnetosensor). This experiment showed that silk could detect the presence and direction of the magnetic field in its environment.

However, given the sensitivity of this pendulum, we pondered that silk must be able to detect magnetic fields of much lower values than that subjected by the permanent magnet. Can silk sense magnetic fields equivalent to geomagnetic magnitude? To check the sensitivity limit of the silk bio-magnetosensor, we built a similar setup shown in figure 3.16(a). We made a small copper coil to generate a magnetic field of very small magnitudes, and a constant current supply was used to power it. The generated magnetic field by the coil was calibrated to the applied current using a sensitive magnetometer with an accuracy of $\pm 2 \mu\text{T}$.

The all silk torsion pendulum discussed above was periodically excited by applying magnetic fields down to geomagnetic magnitudes. Strikingly, when the pendulum was subjected to an (on-off) modulation of the magnetic field, a few degrees deflection of silk-wick was observed down to $B \sim 30 \mu\text{T}$ amplitude (Fig. 3.16(b,c)). This is the first demonstration of the sub-geomagnetic responsivity of silk thread. The deflection of the pendulum was captured using a camera. The video analysis using tracking software provided an accuracy of $\pm 1^\circ$.

3.7.2 Silk based Bio-Magbots

Magnetically activated micro and nano swimmers (also called Magbots) in liquid environments have gained much interest in recent years [116, 115, 20, 129]. These "Magbots" have potential applications in targeted drug/gene delivery, cell manipulation, minimally invasive surgery, biopsy, biofilm disruption/eradication, imaging-guided delivery/therapy/surgery, pollution removal for environmental remediation, and (bio)sensing. Most of these robots are made of inorganic magnetic materials like iron and cobalt. Hence, a major challenge these micro and nano swimmers face is the biocompatibility and biodegradability inside the body for biomedical applications.

In such a scenario, spider silk offers a great alternative. As we have discussed, silk is non-toxic and biocompatible in nature [29, 23]. Moreover, its biodegradability can be controlled [130]. In this section, we demonstrate the application of silk-based magnetic micro-robots in a liquid environment. We built millimeter-sized silk swimmers and floated

them in water. These miniature silk swimmers can be remotely maneuvered (driving, rotation, magnetic trapping/ clustering) in a liquid environment using a magnetic field as low as 20 mT. Such small fields can be easily generated and spatiotemporally controlled with existing MRI and CT scan technologies. We further demonstrated the applications of silk-based microbots in drug delivery, cell manipulation, non-invasive surgery, and bioremediation by transporting a variety of organic materials like plant tissues (onion skin and leaf), animal tissues (human skin), polymers (hair), and immiscible liquids (toluene) across the water surface. Silk-based micro swimmers present a non-toxic, biocompatible, and biodegradable alternative to other micro/nano magnetic robots. They do not need to be extracted from the body after their injection owing to their anti-inflammatory properties, hence providing a significant advancement in biomedical engineering.

Magnetically maneuvering miniaturized silk magbots in liquid environment

We extracted pure dragline silks from multiple spiders and cut them into small 2 mm structures to show a proof of concept of silk-based biological magnetic robots. Such structures could easily float in water and can be manipulated using small magnetic fields. Thus acting as miniaturized magnetic robots.

We show the results of a series of experiments designed to extract work from silk robots on the water for the following maneuvers:

1 Magnetically assisted driving of spider silk swimmers

Magnetic Driving of miniaturized silk swimmers

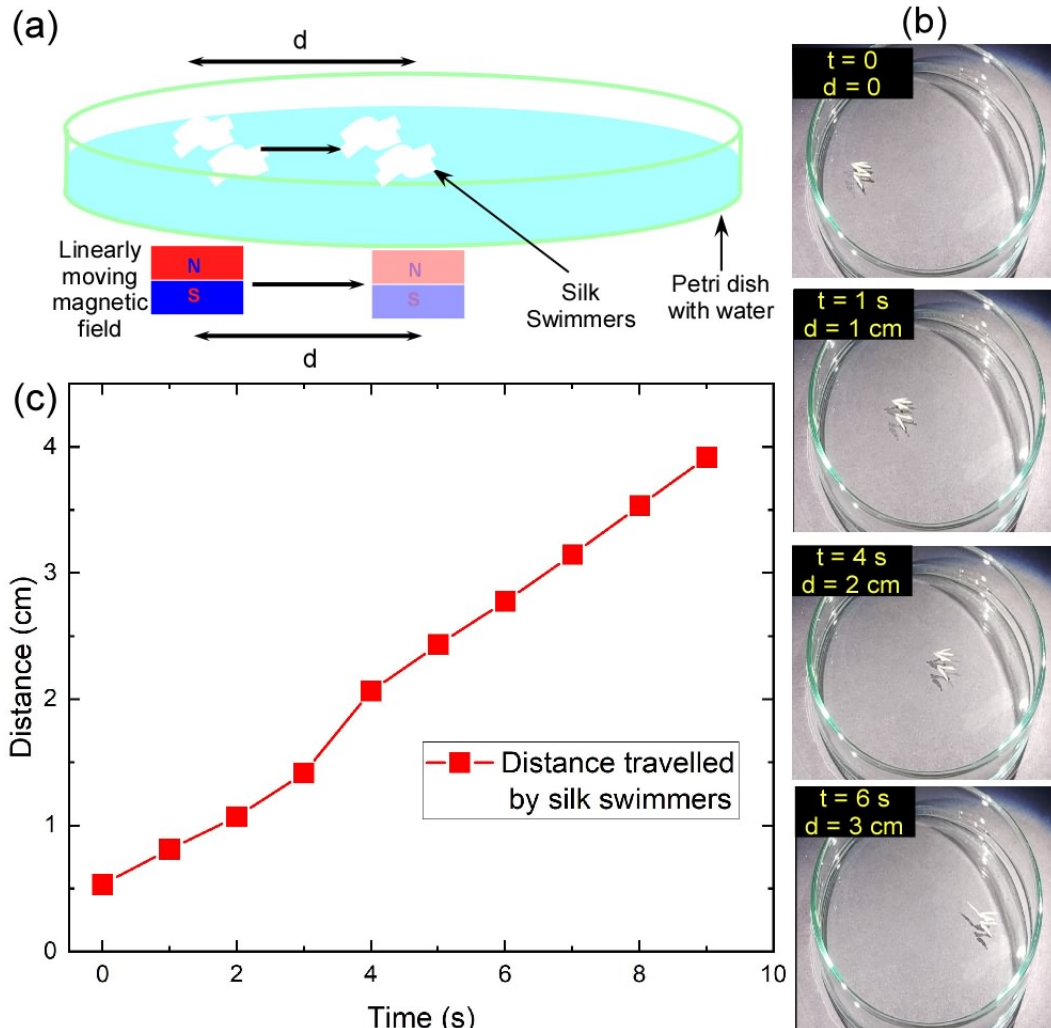


Figure 3.17: **Magnetic driving of silk swimmers.** (a) Schematic of the setup used to show magnetically assisted driving of miniaturized silk swimmers in de-ionized water. The swimmers can be driven on the surface of the water in any suitable manner by controlling the magnetic field produced by the magnet kept below the petri dish. (b) The snapshots of supplementary video 2 (Video-2_Magnetic_Driving) demonstrate this phenomenon. We can see that bunched-up silk swimmers are being driven from the left side of the petri dish to its right side under the influence of a magnetic field of 35 mT. (c) Distance vs. time graph of silk swimmers extracted from Video-2_Magnetic_Driving.

To estimate the force generated by the magnet on the silk swimmers, we performed an experiment where the silk swimmers were kept in the magnetic field gradient of a fixed magnet. A schematic of the setup used to estimate the force experienced by

miniaturized silk swimmers in de-ionized water under the magnetic field gradient generated by a stationary magnet is shown in Fig. 3.18(a). The swimmers get pulled from a place with a low magnetic field to a place with the highest magnetic field, as illustrated. While swimming, they experience a viscous drag of the liquid. Therefore, the net force on the swimmers will be given by:

$$\frac{d(\mu \cdot \vec{B})}{dx} - F_{drag}^{\vec{}} = m \cdot \vec{a}_x \quad (3.1)$$

Here μ is the magnetic moment, \vec{B} is the magnetic field, m is the mass of the silk swimmers, and \vec{a} corresponds to acceleration.

The applied magnetic field was measured at different distances (x-axis in fig. 3.18(a)) using a magnetometer with an accuracy of 0.01 mT (fig. 3.18 (b)). The typical magnitude of the magnetic field was 10-45 mT. The corresponding magnetic moment of the silk swimmers under this applied magnetic field was estimated from the SQUID magnetization data (Fig. 3.2).

We repeated the experiment by changing the vertical distance (y-axis in fig. 3.18(a)). The field gradient generated by a stationary magnet in our experimental setup with respect to x and y dimensions is depicted in fig. 3.18(b). Our observations reveal that magnet exerts maximum force $\left(\frac{d(\mu \cdot \vec{B})}{dx}\right)$ of ≈ 90 nN in field of 45 mT and a maximum force of ≈ 30 nN in the field of 30 mT (Fig. 3.18(c)). Such forces are strong enough for contactless manipulation and transportation of non-magnetic organic cargo in liquid media [131], as shown in the following section.

Force exerted on miniaturized silk swimmers

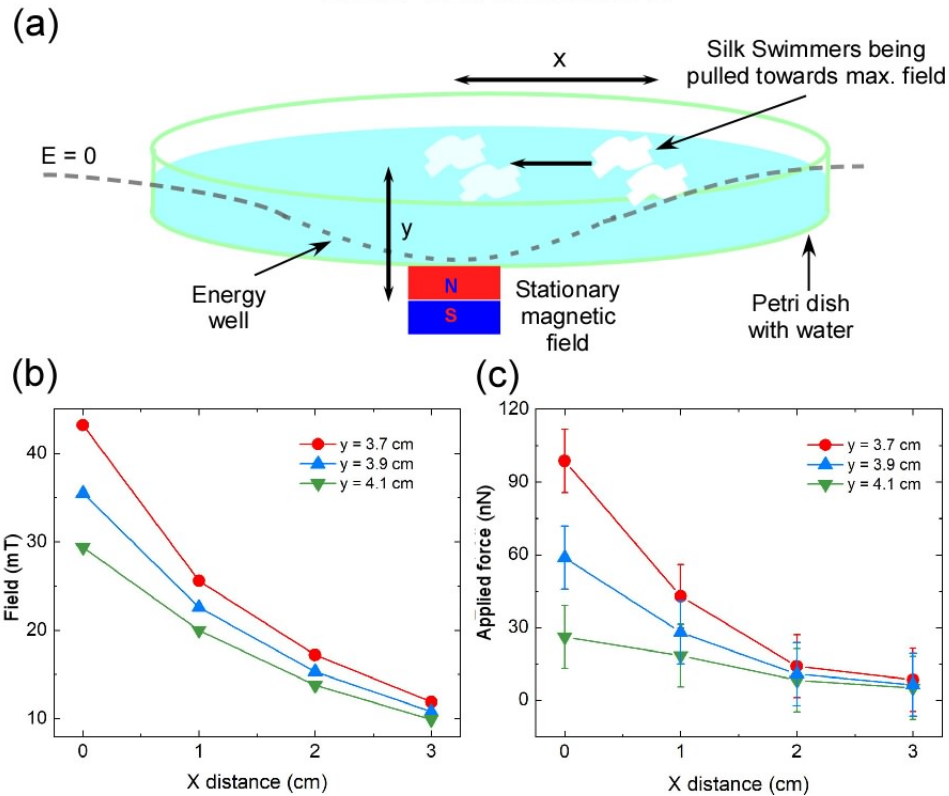


Figure 3.18: **Force exerted on silk swimmers.** (a) Schematic of the setup used to estimate the force experienced by miniaturized silk swimmers in de-ionized water under the magnetic field gradient generated by a stationary magnet. The swimmers get pulled from a place with a low magnetic field to a place with the highest magnetic field, as illustrated. (b) Shows the field gradient generated by a stationary magnet in our experimental setup with respect to x and y dimensions depicted in (a). (c) Shows the applied force experienced by silk swimmers due to strong magnet $\left(\frac{d(\mu \cdot \vec{B})}{dx}\right)$ with respect to their distance from magnet. We can see that magnet exerts a maximum force of 90 nN in a field of 45 mT and a maximum force of 30 nN in a field of 30 mT. As shown in the next section, such forces are strong enough for contactless manipulation and transportation of organic material in liquid media.

2 Magnetically assisted rotation of spider silk swimmers

Magnetic Rotation of miniaturized silk swimmers

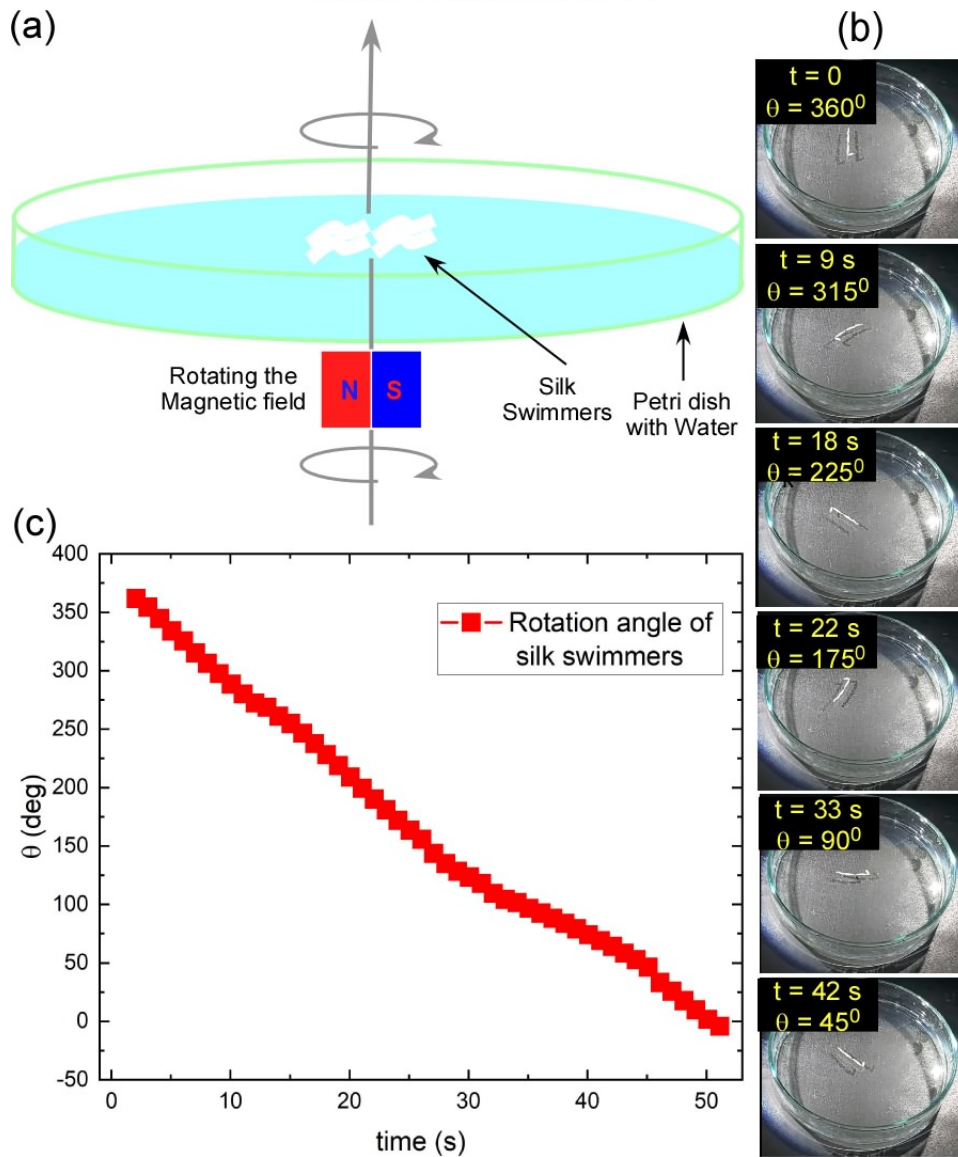


Figure 3.19: **Magnetic rotation of silk swimmers.** (a) Shows the schematic of the setup used to show the magnetically assisted rotation of miniaturized silk swimmers in de-ionized water. The swimmers can be maneuvered in any suitable manner by controlling the magnetic field produced by the magnet kept below the petri dish. (b) The snapshots of supplementary video 3 (Video-3_Magnetic_Rotation) demonstrate this phenomenon. We can see that bunched-up silk swimmers are rotated clockwise and anti-clockwise under a magnetic field of 35 mT. (c) Rotation angle vs. time graph of silk swimmers while being rotated in a clockwise manner in the Video-3_Magnetic_Rotation.

3 Magnetic trapping of spider dragline silk swimmers

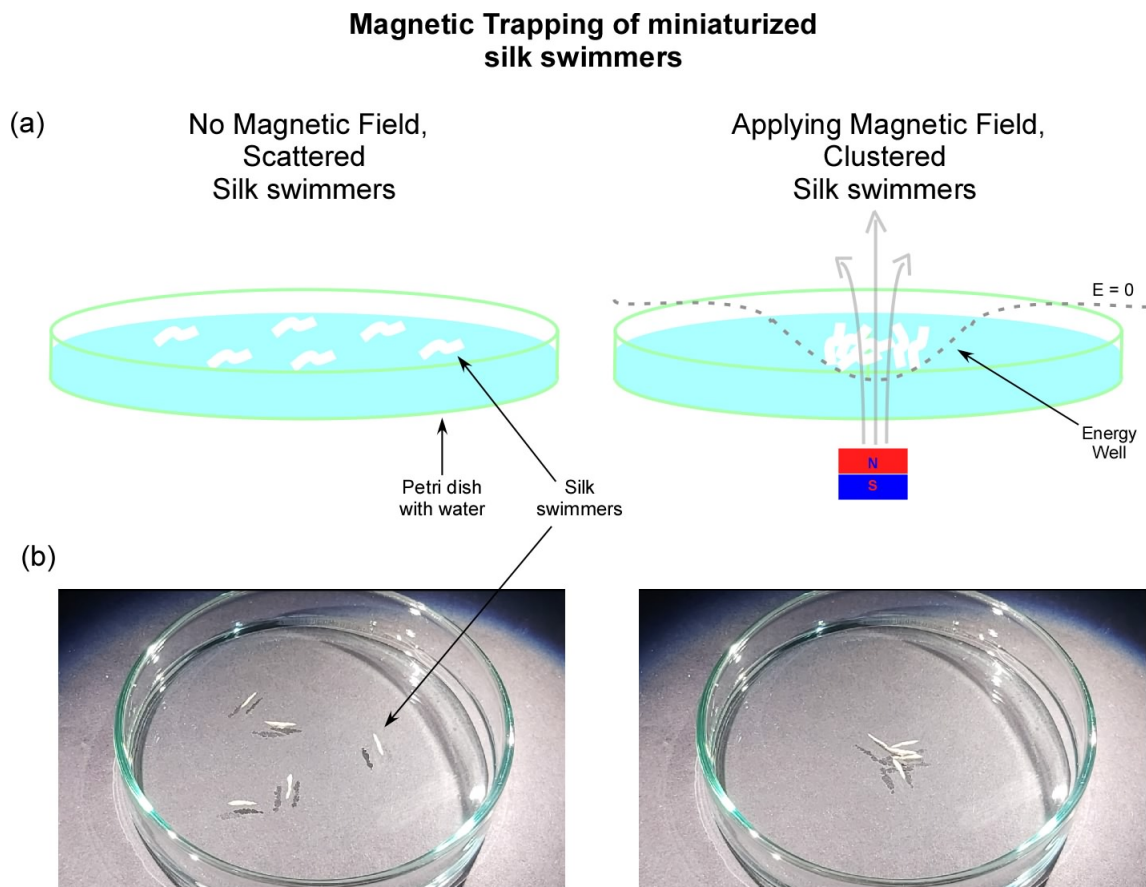


Figure 3.20: **Magnetic trapping of a fleet of silk swimmers.** (a) Shows the schematic of the experiment demonstrating magnetic trapping of silk swimmers at any desired location in de-ionized water with the field of ≈ 35 mT. (b) shows the snapshots of the supplementary video 4 (Video-4_Magnetic_Trapping) showing magnetic trapping of miniaturized silk swimmers. Video also demonstrates that even if we disturb the system by applying external forces (shaking) to scatter the silk swimmers, they return to their trapped location very quickly. This imply that silks can be used as magnetic tweezers for biological materials.

The above three basic maneuvers (magnetic trapping, translatory, and rotatory motion) open several ways these silk-based swimmers can find applications in biomedical engineering and technology. These are also one of the first demonstrations of pure silk-based magbots and tweezers that can be controlled entirely using small magnetic fields [132, 131, 115, 116, 20]. The following section shows some practical applications of these silk robots.

Cargo transport by a cooperative fleet of magnetic silk swimmers

In the previous section, we established that silk-based miniaturized robots could be externally controlled and maneuvered to perform specific primary tasks. This section shows how these basic tasks can help transport organic materials like animal and plant tissues, polymers, and immiscible liquids in a cell-like liquid environment (figs. 3.21-3.26). We show that organic materials do not interact with magnetic fields. However, with the help of silks, we can easily maneuver these materials in liquid environments. These demonstrations help us establish the use of silk robots in drug delivery, cell manipulation, non-invasive surgery, research, and bioremediation. In our experiments, we used silk swimmers of combined mass 4.9 mg under magnetic field ≈ 35 mT, with an average push/pull force of tens of nN on the cargo materials.

Silk swimmers assisting transport of a leaf

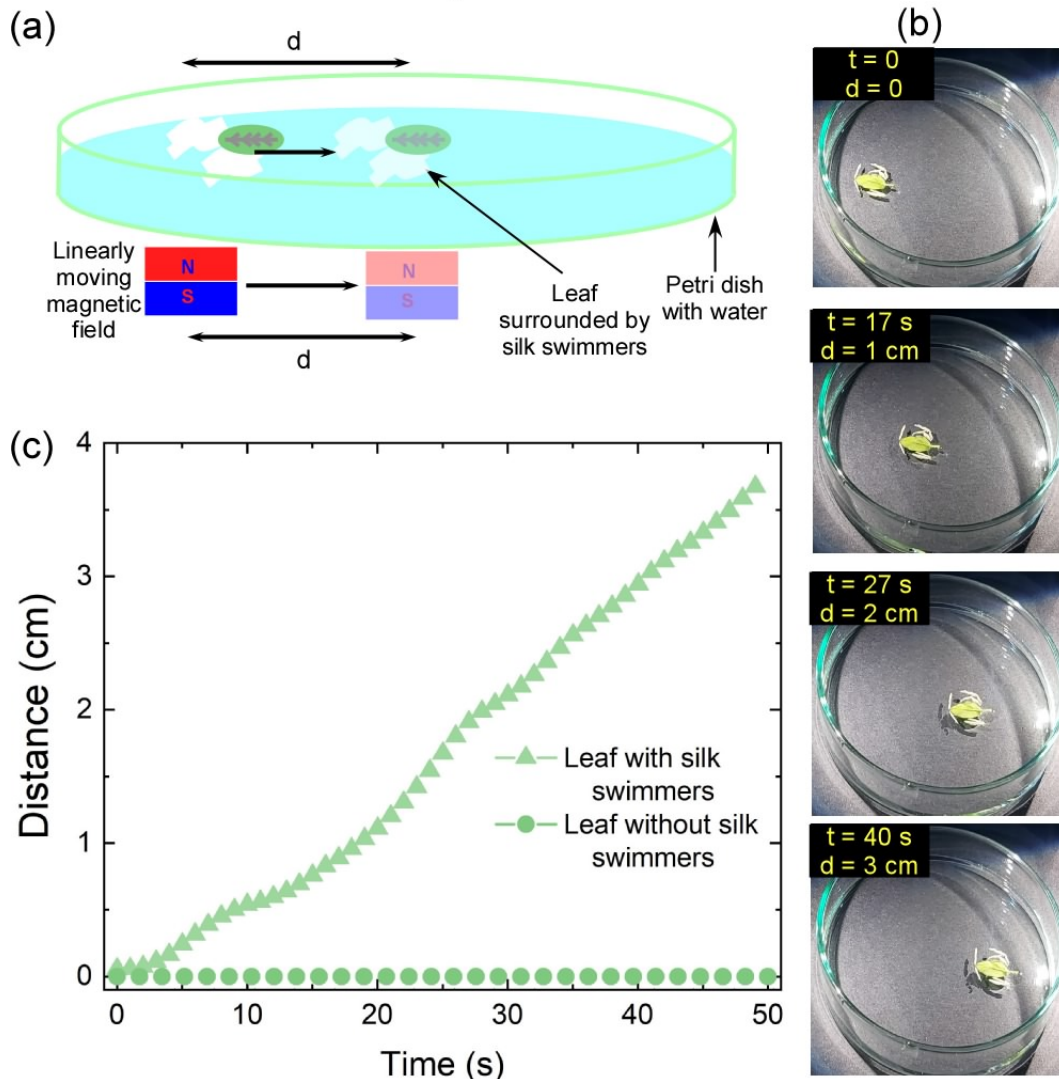


Figure 3.21: **Magnetic transport of cargo leaf using silk swimmers.** (a) Schematic of the experiment showing magnetic transport of cargo leaf using silk swimmers. Tiny silk magnets (magnetic robots) surround a leaf and help in its transportation from one end of petri dish to another end under the influence of magnetic field (b) Snapshots of the supplementary video 5 (Video-5_Leaf_Transport) demonstrating this magnetic transport phenomenon. (c) Distance vs. time graph showing silk-assisted transport of leaf obtained from the Video-5_Leaf_Transport. No displacement of the leaf was possible in the magnetic field without the silk.

Silk swimmers assisting transport of an onion peel

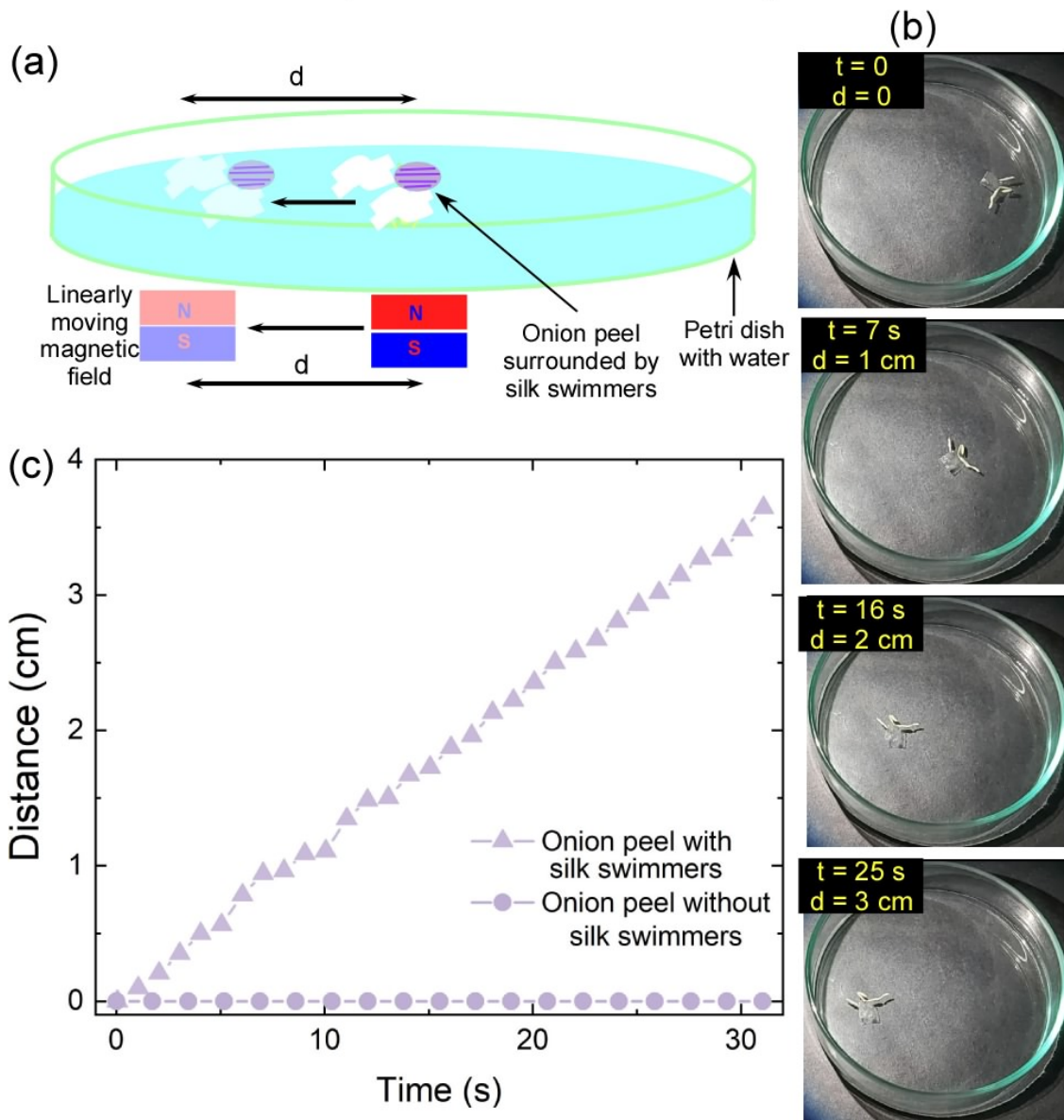


Figure 3.22: **Magnetic transport of onion peel using silk swimmers.** (a) Schematic of the experiment showing magnetic transport of onion peel using silk swimmers. Tiny silk magbots (magnetic robots) surround an onion peel and help in its transportation from one end of petri dish to another end under the influence of magnetic field (b) The snapshots of the supplementary video 6 (Video-6_Onion_peel_Transport) demonstrate this phenomenon. (c) Distance vs. time graph showing silk-assisted transport of onion peel obtained from Video-6_Onion_peel_Transport. Without silk swimmers, the onion peel could not be magnetically transported.

Silk swimmers assisting transport of human skin

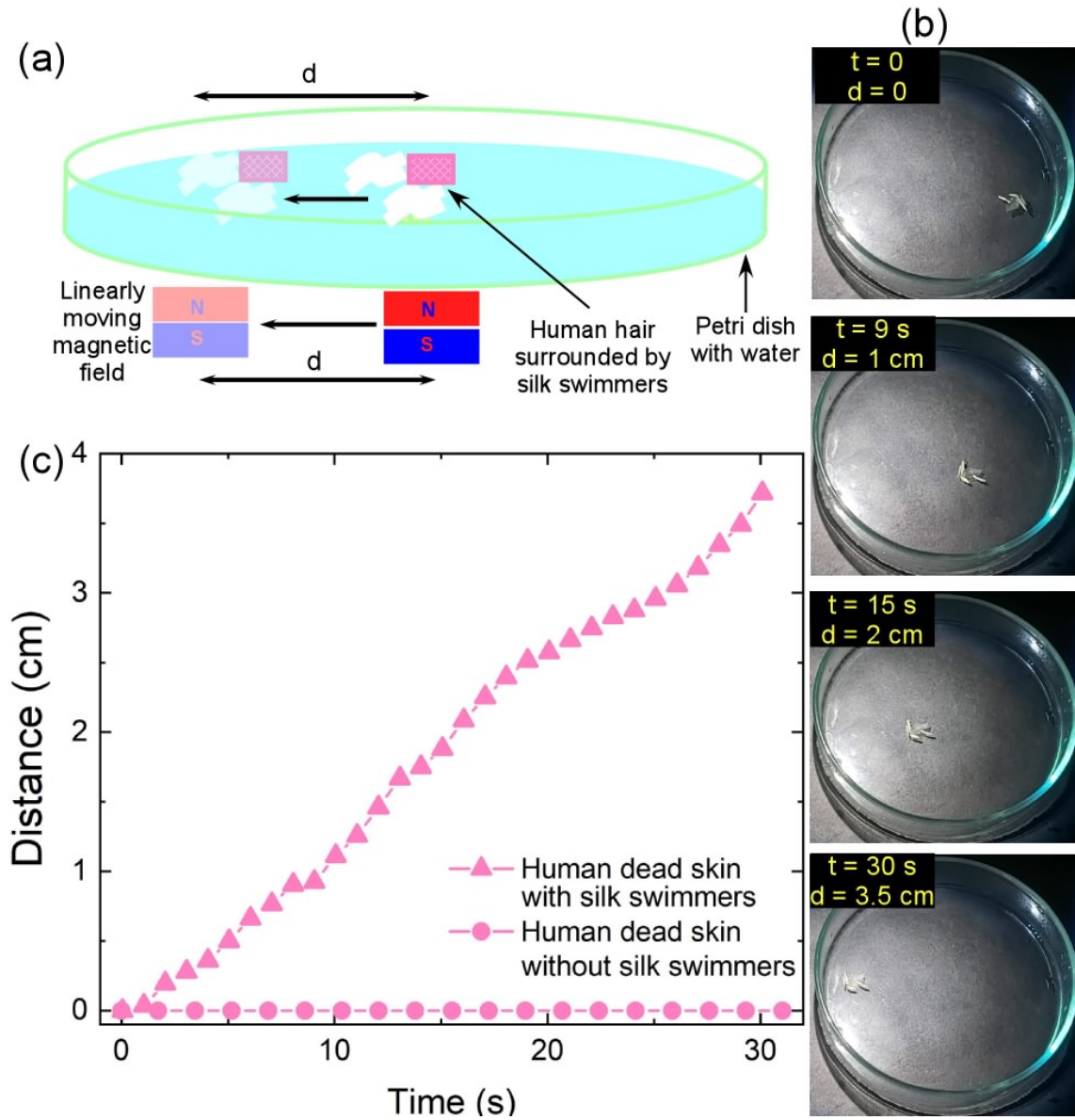


Figure 3.23: **Magnetic transport of human skin using silk swimmers.** (a) Schematic of the experiment showing silk swimmers transporting a piece of dead human skin (from lips) in de-ionized water. Tiny silk magbots (magnetic robots) surround a human skin tissue and help in its transportation from one end of petri dish to another end under the influence of magnetic field (b) Snapshots of the supplementary video 7 (Video-7_Human_Skin_Transport) demonstrate this phenomenon. (c) Distance vs. time graph showing silk-assisted transport of human skin obtained from Video-7_Human_Skin_Transport. Without the silk, no transport was possible in a magnetic field.

Silk swimmers assisting transport of human hair

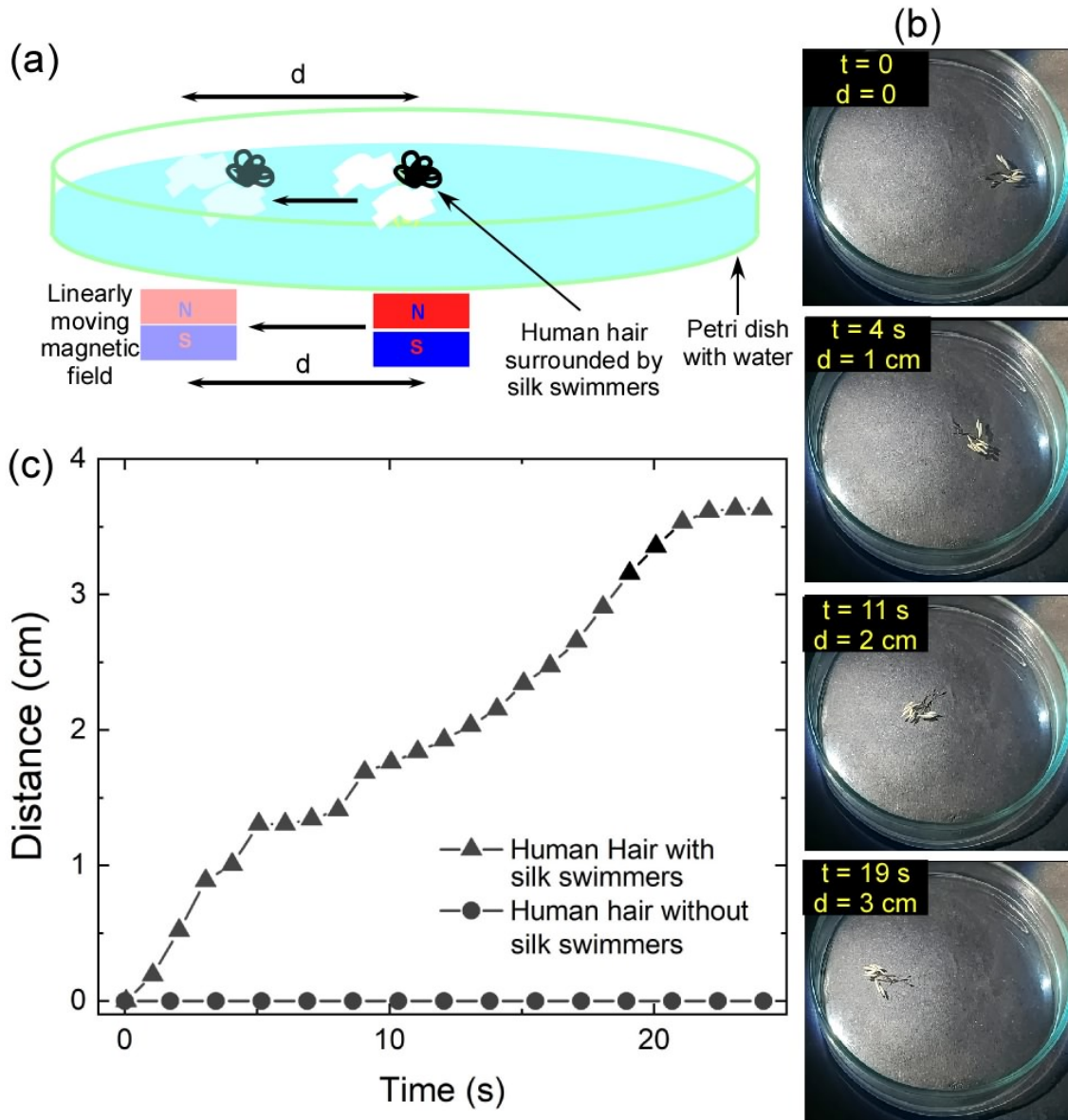


Figure 3.24: **Silk-assisted magnetic transport of human hair fiber.** (a) Schematic of an experiment showing silk swimmers transporting a bundle of human hair. Tiny silk magbots (magnetic robots) surround a human hair strand and help in its transportation from one end of petri dish to another end under the influence of magnetic field (b) Snapshots of the supplementary video 8 (Video-8_Human_Hair_Transport) demonstrate this phenomenon. (c) Distance vs. time graph showing silk-assisted transport of human hair obtained from Video-8_Human_Hair_Transport. The hair could not be magnetically transported without the silk.

Silk swimmers assisting transport of immiscible liquid

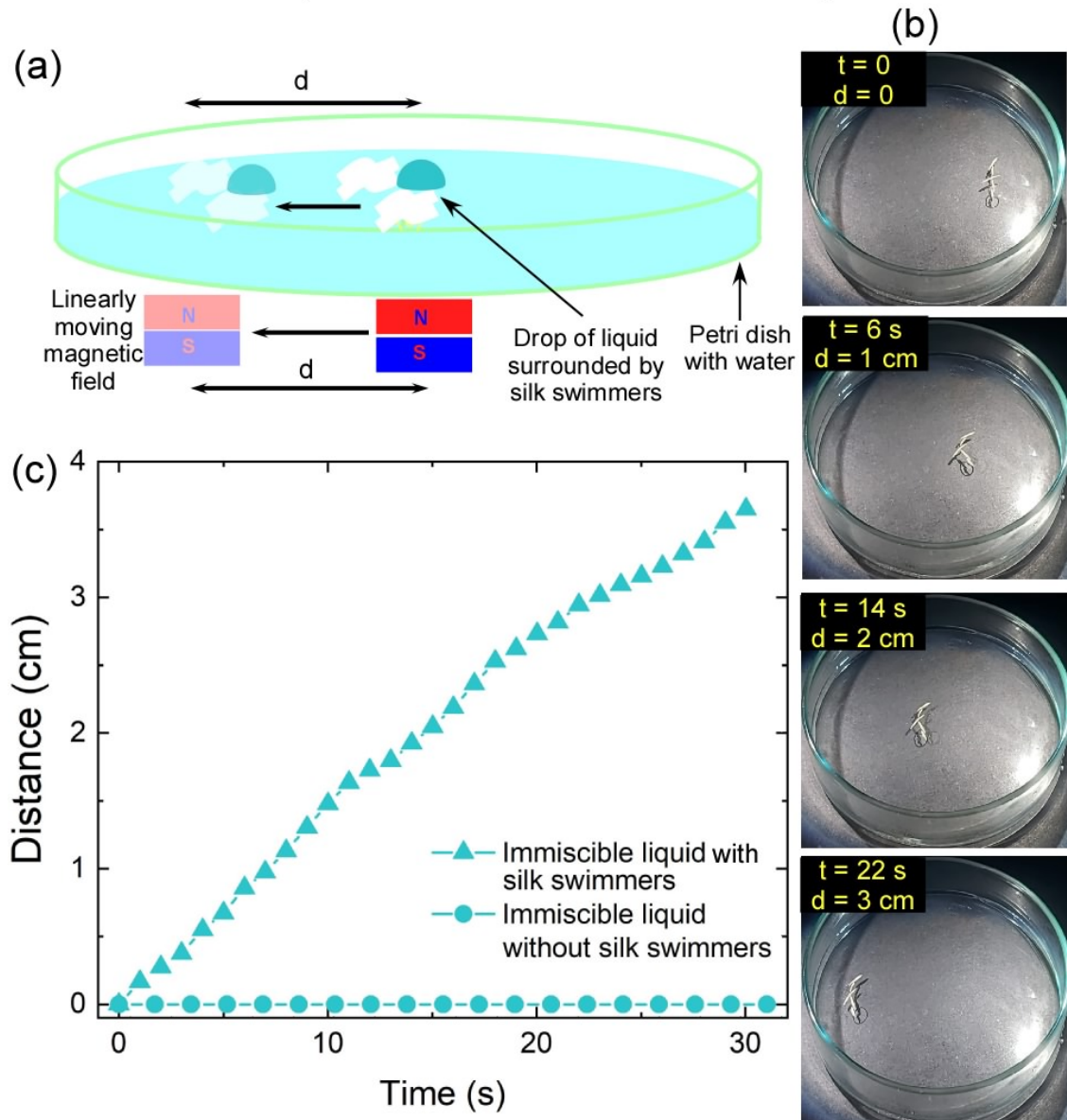


Figure 3.25: **Magnetic transport of non-magnetic oil drop using silk swimmers.** (a) Schematic of an experiment showing silk swimmers transporting an immiscible liquid. Tiny silk magbots (magnetic robots) surround an immiscible liquid and help in its transportation from one end of petri dish to another end under the influence of magnetic field (b) Snapshots of the supplementary video 9 (Video-9_Immiscible_Liquid_Transport) demonstrate this phenomenon. (c) Distance vs. time graph showing silk-assisted transport of liquid drop obtained from Video-9_Immiscible_Liquid_Transport. The drop does not respond to the magnetic field without the silk.

Silk swimmers assisting combining of two liquid drops

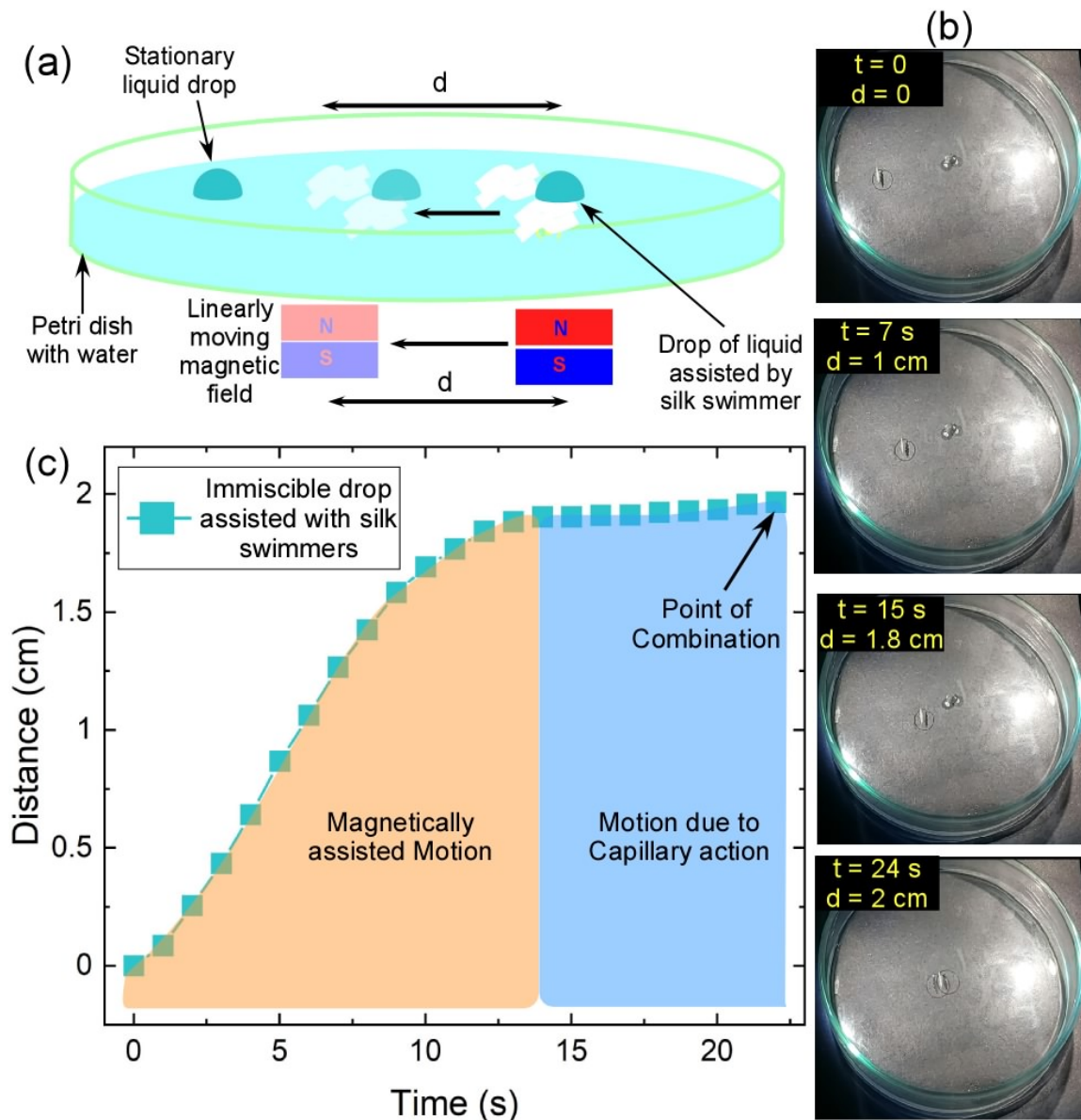


Figure 3.26: **Controlled merging of two fluid drops by magnetic silk swimmers.** (a) Schematic of an experiment showing miniaturized silk swimmers combining one immiscible liquid drop with another stationary drop. Tiny silk magbots (magnetic robots) surround one drop of immiscible liquid and help in its transportation from one end of petri dish to combine with another stationary drop under the influence of magnetic field. (b) Snapshots of the supplementary video 10 (Video-10_Combining_Liquid_Drops) demonstrate this phenomenon. (c) Distance vs. time graph showing silk-assisted merging of droplets obtained from the Video-10_Combining_Liquid_Drops. Capillary force is observed when the two droplets are too close, and the magnetic field is removed. These experiments show possible applications in controlling droplets in biological settings [19, 20].

The above experiments show that pure spider dragline silks (without external doping) can be used as micro/nanoscale magnetic robots to manipulate organic and inorganic materials in liquid environments. These basic maneuvers of transporting organic and inorganic cargo can be extended to perform various advanced functions. Hence, silks and silk-based organic magnets can be used as tools for non-contact and non-invasive surgeries, targeted drug delivery, and enhanced bioimaging. Further advancements in producing silk-based nano/microscale robots can result in better state-of-the-art applications. Silk-based magnetically controllable artificial muscles and scaffolds [118, 119] are another avenues where silks can have a significant impact as biomedical implants and tissue repair materials.

Silks open a new segment of organic protein-based magnets that are completely metal free and biocompatible. Silk and silk-based magnets can sustain their ferromagnetism for a long duration (for years) and up to high temperatures without any degradation in their magnetic properties. Silk-inspired organic magnets with desirable mechanical properties can be fabricated in laboratories.

3.8 Conclusion

In summary, this chapter discusses the entire experimental investigative study I had done to unravel the magnetic properties, origins, and magnetic ordering of spider dragline silks.

Through my detailed research work, I discovered the soft magnetic character of spider dragline silks at room and high temperatures. Investigation into the source of magnetism revealed that the magnetism is attributed to the presence of stable radicals in spider silk and not to the trace amount of iron found in silk. The microscopic defects in spider dragline silk's beta sheets can be understood as the source of these radicals interacting ferromagnetically. Spider dragline silk acts as an amorphous magnet where atomic spins created due to structural defects are trapped in the glassy state in the protein matrix. The stability of such radicals in silk can be attributed to the compact and stiff β -sheets that provide sufficient steric hindrance for these radicals to remain persistent while in close proximity to each other. Random trapping of these radicals in the protein matrix leads to the coexistence of ferromagnetic and antiferromagnetic interactions amongst radicals. Isolated and non-interacting radicals lead to paramagnetism.

I also established a simple mechanism to tune the magnetic moment of spider dragline silks by controlling the defects in their structure via stretching and cutting. In addition, I showed new potential applications exploiting the magnetic character of spider silks.

We showed that silk-based bio-magnetosensors could sense magnetic fields well below the geomagnetic magnitudes with good resolution. Moreover, silk-based bio-magbots can hugely impact biomedical fields for non-invasive surgeries, biopsy, drug delivery, cell/tissue

manipulation, and bionic actuators, to name a few. Moreover, thin silk can also be used in micro electromechanical systems (MEMS) or (NEMS) for biomedical applications.

Besides the applications I have shown, my research opens a new mechanism for obtaining protein-based magnets by engineering specific defects in structural proteins like silk fibers having light amino acids and tightly bound beta-sheet structures. This is the first-ever report of a magnetic protein containing no ferromagnetic metal. The magnetism appears naturally because of atomic defects in this protein and illustrates a novel method to obtain organic magnets.

Moreover, it also hints that spiders could have used such novel property of their dragline silk, also known as the spider's lifeline, for magnetoreception and navigational purposes. In the following chapter, we will discuss experiments that explore the possibility of a spider using its dragline silk for magnetoreception.

Chapter 4

Spider Dragline Silk as a Geomagnetic Compass

4.1 Introduction

The unique ability to detection of geomagnetic fields by living animals, known as magnetoreception, is observed in bacteria, insects, aquatic, non-aquatic animals, and in migratory birds [133, 134, 135, 136, 137, 138, 139, 140, 141]. Researchers have proposed several mechanisms leading to magnetoreception in organisms belonging to various phyla. Suspected causes of magnetoreception in many vertebrates and non-vertebrates are: (i) CRY protein in the eyes of migratory birds [72, 142] (see Chapter 1), (ii) weak magnetic induction in aquatic animals [143, 144], (iii) a protein complex MagR found in the retina [8] (see Chapter 1), and (iv) the presence of magnetite-like minerals in the brain and sensory organs [145, 146]. Even though evidence of magnetoreception in humans has been negligible, recent research in highly controlled environments shows that there is enhanced electrical activity in the human brain when subjected to a rotating magnetic field of geomagnetic magnitudes [136]. This implies that we might be able to sense the change in a magnetic field. However, no known mechanism of how or if spiders can sense geomagnetic fields has been discovered. This encouraged us to probe the area of magnetoreception and check if spiders take cues from the exceptional ferromagnetic properties of their dragline silk for this purpose. This could be a unique and ingenious method of magnetoreception that has never been observed in other insects.

Spider dragline silk's soft magnetic properties have been discussed in detail in our previous chapter. The vast applications that such biomaterials can have are enormous. However, what does dragline silk's soft ferromagnetic property mean for spiders? Was there a reason for the evolution of silk to become ferromagnetic at room temperature? How might the spider manifest this property to its use? These are a few questions that indulged us in a

series of experiments at this chapter's core. In this chapter, we will discuss how a spider might use its dragline silk for magnetoreception and show the direct magneto-mechanical response of its dragline silk towards magnetic fields of geomagnetic order.

4.2 Basic Idea of Experiment

Generally, proteins only exhibit magnetic response when subjected to a strong magnetic field. The effects of a weak magnetic field, such as a geomagnetic field, are negligible, with exceptions like CRY, MagR, and other iron-containing metalloproteins like ferritin. In the previous chapter, we employed a highly sensitive all-silk torsion pendulum fabricated with a single thread of spider dragline silk (SDS). We will use the same torsion pendulum technique because of its high sensitivity to tiny forces in the following experiments. In the previous chapter, we showed that a silk rod made of spider dragline silk could detect fields lower than geomagnetic fields (section 3.7.1). To achieve a magneto-mechanical response from fields of geomagnetic magnitudes from a "*single thread*" of spider dragline silk, we made a new set of changes to our setup, as will be discussed in section 4.4. By applying magnetic fields of geomagnetic magnitude, we show the local excitation of this thread, which produces a deflection of the pendulum in a single shot. Such a torsion pendulum serves as an accurate depiction of a spider rappelling from a height. It gives us a good idea about how spiders might use similar magnetoreception techniques. The experiment has been reproduced several times, using dragline silks of multiple spiders. In addition, our experiment depicts a simple technique to verify the soft magnetism of "*single thread*" of spider dragline silk under ambient conditions. This is typically impossible for sophisticated techniques like SQUID and vibrating sample magnetometers (VSM).

4.3 All Silk Torsion Pendulum experiment again !

This section shows the first set of experiments we did with our all-silk torsion pendulum. The critical difference between these experiments and the ones we did in the previous chapter is that we do not use permanent magnets here. We need a uniform magnetic field and control over magnetic field magnitudes, which are pretty hard to achieve with permanent magnets. Here, we used a pair of Helmholtz coils to produce uniform magnetic fields of desired magnitudes. The following sections will explain the details of our experimental setup.

4.3.1 Experimental set up

We discussed the method of making the silk rod used as a bob for our torsional pendulum in section 3.7.1. The procedure to prepare the all silk torsion pendulum is shown in fig 4.1. We made a sensitive torsional pendulum using a single silk fiber (length, $l = 10$ cm, diameter, $d \approx 3 \mu\text{m}$ (measured using a scanning electron microscope)). We freely suspended the silk rod onto the thread (fig. 4.1(b)). We used a pair of Helmholtz coils with a radius of 20 cm, and 154 turns each to produce a uniform magnetic field. The Helmholtz coils were powered by a stable DC power supply from Keithley. A magnetometer was used to measure the Helmholtz coil's magnetic field during the entire experiment. The magnetic field magnitude was found to be very stable during the experiment. The pendulum was kept between the middle of these coils to experience a uniform magnetic field and was covered by a glass chamber to reduce the disturbance due to surrounding air (fig. 4.1(c)). The setup was kept on a vibration-free table top to reduce the environmental acoustic vibrations. When the magnetic field was applied, an overhead camera was used to record the deflection of the pendulum (silk rod). The recorded video was accurately analyzed later to get the time vs. deflection angle of the pendulum. We used free video analysis tool software called Tracker for this purpose. The pendulum's motion could be accurately tracked with a precision of 0.1 deg. (0.00087 rad.) using this software.

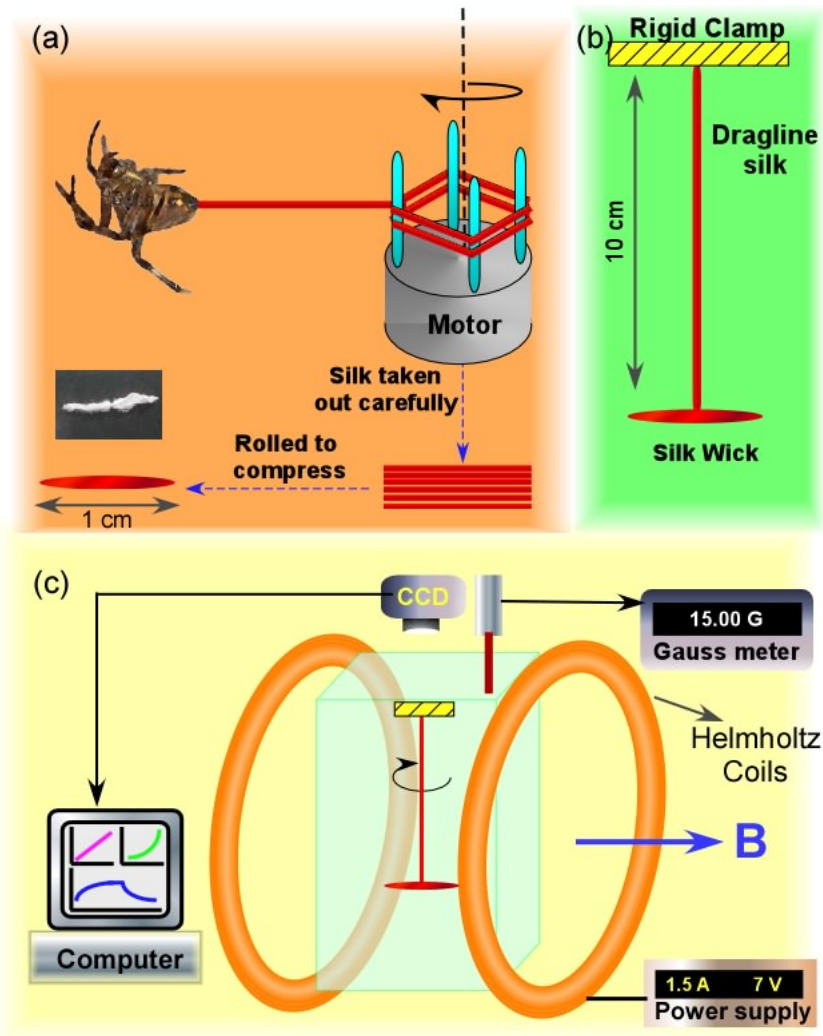


Figure 4.1: **Schematic of the all silk pendulum experiment.** (a): Shows the detailed procedure of preparation of spider silk rod with the image of one of the actual rod prepared for the experiment. (b): Shows the pendulum made using the silk rod. (c): Complete experimental setup where the pendulum is placed in a glass enclosure to eliminate effects of surrounding air flow. The silk rod experiences a uniform magnetic field produced by the Helmholtz coils. A gauss meter was also placed in order to note the magnitude of magnetic field produced by the coils. An overhead camera was used to record the entire experiment.

4.3.2 Experimental Results

In this section, we will discuss the physics as well as the results of the experiment. After setting up the experiment, as shown in figure 4.1(c), we applied a constant uniform magnetic field to the silk pendulum via Helmholtz coils by applying a constant current. The coils were set up to produce a magnetic field in a perpendicular direction to the resting silk rod of the pendulum. When under the influence of a magnetic field, the pendulum would experience a torque and start rotating to align itself with the magnetic field. We applied the field until the silk rod rotated to a new stable equilibrium position under the influence of the magnetic field. Let $\vec{\tau}$ be the torque applied to the spider silk rod of the pendulum and m be the mass of the silk rod ($m \approx 100 \mu\text{g}$), B be the applied magnetic field, and $\vec{\mu}$ and $\vec{\sigma}$ be the magnetic moment and magnetic moment per unit mass.

$$\begin{aligned}\vec{\tau} &= \vec{\mu} \times \vec{B} \\ &= (\vec{\sigma} \times \vec{B})m\end{aligned}\tag{4.1}$$

Assuming that the silk rod and magnetic field are perpendicular in direction, let χ_m be the mass magnetic susceptibility of silk and μ_0 be the magnetic permeability of silk. Then torque experienced by silk in the uniform magnetic field can be simplified to

$$\vec{\tau} = \frac{\chi_m B^2 m}{\mu_0}\tag{4.2}$$

We know that in a torsion pendulum, torque is directly proportional to the angle of twist provided to the pendulum (θ). Let κ be the torsion constant of silk, and hence,

$$\vec{\tau} = \kappa \cdot \vec{\theta}\tag{4.3}$$

We can see that from equations (4.2) and (4.3).

$$\begin{aligned}\theta &= \frac{\chi_m B^2 m}{\mu_0 \cdot \kappa} \\ \theta &\propto B^2\end{aligned}\tag{4.4}$$

We considered these two parameters because we can directly measure them. Hence our experimental results must show a linear relation between θ and B^2 , as was observed and shown in figure 4.2.

4.4 Dragline Silk as Geomagnetic Compass

In the previous chapter, we successfully demonstrated that spider silk could sense magnetic fields lower than the geomagnetic field present in our lab (measured to be $\approx 50 \mu\text{T}$).

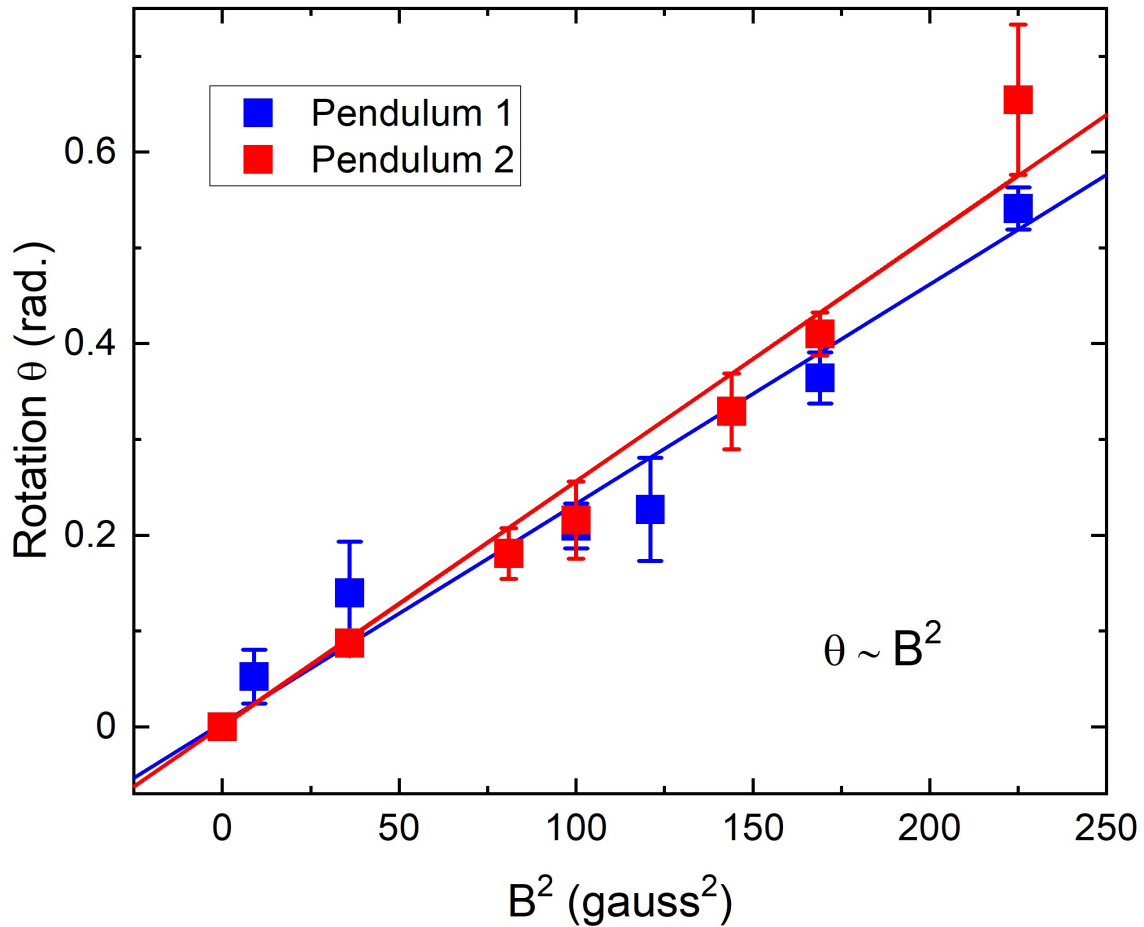


Figure 4.2: **Results of all silk pendulum.** The graphs show the experimental results of our all silk pendulum kept in a uniform magnetic field. In this experiment, we experimentally confirmed that $\theta \propto B^2$ with a small error of ± 0.04 radians in pendulum 1 and ± 0.05 radians in pendulum 2. The data is in strong agreement with the theory.

However, can a spider abseiling from its dragline silk (with a "single thread") detect the magnetic field and thereby navigate its location (like a compass)? To check this, we had to develop a more sensitive setup and replace the silk bob with a non-magnetic one having a similar mass as that of a real spider. We wanted to make such an experimental setup as realistic as possible. A torsion pendulum satisfactorily mimicking a spider suspending from its dragline silk is therefore employed in the following experiments. The procedure for making such a torsion pendulum is explained in figure 4.3. Nevertheless, it must be noted that we have not performed any physiological and behavioral experiments on living spiders to confirm if it actually perceives magnetoreception by this mechanism. We are just hinting at the possibility that spiders have such a unique magnetoreception mechanism at their disposal.

One key factor we must note is that the silk extracted using the procedure described in fig 4.3 is not extracted forcefully from the spider. In the present case (fig. 4.3), we observed

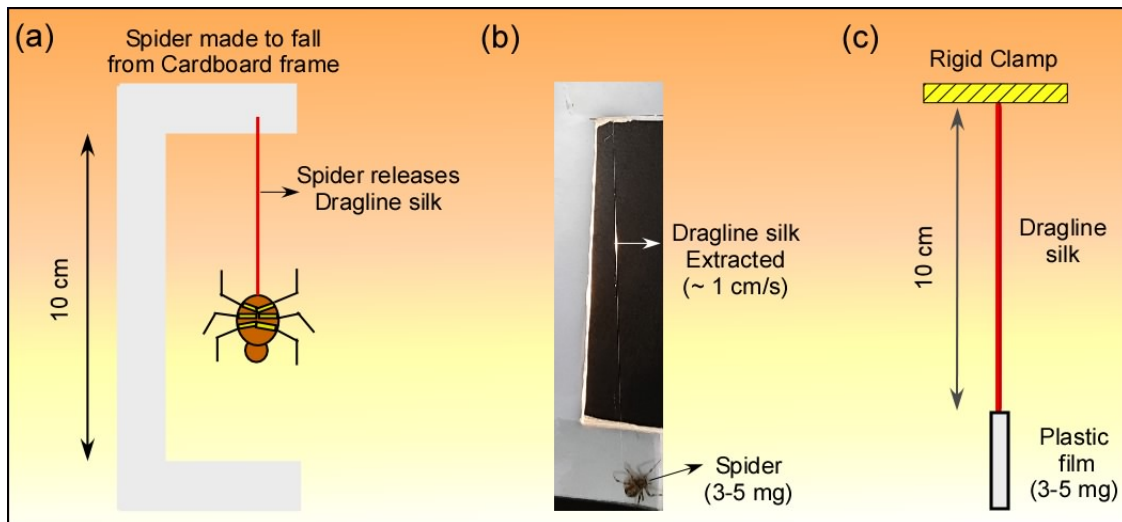


Figure 4.3: **All silk torsion pendulum mimicking spider.** (a) Explains the technique of extracting a single spider dragline silk thread from the spider. A spider is made to fall from the top of a cardboard frame. While freely falling, the spider releases its dragline silk to ensure it safely reaches the ground. As it reaches the bottom end of the frame, we take the silk released by the spider and use it to make our pendulum. (b) shows the picture of the actual frame and spider used to make the pendulum. We found that the spider releases its silk at a natural rate of approximately 1 cm/s. (c) shows the final pendulum made using a thin plastic film that can partially reflect light. We ensured that the weight of the plastic film (non-magnetic) is equivalent to that of the spider, so silk receives equivalent stress as it does from an abseiling spider.

that the spider spun the silk at a rate of $\approx 1 \text{ cm/s}$. However, it must be noted that a spider can spin its silk spinning rates as high as 10 cm/s , depending on the situation. Forceful silk extraction can lead to enhanced structural defects in silk's structure because the spider resists the silk spinning and pulls the silk in the opposite direction. Therefore under the entire silk collection process in section 3.2, silk is under stress. This enhances the chance of defects in its structure as it undergoes a liquid-to-solid transition. However, obtaining a large amount of silk for experimentation without forceful spinning is very difficult.

The following sections provide the complete details of our new magnetosensing silk torsion pendulum.

4.4.1 Experimental setup

These experiments aimed to discover if spider dragline silk can detect and produce a magneto-mechanical response to the changing magnetic field of geomagnetic order. Such a magneto-mechanical response to magnetic field changes can induce magnetoreception in spiders.

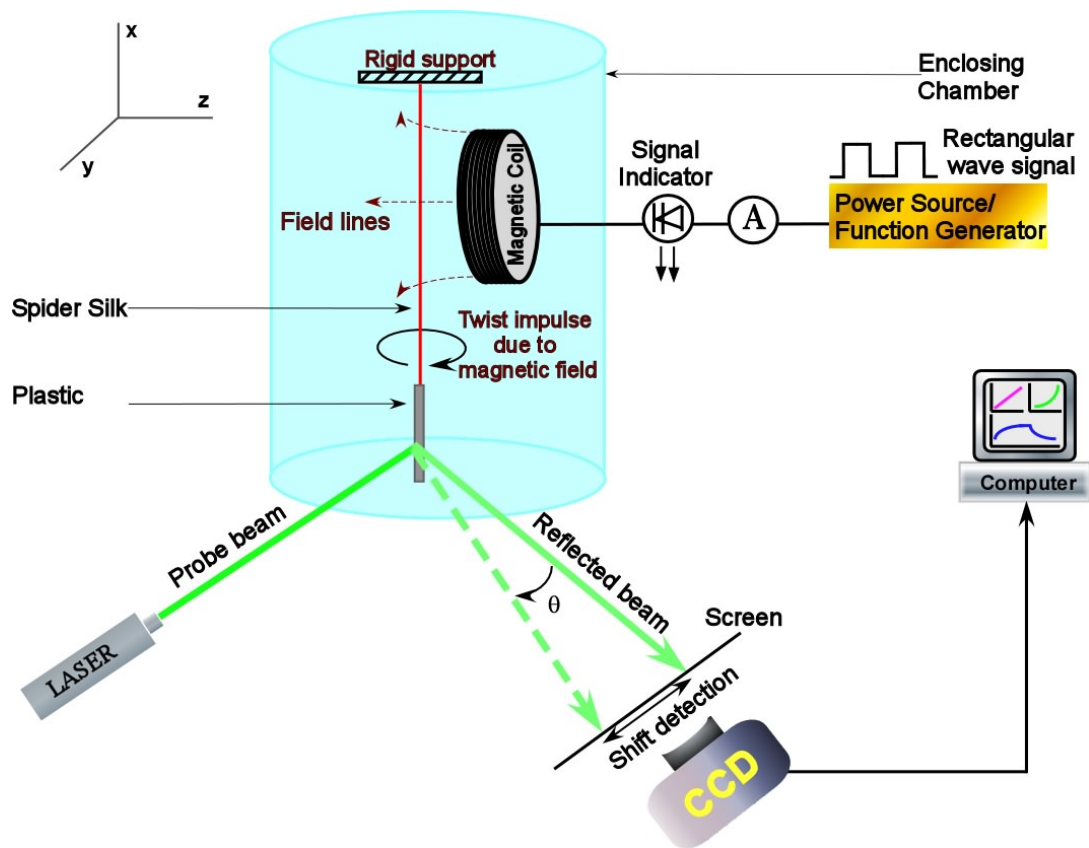


Figure 4.4: **Experimental setup to detect the magnetic response of spider silk.** A probe beam deflection technique (PBDT) was employed by attaching a thin plastic film to the spider silk under study, this plastic beam reflects a small amount of light falling on it, and the reflected spot acts as an indicator of the angular position of the pendulum. The dynamics of the reflected beam were recorded using a camera, and the video was later analyzed using motion tracking software. The magnetic coil is used to excite the silk pendulum locally. A rectangular square wave signal was used to drive the coil for repeated on/off cycles, and the current was measured using an ammeter. A laser diode was also connected as an indicator for on/off cycles. The pendulum was enclosed in an air-tight glass chamber. The entire experiment was kept on a non-magnetic honeycomb vibration-free table.

Since the earth's magnetic field ranges from $33 \mu\text{T}$ (at the equator) to $66 \mu\text{T}$ (at poles), we knew that the magneto-mechanical response, if any, would be extremely small. Hence, we developed a probe beam deflection technique (PBDT) to detect an exceptionally small torsional response due to microtesla magnetic field changes from a very sensitive spider dragline silk pendulum. The basic schematic of the setup is shown in figure 4.4. At the heart of this complex experimental setup lies two significant components: (i) a very sensitive spider silk torsion pendulum and (ii) current-carrying magnetic coils.

Firstly, we will understand how PBDT works. A very sensitive pendulum is made from a single thread of spider dragline silk with a non-magnetic plastic thin film suspended from it. This plastic thin film mimics a suspending spider and has a similar weight to the spider from which the silk was extracted. Next to the silk pendulum (about 3 cm away) lies a current-carrying coil having 150 turns and a radius of 1.5 cm made out of copper wire with a diameter of 0.8 mm (21 gauge). This coil excites the silk thread locally by producing a magnetic field of the desired magnitude. The pendulum rests under ambient conditions and is protected from airflow by keeping the apparatus inside a sealed glass chamber, as shown in fig.4.4. The entire setup was kept on a non-magnetic honeycomb table to protect it from acoustic and mechanical noise. We use a low-powered collimated laser ($2 - 3 \mu\text{W}$; beam width $w_0 \approx 1 \text{ mm}$) as a probe beam pointing at the center of plastic film (suspended from the pendulum). The plastic film partially reflects this laser beam onto a screen. This reflection spot on a screen serves as an indicator of the angular position of our pendulum. This improved the angular resolution of our experiment by ten times more than the previous technique of using an overhead camera (section 4.3). Therefore we could now resolve a torsional response of about 0.1 deg. We used a function generator (Tektronix) to power the magnetic coil and produced a continuous on-off magnetic field cycle over a fixed time interval. The dynamics of the reflected spot were recorded using a camera. We used a laser diode in series with a coil to track the signal switching from the function generator powering the coil. An ammeter (Keysight) with an accuracy of $10 \mu\text{A}$ was also connected in series to the function generator to check the current flowing through the coils accurately. The magnetic field was very precisely and accurately calibrated (error of $\pm 2 \mu\text{T}$) to the current using a 3-axis hall probe (Alpha labs Inc.) magnetometer. Moreover, the coil was carefully kept at a sufficiently far distance (about 6 cm above) from plastic film to eliminate any magnetic field effect on it. The magnetic field reaching the film was 100-times lower than that reaching the silk and lower than $1 \mu\text{T}$ at all times.

One can see that this experiment's applied magnetic field is nonuniform. From our high school knowledge, we know that the magnetic field generated by a current carrying coil at a distance, z from the center of the coil along the line passing through origin is given as:

$$B_z = \frac{\mu_0 I}{2} \frac{a^2}{(z^2 + a^2)^{3/2}} \quad (4.5)$$

Here I is the current passing through the coil, and a is the radius of the coil.

However, in this experiment, equations (4.6-4.8) give a highly accurate solution of the magnetic field produced by a current-carrying coil. These equations use elliptical integrals of type 1, $K(k^2)$ and type 2, $E(k^2)$. For the purpose of simplicity, let $\rho^2 = x^2 + y^2$, $r^2 = x^2 + y^2 + z^2$, $\alpha^2 = a^2 + r^2 - 2a\rho$, $\beta^2 = a^2 + r^2 + 2a\rho$, $k^2 = 1 - \frac{\alpha^2}{\beta^2}$, $\gamma^2 = x^2 - y^2$ and $C = \frac{\mu_0}{\pi}$

$$B_x = \frac{C_{xz}}{2\alpha^2\beta\rho^2} [(a^2 + r^2)E(k^2) - \alpha^2K(k^2)] \quad (4.6)$$

$$B_y = \frac{C_{yz}}{2\alpha^2\beta\rho^2} [(a^2 + r^2)E(k^2) - \alpha^2K(k^2)] \quad (4.7)$$

$$B_z = \frac{C}{2\alpha^2\beta} [(a^2 - r^2)E(k^2) + \alpha^2K(k^2)] \quad (4.8)$$

Because of the nonuniform nature of the magnetic field, we cannot expect a linear relationship between the angle of rotation θ_p and the magnetic field B^2 for such a pendulum, as shown in fig. 4.2. The next section shows that even a single silk thread can sense the magnetic field changes in its nearby environment.

4.4.2 Experimental Results

As explained previously, before setting up the experiment, we accurately measured the magnetic field's value (in all three directions) at a fixed distance (3 cm) from coils for different current values. Then the pendulum was accurately placed 3 cm away from the coils. In order to power the coils, we used a function generator and a square wave signal with a frequency close to the pendulum's natural frequency to obtain maximum response (resonance condition). The experiment ran for several complete cycles for each magnetic field value. We also ensured that the signal's current value was stable throughout each experiment, so the magnitude of the magnetic field produced by coils remained constant over the period. The entire experiment was done in a dark empty room to reduce noise and ensure accurate tracking of the pendulum. Experiments were started only after ensuring that the silk pendulum was highly stable and not picking any noises so we could confirm that we got clean signals. The experiment was recorded on a camera, as explained in fig. 4.4, and the video was later analyzed. This experiment was repeated for three spider silk pendulums made from different spiders.

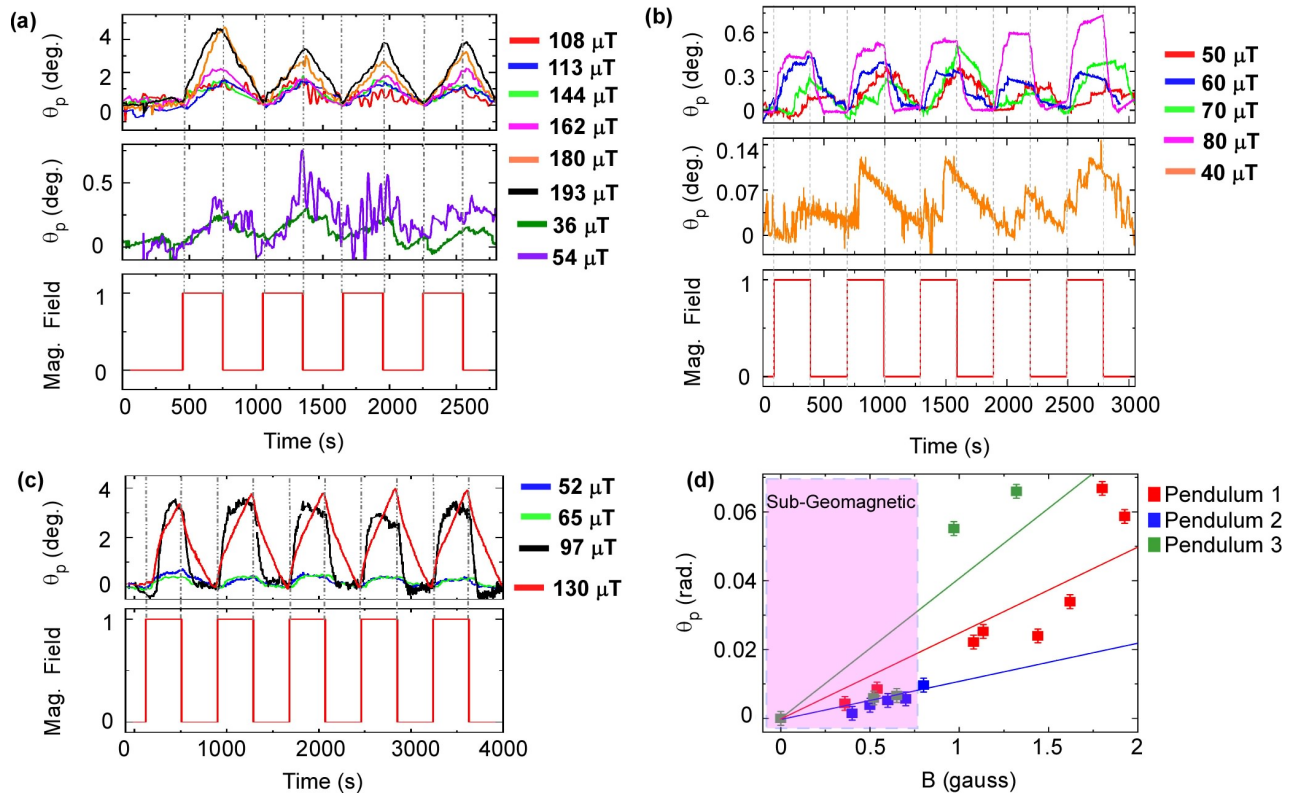


Figure 4.5: **Geomagnetic sensing by dragline silks.** (a-c) shows the one-to-one rotational response of 3 different spider dragline silks to the magnetic field of different magnitudes differentiated by the color code given in the index. The similar frequency of changing magnetic field and rotation of spider silk pendulum implies a strong correlation between them. The 0 and 1 in magnetic field graphs represent the period for which the magnetic field signal was switched off and on, respectively. Moreover, we can also see that the magneto-mechanical response of dragline silk at a subgeomagnetic field changes well below ($66 \mu\text{T}$). These results depict that spiders might get magnetoreception cues from their dragline silk when it experiences changes in magnetic fields. (d) shows the rotation of pendulums with respect to the applied magnetic field for all three pendulums. The colored lines are for visual aid. We can see that even a "single silk thread" can detect geomagnetic fields in all three cases.

The results of the experiment are shown in fig. 4.5 A mechanical oscillation in spider silk with a similar frequency as that of the applied magnetic field used to excite it inevitably proved their relationship. The data was collected by varying magnetic fields, \vec{B} from $30 \mu\text{T}$ to $200 \mu\text{T}$. From our observations, we can confirm that SDS can sense the change in magnetic field up to geomagnetic magnitudes, i.e., $30 - 60 \mu\text{T}$. We did not compensate for the constant earth's field because of the experimental limitations of PBDT. We only illustrated SDS's detection of a 'change' in the magnetic field. We can observe that in fields $\leq 70 \mu\text{T}$ (geomagnetic limit), the deflection of spider silk is generally less than a

degree, which might appear relatively small. However, insects have high sensitivity to extremely small forces and have been reported to detect nano Newton forces on their body hair [147, 148]. Therefore such small deflections can easily open the possibility that a spider might use the extraordinary property of its silk in some ingenious way for navigational and migratory purposes.

4.5 Conclusions

In this chapter, we wanted to explore if the magnetic properties of dragline silks of spiders emerged due to the evolutionary engineering of silk over millions of years and provide a functional advantage to them or are just an additional property we discovered.

Through our extensive experimentation, we showed that the magnetism of spider dragline silk provides a capability of magnetoreception to spiders. Even a single thread of dragline silk can be used to detect sub-geomagnetic field changes in the surrounding environment. Spiders might be able to take advantage of such behavior for navigation and understanding their nearby environment.

However, it must be emphasized here that we have not done any physiological or behavioral studies on living spiders to confirm if the spider actually utilizes its dragline silks for magnetoreception. We have only presented the possibility that spiders can have a unique magnetoreception mechanism that other organism lack.

Our research also showed that a "*single micrometer thick thread*" of spider dragline silk could be used as a thin biological magnetic wire (with exceptional mechanical properties). This can have brilliant applications like extremely light and micrometer-thin magnetic sensors in biomedical and technological sectors. Such bio-inspired magnetic microwires can be manipulated in a contactless manner by changing magnetic fields and be used in biomedical and construction applications.

Chapter 5

Intrinsic Magnetism of Silkworm Silks

5.1 Introduction

Silkworms produce only one kind of silk, which makes up the cocoon for the morphogenesis of silkworm pupae to a moth. We have discussed various properties and functions it plays in protecting and nurturing silkworms in their cocoons (Chapter 1). While looking at its molecular structure and amino acid sequencing, we can see that silkworm silks are made of the same amino acids: glycine and alanine. In addition, their beta-sheets comprise of same $(GA)_n$ sequences as that of spider silks. Hence one wonders if silkworm silks depict the ferromagnetic character as well. This was our motivation for exploring the magnetic properties of silkworm silk.

We must mention that silkworm cocoon membranes (SCM) have shown ferromagnetic response at room temperature previously [33]. In that study, the source of magnetism was attributed to the minuscule presence of ferromagnetic elements like iron, nickel, cobalt, and gadolinium in silk cocoon membranes which could only be found in parts per billion (ppb) concentrations. A closer look at their data can confirm that the concentration of ferromagnetic elements was insufficient to produce saturation magnetization reported for SCM (≈ 0.05 emu/g). Therefore, there was a gap in that study. However, the study acknowledged the presence of stable carbon radicals in silk.

In this chapter, we will see that silkworm silks show similar magnetic behavior as spider draglines. Silks showing ferromagnetic response at ambient temperatures and the origin of magnetism can again be linked to stable carbon radicals. The magnetism of silkworm silks can be enhanced by creating additional structural defects. A thorough investigation of the magnetic properties of silkworm silk, including magnetometry, thermomagnetic analysis, magnetic resonance spectroscopy, and detailed elemental analysis, was done.

5.2 Preparation of pristine silkworm silks

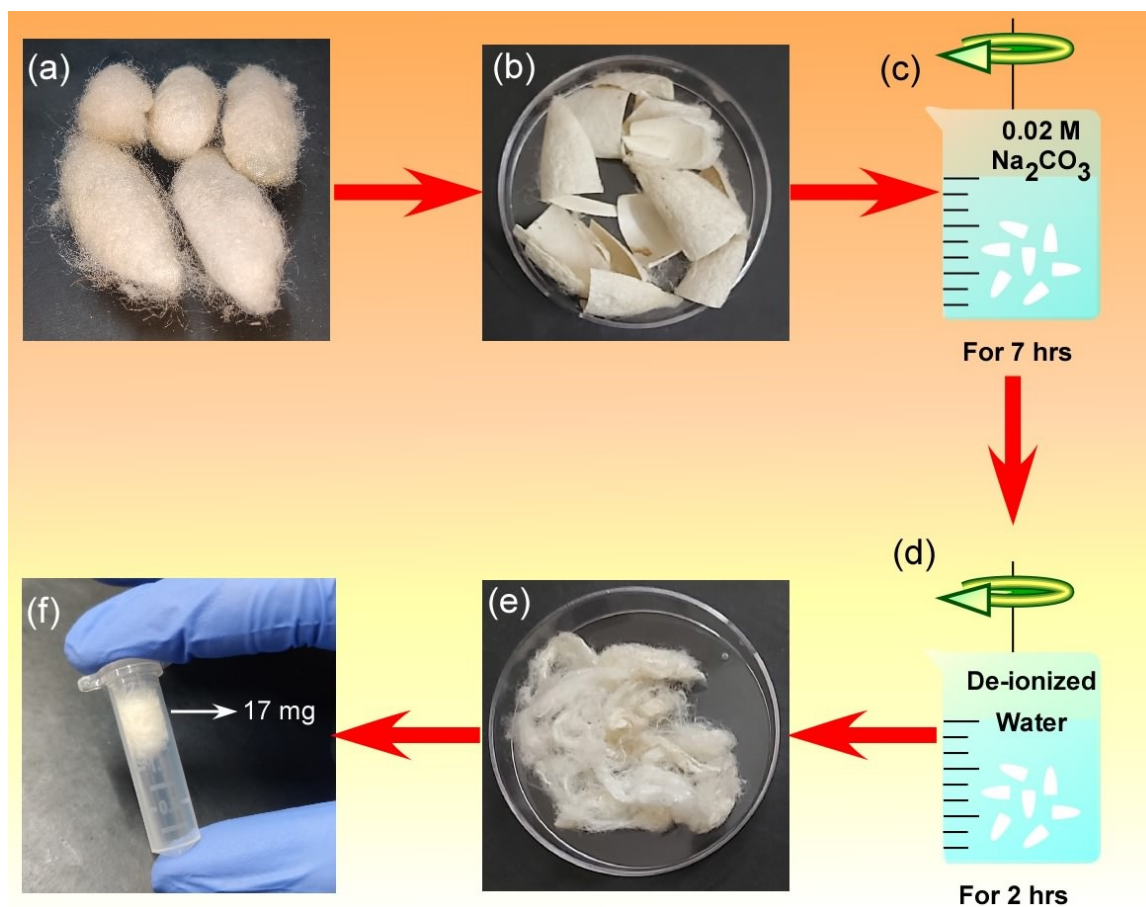


Figure 5.1: **Preparation of pristine silk samples:** The figure shows a detailed step-by-step procedure for preparing pristine silkworm silk samples for magnetization experiments. (a) shows the picture of *B. mori* silk cocoon membranes (SCM) collected from a silk farm. (b) shows the pieces of SCM after cutting them with ceramic scissors. Ceramic scissors were used instead of metallic ones to avoid contamination of SCM with metallic impurities. (c-e) Degumming the silks removes unwanted impurities and sericin from SCM's surface. The cut silk pieces were cleaned in 0.02 M solution of Na_2CO_3 for 7 hours and later were cleaned with deionized water for 2 hours. These silks were then air-dried for about 18 hours to remove moisture. (f) Shows the sample kept in cleaned and sterilized MCT for experimentation. Utmost care was taken to avoid any metallic contamination of silk and samples were handled only using clean latex gloves.

To investigate the intrinsic magnetism of silkworm silk, we prepared silk samples taking extreme measures to avoid contamination. The silk was obtained from silk cocoons bought from silk farms in Karnataka, India. The cocoon was cut to remove the insect from them. These cut cocoons need to be cleaned thoroughly to remove impurities. We used ceramic

scissors to avoid metallic contamination and cut the silk cocoon membranes (SCM) into small pieces, and then cleaned them with clean deionized water for 30 mins. These silks were rewashed using a 0.02 M solution of sodium bi-carbonate Na_2CO_3 in deionized water for 7 hours. After completing this, the silks were cleaned using deionized water for another 2 hours to remove any contaminant on the silk surface. The cleaning process ensures not only the removal of unwanted contaminants but also the removal of sericin on the surface of silks (see chapter 1). This process is also known as the degumming of silk. After cleaning we are left with pure natural silk fibroin. The cleaned silks were later dried in the air in a clean environment for 16-18 hours to remove moisture. This concluded the cleaning process of silk, and then these silk samples were stored in cleaned and sterilized microtubes (MCTs).

We followed our previous methodologies (as in chapter 3) for investigating magnetism in the silkworm silk samples and prepared for the following experiments:

- Magnetometry (M-H) using SQUID magnetometer at different temperatures
- Thermomagnetic (M-T) experiments using SQUID magnetometer at constant magnetic field
- Elemental analysis using EDX, XPS, XAS, and ICPMS

In the following sections, we will discuss our detailed results of the above-stated experiments and compare the magnetic properties of silkworm silks with spider dragline silks. The experimental methodology for these experiments is similar to the one followed in chapter 3.

5.3 Magnetometry of Silkworm Silks

Once the silks were cleaned and degummed (removal of sericin), we carried out the magnetization experiments using the SQUID magnetometer. The samples were accurately weighed before commencing the experiments. The basic procedure of the experiment was kept similar to that described in chapter 3. The mass of silkworm silk mounted for experimentation was (≥ 15 mg) for accurate results free from background errors. We were cautious while mounting the samples to the quartz-half tube. We also weighed the amount of Teflon being used (≈ 4 mg for all samples). We were careful not to stretch the Teflon as it can cause ferromagnetically coupled dangling bonds and lead to false results [102].

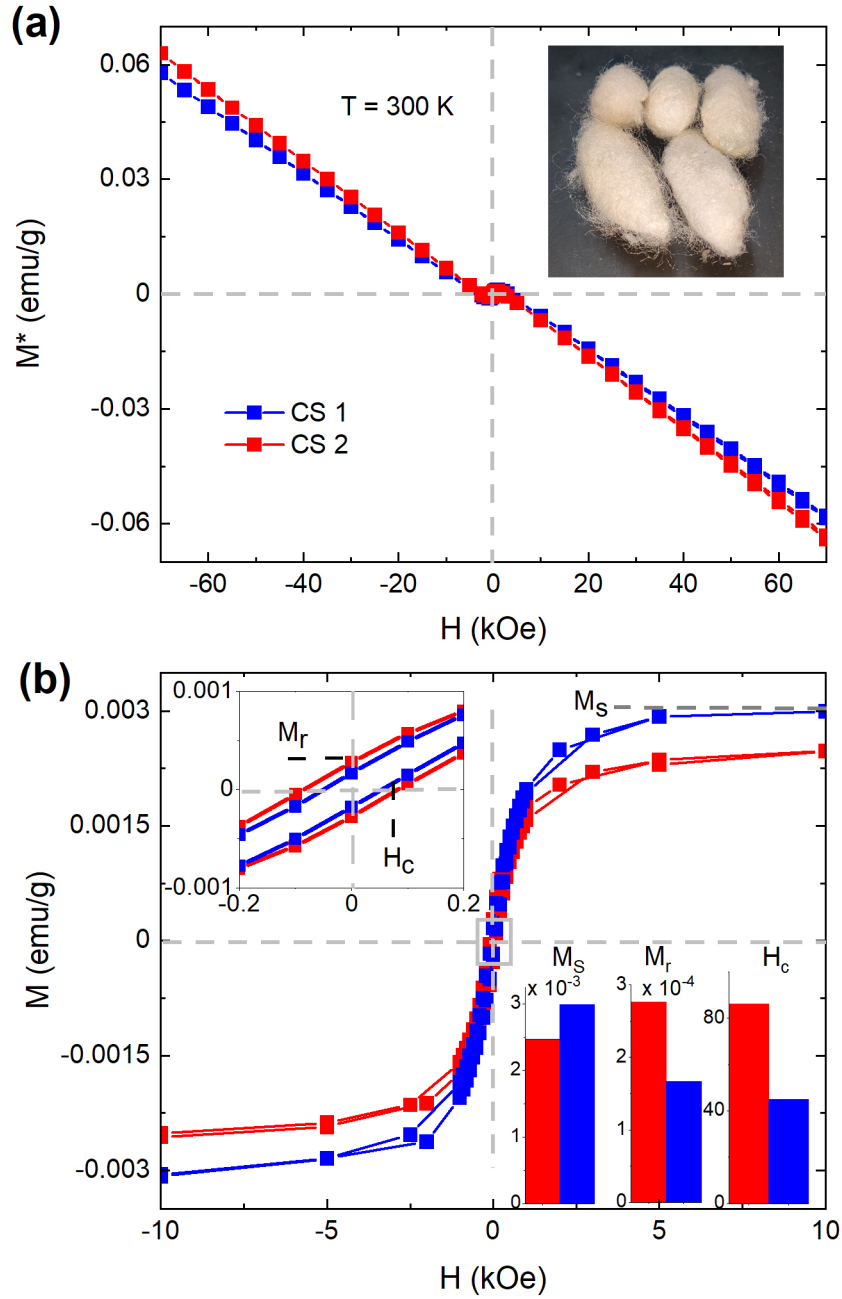


Figure 5.2: **MH of silkworm silk at 300 K.** (a): At high magnetic fields, the diamagnetic contribution of silk dominates heavily over its ferromagnetic contributions typically above 3000 Oe. M^* stands for data before diamagnetic subtraction. (b): M-H relation after subtracting diamagnetic contribution at 300 K. Upper inset: zoom of hysteresis loop showing coercivity and remnant magnetization. Lower inset: distribution of H_c , M_r and M_s for two samples. Mean values of these parameters are $M_s = 2.8 \pm 0.33 \times 10^{-3}$ emu/g, $H_c = 65 \pm 20.0$ Oe and $M_r = 2.22 \pm 0.55 \times 10^{-4}$ emu/g.

The data of SQUID magnetization for silkworm silk samples at room temperature (300 K) is shown in figure 5.2. We can see the raw magnetization data without diamagnetic

subtraction in 5.2(a). For fields ($> 3000 \text{ Oe}$), the silks were dominantly diamagnetic with a susceptibility of $\chi_D \approx -1.34 \pm 0.058 \times 10^{-8} \text{ emu}/(g \cdot \text{Oe})$ (average of 2). Figure 5.2(b) shows the data after diamagnetic subtraction from raw data depicting clear saturation magnetization, $M_s = 2.8 \pm 0.33 \times 10^{-3} \text{ emu}/g$ (average of 2 samples) and coercive field, $H_c = 65 \pm 20 \text{ Oe}$ (average of 2 samples) in silkworm silk samples. A remnant magnetization $M_r = 2.22 \pm 0.55 \times 10^{-4} \text{ emu}/g$ (average of 2 samples) is also observed in all silk samples. The left inset of figure 5.2(b) provides a zoom of the data near zero magnetic field after subtraction. In comparison with spider silk samples, the fundamental magnetic values of silkworm silks are an order of magnitude smaller. The reason for such smaller values is believed to lie in the different sample preparation methods for both types of silks. In the case of spiders, dragline silk was forcefully spun from its spinnerets, with the spider resisting the spinning process, which caused tension in the silk thread and thereby created many defects in its structure. Whereas, in the case of silkworms, the silk cocoons were produced by silkworms at their natural spinning rates and not forcefully; therefore, it contains fewer defects in its structure as compared to spider dragline silk. Using the known molecular weight of silk fibroin of ca. 400 kDa [149], we get a magnetic moment of $\sim 0.2 \mu_B$ per protein molecule at room temperature, which in comparison to spider silk is an order of magnitude smaller ($\approx 3 \mu_B$ per molecule for spider dragline silk). In section 5.4.2, we will show that one can increase the magnetic parameters like M_s , H_c , M_r by increasing the defects in silkworm silk's structure, just as was done in the case of spider silks (section 5.4.2). The MH analysis implies that silkworm silk also exhibits a soft ferromagnetic character at room temperatures.

To ensure that the magnetic signals from silk are clean and much above the background, we compared the SQUID magnetization data $M(H)$ obtained from the silkworm silk samples with the background data from the empty sample holder (the quartz half tube and Teflon without the silk samples) under otherwise identical conditions. Fig 5.3 shows that the background of the empty sample holder is negligibly small. Also, for the fields (e.g., 60 kOe), the diamagnetic response of silk is much larger than the background. Notably, the empty sample holder showed no hysteresis (see zoom below 2 kOe).

Magnetization data at 10 K of silkworm silk samples is shown in figure 5.4. Figures 5.4 (a) shows the raw magnetization data without diamagnetic subtraction, and figure 5.4(b) shows the data after diamagnetic subtraction from raw data depicting clear enhancement of magnetic character from room temperature, with significant increase in remnant magnetization, $M_r = 7.91 \pm 0.8 \times 10^{-4} \text{ emu}/g$ and coercive field, $H_c = 223 \pm 27 \text{ Oe}$. Similar to spider silks, we observed a lack of saturation in magnetization even at a very high magnetic field of 7 T in silkworm silk samples. The inset of figure 5.4(b) provides a close-up look at the data after subtraction to show the presence of hysteresis. The analysis of this MH

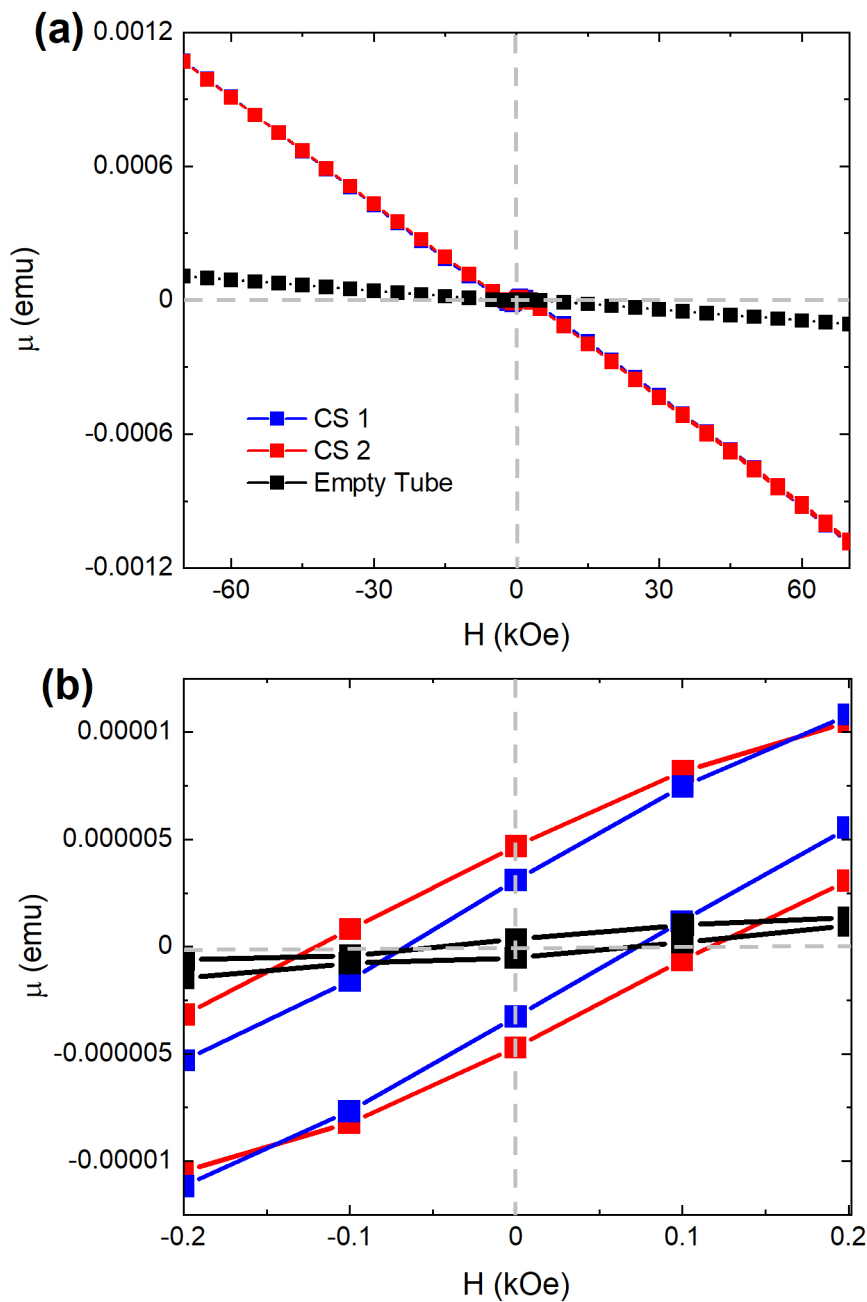


Figure 5.3: **Comparison between MH data for empty tube background and with silk.** The background SQUID data was obtained with an empty tube (Black). We note that the background is negligibly diamagnetic compared to silkworm silk (SS). Hence, throughout the experiments, we performed diamagnetic background subtraction by using high field data (of CS) at 300 K. Bottom graph shows zoom near zero fields. The background does not show any hysteresis. It must be noted that an empty holder means a quartz half tube with Teflon tape but without silk samples.

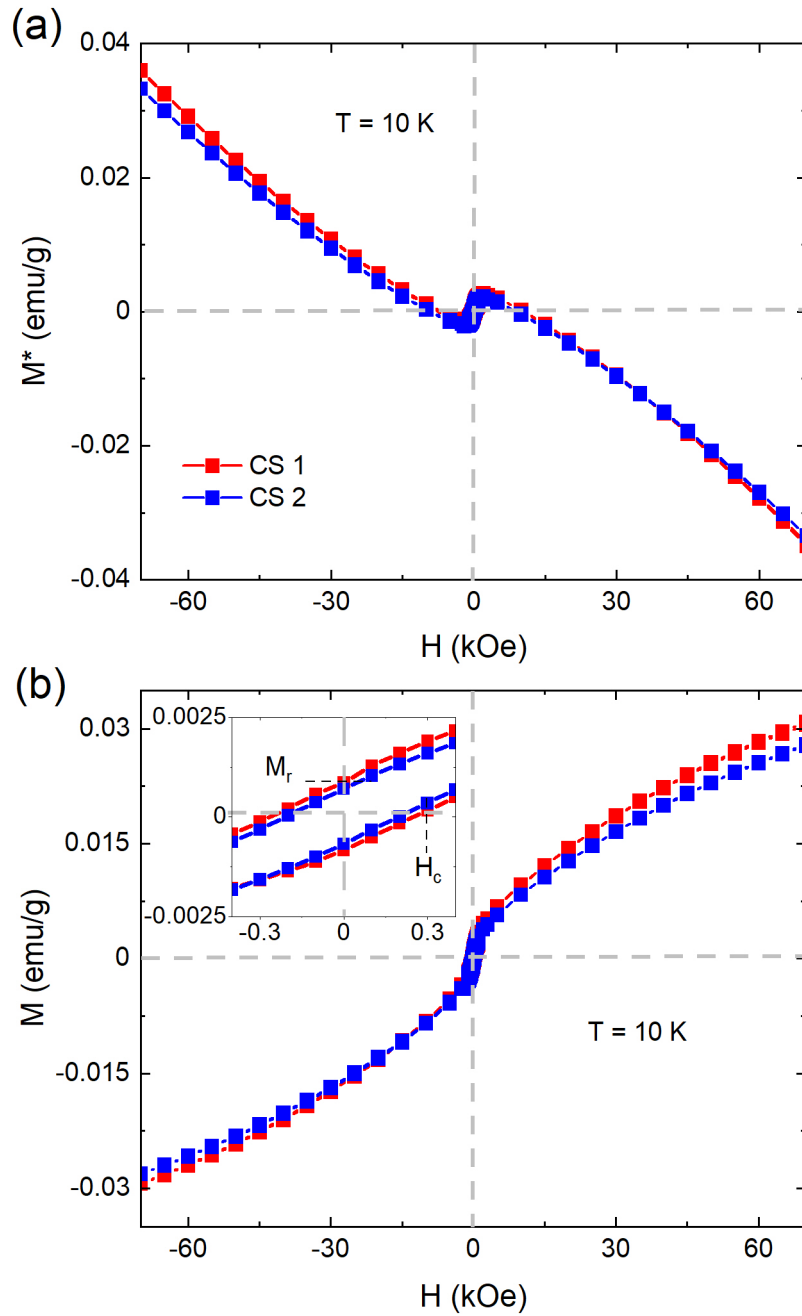


Figure 5.4: **MH data of silkworm silks at 10 K.** (a): The magnetization of silk has increased significantly when compared with data collected at 300 K. (b): MH relation after subtracting diamagnetic contribution at 10 K. We can see that the magnetization doesn't saturates even at magnetic fields of 7 T and keeps increasing linearly. This suggests the coexistence of ferromagnetically interacting ($J > 0$) and non-interacting spins in silk samples. Average remnant magnetization increases to $M_r = 7.91 \pm 0.8 \times 10^{-4} \text{ emu/g}$ and coercive field, $H_c = 223 \pm 27 \text{ Oe}$. The average paramagnetic susceptibility, $\chi_p = 3.1 \pm 0.11 \times 10^{-7} \text{ emu/(g} \cdot \text{Oe)}$.

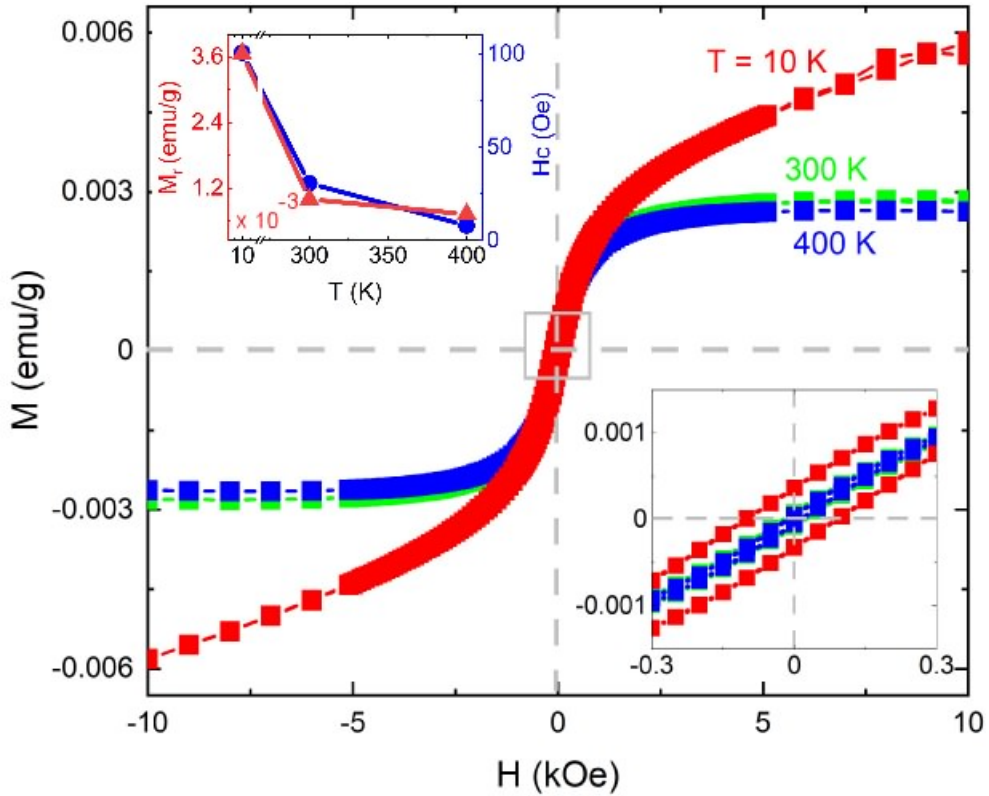


Figure 5.5: **Comparing M-H curves of silk at different temperatures.** The data depicts the soft ferromagnetic character of silks at 10 K, 300 K, and 400 K. Left inset: Comparison of H_c and M_r at these temperatures. As the temperature increases, we can see a steady drop in M_r and H_c . Right Inset: Zoom of data near zero field in M_r and H_c .

data implies that silkworm silk exhibits the coexistence of ferromagnetically interacting and non-interacting magnetic spins. The paramagnetic susceptibility of silk samples at 10 K was found to be $\chi_p = 3.1 \pm 0.11 \times 10^{-7} \text{ emu}/(\text{g} \cdot \text{Oe})$ (average of 2). A prominent source of paramagnetism in silk can be the free radicals formed due to microscopic defects within its structure [128]. Compared to spider silk, the χ_p of silkworm silk is also ten times smaller than that of spider silks. This again strengthens our claim that the forceful spinning of silk leads to a larger number of atomic defects in its structure. However, a thorough investigation of silkworm silks must be done to check the presence of ferromagnetic impurities like iron, nickel, cobalt, etc.

The magnetization of silk samples was stable over quite a long time as the samples were stored at room temperature and 50% relative humidity. This implies that silk-based organic magnets can be stored in the laboratory for a long time. Similar to spider dragline silks, we also find that silkworm silk's magnetic character is well preserved at temperatures significantly higher than ambient, i.e., at 400 K (127° C) (fig. 5.5). Silkworm silk is known to have degraded drastically above 473 K [122]. We did not take readings for higher temper-

atures to prevent the silk from undergoing an irreversible glass transition and destroying its inherent structure.

5.4 Origin of Magnetism in Silkworm Silks

We have discovered the ferromagnetic character of silkworm silks (as shown by spider dragline silk) and believe that it is an inherent property of silk because of naturally occurring defects in β -sheet structures and not because of ferromagnetic impurities in them. However, to establish our claims, we will again have to investigate the presence (or absence) of ferromagnetic impurities (especially d-block elements) in silkworm silks to discover the true origin of magnetism in these materials.

5.4.1 Elemental Analysis

In this section, we confirm the absence of any ferromagnetic impurity in our samples using the same elemental analysis techniques (EDX, XPS, XAS, and ICPMS) we used for spider dragline silks. Our experiments agree with previous impurity analysis done on silks [33] and show that the observed magnetic properties of spider silk cannot be due to any metallic impurities. Our elemental data and concluding analysis are detailed below:

Elements	Atomic No.	Series	Unn. Conc. (Wt.%)	Norm. Conc. (Wt.%)	Atomic Conc. (at. %)	Error (Wt. %)
C	6	K-Series	65.18	65.18	63.7	10.4
O	8	K-Series	22.02	22.02	20.7	9.1
N	7	K-Series	12.80	12.80	16.6	6.6
Fe	26	K-Series	0	0	0	0
Ni	28	K-Series	0	0	0	0
Mn	25	K-Series	0	0	0	0
Co	27	K-Series	0	0	0	0
Cr	24	K-Series	0	0	0	0
		Total	100.00	100.00	100.00	

Table 5.1: **EDX Analysis.** Atomic concentration of selected elements in three independent samples of the silkworm silk.

- (1) **Energy dispersive X-ray spectrum (EDX):** The silk samples were coated with gold, and their EDX spectrum was taken using an electron beam of energies from 10 to 20

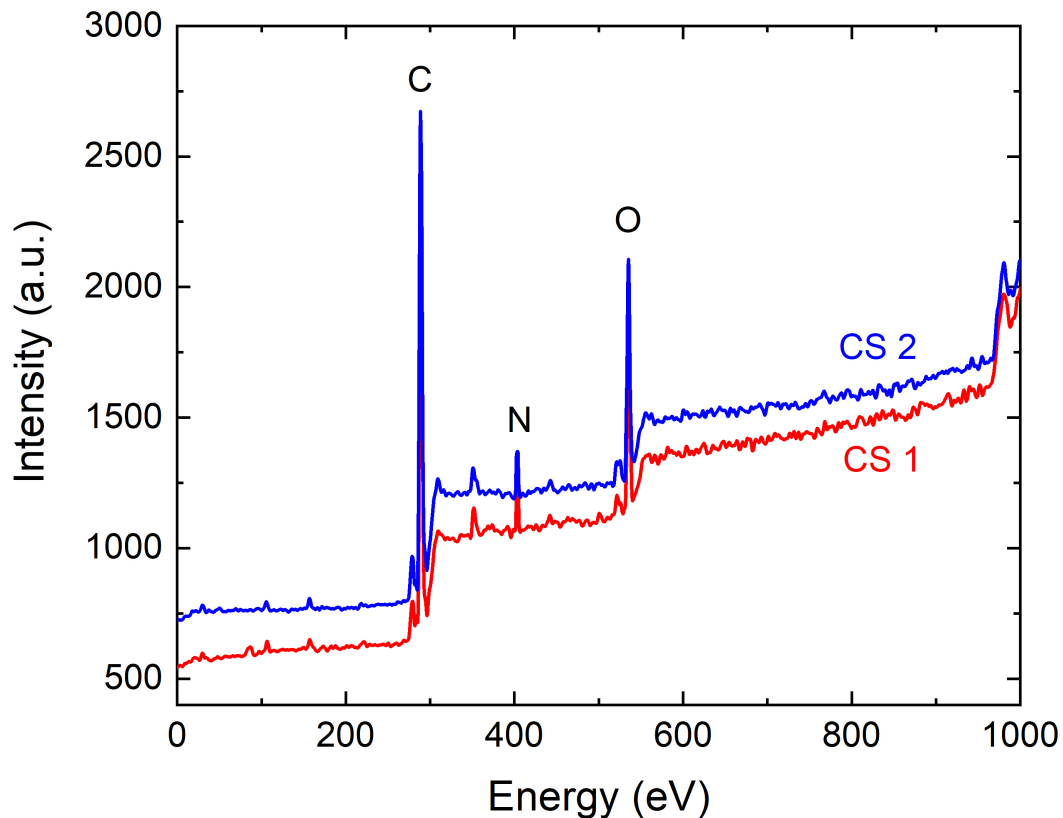


Figure 5.6: **XPS survey scan for three pristine silkworm silk samples.** The consistent peaks corresponding to carbon (C), oxygen (O), and nitrogen (N) are visible in both survey as well as core scans. We also got weak signals for other known elements like calcium (350 eV). However, there was no signal of any transition d-block and f-block elements in the survey scan. These measurements were performed on uncoated silk samples. Target plate area was $1\text{ cm} \times 1\text{ cm}$. The scan area of XPS is typically in μm^2 , and scanning depth is up to 10 nm . Measurements were performed in a high vacuum of 10^{-9} mbar

KeV. The typical spot size of the beam was a few μm^2 . The instrument was benchmarked and calibrated prior to measurements. We scanned about 4 to 5 locations on each sample.

The results obtained are shown in Table 5.1. The dominant contribution in the sample was C, N, O. We detected zero concentration of Fe, Mn, Ni, and Co for all the silk samples. The minimum detection limit of the EDX spectroscopy was 3000 ppm.

- (2) **X-ray photoelectron spectrum (XPS):** Prior to the experiments, we calibrated the XPS using pure silver thin film. We found that signals were shifted $\approx 4\text{ eV}$ in survey scans. Two silk samples were used for the XPS scan. The X-ray source was Aluminium (Al) K_{α} . Silk samples were uniformly spread with the help of carbon tape and used to stick the silk on the copper target plate. The survey scan is shown in Fig. 5.6 for all samples. The major atomic components like carbon (C), oxygen

(O), and nitrogen (N) were visible. However, there was no detectable signal for any ferromagnetic transition element in the d-block or f-block (Fe, Ni, Co, Gd).

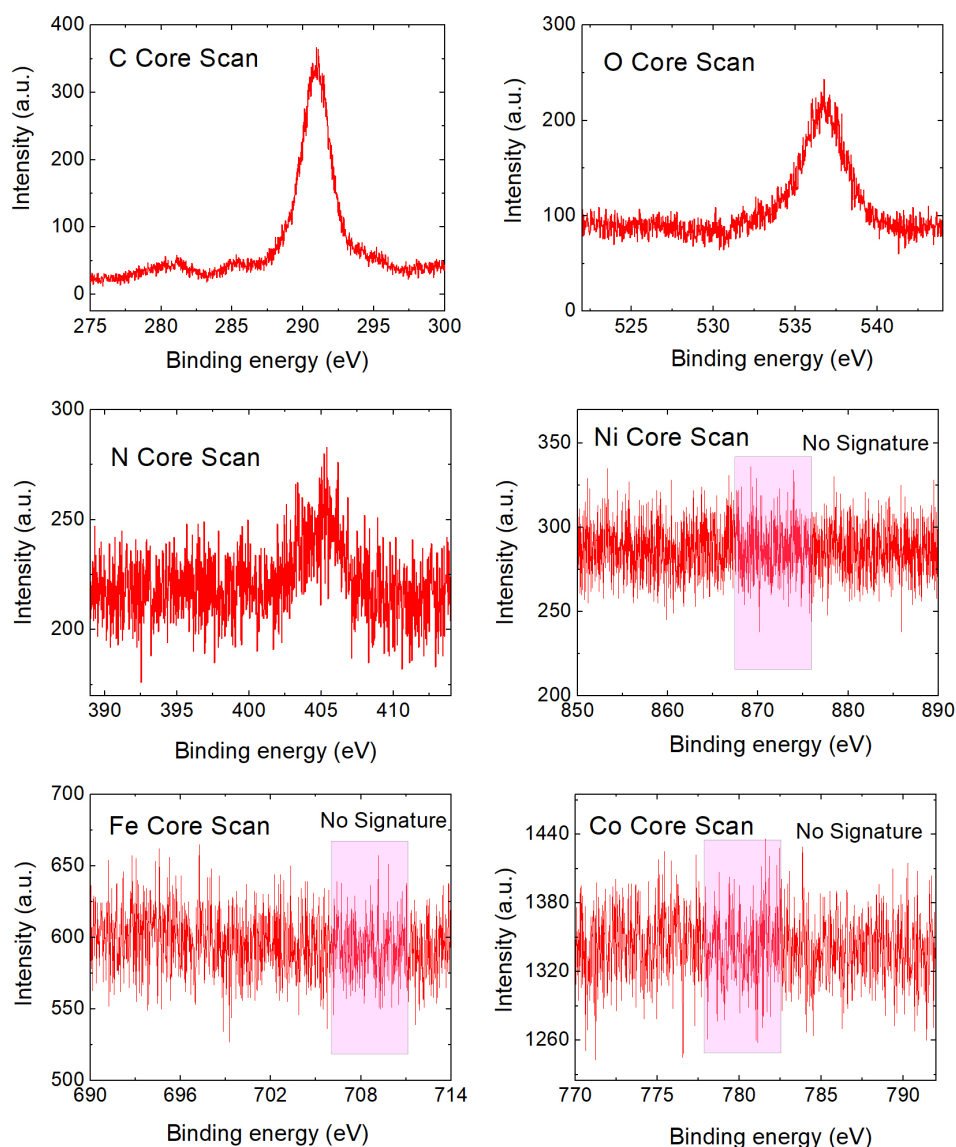


Figure 5.7: Core XPS scans confirming the absence of ferromagnetic elements. We further took dedicated core scans to detect the key elements (Fe, Co, Ni) that can be ferromagnetic at room temperature. The above results were obtained after five complete scans near their specified energy spectra; still, no signal was found above the background noise level. Fe's expected primary 2p signal lies from 706 eV to 710 eV. Ni's expected primary 2p signal lies from 852 eV to 855 eV. Expected primary 2p signal of Co lies from 778 eV to 779 eV [NIST XPS Database].

To reconfirm their absence in silk, we repeated dedicated core scans for Fe, Ni, and Co, as shown in Fig.5.7. The core scans were obtained by 5 complete scans of the specified energy range, where their signals are expected, and yet no signal was de-

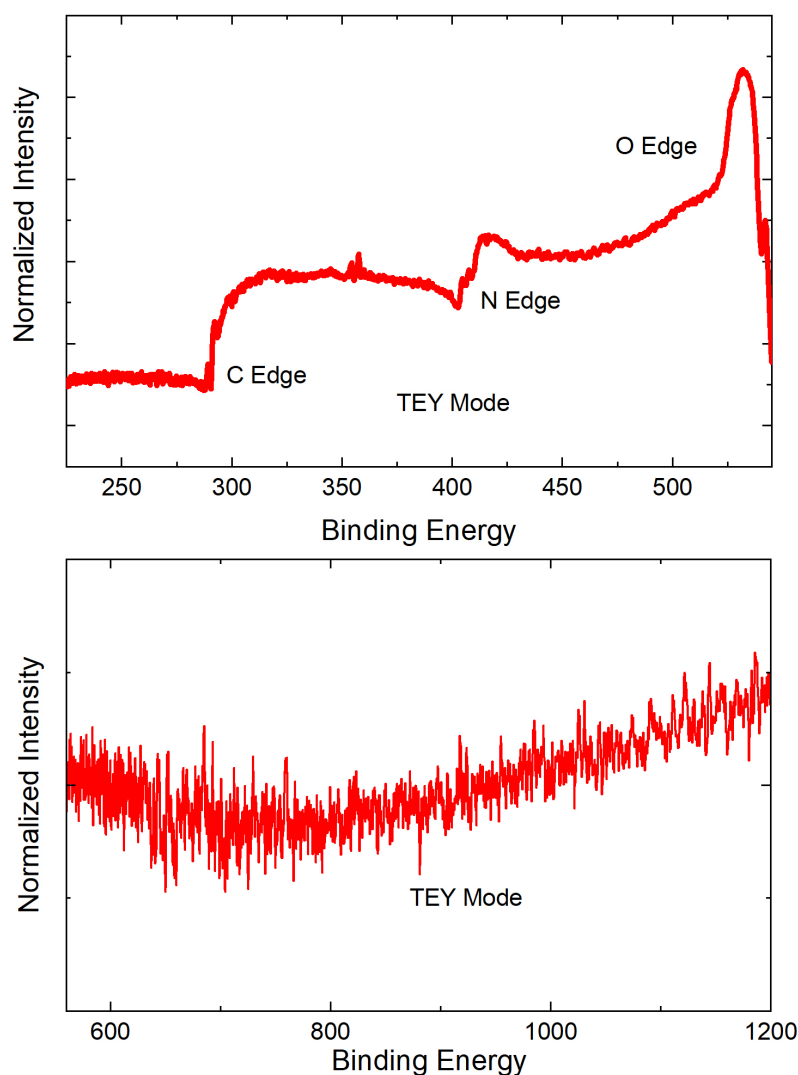


Figure 5.8: **XAS spectrum of silkworm silk samples.** The absorption edges of C, N, and O are visible. No absorption could be detected for heavy ferromagnetic atomic numbers (lower graph) like Fe, Ni, Co, or Mn.

tected. The detection period per scan was set at 300 s. The XPS can accurately detect the presence of an element on the surface of samples up to an atomic concentration of 100 parts per million (ppm).

- (3) **X-ray absorption spectroscopy (XAS):** Two silk bundle samples were analyzed using XAS in total electron yield (TEY) mode. The X-ray source was Indus 2, a synchrotron at Raja Raman Center for Advanced Technology (RRCAT), Indore, India. The obtained spectrum is shown in Fig.5.8. Here also, we could easily detect the basic atomic constituents of spider silk like C, N, and O. However, the scan for heavy transition metals (Fe, Ni, Co, and Mn) showed no detectable signal.

XAS in TEY mode can detect the presence of an element in a sample for more considerable depths (beneath the surface) than the XPS scan, with accuracies of about 10

ppm. The absence of any signal in this range also means that the d-block ferromagnetic elements were absent.

(4) **ICP-MS:** ICPMS grade HNO₃ and HCl were used for digestion, and high-performance liquid chromatography (HPLC) grade water was used for dilution purposes. 200 mg of silkworm silks was used for this experiment. The silks were microwave digested in a mixture of 5 ml of HNO₃ and 3 ml of HCl acids for 1 hour at a temperature of 220° C. After the silk was completely dissolved, 1 ml of the solution was diluted using 99 ml of water. Later the solution was filtered using 0.45 μm PTFE syringe filter. The filtered solution was then ready for experimentation. The calibration standards for ICPMS were then prepared from 1 ppb conc. to 10 ppm conc. Thermofisher ICP-MS (iCAP-RQ) instrument was used for the experiment. For assurance of the reliability of our results, we first experimented on a blank solution (sample without silks) to check the conc. of ferromagnetic impurities in the background solution. We used the same equipment and chemicals (acid, water, and syringe filter) to prepare the blank and silk solutions. We find that the concentration of ferromagnetic impurities in silk is << 0.1% (see table 5.2). The conc. of iron in silk is 1.58 mg/kg. Such a small conc. of iron cannot result in high saturation magnetization observed for silk. As one can calculate, the saturation magnetization of silk due to iron with 1.58 mg/kg conc. will be ten times smaller than the one expressed by our samples. Hence iron impurity cannot be envisaged as the source of ferromagnetism in our system.

Element	Iron	Nickel	Cobalt	Manganese
Concentration in blank solution	< 0 ng/kg	0.21 μg/kg	< 0 ng/kg	0.48 μg/kg
Concentration in silkworm silk	1.58 mg/kg	0.30 mg/kg	1.99 μg/kg	70 μg/kg

Table 5.2: **Concentration of ferromagnetic elements in silks.**

Our elemental characterization results indicate that the amount of ferromagnetic transition metals like Fe, Mn, Ni, and Co is negligible and insufficient to account for ferromagnetism in silk fibroins. Hence we suspect that the observed ferromagnetic response is a result of the ferromagnetic coupling of dangling bonds in silkworm silk.

However, to prove this conjecture, we must check if increasing the defects in silkworm silks can increase their magnetic characteristics, just as we did in the case of spider dragline silks.

5.4.2 Enhancement in magnetism of silk by tensile rupturing and cutting

To confirm the magnetostructural relationship of silkworm silks, we followed the same procedure as was carried out for spider dragline silk. Simple mechanisms such as excessive tensile loading and mechanical cutting were designed to enhance atomic defects in silkworm silks. Our results showed an enhancement in deformed silk's saturation magnetization, implying an increased number of ferromagnetically coupled spins in silk's hierarchical structure.

Below we elaborate on the two mechanisms used to deform the silk: (a) rupturing by tensile loading and (b) cutting into multiple small pieces.

Enhanced magnetization by tensile rupturing

Silk fibroin comprises nanocrystals β sheets of poly-(Gly-Ala) sequences. These nanocrystals make $\geq 50\%$ of silk fibroin. The nanocrystals are connected via amorphous domains of random amino acid sequences. Stretching silkworm silk using extreme stress deforms the *beta* sheets, and they eventually break. In effect, extreme tensile loading could enhance the atomic defects due to chain rupture or shear deformation of silk nanocrystals.

We observed that the saturation magnetization of the silk sample increases after rupturing it by extreme tensile stretching (strain rate of 5 mm/sec) (Fig. 5.9). The schematic illustration of the procedure to stretch the silk is shown in Fig. 5.9. We performed the following magnetization measurements sequentially:

- (1) First, the M-H curve of the pristine silkworm silk was measured at $T = 300 \text{ K}$ and $T = 10 \text{ K}$ (Sample label: CS 1 Pristine).
- (2) The same sample was then ruptured into small pieces by excessive stretching (CS 1 Ruptured), and the magnetization was measured again.

Rupturing silk into small pieces by stretching at a constant strain rate of 5 mm/sec increased the saturation magnetization of silk by 20% , implying that the number of ferromagnetically coupled dangling bonds increases with the increase in the number of defects in silk. The enhancement is observed both at $T = 300 \text{ K}$ and at low temperature at $T = 10 \text{ K}$. In comparison, the ruptured spider silk showed a 50% increase in saturation magnetization compared to its pristine counterparts. Apart from ferromagnetically coupled spins, free radicals in silk also increased significantly once the silk was ruptured. This is evident from the increased paramagnetic susceptibility of ruptured silk at $T = 10 \text{ K}$ compared to pristine silk (fig. 5.9(d)). Change in magnetic properties of silkworm silk by mechanical

stretching confirmed silk's structural and magnetic relationship while ruling out any other possible origin of its magnetism.

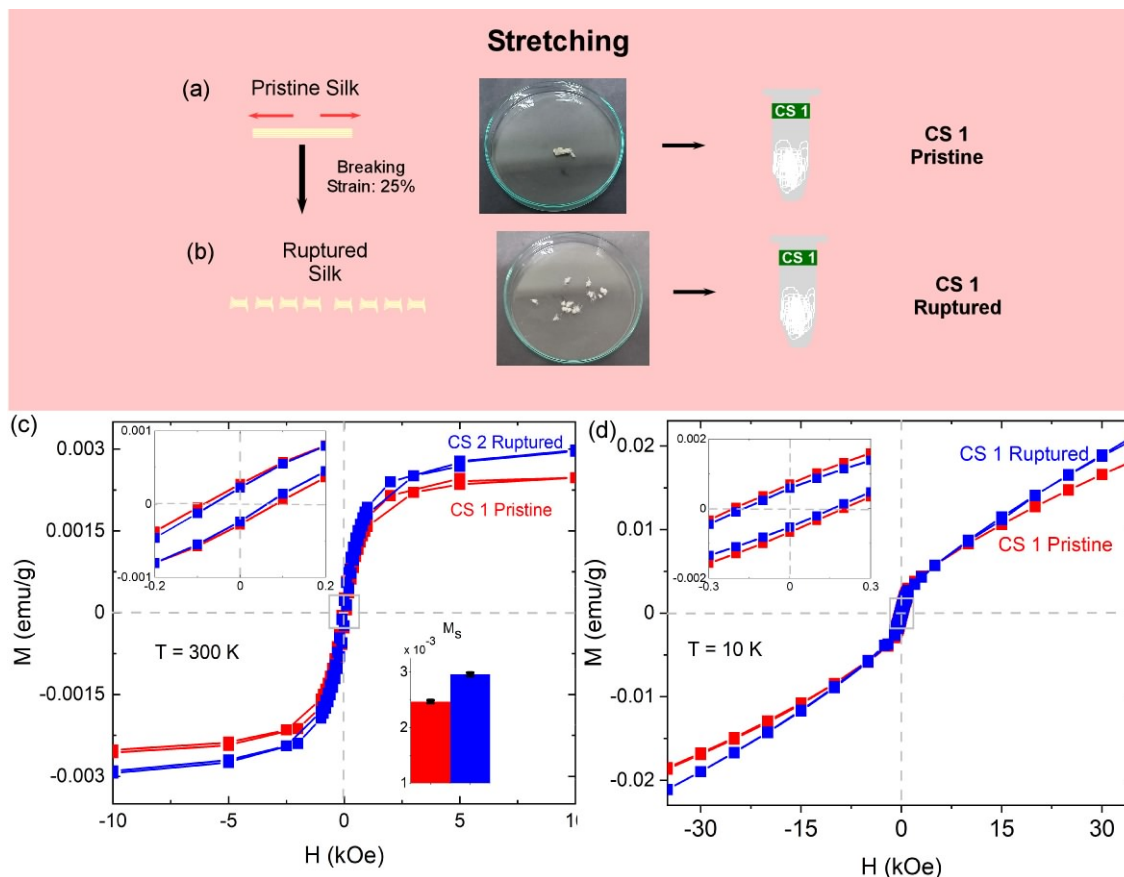


Figure 5.9: **Magnetometry with pristine and tensile ruptured silk.** Procedure of a series of experiments performed by stretching the silk is depicted along with the photographs of the actual silk sample. (a) shows the silk in its pristine form before stretching. This silk was ruptured into multiple small pieces by the stretching mechanism shown in (b). (c) Magnetometry data of the above two cases ((a) and (b)) at 300 K and 10 K (d). The inset on the left (c) shows a zoom of the data near zero magnetic field to highlight the comparison of M_r and H_c of ruptured and pristine silk samples. The inset on the right (c) shows a bar graph to compare the M_s of ruptured and pristine silk samples. The error bar highlights that the observed change in M_s is well above the experimental error.

Enhanced magnetization by mechanical cutting

Another method of deforming silk is mechanical cutting, as illustrated in Fig. 5.10. We used ceramic scissors to cut the pristine silkworm silks into small pieces to avoid any potential contamination of metal. We cut the silk with an approximate cut density of 120 cuts/cm. The magnetic measurements of this type were performed sequentially in the following manner :

- (i) First, the pristine silkworm silk was measured at $T = 300$ K and $T = 10$ K (CS 2).
- (ii) The same sample was cut into multiple pieces, and the cut silk (CS 2 Cut) was measured again.

Upon cutting the silk, its saturation magnetization increased by 11% compared to that of pristine silk, which is above the experimental error. The enhancement is modest in magnitude compared to the previous stretching mechanism because stretching produces defects uniformly throughout the silk sample compared to cutting, where defects are formed only where a cut has been made. We could see an increase in non-interacting dangling bonds in cut silk reflected in its increased paramagnetic behavior at $T = 10$ K compared to pristine silk. Nevertheless, it again provides conclusive evidence that the magnetic properties of silk are directly related to atomic defects in its structure.

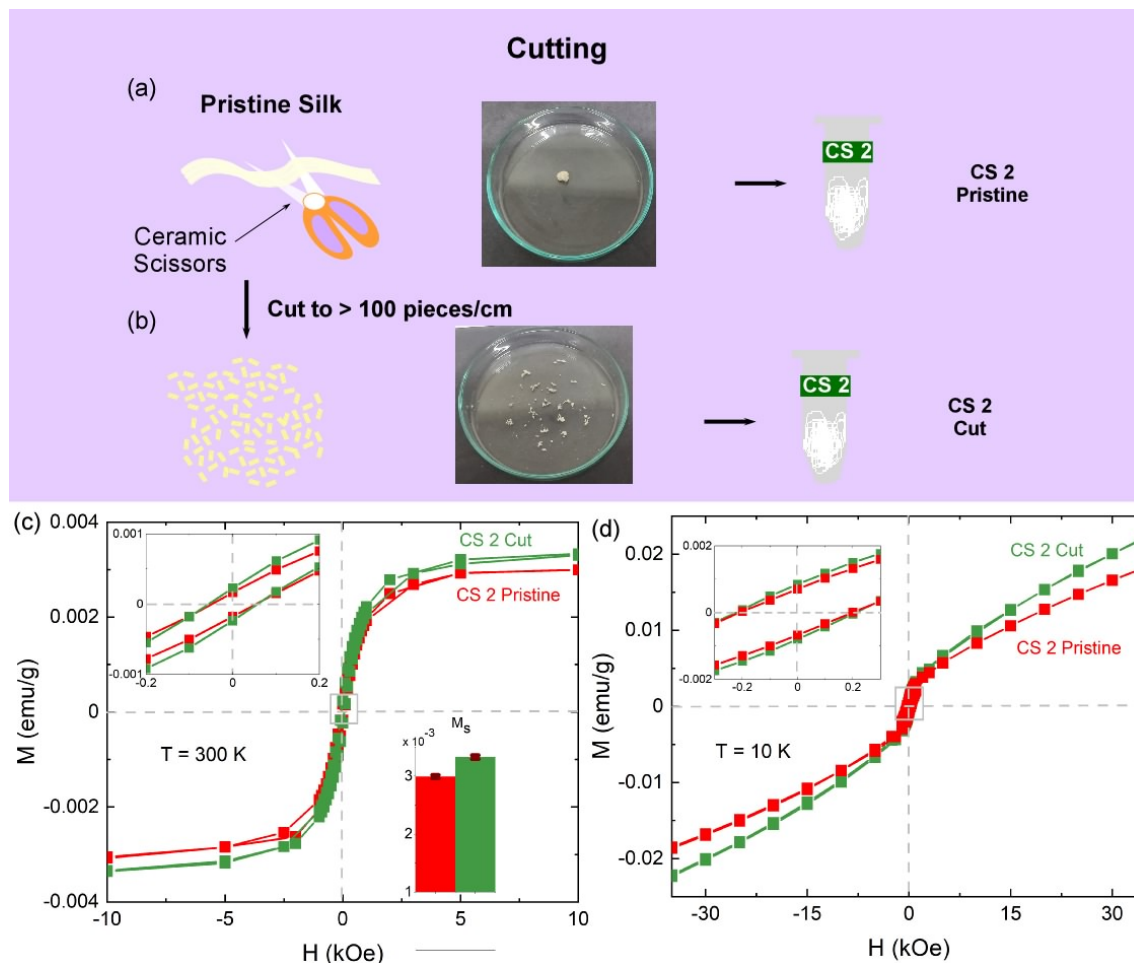


Figure 5.10: **Magnetometry with pristine and cut silk.** Procedure of a series of experiments performed by cutting silk is depicted along with photographs of the actual silk sample. (a) shows the silk in its pristine form before cutting. This silk was cut to over 100 pieces/cm using ceramic scissors, as shown in (b). (c) Magnetometry data of the above two cases ((a) and (b)) at 300 K and 10 K (d). The inset on the left (c) shows the zoom of the data near zero magnetic field to highlight the comparison of M_r and H_c of cut and pristine silk samples. The inset on the right (c) shows a bar graph to compare the M_s of cut and pristine silk samples. The error bar highlights that the observed change in M_s is well above the experimental error.

5.5 Magnetic Ordering of silkworm silks

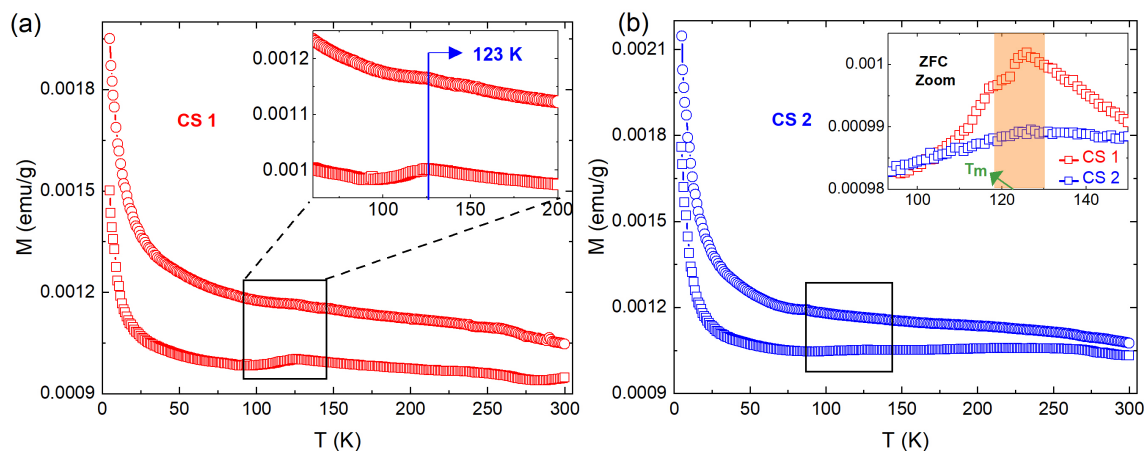


Figure 5.11: **FC-ZFC DC magnetization of silk samples.** (a-b): The FC data was taken at 1 kOe field. The background of oxygen has been subtracted from the samples. We can see that the magnetic transition near 120 K is consistent for all independent silk samples (highlighted by a box in each graph). The inset of the graph (a) shows the transition in FC and ZFC near 120 K. Inset of graph (b) shows the zoom ZFC curves of both CS 1 and CS 2 to highlight consistency in magnetic phase transition in silkworm silks.

Our investigation established that the magnetism of silkworm silks originates from interacting radicals in their structure. However, from our low-temperature MH results (10 K), it is clear that non-interacting radical spins coexist with ferromagnetically interacting radicals. Moreover, EPR data showed that clusters of ferromagnetically interacting radical spins exist in silk samples. Therefore, it is essential to understand the exact nature of magnetic ordering of spider dragline silk samples.

To unravel the magnetic ordering of silkworm silk, we did the thermomagnetic analysis, where silk's magnetization was measured at a constant magnetic field with changing temperature (MT characteristics). The experiments were performed at a constant magnetic field of 1000 Oe, and the temperature range set for the experiment was from 5 K - 300 K. As mentioned previously, performing experiments at higher temperatures can lead to the denaturation of silk samples. Thus the maximum temperature for experimentation was limited to 300 K. Both zero field-cooled (ZFC) and field-cooled (FC) responses were taken. The results of our thermomagnetic characterization are provided in figure 5.11.

We discussed the issue of air getting trapped in the fibrous ball of silk in Chapter 3 (section 3.5) in detail. Here we encounter the same problem. Therefore, the data presented in fig. 5.11 has been modified to remove the oxygen signature using the procedure explained in appendix C.

Once again, we see that independent silks show very similar MT characteristics, indicating their magnetic behavior's robustness. Moreover, one can not disregard the similarity between the MT characteristics of silkworm silks and spider dragline silks. Going from 300 K to 5 K (right to left), we see that ZFC and FC curves diverge at 300 K. This indicates an explicit spin-glass ordering in silk fibroins. On further cooling, we can see another re-entrant transition occurring around temperature $T = 120$ K, highlighted in graphs 5.11 (a-b) using a rectangular box. Such MT characteristics are again implicative of cluster spin glass magnetic ordering similar to spider dragline silks. One can concur that the re-entrant transition around temperature $T = 120$ K in all silks is reminiscent of spin-glass order and shows a crossover from ferromagnetic to asperomagnetic ordering as on further freezing the sample, the transverse components of the spin are frozen in random directions. The repeatability of silk MT behavior in independent silk samples is remarkable. It reinforces that silk's magnetic behavior is highly robust and linked to its inherent structure, not external impurities.

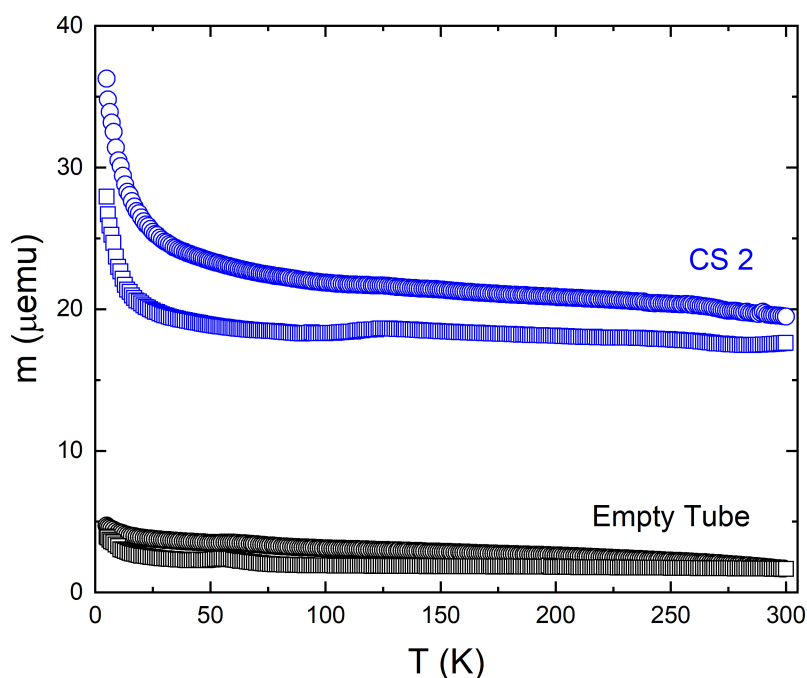


Figure 5.12: **Comparison of MT data between empty tube background and silk.** The MT data of the background in the absence of silkworm silk (black) show negligible magnetization for ZFC and FC with an applied magnetic field of 1000 Oe. Even at low temperatures < 40 K, magnetization data of empty tube is negligible as compared to spider silk, thus confirming the presence of non-interacting spins in silks. The silk data shown here is corrected by subtracting the oxygen background from them using the procedure explained in Appendix C. No oxygen correction was done in the empty tube.

Below 50 K, we can see that paramagnetism due to non-interacting and isolated radicals

present in silk starts dominating the magnetization data. This can be understood since the magnetic moment of paramagnets is inversely proportional to temperature ($M \propto \frac{1}{T}$). This is another confirmation of the presence of stable free radicals in silk. However, to ensure that these indeed are the paramagnetic signature of silkworm silk and not because of impurities from the background, we compared the MT results obtained from silk data to MT data of quartz holder and Teflon without the silk samples present in them (fig.5.12).

Thus, silkworm silks also behave as amorphous magnets with spins trapped in the glassy state in a protein matrix. Our thermomagnetic analysis establishes that silkworm silk exhibits spin-glass (or cluster spin glass) magnetic order. Random trapping of radicals in amorphous protein matrix brings out the coexistence of a variety of magnetic orders in silk structure such as ferromagnetism ($J > 0$), antiferromagnetism ($J < 0$), and paramagnetism ($J = 0$).

5.6 Representation of magnetic spins in silkworm silks

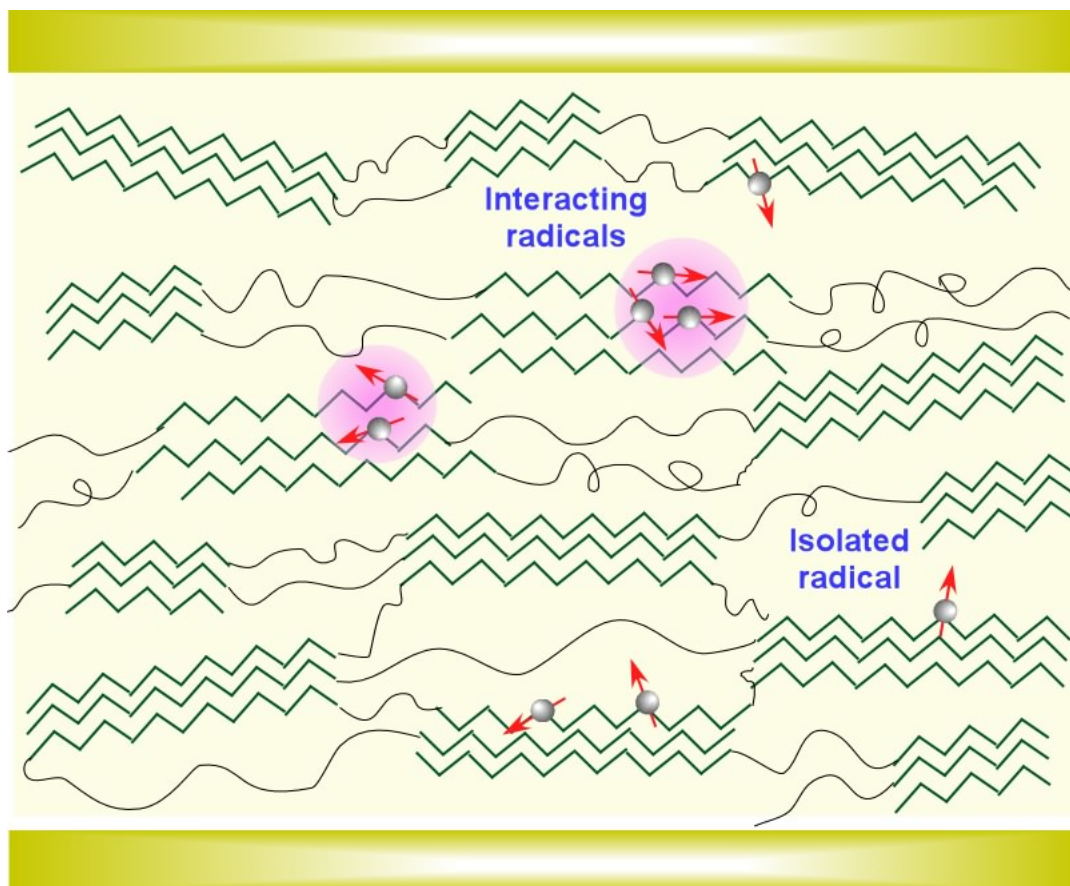


Figure 5.13: **Magnetic representation of silkworm silk.** The figure indicates that atomic defects in crystalline β sheets (green structures) of silk fibroin lead to the existence of free (isolated) and interacting radicals (shown in pink bubble).

Once again, in our quest to understand the origin of magnetism in pristine silkworm silks, it is clear that the source of magnetism cannot be linked to usual ferromagnetic d-block elements like iron, cobalt, nickel, etc. In fact, by deforming the silk structure and increasing the number of defects in it, one can tune its magnetism. Thereby, we concluded that the source of magnetism is the persistent radicals generated in silk's structure due to atomic defects in its structure. These defects arise during the silk-spinning process. The presence of such microvoids and defects in naturally spun silk has been discussed in the literature [128, 150].

Given the robust magnetic character of silk fibroins, the origin of magnetism has to be the repetitive $(GA)_n$ motif. All essential properties of proteins originate from their repeating motifs, and hence magnetism in silk fibroins must arise from atomic defects in poly-(Gly-Ala) β -sheets. These beta-sheets form highly rigid, dense, and compact crystallite structures of nanometer dimensions. The radicals formed on these β -sheet crystallites are compactly packed and protected sterically; thus, they can remain stable at room and high temperatures.

Moreover, as explained in chapter 3 (section 3.6), it was found that radicals created in beta sheets in small concentrations do not affect their mechanical stiffness [127]. On stretching silks, β -sheets undergo a slip-stick motion causing shear stress in their structure. This shear stress leads to displacement and rotation of amino acid chains forming the β -sheet. Reorienting sheets by breaking and reforming hydrogen bonds can cause minor structural atomic defects. Moreover, reorientation of existing radicals can bring about changes in their relative distances and conformation angles, affecting their magnetic interactions (exchange constant, J). Hence by controlling the strain and stress applied to the silk, one might also be able to tune the magnetic properties of silkworm silks.

Silkworm silks, just as spider silk system, from our observations, have a cluster spin glass magnetic ordering. A magnetic representation of radicals in silk fibroin is shown in fig. 5.13.

5.7 Comparison of magnetic properties of silk fibroin and spider silk

At the beginning of the chapter, we wanted to study the intrinsic magnetism of silkworm silks in detail. From our observation of the magnetism of spider silks, we expected the origin of magnetism in silkworm silk to be similar. This could be expected because both silks are made from the same amino acids: glycine and alanine. Our rigorous investigation showed that silk fibroins' magnetic character, ordering, and origin is similar to that observed

in spider dragline silks.

Our experimentation on silk fibroins has demonstrated that their soft magnetic nature is an intrinsic property that originates from organic radicals formed due to structural defects and not because of the minuscule impurity of iron (at sub-ppm level). Observing the robust ferromagnetic character and magnetic ordering of independent silk fibroins obtained from different silkworms, we concluded that the magnetic properties of silk fibroins must be related to their repetitive $(GA)_n$ motif. In fact, silkworm silks are made of $\approx 70\%$ of $(GA)_n$ sequence. Our results imply that poly-(Gly-Ala) beta sheets are a significant source of stable free radicals in silk materials. It was also confirmed computationally. DFT calculations confirmed that radicals at carbon and nitrogen atoms of the backbone, as well as side chains of $(GA)_n$ β -sheets can result in various configurations where these radicals can interact and form ferromagnetic or antiferromagnetic ground states based on the distances between these radicals [127].

Throughout this chapter, we compared the magnetism of silkworm silks with that of spider silk and found fundamental similarities between them. However, we also observed a difference in the order of magnitude between the magnetization of two types of silks. This observation enlightens us about the crucial importance and influence of the silk-spinning process on its magnetism. Insects have a valve that pulls and regulates the thickness of silk emerging from the spinnerets [1, 53]. Mechanical pulling holds a vital role in final silk formation as it undergoes a liquid-to-solid transition and can alter the structure of silk [54]. In the case of forceful silk spinning in spiders, spiders try to resist the silk spinning and pull the silk in the opposite direction creating stress on semi-crystalline silk emerging out of their glands. This influences the formation of β - sheets in spider silk and induces multiple defects in their structure. Therefore, we get an enhanced magnetic character of spider dragline silks. In the silkworm case, the silk was not spun forcefully; therefore, its structures might have fewer defects than in spider dragline silks. This is reflected in silkworm silk's magnetic properties, which are ten times smaller than spider silk's. However, further experiments will be needed to verify this hypothesis. More experiments in this direction will help us fabricate artificial protein based organic magnets with enhanced magnetization compared to natural silk polymers.

Furthermore, we find that the magnetic ordering of silkworm silks is similar to that of spider silks. The spin glass behavior of silks and the transition from ferromagnetic to asperomagnetic ordering at similar temperature $T \approx 120$ K imply that radicals in the β - sheets formed of $(-GA)_n$ motifs cause ferromagnetism in both silks. One can easily link the origin of magnetism in both silks. We could see that the magnetic transition in silkworm silks at $T \approx 120$ K was not as prominent as in spider silks. This is again linked to the smaller number of radicals in silk fibroin samples compared to spider dragline silk

samples. β -sheets of $(A)_n$ might also result in similar magnetic ordering, but there is no direct experimental method to confirm this.

Spider silks have poly-alanine $(A)_n$ repeat motif in addition to poly-(Gly-Ala), which also forms β -sheet structures. Radicals in $(A)_n$ might also show magnetic interaction. A thorough theoretical study is required to understand the stable radicals' atomic sites and their mode of exchange interaction in β -sheets of $(A)_n$.

In chapter 3, we saw magnetic silks' applications and their impact on the biomedical and technological industries. In this chapter, we provided further evidence that natural silks' unique structure provides surprising mechanical and remarkable magnetic properties. The magnetic properties of spiders and silkworm silks provide a new model for producing organic magnets with simple amino acid sequences and more accessible processing techniques.

Chapter 6

Concluding Remarks and Future Perspectives

6.1 Summary

At the beginning of the thesis, we talked about marvels of technology inspired by nature and how nature has always guided technologists to make landmark breakthroughs. The presented research work is again a small example of how millions of years of evolution helped spiders and silkworms engineer a way to develop organic magnets by employing their natural silk spinning technique using simple amino acids.

In chapter 3, we discovered the magnetism of pure spider dragline silk using a sensitive SQUID magnetometer and EPR spectroscopy. In extension to that, in chapter 4, we also showed that spiders might use the astounding ferromagnetic nature of their dragline as a source for magnetoreception. Silks have evolved their molecular structure to obtain exceptionally strong, tough, magnetically responsive fibers to support their host insect. Based on the similarity of amino acid sequences of spider silk (spidroin) and silkworm silk (fibroin), we investigated and found that silkworm silk also has an intrinsic magnetic character, as discussed in chapter 5. The origin of magnetism in both silks is attributed to organic radicals formed due to atomic defects in β -sheets of these silks.

β -sheets made of amino acid sequence '(GA)_n' are found in spider dragline and silkworm cocoon silks. Whereas β -sheets formed by the amino acid sequence '(A)_n' is exclusively found in spider dragline silks. The high density of hydrogen bonding in these β -sheet structures results in very tight binding of amino acid chains. β -sheets are responsible for the incredible strength of naturally occurring silks (chapter 1) and result in an environment where the radicals present within their structures can stay persistent for a very long time. The substantial steric hindrance of β -sheets protects the radicals within from the attack of external reactive species. When such radicals are close to each other, they

interact. The interaction can be ferromagnetic or antiferromagnetic based on their configuration and distance. DFT calculations confirmed that radicals at carbon and nitrogen atoms of the backbone, as well as side chains of $(GA)_n$ β -sheets, can result in various configurations where these radicals can directly interact and form ferromagnetic or antiferromagnetic ground states based on the distances between these radicals [127].

In conclusion, the research work has achieved the following results:

- Discovery of intrinsic magnetism of natural silk polymers.
- Understanding the magnetic properties and origin of magnetism in natural silks.
- Interpreting the magnetic ordering of natural silks.
- Designing new potential applications for natural silk polymers in technological and biomedical sectors.
- Laying out a potential method of magnetoreception used by spiders.

We will now discuss the future perspectives of the above discoveries.

6.2 Future Perspectives

A few future perspectives of the research were described in chapter 3. The presented research anticipates abundant applications such as fabricating all-protein magnetic utilities like rods, films, needles, etc. Development of magnetically activated silk-based artificial muscles, miniature robots for targeted drug delivery, magnetic traps, and scaffolds for growing cells/tissues/organs. Our work opens the intriguing potential of silk in developing ultra-light bio-magnetosensors, silk-based nano-mechanical devices, etc. Our results have implications in biomedical engineering, quantum biology, material science, magnetogenetics, and magnetic imaging.

Besides the above-stated applications, biomimicking these silk proteins can unfold a new avenue to fabricate organic magnets with exceptional mechanical, thermal, and optical properties. Another strength of such organic magnets comes from the simplicity with which these magnets can be produced, a simple protein processing in water under ambient conditions, compared to conventional magnets, which require pretty complex and energy-consuming resources. Moreover, biomimicking the silk structures can guide the development of artificial protein-based organic magnets operating at ambient and high temperatures.

Appendix A

Magnetic units conversion from CGS to SI

The following table provides the conversion table for magnetic units used in my research work from Gaussian or cgs units to SI units.

Quantity	Symbol	Gaussian units	Conversion factor	SI Units
Magnetic flux density	B	gauss (G)	10^{-4}	Tesla (T)
Magnetic Flux	ϕ	$G \cdot cm^2$	10^{-8}	Weber (Wb)
Magnetic field strength	H	Oersted (Oe)	$\frac{10^3}{4\pi}$	A/m
Mass magnetization	σ, M	emu/g	1	$A \cdot m^2/kg$
Magnetic moment	m	emu	10^{-3}	$A \cdot m^2$
Mass susceptibility	χ_m	$emu/g \cdot Oe$	$4\pi \times 10^{-3}$	m^3/kg

Table A.1: **Conversion table for magnetic units.** Multiply the value of "Quantity" expressed in cgs or Gaussian units by the "Conversion factor" to get the equivalent value in "SI units." (Adapted from IEEE magnetics.)

Appendix B

Magnetic Transitions of Oxygen

It is well known that oxygen under pressure and low temperatures undergo liquefaction at around 90 K. Liquid oxygen behaves as a paramagnet due to the presence of unpaired electrons. Further decreasing the temperature leads to its solidification. At lower temperatures, oxygen solid undergoes a magnetic transition of paramagnetic to antiferromagnetic. As we keep lowering the temperature, oxygen solid undergoes other structural transitions, affecting its magnetic moment. Solid oxygen present near 40 -50 K is also paramagnetic. We must note that all these structural and magnetic phase transitions are very sensitive to pressure and temperature, and thus these transition temperatures can vary.

In our experiment, the pressure is always kept constant throughout the SQUID magnetometer measurements, around 6-7 torr. We have described in section 3.5 that some air is always trapped in these bundles because of their fibrous nature when we compress them to load them in a SQUID magnetometer. The trapped oxygen (O_2 from the air) in these bundles starts undergoing several magnetic transitions as we reach temperatures below 75 K. In figure B.1, we highlight the transitions in our MT data because oxygen is trapped in the sample. These transitions are not actual magnetic transitions of silks but belong to trapped oxygen. A comparison between the transitions in our silks observed around 60 K and oxygen-thin films adsorbed on the surface of graphite is shown in figure B.1. We proved the absence of magnetic transition in silk samples around 60 K by preparing oxygen-free spider silks (Appendix C).

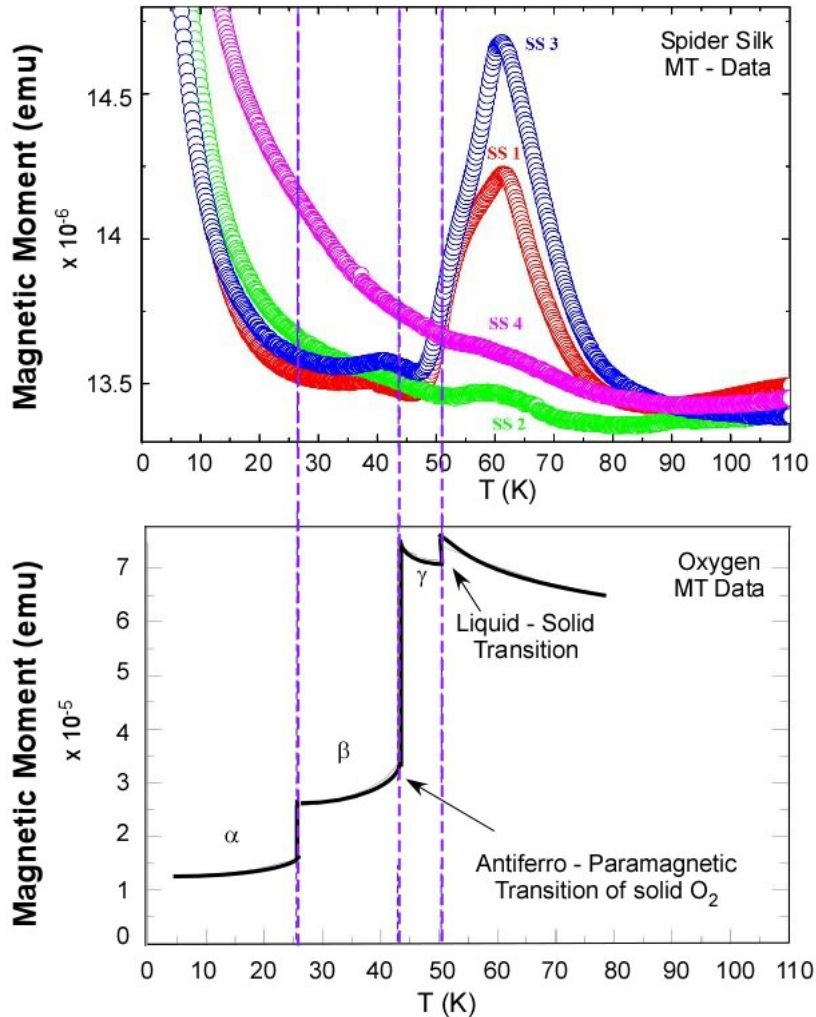


Figure B.1: **Comparison of magnetic transition in silk and oxygen at $T = 60$ K.** Comparison of magnetic moments of solid oxygen and spider dragline silks data. Note that the silk's magnetic signatures are consistent in all four samples and transition at 60 K correlates with two magnetic transitions of solid oxygen. The oxygen data is taken from [21] Below 30 K, the paramagnetism of silk samples overwhelms the α magnetic transition of oxygen solid, and hence it does not appear in our data. The magnetization data of silk are normalized for ease of comparison.

Appendix C

Sample preparation and thermomagnetic analysis of oxygen-free spider silk

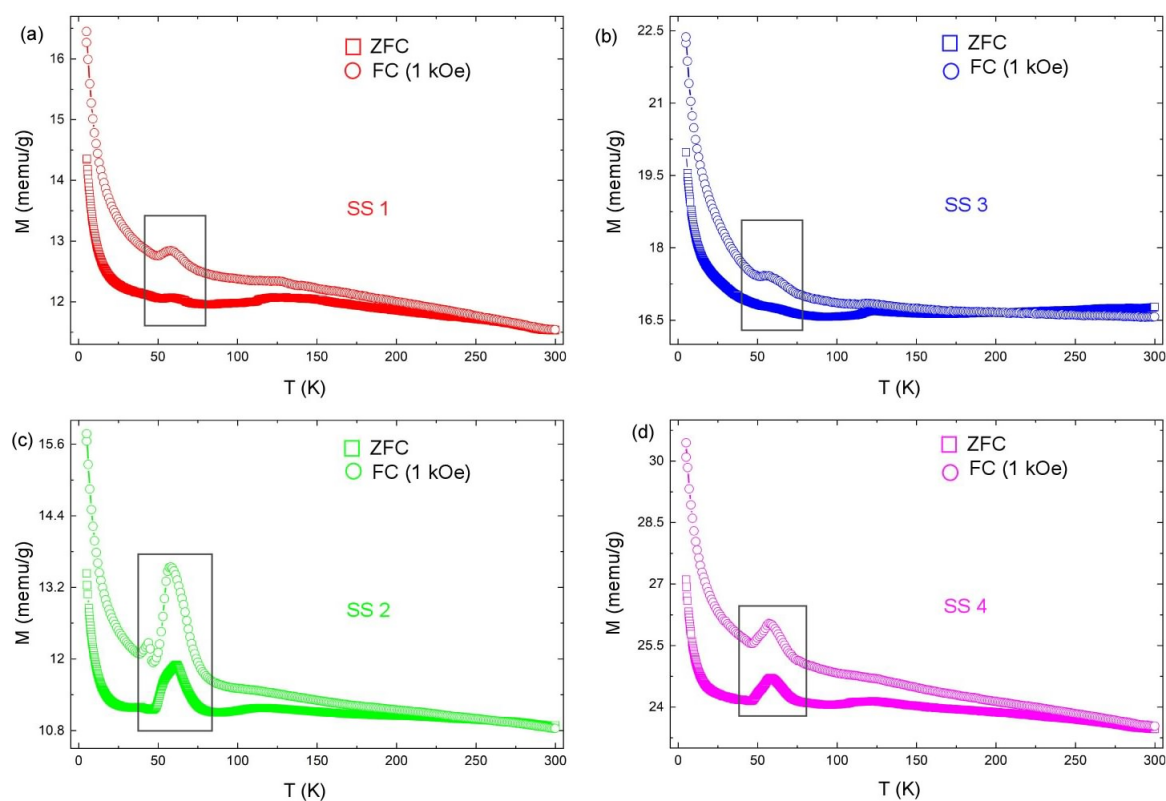


Figure C.1: FC-ZFC DC magnetization of four pristine samples SS1-SS4. (a-d): The FC data was taken at 1 kOe field without subtracting the oxygen data. We can see large Para-AFM transition bumps in the temperature range of 40 K - 60 K, highlighted with rectangular boxes. These belong to oxygen. These samples were prepared in ambient atmospheric conditions.

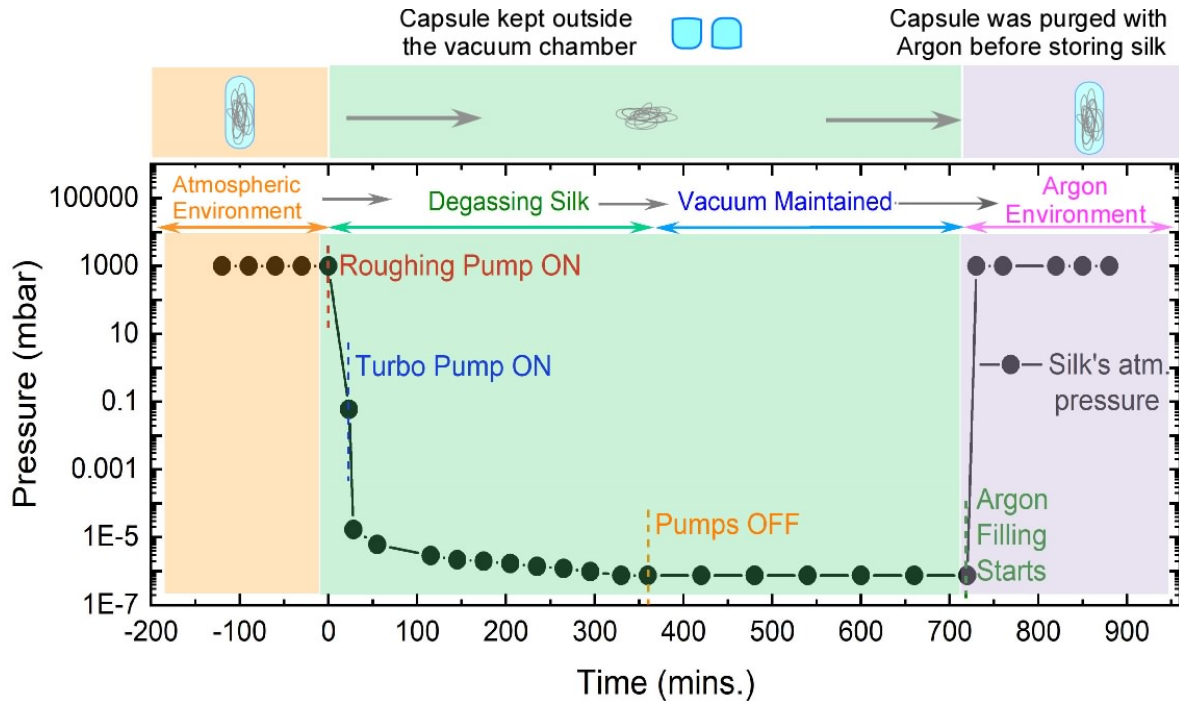


Figure C.2: **Preparation of oxygen-free silk sample for SQUID magnetometry.** The degassing/purging process of the silk is quantified in terms of the pressure in the chamber vs. time. After the pressure was reduced to 7.0×10^{-7} mbar, argon was pumped into the chamber till the pressure reached back to over 1 bar. The oxygen-free sample was carefully sealed in the argon-purged capsule in the argon environment.

We systematically prepared oxygen-free silk samples to obtain the MT characteristics at low temperatures (< 75 K) from the pristine silk. This is necessary because it is known that molecular oxygen from ambient air sometimes gets adsorbed on the sample surface and produces magnetic signals in the range of 40-70K [21, 151].

In our case, when the freshly extracted silk is compressed and filled in the MCT, it is likely that the oxygen from ambient air could enter and get trapped in our fibrous samples. During the variable temperature magnetization (MT) experiment, as soon as the temperature reaches below 90 K, the oxygen in this trapped air starts liquifying and eventually solidifies below its melting temperature. The phase transitions of the molecular oxygen are known to produce a broad AFM to paramagnetic transition signal at around 60 K [151]. Such signatures of molecular oxygen have been previously observed when the oxygen is adsorbed on various surfaces (graphite, palladium) during the measurements. The magnetic signals appear even with the atomic-scale thickness of adsorbed oxygen layer [21]. In all the four silk samples (SS1-SS4), we observed a broad hump in the temperature range 40 K – 90 K (fig. C.1). Therefore, it is necessary to confirm whether this structure is a property of the silk's magnetism or an artifact due to molecular oxygen trapped in the silk

sample.

To settle the above dilemma experimentally, we decided to replace the trapped air in the silk bundles with an inert gas such as argon which does not exhibit any magnetic signature. Our experimental procedure to prepare oxygen-free samples is schematically depicted in Fig. C.2. The silk samples were prepared at ambient conditions (297 K and 50% RH) and kept in a high vacuum (10^{-7} torr) for about 700 min. Then the chamber was purged with argon gas at a slight overpressure of 1.2 atm pressure. The capsule was also purged with argon gas (Fig. C.2), and the samples were sealed in the capsule in the argon environment for MT characteristics. Our process of degassing silk in a high vacuum ensured the complete removal of oxygen (air) trapped in the bundle. Purging silk with argon gas ensured that the samples were stored in an inert atmosphere to purify the magnetic signature of silk. Thus prepared capsules with silk in an argon environment were loaded directly on the tube of the SQUID magnetometer, and MT measurements were done.

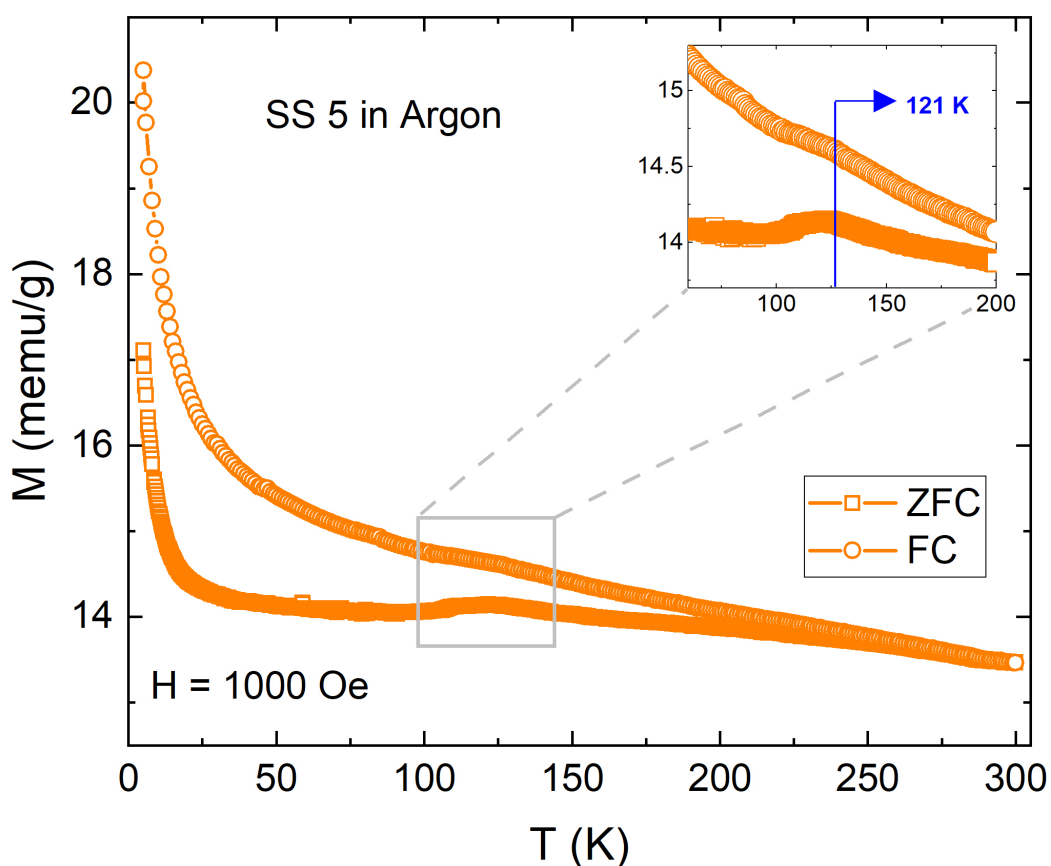


Figure C.3: **MT graph on silk in argon environment.** Note that the magnetic hump (near 60 K) disappeared once the air (oxygen) was replaced with argon. We also observe that the magnetic phase transition (see inset) persists at 120 K, which is consistent with all the silk samples as shown in Fig. 3.12.

MT magnetic measurement on oxygen-free silk is shown in Fig. C.3. Removing oxy-

gen from the sample eliminated the hump-like signatures previously observed in SS 1-4 samples. This measurement concluded that the magnetic phase transition at 60 K cannot be a feature of silk. We confirmed that the magnetic transition near 120 K is persistent in all the silk samples indicating that it is an intrinsic magnetic signature of natural silks.

C.1 Isolation of silk's magnetic signals from molecular oxygen near 60 K

From the previous section, it is clear that spider silk does not exhibit any phase transition around a temperature range of 40 - 90 K; instead, it arises due to magnetic states of oxygen trapped in silk bundles. Hence we are allowed to remove such backgrounds from all our MT data. Moreover, from Fig. C.3, we also found that the data in the range mentioned earlier can be fitted very closely by a second-degree polynomial ($y = a + bx + cx^2$). In the following Fig. C.4, we use this simple interpolation technique to subtract 60 K background from all our MT data.

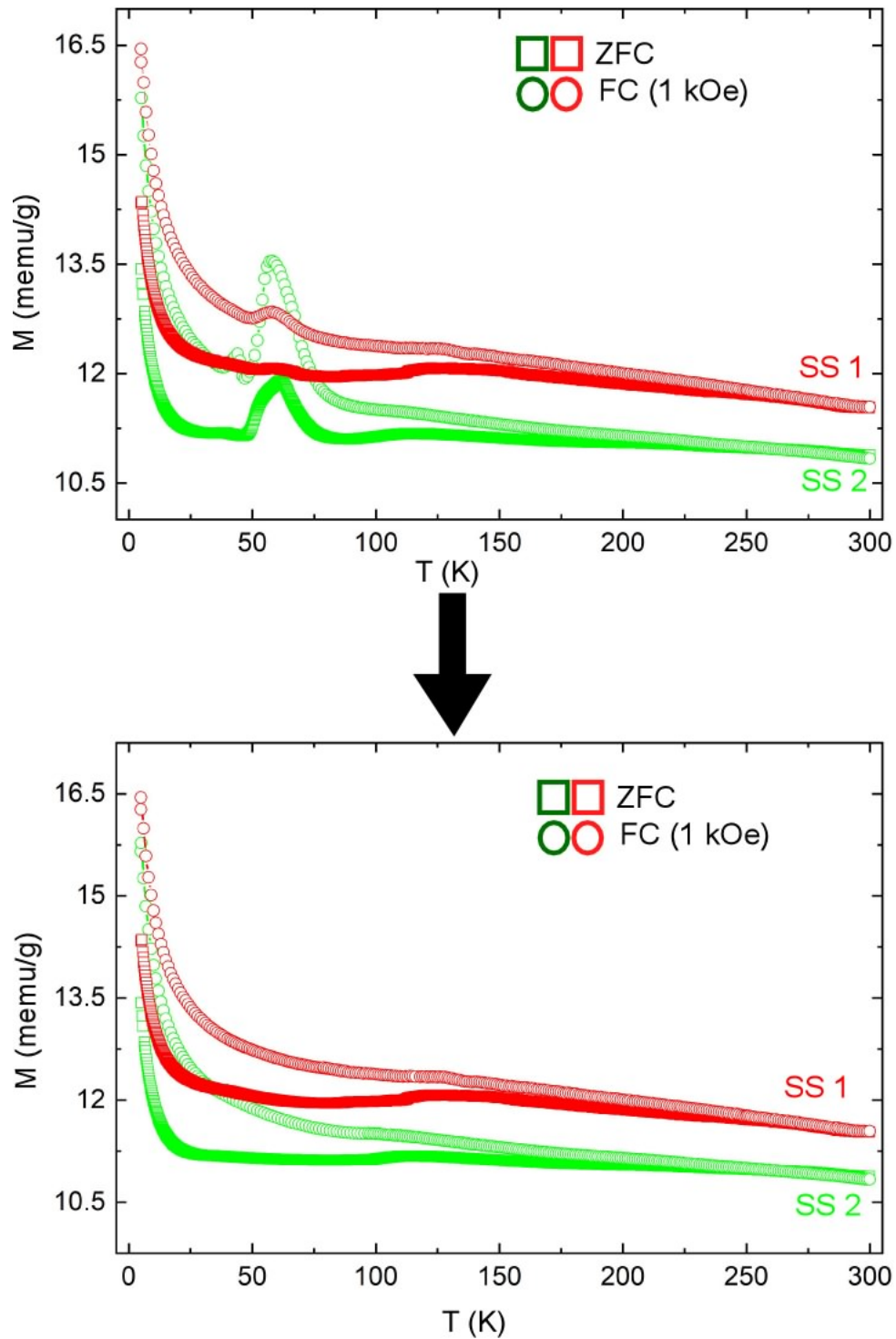


Figure C.4: **Purification of silk’s magnetism from low-temperature oxygen background.** The hump-like feature around 60 K was subtracted from the original data (top curve) using a polynomial fitting.

Appendix D

Calculation of magnetic moment per molecule for both silks

From chapter 3 and 5, we know the average saturation magnetization, M_s of spider and silkworm silks are 0.027 emu/g and 0.0028 emu/g respectively. The molar mass, M' of spider and silkworm silks are approximately 600 kg and 400 kg respectively [120, 149]. Knowing these two parameters, the following equation can be used to calculate the magnetic moment per molecule (ν) of a magnetic substance.

$$\nu = \frac{M_s(\text{emu/g}) \times M'(\text{g}) \times 1.07 \times 10^{20}(\mu_B/\text{emu})}{N_A} \mu_B/\text{molecule} \quad (\text{D.1})$$

Here N_A represents Avogadro number i.e. 6.022×10^{23} . Hence inserting the values of M_s and M' for each silk gives us their respective magnetic moment per molecule.

Bibliography

- [1] L. Eisoldt, A. Smith, and T. Scheibel, “Decoding the secrets of spider silk,” *Materials Today*, vol. 14, no. 3, pp. 80–86, 2011.
- [2] J. G. Hardy, L. M. Römer, and T. R. Scheibel, “Polymeric materials based on silk proteins,” *Polymer*, vol. 49, no. 20, pp. 4309–4327, 2008.
- [3] N. Du, Z. Yang, X. Y. Liu, Y. Li, and H. Y. Xu, “Structural origin of the strain-hardening of spider silk,” *Advanced Functional Materials*, vol. 21, no. 4, pp. 772–778, 2011.
- [4] C. M. Hurd, “Varieties of magnetic order in solids,” *Contemporary Physics*, vol. 23, no. 5, pp. 469–493, 1982.
- [5] J. M. D. Coey, *Magnetism and Magnetic Materials*. Cambridge University Press, 2010.
- [6] M. Krnel, S. Vrtnik, A. Jelen, P. Koželj, Z. Jagličić, A. Meden, M. Feuerbacher, and J. Dolinšek, “Speromagnetism and asperomagnetism as the ground states of the tbdy-ho-er-tm “ideal” high-entropy alloy,” *Intermetallics*, vol. 117, p. 106680, 2020.
- [7] Y. Zhang, G. P. Berman, and S. Kais, “The radical pair mechanism and the avian chemical compass: Quantum coherence and entanglement,” *International Journal of Quantum Chemistry*, vol. 115, no. 19, pp. 1327–1341, 2015.
- [8] S. Qin, H. Yin, C. Yang, Y. Dou, Z. Liu, P. Zhang, H. Yu, Y. Huang, J. Feng, J. Hao, *et al.*, “A magnetic protein biocompass,” *Nature materials*, vol. 15, no. 2, pp. 217–226, 2016.
- [9] M. Ballester, J. Riera-Figueras, J. Castaner, C. Badfa, and J. M. Monso, “Inert carbon free radicals. i. perchlorodiphenylmethyl and perchlorotriphenylmethyl radical series,” *Journal of the American Chemical Society*, vol. 93, no. 9, pp. 2215–2225, 1971.

- [10] R. Tamura, Y. Uchida, and K. Suzuki, “Magnetic and electric properties of organic nitroxide radical liquid crystals and ionic liquids,” in *Nitroxides* (A. I. Kokorin, ed.), ch. 6, Rijeka: IntechOpen, 2012.
- [11] J. Veciana and H. Iwamura, “Organic magnets,” *MRS Bulletin*, vol. 25, no. 11, p. 41–51, 2000.
- [12] J. Veciana, *Organic Magnetic Materials*, pp. 425–448. Dordrecht: Springer Netherlands, 1996.
- [13] J. S. Miller, “Organic- and molecule-based magnets,” *Materials Today*, vol. 17, no. 5, pp. 224–235, 2014.
- [14] M. Buchner, K. Höfler, B. Henne, V. Ney, and A. Ney, “Tutorial: Basic principles, limits of detection, and pitfalls of highly sensitive squid magnetometry for nanomagnetism and spintronics,” *Journal of Applied Physics*, vol. 124, no. 16, p. 161101, 2018.
- [15] P. Marcon and K. Ostanina, “Overview of methods for magnetic susceptibility measurement,” *Progress in Electromagnetics Research Symposium*, 01 2012.
- [16] M. Newville, “Fundamentals of XAFS,” *Reviews in Mineralogy and Geochemistry*, vol. 78, pp. 33–74, 01 2014.
- [17] S. C. Wilschefski and M. R. Baxter, “Inductively coupled plasma mass spectrometry: introduction to analytical aspects,” *The Clinical Biochemist Reviews*, vol. 40, no. 3, p. 115, 2019.
- [18] A. A. Ammann, “Inductively coupled plasma mass spectrometry (icp ms): a versatile tool,” *Journal of Mass Spectrometry*, vol. 42, no. 4, pp. 419–427, 2007.
- [19] Z. Wu, J. Troll, H.-H. Jeong, Q. Wei, M. Stang, F. Ziemssen, Z. Wang, M. Dong, S. Schnichels, T. Qiu, and P. Fischer, “A swarm of slippery micropropellers penetrates the vitreous body of the eye,” *Science Advances*, vol. 4, no. 11, p. eaat4388, 2018.
- [20] M. Hu, H.-J. Butt, K. Landfester, M. B. Bannwarth, S. Wooh, and H. Thérien-Aubin, “Shaping the assembly of superparamagnetic nanoparticles,” *ACS Nano*, vol. 13, no. 3, pp. 3015–3022, 2019. PMID: 30802035.
- [21] S. Gregory, “Magnetic susceptibility of oxygen adsorbed on graphite,” *Phys. Rev. Lett.*, vol. 40, pp. 723–725, Mar 1978.

- [22] Z. Shao and F. Vollrath, “Surprising strength of silkworm silk,” *Nature*, vol. 418, no. 6899, pp. 741–741, 2002.
- [23] H. Tao, D. L. Kaplan, and F. G. Omenetto, “Silk materials – a road to sustainable high technology,” *Advanced Materials*, vol. 24, no. 21, pp. 2824–2837, 2012.
- [24] C. Wang, K. Xia, Y. Zhang, and D. L. Kaplan, “Silk-based advanced materials for soft electronics,” *Accounts of Chemical Research*, vol. 52, no. 10, pp. 2916–2927, 2019. PMID: 31536330.
- [25] W. Huang, S. Ling, C. Li, F. G. Omenetto, and D. L. Kaplan, “Silkworm silk-based materials and devices generated using bio-nanotechnology,” *Chem. Soc. Rev.*, vol. 47, pp. 6486–6504, 2018.
- [26] J. A. Kluge, O. Rabotyagova, G. G. Leisk, and D. L. Kaplan, “Spider silks and their applications,” *Trends in Biotechnology*, vol. 26, no. 5, pp. 244–251, 2008.
- [27] C. Li, C. Guo, V. Fitzpatrick, A. Ibrahim, M. J. Zwierstra, P. Hanna, A. Lechtig, A. Nazarian, S. J. Lin, and D. L. Kaplan, “Design of biodegradable, implantable devices towards clinical translation,” *Nature Reviews Materials*, vol. 5, no. 1, pp. 61–81, 2020.
- [28] F. Vollrath and D. Porter, “Spider silk as archetypal protein elastomer,” *Soft Matter*, vol. 2, pp. 377–385, 2006.
- [29] D. Ebrahimi, O. Tokareva, N. G. Rim, J. Y. Wong, D. L. Kaplan, and M. J. Buehler, “Silk—its mysteries, how it is made, and how it is used,” *ACS Biomaterials Science & Engineering*, vol. 1, no. 10, pp. 864–876, 2015. PMID: 27398402.
- [30] L. Römer and T. Scheibel, “The elaborate structure of spider silk,” *Prion*, vol. 2, no. 4, pp. 154–161, 2008. PMID: 19221522.
- [31] F. G. Omenetto and D. L. Kaplan, “New opportunities for an ancient material,” *Science*, vol. 329, no. 5991, pp. 528–531, 2010.
- [32] Y. Zheng, H. Bai, Z. Huang, X. Tian, F.-Q. Nie, Y. Zhao, J. Zhai, and L. Jiang, “Directional water collection on wetted spider silk,” *Nature*, vol. 463, no. 7281, pp. 640–643, 2010.
- [33] M. Roy, A. Dubey, S. K. Singh, K. Bhargava, N. K. Sethy, D. Philip, S. Sarkar, A. Bajpai, and M. Das, “Soft magnetic memory of silk cocoon membrane,” *Scientific Reports*, vol. 6, no. 1, pp. 1–6, 2016.

- [34] S. Osaki, “Spider silk violin strings with a unique packing structure generate a soft and profound timbre,” *Phys. Rev. Lett.*, vol. 108, p. 154301, Apr 2012.
- [35] C. Riekkel, M. Burghammer, and M. Rosenthal, “Nanoscale x-ray diffraction of silk fibers,” *Frontiers in Materials*, vol. 6, 2019.
- [36] L. F. Drummy, B. L. Farmer, and R. R. Naik, “Correlation of the β -sheet crystal size in silk fibers with the protein amino acid sequence,” *Soft Matter*, vol. 3, pp. 877–882, 2007.
- [37] Z. Yang, D. T. Grubb, and L. W. Jelinski, “Small-angle x-ray scattering of spider dragline silk,” *Macromolecules*, vol. 30, no. 26, pp. 8254–8261, 1997.
- [38] G. R. Plaza, J. Pérez-Rigueiro, C. Riekkel, G. B. Perea, F. Agulló-Rueda, M. Burghammer, G. V. Guinea, and M. Elices, “Relationship between microstructure and mechanical properties in spider silk fibers: identification of two regimes in the microstructural changes,” *Soft Matter*, vol. 8, pp. 6015–6026, 2012.
- [39] I. Marcotte, J. D. van Beek, and B. H. Meier, “Molecular disorder and structure of spider dragline silk investigated by two-dimensional solid-state nmr spectroscopy,” *Macromolecules*, vol. 40, no. 6, pp. 1995–2001, 2007.
- [40] J. D. van Beek, S. Hess, F. Vollrath, and B. H. Meier, “The molecular structure of spider dragline silk: Folding and orientation of the protein backbone,” *Proceedings of the National Academy of Sciences*, vol. 99, no. 16, pp. 10266–10271, 2002.
- [41] C. Dicko, D. Knight, J. M. Kenney, and F. Vollrath, “Structural conformation of spidroin in solution: a synchrotron radiation circular dichroism study,” *Biomacromolecules*, vol. 5, no. 3, pp. 758–767, 2004. PMID: 15132658.
- [42] M. Boulet-Audet, F. Vollrath, and C. Holland, “Identification and classification of silks using infrared spectroscopy,” *Journal of Experimental Biology*, vol. 218, pp. 3138–3149, 10 2015.
- [43] J. Sirichaisit, V. L. Brookes, R. J. Young, and F. Vollrath, “Analysis of structure/property relationships in silkworm (*bombyx mori*) and spider dragline (*nephila edulis*) silks using raman spectroscopy,” *Biomacromolecules*, vol. 4, no. 2, pp. 387–394, 2003. PMID: 12625736.
- [44] B. Lee, E. Pires, A. M. Pollard, and J. S. McCullagh, “Species identification of silks by protein mass spectrometry reveals evidence of wild silk use in antiquity,” *Scientific reports*, vol. 12, no. 1, pp. 1–16, 2022.

- [45] C. Larracas, R. Hekman, S. Dyrness, A. Arata, C. Williams, T. Crawford, and C. A. Vierra, “Comprehensive proteomic analysis of spider dragline silk from black widows: A recipe to build synthetic silk fibers,” *International Journal of Molecular Sciences*, vol. 17, no. 9, 2016.
- [46] F. Takei, Y. Kikuchi, A. Kikuchi, S. Mizuno, and K. Shimura, “Further evidence for importance of the subunit combination of silk fibroin in its efficient secretion from the posterior silk gland cells.,” *Journal of Cell Biology*, vol. 105, pp. 175–180, 07 1987.
- [47] M. Xu and R. V. Lewis, “Structure of a protein superfiber: spider dragline silk.,” *Proceedings of the National Academy of Sciences*, vol. 87, no. 18, pp. 7120–7124, 1990.
- [48] X. Liu and K.-Q. Zhang, “Silk fiber — molecular formation mechanism, structure-property relationship and advanced applications,” in *Oligomerization of Chemical and Biological Compounds* (C. Lesieur, ed.), ch. 3, Rijeka: IntechOpen, 2014.
- [49] S. Ketten, Z. Xu, B. Ihle, and M. J. Buehler, “Nanoconfinement controls stiffness, strength and mechanical toughness of β -sheet crystals in silk,” *Nature materials*, vol. 9, no. 4, pp. 359–367, 2010.
- [50] T. Asakura and J. Yao, “ ^{13}C cp/mas nmr study on structural heterogeneity in bombyx mori silk fiber and their generation by stretching,” *Protein Science*, vol. 11, no. 11, pp. 2706–2713, 2002.
- [51] G. P. Holland, J. E. Jenkins, M. S. Creager, R. V. Lewis, and J. L. Yarger, “Quantifying the fraction of glycine and alanine in β -sheet and helical conformations in spider dragline silk using solid-state nmr,” *Chem. Commun.*, pp. 5568–5570, 2008.
- [52] J. E. Jenkins, M. S. Creager, R. V. Lewis, G. P. Holland, and J. L. Yarger, “Quantitative correlation between the protein primary sequences and secondary structures in spider dragline silks,” *Biomacromolecules*, vol. 11, no. 1, pp. 192–200, 2010. PMID: 20000730.
- [53] H.-J. Jin and D. L. Kaplan, “Mechanism of silk processing in insects and spiders,” *Nature*, vol. 424, no. 6952, pp. 1057–1061, 2003.
- [54] F. Vollrath and D. P. Knight, “Liquid crystalline spinning of spider silk,” *Nature*, vol. 410, no. 6828, pp. 541–548, 2001.

- [55] M. Heim, D. Keerl, and T. Scheibel, "Spider silk: From soluble protein to extraordinary fiber," *Angewandte Chemie International Edition*, vol. 48, no. 20, pp. 3584–3596, 2009.
- [56] T. Yucel, P. Cebe, and D. L. Kaplan, "Structural origins of silk piezoelectricity," *Advanced Functional Materials*, vol. 21, no. 4, pp. 779–785, 2011.
- [57] J. N. Monks, B. Yan, N. Hawkins, F. Vollrath, and Z. Wang, "Spider silk: Mother nature's bio-superlens," *Nano Letters*, vol. 16, no. 9, pp. 5842–5845, 2016. PMID: 27531579.
- [58] G. Perotto, Y. Zhang, D. Naskar, N. Patel, D. L. Kaplan, S. C. Kundu, and F. G. Omenetto, "The optical properties of regenerated silk fibroin films obtained from different sources," *Applied Physics Letters*, vol. 111, no. 10, p. 103702, 2017.
- [59] D. M. Chow, K. H. Tow, F. Vollrath, I. Dicaire, T. Gheysens, and L. Thévenaz, "Shedding light on the optical properties of spider silk fiber," in *2015 IEEE Photonics Conference (IPC)*, pp. 333–334, 2015.
- [60] F. G. Omenetto and D. L. Kaplan, "A new route for silk," *Nature Photonics*, vol. 2, no. 11, pp. 641–643, 2008.
- [61] X. Huang, G. Liu, and X. Wang, "New secrets of spider silk: Exceptionally high thermal conductivity and its abnormal change under stretching," *Advanced Materials*, vol. 24, no. 11, pp. 1482–1486, 2012.
- [62] P. Bhattacharjee, B. Kundu, D. Naskar, H.-W. Kim, T. K. Maiti, D. Bhattacharya, and S. C. Kundu, "Silk scaffolds in bone tissue engineering: An overview," *Acta Biomaterialia*, vol. 63, pp. 1–17, 2017.
- [63] J. Coey and P. Readman, "New spin structure in an amorphous ferric gel," *Nature*, vol. 246, no. 5434, pp. 476–478, 1973.
- [64] J. Coey and P. Readman, "Characterisation and magnetic properties of natural ferric gel," *Earth and Planetary Science Letters*, vol. 21, no. 1, pp. 45–51, 1973.
- [65] M. Babaei, I. C. Jones, K. Dayal, and M. S. Mauter, "Computing the diamagnetic susceptibility and diamagnetic anisotropy of membrane proteins from structural subunits," *Journal of Chemical Theory and Computation*, vol. 13, no. 6, pp. 2945–2953, 2017. PMID: 28418668.
- [66] D.-C. Yin, "Protein crystallization in a magnetic field," *Progress in Crystal Growth and Characterization of Materials*, vol. 61, no. 1, pp. 1–26, 2015.

- [67] N. I. Wakayama, “Effects of a strong magnetic field on protein crystal growth,” *Crystal Growth & Design*, vol. 3, no. 1, pp. 17–24, 2003.
- [68] D. L. Worcester, “Structural origins of diamagnetic anisotropy in proteins.,” *Proceedings of the National Academy of Sciences*, vol. 75, no. 11, pp. 5475–5477, 1978.
- [69] A. R. Jones, “Magnetic field effects in proteins,” *Molecular Physics*, vol. 114, no. 11, pp. 1691–1702, 2016.
- [70] H. Hayashi and T. Azumi, *Dynamic Spin Chemistry: Magnetic Controls and Spin Dynamics of Chemical Reactions*. Kodansha, 1998.
- [71] K. Schulten, C. E. Swenberg, and A. Weller, “A biomagnetic sensory mechanism based on magnetic field modulated coherent electron spin motion,” *Zeitschrift für Physikalische Chemie*, vol. 111, no. 1, pp. 1–5, 1978.
- [72] P. J. Hore and H. Mouritsen, “The radical-pair mechanism of magnetoreception,” *Annual Review of Biophysics*, vol. 45, no. 1, pp. 299–344, 2016. PMID: 27216936.
- [73] R. J. Gegear, L. E. Foley, A. Casselman, and S. M. Reppert, “Animal cryptochromes mediate magnetoreception by an unconventional photochemical mechanism,” *Nature*, vol. 463, no. 7282, pp. 804–807, 2010.
- [74] J. Xu, L. E. Jarocho, T. Zollitsch, M. Konowalczyk, K. B. Henbest, S. Richert, M. J. Goleworthy, J. Schmidt, V. Déjean, D. J. Sowood, *et al.*, “Magnetic sensitivity of cryptochrome 4 from a migratory songbird,” *Nature*, vol. 594, no. 7864, pp. 535–540, 2021.
- [75] T. L. Li, Z. Wang, H. You, Q. Ong, V. J. Varanasi, M. Dong, B. Lu, S. P. Paşca, and B. Cui, “Engineering a genetically encoded magnetic protein crystal,” *Nano Letters*, vol. 19, no. 10, pp. 6955–6963, 2019. PMID: 31552740.
- [76] P. Turek, K. Nozawa, D. Shiomi, K. Awaga, T. Inabe, Y. Maruyama, and M. Kinoshita, “Ferromagnetic coupling in a new phase of the p-nitrophenyl nitronyl nitroxide radical,” *Chemical Physics Letters*, vol. 180, no. 4, pp. 327–331, 1991.
- [77] Z. Wang and W. Qin, “Organic magnetoelectric and optomagnetic couplings: perspectives for organic spin optoelectronics,” *NPG Asia Materials*, vol. 13, no. 1, pp. 1–12, 2021.
- [78] A. Izuoka, S. Murata, T. Sugawara, and H. Iwamura, “Molecular design and model experiments of ferromagnetic intermolecular interaction in the assembly of high-spin organic molecules. generation and characterization of the spin states of isomeric

- bis (phenylmethylenyl)[2.2] paracyclophanes,” *Journal of the American Chemical Society*, vol. 109, no. 9, pp. 2631–2639, 1987.
- [79] J. S. Miller, J. C. Calabrese, H. Rommelmann, S. R. Chittipeddi, J. H. Zhang, W. M. Reiff, and A. J. Epstein, “Ferromagnetic behavior of $[\text{Fe}(\text{C}_5\text{Me}_5)_2]^+ \cdot [\text{TCNE}]^-$ structural and magnetic characterization of decamethylferrocenium tetracyanoethenide, $[\text{Fe}(\text{C}_5\text{Me}_5)_2]^+ \cdot [\text{TCNE}]^- \cdot \text{mecn}$ and decamethylferrocenium pentacyanopropenide, $[\text{Fe}(\text{C}_5\text{Me}_5)_2]^+ \cdot [\text{C}_3(\text{CN})_5]^-$,” *Journal of the American Chemical Society*, vol. 109, no. 3, pp. 769–781, 1987.
- [80] J.-H. Her, P. W. Stephens, J. Ribas-Ariño, J. J. Novoa, W. W. Shum, and J. S. Miller, “Structure and magnetic interactions in the organic-based ferromagnet decamethylferrocenium tetracyanoethenide, $[\text{Fe}(\text{C}_5\text{Me}_5)_2]^+ \cdot [\text{TCNE}]^-$,” *Inorganic Chemistry*, vol. 48, no. 8, pp. 3296–3307, 2009.
- [81] P. Perlepe, I. Oyarzabal, A. Mailman, M. Yquel, M. Platunov, I. Dovgaliuk, M. Rouzières, P. Négrier, D. Mondieig, E. A. Suturina, M.-A. Dourges, S. Bonhommeau, R. A. Musgrave, K. S. Pedersen, D. Chernyshov, F. Wilhelm, A. Rogalev, C. Mathonière, and R. Clérac, “Metal-organic magnets with large coercivity and ordering temperatures up to 242 K,” *Science*, vol. 370, no. 6516, pp. 587–592, 2020.
- [82] N. A. Zaidi, S. Giblin, I. Terry, and A. Monkman, “Room temperature magnetic order in an organic magnet derived from polyaniline,” *Polymer*, vol. 45, no. 16, pp. 5683–5689, 2004.
- [83] H. Phan, T. S. Heng, D. Wang, X. Li, W. Zeng, J. Ding, K. P. Loh, A. T. Shen Wee, and J. Wu, “Room-temperature magnets based on 1,3,5-triazine-linked porous organic radical frameworks,” *Chem*, vol. 5, no. 5, pp. 1223–1234, 2019.
- [84] J. Mahmood, J. Park, D. Shin, H.-J. Choi, J.-M. Seo, J.-W. Yoo, and J.-B. Baek, “Organic ferromagnetism: Trapping spins in the glassy state of an organic network structure,” *Chem*, vol. 4, no. 10, pp. 2357–2369, 2018.
- [85] J. Tuček, K. Holá, A. B. Bourlinos, P. Błoński, A. Bakandritsos, J. Ugolotti, M. Dubecký, F. Karlický, V. Ranc, K. Čépe, *et al.*, “Room temperature organic magnets derived from sp^3 functionalized graphene,” *Nature communications*, vol. 8, no. 1, pp. 1–12, 2017.
- [86] P. Esquinazi, D. Spemann, R. Höhne, A. Setzer, K.-H. Han, and T. Butz, “Induced magnetic ordering by proton irradiation in graphite,” *Phys. Rev. Lett.*, vol. 91, p. 227201, Nov 2003.

- [87] A. V. Rode, E. G. Gamaly, A. G. Christy, J. G. Fitz Gerald, S. T. Hyde, R. G. Elliman, B. Luther-Davies, A. I. Veinger, J. Androulakis, and J. Giapintzakis, “Unconventional magnetism in all-carbon nanofoam,” *Phys. Rev. B*, vol. 70, p. 054407, Aug 2004.
- [88] T. Junghoefer, A. Calzolari, I. Baev, M. Glaser, F. Ciccullo, E. Giangrisostomi, R. Ovsyannikov, F. Kielgast, M. Nissen, J. Schwarz, N. M. Gallagher, A. Rajca, M. Martins, and M. B. Casu, “Magnetic behavior in metal-free radical thin films,” *Chem*, vol. 8, no. 3, pp. 801–814, 2022.
- [89] O. Céspedes, M. S. Ferreira, S. Sanvito, M. Kociak, and J. M. D. Coey, “Contact induced magnetism in carbon nanotubes,” *Journal of Physics: Condensed Matter*, vol. 16, pp. L155–L161, mar 2004.
- [90] L. L. Song, X. H. Zheng, R. L. Wang, and Z. Zeng, “Dangling bond states, edge magnetism, and edge reconstruction in pristine and b/n-terminated zigzag graphene nanoribbons,” *The Journal of Physical Chemistry C*, vol. 114, no. 28, pp. 12145–12150, 2010.
- [91] T. Pakornchote, A. Ektarawong, A. Sukserm, U. Pinsook, and T. Bovornratanaraks, “Presence and absence of intrinsic magnetism in graphitic carbon nitrides designed through c–n–h building blocks,” *Scientific reports*, vol. 12, no. 1, pp. 1–13, 2022.
- [92] T. Makarova, “Magnetic properties of carbon structures,” *Semiconductors*, vol. 38, no. 6, pp. 615–638, 2004.
- [93] H. Ohldag, T. Tyliczszak, R. Höhne, D. Spemann, P. Esquinazi, M. Ungureanu, and T. Butz, “ π -electron ferromagnetism in metal-free carbon probed by soft x-ray dichroism,” *Phys. Rev. Lett.*, vol. 98, p. 187204, May 2007.
- [94] M. M. Ugeda, I. Brihuega, F. Guinea, and J. M. Gómez-Rodríguez, “Missing atom as a source of carbon magnetism,” *Phys. Rev. Lett.*, vol. 104, p. 096804, Mar 2010.
- [95] P. O. Lehtinen, A. S. Foster, Y. Ma, A. V. Krasheninnikov, and R. M. Nieminen, “Irradiation-induced magnetism in graphite: A density functional study,” *Phys. Rev. Lett.*, vol. 93, p. 187202, Oct 2004.
- [96] O. Volnianska and P. Boguslawski, “Magnetism of solids resulting from spin polarization of p orbitals,” *Journal of Physics: Condensed Matter*, vol. 22, p. 073202, feb 2010.

- [97] Y. Ma, A. S. Foster, A. Krasheninnikov, and R. M. Nieminen, “Nitrogen in graphite and carbon nanotubes: Magnetism and mobility,” *Physical Review B*, vol. 72, no. 20, p. 205416, 2005.
- [98] A. W. Mombrú, H. Pardo, R. Faccio, O. F. de Lima, E. R. Leite, G. Zanelatto, A. J. C. Lanfredi, C. A. Cardoso, and F. M. Araújo-Moreira, “Multilevel ferromagnetic behavior of room-temperature bulk magnetic graphite,” *Phys. Rev. B*, vol. 71, p. 100404, Mar 2005.
- [99] Y. Ito, C. Christodoulou, M. V. Nardi, N. Koch, M. Kläui, H. Sachdev, and K. Müllen, “Tuning the magnetic properties of carbon by nitrogen doping of its graphene domains,” *Journal of the American Chemical Society*, vol. 137, no. 24, pp. 7678–7685, 2015. PMID: 25932672.
- [100] B. Narymbetov, A. Omerzu, V. V. Kabanov, M. Tokumoto, H. Kobayashi, and D. Mihailovic, “Origin of ferromagnetic exchange interactions in a fullerene–organic compound,” *Nature*, vol. 407, no. 6806, pp. 883–885, 2000.
- [101] N. Parkansky, B. Alterkop, R. Boxman, G. Leitus, O. Berkh, Z. Barkay, Y. Rosenberg, and N. Eliaz, “Magnetic properties of carbon nano-particles produced by a pulsed arc submerged in ethanol,” *Carbon*, vol. 46, no. 2, pp. 215–219, 2008.
- [102] Y. Ma, Y. Lu, J. Yi, Y. Feng, T. Heng, X. Liu, D. Gao, D. Xue, J. Xue, J. Ouyang, *et al.*, “Room temperature ferromagnetism in teflon due to carbon dangling bonds,” *Nature Communications*, vol. 3, no. 1, pp. 1–8, 2012.
- [103] N. Sriplai, S. Pinitsoontorn, A. Chompoosor, S. Amnuaypanich, S. Maensiri, and V. Amornkitbamrung, “Ferromagnetism in metal-free polymers,” *IEEE Magnetics Letters*, vol. 6, pp. 1–4, 2015.
- [104] D. Hautot, Q. A. Pankhurst, and J. Dobson, “Superconducting quantum interference device measurements of dilute magnetic materials in biological samples,” *Review of Scientific Instruments*, vol. 76, no. 4, p. 045101, 2005.
- [105] E. N. Kaufmann, *Characterization of Materials, 2 Volume Set*. 2003.
- [106] A. G. Shard, “Detection limits in xps for more than 6000 binary systems using al and mg k x-rays,” *Surface and Interface Analysis*, vol. 46, no. 3, pp. 175–185, 2014.
- [107] B. Ranby and J. F. Rabek, *ESR spectroscopy in polymer research*, vol. 1. Springer Science & Business Media, 2012.

- [108] E. Coronado, “Molecular magnetism: from chemical design to spin control in molecules, materials and devices,” *Nature Reviews Materials*, vol. 5, no. 2, pp. 87–104, 2020.
- [109] J. S. Miller, J. H. Zhang, and W. M. Reiff, “Ferromagnetic behavior of linear chain charge transfer complexes. structural and magnetic characterization of decamethylferrocenium hexacyanobutadienide (1:1): [fe(c5me5)2].cntdot.+[c4(cn)6].cntdot.-,” *Journal of the American Chemical Society*, vol. 109, no. 15, pp. 4584–4592, 1987.
- [110] D. c. v. A. Pejaković, C. Kitamura, J. S. Miller, and A. J. Epstein, “Photoinduced magnetization in the organic-based magnet $\text{Mn}(\text{TCNE})_x\text{y}(\text{ch}_2\text{cl}_2)$,” *Phys. Rev. Lett.*, vol. 88, p. 057202, Jan 2002.
- [111] A. Rajca, J. Wongsriratanakul, and S. Rajca, “Magnetic ordering in an organic polymer,” *Science*, vol. 294, no. 5546, pp. 1503–1505, 2001.
- [112] O. V. Yazyev and L. Helm, “Defect-induced magnetism in graphene,” *Phys. Rev. B*, vol. 75, p. 125408, Mar 2007.
- [113] J. Červenka, M. Katsnelson, and C. Flipse, “Room-temperature ferromagnetism in graphite driven by two-dimensional networks of point defects,” *Nature Physics*, vol. 5, no. 11, pp. 840–844, 2009.
- [114] P. Esquinazi, A. Setzer, R. Höhne, C. Semmelhack, Y. Kopelevich, D. Spemann, T. Butz, B. Kohlstrunk, and M. Lösche, “Ferromagnetism in oriented graphite samples,” *Phys. Rev. B*, vol. 66, p. 024429, Jul 2002.
- [115] H. Zhou, C. C. Mayorga-Martinez, S. Pané, L. Zhang, and M. Pumera, “Magnetically driven micro and nanorobots,” *Chemical Reviews*, vol. 121, no. 8, pp. 4999–5041, 2021.
- [116] J. Li, B. E.-F. de Ávila, W. Gao, L. Zhang, and J. Wang, “Micro/nanorobots for biomedicine: Delivery, surgery, sensing, and detoxification,” *Science Robotics*, vol. 2, no. 4, p. eaam6431, 2017.
- [117] E. L. Mayes, F. Vollrath, and S. Mann, “Fabrication of magnetic spider silk and other silk-fiber composites using inorganic nanoparticles,” *Advanced Materials*, vol. 10, no. 10, pp. 801–805, 1998.
- [118] X. Liu, Y. Sun, B. Chen, Y. Li, P. Zhu, P. Wang, S. Yan, Y. Li, F. Yang, and N. Gu, “Novel magnetic silk fibroin scaffolds with delayed degradation for potential long-distance vascular repair,” *Bioactive materials*, vol. 7, pp. 126–143, 2022.

- [119] S. K. Samal, M. Dash, T. Shelyakova, H. A. Declercq, M. Uhlarz, M. Banobre-Lopez, P. Dubruel, M. Cornelissen, T. Herrmannsdorfer, J. Rivas, *et al.*, “Biomimetic magnetic silk scaffolds,” *ACS applied materials & interfaces*, vol. 7, no. 11, pp. 6282–6292, 2015.
- [120] T. Matsuhira and S. Osaki, “Molecular weight of nephila clavata spider silk,” *Polymer journal*, vol. 47, no. 6, pp. 456–459, 2015.
- [121] Frische, Maunsbach, and Vollrath, “Elongate cavities and skin–core structure in nephila spider silk observed by electron microscopy,” *Journal of Microscopy*, vol. 189, no. 1, pp. 64–70, 1998.
- [122] S. Y. Cho, Y. S. Yun, S. Lee, D. Jang, K.-Y. Park, J. K. Kim, B. H. Kim, K. Kang, D. L. Kaplan, and H.-J. Jin, “Carbonization of a stable β -sheet-rich silk protein into a pseudographitic pyroprotein,” *Nature communications*, vol. 6, no. 1, pp. 1–7, 2015.
- [123] H. Sogawa, K. Nakano, A. Tateishi, K. Tajima, and K. Numata, “Surface analysis of native spider draglines by fe-sem and xps,” *Frontiers in Bioengineering and Biotechnology*, vol. 8, 2020.
- [124] A. Choudhary, D. Gandla, G. R. Krow, and R. T. Raines, “Nature of amide carbonylcarbonyl interactions in proteins,” *Journal of the American Chemical Society*, vol. 131, no. 21, pp. 7244–7246, 2009. PMID: 19469574.
- [125] F. Bou-Abdallah and N. D. Chasteen, “Spin concentration measurements of high-spin ($g= 4.3$) rhombic iron (iii) ions in biological samples: theory and application,” *JBIC Journal of Biological Inorganic Chemistry*, vol. 13, no. 1, pp. 15–24, 2008.
- [126] C. Legein, J. Buzare, J. Emery, and C. Jacoboni, “Electron paramagnetic resonance determination of the local field distribution acting on cr^{3+} and fe^{3+} in transition metal fluoride glasses (tmfg),” *Journal of Physics: Condensed Matter*, vol. 7, no. 20, p. 3853, 1995.
- [127] V. Ranade, B. Panda, R. J. Choudhary, R. Ahuja, and K. P. Singh, “Atomic defects magnetize spider silks,” *Unpublished results*, 2022.
- [128] R. Robson, “Microvoids in bombyx mori silk. an electron microscope study,” *International journal of biological macromolecules*, vol. 24, no. 2-3, p. 145—150, 1999.
- [129] J. Wang and W. Gao, “Nano/microscale motors: biomedical opportunities and challenges,” *ACS nano*, vol. 6, no. 7, pp. 5745–5751, 2012.

- [130] D. N. Rockwood, R. C. Preda, T. Yücel, X. Wang, M. L. Lovett, and D. L. Kaplan, “Materials fabrication from bombyx mori silk fibroin,” *Nature protocols*, vol. 6, no. 10, pp. 1612–1631, 2011.
- [131] K. C. Neuman and A. Nagy, “Single-molecule force spectroscopy: optical tweezers, magnetic tweezers and atomic force microscopy,” *Nature methods*, vol. 5, no. 6, pp. 491–505, 2008.
- [132] C. Gosse and V. Croquette, “Magnetic tweezers: Micromanipulation and force measurement at the molecular level,” *Biophysical Journal*, vol. 82, no. 6, pp. 3314–3329, 2002.
- [133] C. V. Mora, M. Davison, J. Martin Wild, and M. M. Walker, “Magnetoreception and its trigeminal mediation in the homing pigeon,” *Nature*, vol. 432, no. 7016, pp. 508–511, 2004.
- [134] R. Blakemore, “Magnetotactic bacteria,” *Science*, vol. 190, no. 4212, pp. 377–379, 1975.
- [135] W. Wiltschko and R. Wiltschko, “Magnetic orientation and magnetoreception in birds and other animals,” *Journal of comparative physiology A*, vol. 191, no. 8, pp. 675–693, 2005.
- [136] L. E. Foley, R. J. Gegear, and S. M. Reppert, “Human cryptochrome exhibits light-dependent magnetosensitivity,” *Nature communications*, vol. 2, no. 1, pp. 1–3, 2011.
- [137] C. X. Wang, I. A. Hilburn, D.-A. Wu, Y. Mizuhara, C. P. Cousté, J. N. H. Abrahams, S. E. Bernstein, A. Matani, S. Shimojo, and J. L. Kirschvink, “Transduction of the geomagnetic field as evidenced from alpha-band activity in the human brain,” *eNeuro*, vol. 6, no. 2, 2019.
- [138] J. B. Phillips, “Two magnetoreception pathways in a migratory salamander,” *Science*, vol. 233, no. 4765, pp. 765–767, 1986.
- [139] R. A. Holland, K. Thorup, M. J. Vonhof, W. W. Cochran, and M. Wikelski, “Bat orientation using earth’s magnetic field,” *Nature*, vol. 444, no. 7120, pp. 702–702, 2006.
- [140] S. Begall, J. Červený, J. Neef, O. Vojtěch, and H. Burda, “Magnetic alignment in grazing and resting cattle and deer,” *Proceedings of the National Academy of Sciences*, vol. 105, no. 36, pp. 13451–13455, 2008.

- [141] V. Hart, P. Nováková, E. P. Malkemper, S. Begall, V. Hanzal, M. Ježek, T. Kušta, V. Němcová, J. Adámková, K. Benediktová, *et al.*, “Dogs are sensitive to small variations of the earth’s magnetic field,” *Frontiers in Zoology*, vol. 10, no. 1, pp. 1–12, 2013.
- [142] C. T. Rodgers and P. J. Hore, “Chemical magnetoreception in birds: The radical pair mechanism,” *Proceedings of the National Academy of Sciences*, vol. 106, no. 2, pp. 353–360, 2009.
- [143] A. J. KALMIJN, “The Electric Sense of Sharks and Rays,” *Journal of Experimental Biology*, vol. 55, pp. 371–383, 10 1971.
- [144] A. Mathis and F. R. Moore, “Geomagnetism and the homeward orientation of the box turtle, *terrapene carolina*,” *Ethology*, vol. 78, no. 4, pp. 265–274, 1988.
- [145] I. A. Solov’yov and W. Greiner, “Theoretical analysis of an iron mineral-based magnetoreceptor model in birds,” *Biophysical Journal*, vol. 93, no. 5, pp. 1493–1509, 2007.
- [146] G. C. Nordmann, T. Hochstoeger, and D. A. Keays, “Magnetoreception—a sense without a receptor,” *PLoS biology*, vol. 15, no. 10, p. e2003234, 2017.
- [147] A. M. K. Dagamseh, R. J. Wiegerink, T. S. J. Lammerink, and G. J. M. Krijnen, “Towards a high-resolution flow camera using artificial hair sensor arrays for flow pattern observations,” *Bioinspiration & Biomimetics*, vol. 7, p. 046009, sep 2012.
- [148] Y. Ozaki, T. Ohyama, T. Yasuda, and I. Shimoyama, “An air flow sensor modeled on wind receptor hairs of insects,” in *Proceedings IEEE Thirteenth Annual International Conference on Micro Electro Mechanical Systems (Cat. No. 00CH36308)*, pp. 531–536, IEEE, 2000.
- [149] S. Inoue, K. Tanaka, F. Arisaka, S. Kimura, K. Ohtomo, and S. Mizuno, “Silk fibroin of bombyx mori is secreted, assembling a high molecular mass elementary unit consisting of h-chain, l-chain, and p25, with a 6:6:1 molar ratio*,” *Journal of Biological Chemistry*, vol. 275, no. 51, pp. 40517–40528, 2000.
- [150] T. Asakura, J. Yao, T. Yamane, K. Umemura, and A. S. Ulrich, “Heterogeneous structure of silk fibers from bombyx mori resolved by ¹³C solid-state nmr spectroscopy,” *Journal of the American Chemical Society*, vol. 124, no. 30, pp. 8794–8795, 2002. PMID: 12137522.
- [151] S. Gregory, “Adsorbed oxygen as an amorphous antiferromagnetic system,” *Phys. Rev. Lett.*, vol. 39, pp. 1035–1038, Oct 1977.